MinEx CRC Limited
26 Dick Perry Avenue, Kensington, WA, 6151
PO Box 1130, Bentley, WA, 6102, Australia
admin@minexcrc.com.au

MinEx CRC
ABN: 66 625 533 913

MinEx CRC provides financial support to the value of $1K to promote Honours and Masters by Coursework projects that are aligned with the mission of MinEx CRC and to encourage young researchers toward a career in mineral exploration research. Projects are not restricted to MinEx CRC Participants and Affiliates.

Please note that the content of this thesis has not been subjected to peer-review and subsequent corrections.

Australian Government
Department of Industry, Science and Resources
Cooperative Research Centres Program

Geochemistry of the Loch Lilly-Kars volcanics and correlation along the Tasman Line, Eastern Australia

Violet Perry

Supervisors: Honorary Associate Professor Robin Offler, Ryan Dwyer, Dr David Boutelier

Co-Supervisors: Dr John Greenfield and Dr Alistair Hack

April 2021

Contents

1 Introduction **1**

1.1 Background 1

1.2 Geological Setting 2

1.2.1 Koonenberry Belt 4

1.2.2 Loch Lilly-Kars Belt 5

1.2.3 Adelaide Fold Belt 7

1.2.4 Glenelg River Complex 8

1.2.5 Mount Stavely Volcanic Complex 8

1.3 Tectonic Models 9

1.3.1 East-dipping subduction zone and polarity reversal. 9

1.3.2 West-dipping subduction zone. 12

1.4 Knowledge Gaps 18

1.5 Aims of this Study 18

2 Data and Methodology **20**

2.1 Data Accessed 20

2.2 Methods 21

2.2.1 Remote Sampling 21

2.2.2 Sample Preparation 22

2.2.3 Zircon Geochronology 24

2.2.4 Titanite Geochronology 27
2.2.5 Geochemistry 28
2.2.6 Sm-Nd Isotopic Analysis 29
2.2.7 Petrography 30

3 Petrography **31**

4 Geochemistry **33**

4.1 Introduction 33
4.2 Loch Lilly-Kars 34
4.3 Koonenberry 40

5 Zircon Geochronology **48**

5.1 Introduction 48
5.2 Zircon Morphology 50
5.2.1 VP001 50
5.2.2 VP002 51
5.2.3 VP007 51
5.2.4 VP008 52
5.2.5 VP012 52
5.2.6 VP013 53
5.2.7 PJG0059 55
5.2.8 PJG0080 55
5.2.9 PJG0082 56
5.3 Trace Elements 56
5.4 U-Pb Ages 58
5.4.1 VP001 58
5.4.2 VP002 59
5.4.3 VP008 61

5.4.4 VP012 63
5.4.5 VP013 67
5.4.6 PJG0059 69
5.4.7 PJG0080 71
5.4.8 PJG0082 73
5.5 Lu-Hf Isotope Signatures 75

6 Sm-Nd Isotopic Analysis **77**
6.1 Introduction 77
6.2 Sm-Nd Isotopes 78

7 Titanite Geochronology **79**
7.1 Introduction 79
7.2 Titanite Morphology 80
7.2.1 VP003 and VP004 80
7.2.2 VP006 and VP007 81
7.3 U-Pb Ages 83
7.3.1 VP003 83
7.3.2 VP004 83
7.3.3 VP006 and VP007 84
7.4 Interpretation 84

8 Discussion **86**
8.1 Interpretation of Loch Lilly-Kars Geochemistry 86
8.1.1 Delamerian 87
8.1.2 Late Silurian to Early Devonian 89
8.2 Interpretation of the Koonenberry Geochemistry 91
8.3 Correlation with the Adelaide Fold Belt, Glenelg River Complex and Mount Stavely Complex 95

8.4 Sm-Nd and Lu-Hf Isotopes 99

9 Conclusions and Recommendations for Future Work 106

10 References 108

A Seismic Line 121

B Sample List 123

C Sample Descriptions 126

C.0.1 VP001 126

C.0.2 VP002 128

C.0.3 VP003 130

C.0.4 VP004 132

C.0.5 VP005 133

C.0.6 VP006 135

C.0.7 VP007 136

C.0.8 VP008 138

C.0.9 VP009 138

C.0.10 VP010 140

C.0.11 VP012 143

C.0.12 VP013 144

C.0.13 PJG0058 146

C.0.14 PJG0059 148

C.0.15 PJG0080 148

C.0.16 PJG0082 150

C.0.17 DD89GR05 - 83.5 m 152

C.0.18 DD89GR05 - 95 m 154

D Geochemistry Data 156

E Geochronology Data **185**

F Sm-Nd Isotopic Data **261**

G Trace Element Data **264**

H Lu-Hf Data **282**

I Response to Reviewer Comments **292**

I.1 Reviewer 1 292

I.1.1 General 292

I.1.2 Comment 1.1 292

I.1.3 Comment 1.2 293

I.1.4 Comment 1.3 293

I.1.5 Comment 1.4 293

List of Figures

1.1 Location of the Delamerian Orogen 2

1.2 Geophysical Trend Line of Cambrian Volcanics 4

1.3 East-dipping Subduction Zone Model 10

1.4 Spidergram for Typical Subduction Zone Rock Types 11

1.5 West-dipping Subduction Zone Model 13

1.6 Structural Domains of the Koonenberry and Loch Lilly-Kars Belts NSW 15

1.7 Bunda Cross-Section Profile 16

1.8 Geophysical Cross-Section of the Loch Lilly Kars Belt 17

3.1 Map of Sample Locations 32

4.1 Zr/TiO_2 vs Nb/Y Discrimination Diagram for the Loch Lilly-Kars Volcanics 34

4.2 Chondrite-normalised Patterns for Mafic Rocks of the Loch Lilly-Kars 36

4.3 NMORB-normalised Patterns for Mafic Rocks of the Loch Lilly-Kars 37

4.4 Chondrite-normalised Patterns for Intermediate to Felsic Rocks of the Loch Lilly-Kars 38

4.5 NMORB-normalised Patterns for Intermediate to Felsic Rocks of the Loch Lilly-Kars 39

4.6 Th/Yb vs Nb/Yb Discrimination Diagram for Mafic Rocks of the Loch Lilly-Kars 40
4.7 Th-Zr-Nb Discrimination Diagram for Mafic Rocks of the Loch Lilly-Kars 41
4.8 Th/Yb vs Ta/Yb and Th/Ta vs Yb Discrimination Diagrams for Intermediate to Felsic Rocks of the Loch-Lilly Kars 42
4.9 Chondrite-normalised (A) and NMORB-normalised Patterns for VP010 43
4.10 Zr/TiO_2 vs Nb/Y Discrimination Diagram for Volcanic Rocks of the Koonenberry 43
4.11 Chondrite-normalised Patterns for Mafic Rocks of the Koonenberry . 44
4.12 NMORB-normalised Patterns for Mafic Rocks of the Koonenberry . . 45
4.13 Th/Yb vs Nb/Yb Discrimination Diagram for Mafic Rocks of the Koonenberry 46
4.14 Th-Zr-Nb Discrimination Diagram for Mafic Rocks of the Koonenberry 47

5.1 Transmitted Light and Cathodoluminescence Images of Zircon for VP001 51
5.2 Transmitted Light and Cathodoluminescence Images of Zircon for VP002 52
5.3 Transmitted Light and Cathodoluminescence Images of Zircon for VP008 53
5.4 Transmitted Light and Cathodoluminescence Images of Zircon for VP012F 54
5.5 Transmitted Light and Cathodoluminescence Images of Zircon for VP012M 54
5.6 Transmitted Light and Cathodoluminescence Images of Zircon for PJG0059 55

5.7 Transmitted Light and Cathodoluminescence Images of Zircon for PJG0080 56
5.8 Transmitted Light and Cathodoluminescence Images of Zircon for PJG0082 57
5.9 Zircon Trace Element Patterns for Loch Lilly-Kars and Koonenberry Samples 57
5.10 Concordia and Weighted Mean Average Diagrams for VP001 60
5.11 Concordia and Weighted Mean Average Diagrams for VP002 62
5.12 Concordia and Weighted Mean Average Diagrams for VP008 64
5.13 Concordia and Weighted Mean Average Diagrams for VP0012F . . . 66
5.14 Concordia and Weighted Mean Average Diagrams for VP0012M . . . 68
5.15 Concordia and Weighted Mean Average Diagrams for PJG0059 . . . 70
5.16 Concordia and Weighted Mean Average Diagrams for PJG0080 . . . 72
5.17 Concordia and Weighted Mean Average Diagrams for PJG0082 . . . 74
5.18 ϵHf values of igneous rocks of the Loch Lilly-Kars and Koonenberry. Loch Lilly-Kars drill core samples include VP001, VP002, VP008, VP012F and VP012M. Koonenberry outcrop samples include PJG0059, PJG0080 and PJG0082. 76

7.1 Crossed-polars and Plane-polarised Light Images of TS VP003-2 . . . 80
7.2 Transmitted Light and Backscattered-Electron Images of Titanite Grains from VP003. 81
7.3 Transmitted Light and Backscattered-Electron Images of Titanite Grains from VP004. 81
7.4 Transmitted Light and Backscattered-Electron Images of Titanite Grains from VP006. 82
7.5 Transmitted Light and Backscattered-Electron Images of Titanite Grains from VP007. 82

7.6 Wetherill-type Concordia diagram for VP003. 84
7.7 Wetherill-type Concordia diagram for VP004. 85
7.8 Wetherill-type Concordia diagram for VP006 and VP007. 85

8.1 Th/Yb vs Nb/Yb Discrimination Diagram Comparing the Siluro-Devonian LLK with Other Rift-Related Suites in the Tasmanides. . . 90
8.2 NMORB-normalised Patterns for the Wertago Volcanics 91
8.3 NMORB-normalised Patterns for the Bittles Tank Volcanics, Nuntherungie Dolerite and Kayrunnera Gabbro 93
8.4 NMORB-normalised Patterns for the Black Hill Gabbroic Complex Compared to Loch Lilly-Kars Samples 98
8.5 ϵNd Values of Igneous Rocks of the Delamerian and Lachlan Orogens 100
8.6 ϵHf Values of Igneous Rocks of the Delamerian and Lachlan Orogens 101

A.1 GA Seismic Line 122

C.1 Core sample VP001 from LLK drill hole EHK1. 127
C.2 XPL and PPL Images of VP001 127
C.3 Core sample VP002 from LLK drill hole EHK2. 129
C.4 XPL and PPL Images of VP002 129
C.5 XPL and PPL Images of VP002-02 130
C.6 Core sample VP003 from LLK drill hole EHK3. 131
C.7 XPL and PPL Images of VP003. 131
C.8 XPL and PPL Images of VP003. 132
C.9 Core sample VP004 from LLK drill hole EHK3. 133
C.10 XPL and PPL Images of VP004. 134
C.11 XPL and PPL Images of VP004. 134
C.12 Core sample VP005 from LLK drill hole EHK3. 135
C.13 XPL and PPL Images of VP005. 135

C.14 Core sample VP006 from LLK drill hole NBH004. 136
C.15 XPL and PPL Images of VP006. 136
C.16 Core sample VP007 from LLK drill hole NBH004. 137
C.17 XPL and PPL Images of VP007. 137
C.18 Core sample VP008 from LLK drill hole NBH005. 138
C.19 XPL and PPL Images of VP008. 139
C.20 XPL and PPL Images of VP008. 139
C.21 Core sample VP009 from LLK drill hole NBH005. 140
C.22 XPL and PPL Images of VP009. 141
C.23 Core sample VP010 from LLK drill hole NBH005. 142
C.24 XPL and PPL Images of VP010. 142
C.25 XPL and PPL Images of VP010. 142
C.26 XPL and PPL Images of VP010. 143
C.27 Core sample VP012 from LLK drill hole NBH009. 144
C.28 XPL and PPL Images of VP012. 144
C.29 XPL and PPL Images of VP012-02. 145
C.30 XPL and PPL Images of VP012-03. 145
C.31 Core sample VP013 from LLK drill hole NBH012. 146
C.32 XPL and PPL Images of VP013. 146
C.33 Koonenberry outcrop sample PJG0058. 147
C.34 XPL and PPL Images of PJG0058. 147
C.35 Koonenberry outcrop sample PJG0059. 148
C.36 XPL and PPL Images of PJG0059. 149
C.37 Koonenberry outcrop sample PJG0080. 150
C.38 XPL and PPL Images of PJG0080. 151
C.39 Koonenberry outcrop sample PJG0082. 151
C.40 XPL and PPL Images of PJG0082. 152

C.41 Core sample DD89GR05-83.5 from Koonenberry drill hole DD89GR05.153
C.42 XPL and PPL Images of DD89GR05-83.5. 153
C.43 XPL and PPL Images of DD89GR05-83.5. 153
C.44 Core sample DD89GR05-95 from Koonenberry drill hole DD89GR05. 155
C.45 XPL and PPL Images of DD89GR05-95. 155
C.46 XPL and PPL Images of DD89GR05-95. 155

List of Tables

2.1 Zircon Standard Ages 25
2.2 Hafnium Standards 26

5.1 Existing Ages for the Loch Lilly-Kars 49
5.2 Zircon U-Pb Results 58

6.1 Sm-Nd Results 78

7.1 Titanite U-Pb Results 83

B.1 List of samples for this project 123

D.1 Raw Geochemistry Data (LLK) 157
D.2 Raw Geochemistry Data (Koonenberry) 181

E.1 Raw Zircon Geochronology Data from Session One 186
E.2 Raw Zircon Geochronology Data from Session Two 228
E.3 Raw Titanite Geochronology Data 247

F.1 Raw Sm-Nd Data 262

G.1 Raw Zircon Trace Element Data 265

H.1 Raw Zircon Lu-Hf Data 283

Declaration

Except where due reference is made, this thesis is of original research and contains no material previously published or submitted to another institution or university.

Violet Eve Angela Perry April 2021

Abstract

This project focuses on the age, geochemical and isotopic characteristics of the Loch Lilly-Kars Belt in western New South Wales, Australia to provide a better understanding of the tectonic setting of this segment southeast of the Tasman Line and correlate with other regions of the Delamerian Orogen. The Loch Lilly-Kars Belt is inferred to be the continuation of the Koonenberry Belt sequence of the Cambrian Mount Wright and Bittles Tank Volcanics and is entirely undercover, therefore knowledge of the basement rocks is based on a limited number of drill holes and geophysical imagery. Previous studies and exploration programs have assessed the potential for porphyry Cu mineralisation, focusing largely on the intermediate to felsic rocks, however, the mafic units remain largely unconstrained and poorly understood in regards to age and tectonic setting.

U-Pb zircon and titanite analyses of six Loch Lilly-Kars mafic to intermediate samples from this study reveal that there are Cambrian and Late Silurian to Early Devonian igneous intrusive sequences as well as localised deformation or thermal events at 430 to 420 Ma. Previous studies have also identified a Cambrian calc-alkaline, continental arc sequence that has been correlated with the Mount Wright Volcanics, thus it is evident that the Loch Lilly-Kars records multiple episodes of magmatic activity.

This study also analysed five samples previously interpreted to belong to the Bittles

Tank Volcanics of the Koonenberry Belt. U-Pb analysis of zircons recovered from two of the mafic samples returned unexpected results of Siluro-Devonian ages, younger than the inferred Cambrian age of 510 Ma for the Bittles Tank Volcanics. However, a third mafic sample returned an age of 509 ± 1.17 Ma and shows very strong geochemical similarities to the Bittles Tank Volcanics.

Geochemical investigation reveals that the northern Delamerian (Koonenberry and Loch Lilly-Kars Belts) and the southern Delamerian (Adelaide Fold Belt, Glenelg River Complex and Mount Stavely Complex) show distinct differences, possibly due to differences in mantle sources and basement architecture. This is reflected in the Sm-Nd and Lu-Hf isotopic analyses, revealing arrays that display a mix of mantle-like and crustal values for the northern Delamerian, whereas the southern Delamerian is more compressed towards negative, crustal-like values. This indicates a more significant contribution of the ancient cratonic crustal component is present in the southern Delamerian.

The Siluro-Devonian calc-alkaline Loch Lilly-Kars samples show similarities to the continental rift-related Wertago Volcanics of the Koonenberry Belt, as well as other rift-related volcanic sequences of the Lachlan and Thomson Orogenies. Sm-Nd and Lu-Hf isotopic analyses for the Siluro-Devonian Loch Lilly-Kars sequence reveal an almost identical isotopic signature of mixing between mantle-like and crustal source components, and display a return to more juvenile isotopic compositions more rapidly than observed in the Lachlan Orogen.

Acknowledgements

This project was funded and supported by the University of Newcastle, Newcastle Institute for Energy and Resources (NIER), Geological Survey of NSW (GSNSW) and MinEx CRC.

First and foremost I would like to thank my supervisors Robin Offler, Ryan Dywer and David Boutelier who have provided continual support and guidance throughout this project. Thank you for always finding the time for discussing details of the project, answering my many questions and providing expert advise.

I would also like to acknowledge and again thank Ryan for his extensive knowledge of geochronology as well as for the training and assistance with rock crushing, mineral separation and the tedious task that is the mounting of zircon grains. Thank you for taking the time to discuss any topic and help get things done.

A big thank you to Brian Casey at the Broken Hill Drill Core Library for remote sampling. This project would not have been possible without his assistance and I am extremely grateful for the time spent in organising, sampling and packaging the samples for delivery to NIER.

Thank you Phil Gilmore and John Greenfield at the GSNSW for providing expert advice and insight into difficult concepts, as well as for helping set the scope of the project. I wish we could have completed the field work as it would have been an incredible experience to work alongside you both in the field. Again, thank you Phil

for organising the remote sampling and providing rock samples and thin sections from the Koonenberry.

I would also like to thank the following people for making this project possible.

Dr. Roland Mass, Isotope Geoscience Group, School of Earth Sciences, University of Melbourne.

Dr. Hui-Qing Huang (Jeffrey) (James Cook University) for completing the titanite analytical procedures.

Professor Chris Clark and Professor Chris Kirkland (Curtin University) for completing the zircon analytical procedures.

Yan Yan Sun (University of Newcastle) for the training and assistance in making thin sections and performing epoxy resin polishing.

Finally, thank you to my partner Jai Roby for the love, support and encouragement.

Chapter 1

Introduction

1.1 Background

The Delamerian Orogen is situated between the Precambrian cratons of Australia and the Paleozoic to Mesozoic orogenic belts of Eastern Australia (Fig 1.1), encompassing Precambrian and Early Cambrian rock sequences that were metamorphosed and deformed throughout the Cambrian (Foden et al., 2006). This orogen is known to have developed along the paleo-Pacific margin coincident with the assembly of the Gondwana supercontinent (Foden et al., 2020), although the tectonic setting and geological evolution of the Delamerian Orogen in New South Wales (NSW), Victoria (VIC) and South Australia (SA) is not well constrained (Crawford et al., 1997). East Gondwana in south-eastern Australia was a passive margin during the Neoproterozoic, involving rifting of the continental crust following the separation of Rodinia (Greenfield et al., 2011). However, there are conflicting ideas and two main tectonic models proposed to explain the presence of Cambrian tholeiitic and calc-alkaline volcanics eastward of this passive margin (Greenfield et al., 2011); namely that these volcanics were produced by post collisional volcanism, or they represent a fossil volcanic arc.

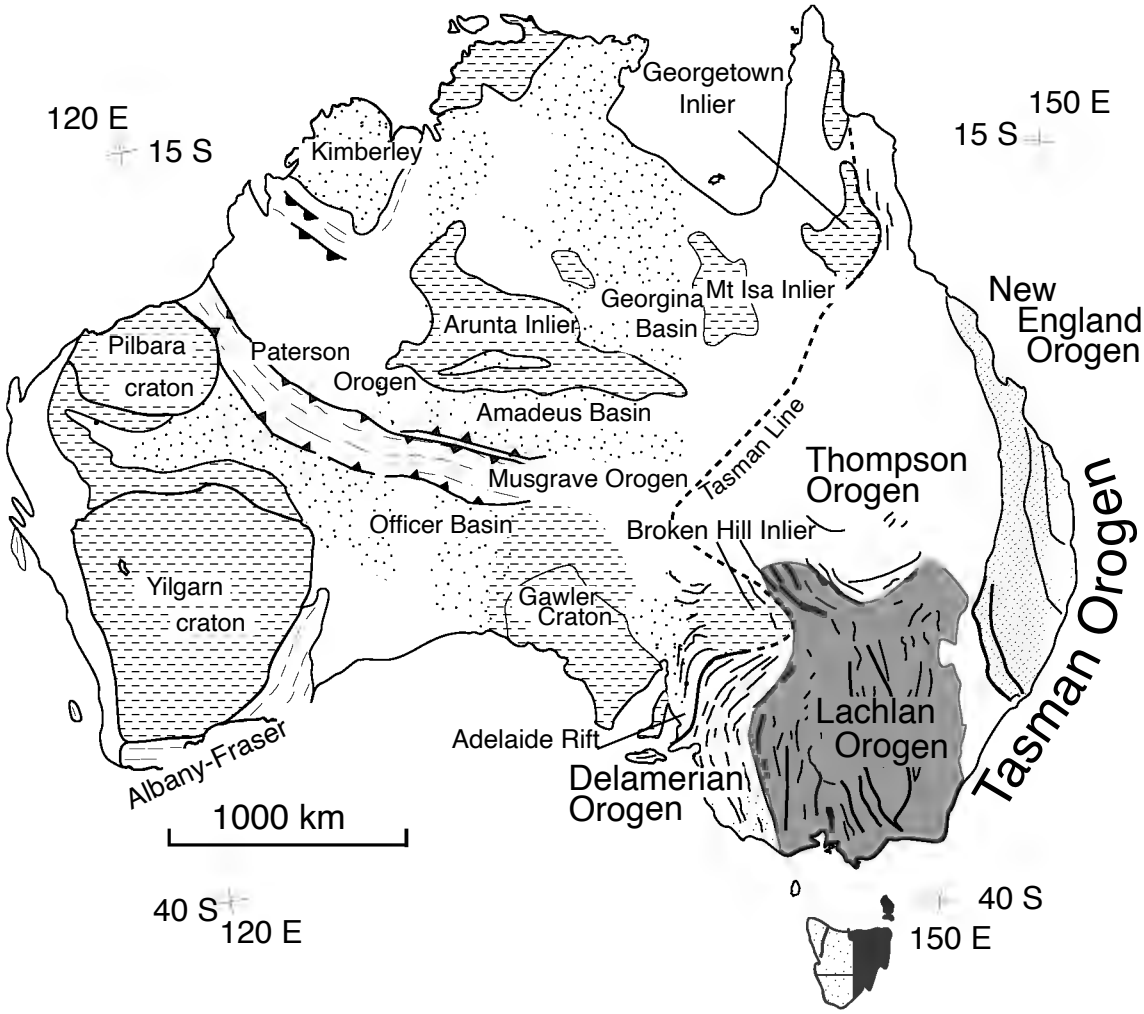

Figure 1.1: Map of the major Australian geological components, displaying the location of the Delamerian Orogen and the Tasman Line in Eastern Australia. (Modified from Foster and Gray 2000).

1.2 Geological Setting

The Delamerian Orogen marks a major shift in the tectonic setting of the Australian continent involving the transition from a Neoproterozoic passive margin to an active subduction zone along the eastern Gondwanan margin (Rosenbaum 2018), and initiation of the tectonic style characteristic of present day west Pacific margins (Foden et al., 2020). Regions of the Delamerian Orogen on mainland Australia include the Koonenberry Belt and Loch Lily-Kars Belt in NSW, the Adelaide Fold Belt in SA, as well as the Glenelg River Complex and Mt Stavely Complex in VIC. These areas

appear to follow a sinuous geophysical trend line (Fig 1.2), which closely resembles the shape of the Tasman Line (Fig 1.1), the suture marking the edge of Proterozoic Australia (Direen and Crawford, 2003). Remnants of volcanic arcs active during the Delamerian Orogen are preserved in NSW and VIC, including the Koonenberry Belt c. 510 Ma Mount Wright Arc extensively studied by Greenfield et al. (2011) and the potentially corresponding sequences of the Loch Lilly-Kars Belt in NSW, as well as the c. 520-500 Ma Mount Stavely Volcanic Complex in VIC. The Delamerian Orogen extends to Tasmania (Tyennan Orogen) as well as further south to Antarctica (Ross Orogen), where Cambrian calc-alkaline volcanics have been identified within the Mt Read Volcanic Complex and Bowers Rift (Foster et al., 2005) respectively. These volcanics are considered equivalents to that of the Mount Stavely Complex with respect to geochemistry, suggesting a continuation in magmatism along the Gondwana margin (Foster et al., 2005).

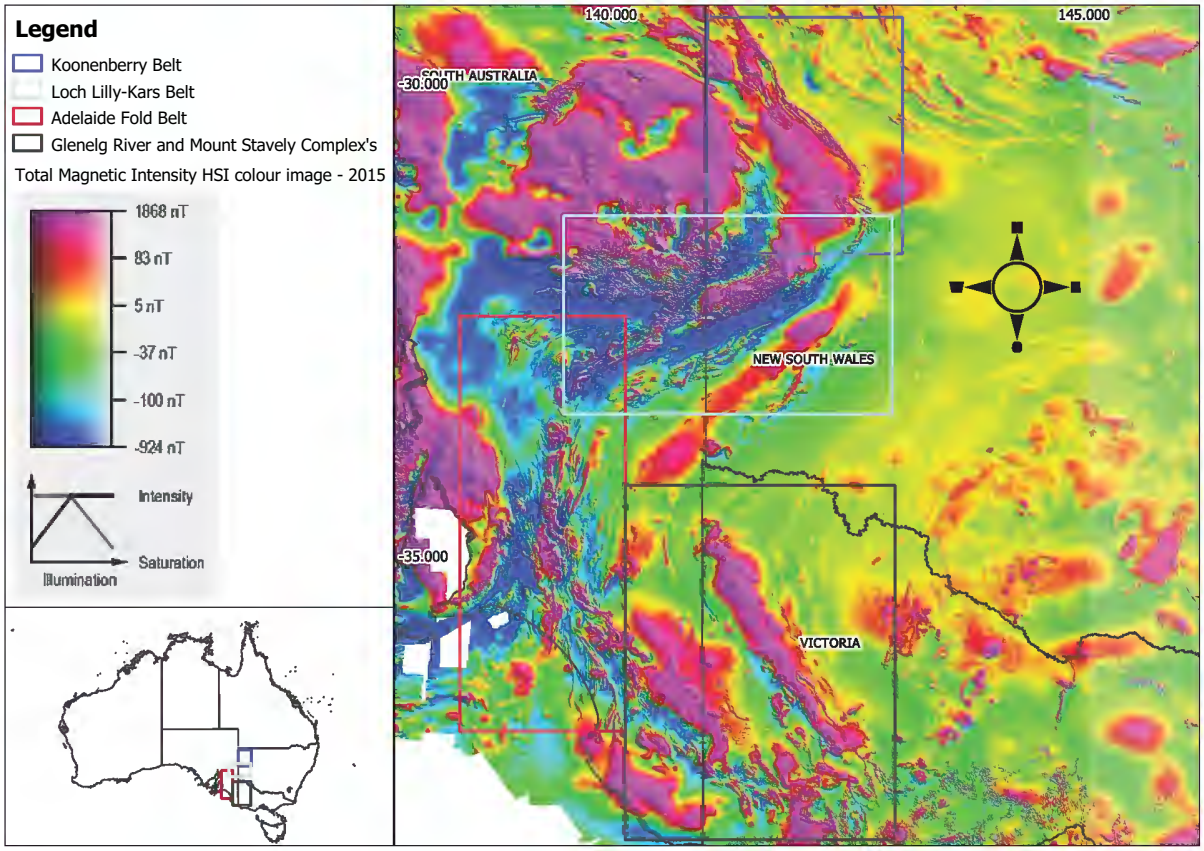

Figure 1.2: Total magnetic intensity (TMI) geophysics image overlain by regions containing Cambrian volcanic sequences that lie on a magnetic trend (TMI image supplied by Geoscience Australia).

1.2.1 Koonenberry Belt

The Koonenberry Belt trends NW-SE adjacent to the Broken Hill Block (Curnamona Province), covering an area of approximately 80 km by 300 km (Fig 1.2). This belt contains outcrops of Neoproterozoic to Cambrian volcanic rocks (Greenfield et al., 2011) which preserve various phases of igneous activity indicated by changes in geochemistry and age. The volcanic phases include the alkaline rift-related Mt Arrowsmith volcanics of the Grey Range Group (580 Ma), tholeiitic and calc- alkaline Mount Wright Volcanics (510 Ma) of the Gnalta Group, and tholeiitic and calc-alkaline Bittles Tank Volcanics of the Ponto Group also of Cambrian age

(Greenfield et al., 2011).

1.2.2 Loch Lilly-Kars Belt

The Loch Lilly-Kars Belt (LLK) extends along the southern edge of the Broken Hill Block in western NSW, encompassing an area of 40 km by 200 km and trending NE-SW (Fig 1.2). Unlike the Koonenberry Belt the Loch Lilly-Kars is entirely undercover, covered by up to 300 m of sediments ranging from Mesozoic to Cenozoic in age (Baatar et al., 2019). Therefore knowledge of the basement rocks is limited and largely reliant on geophysical data and drill cores which intersect calc-alkaline and tholeiitic volcanic units inferred to be Cambrian age (Greenfield et al., 2011). Crawford (2013) states that exploration targeting magnetic highs encountered volcanic and intrusive rocks that compositionally correlate with the Mt Read Volcanics and Mt Stavely Belt rocks which are calc-alkaline and shoshonitic in character. Additionally, Greenfield et al., (2011) has interpreted the Loch Lilly-Kars Belt to be the continuation of Koonenberry Belt sequence of tholeiitic and calk-alkaline arc rocks.

Previous Exploration in the Loch Lilly-Kars Belt

The Loch Lilly-Kars Belt has been subject to various exploration and drilling programs to assess the potential of basement rocks hosting porphyry copper mineralisation. There are 5 main exploration programs that targeted basement rocks of the Loch Lilly-Kars namely, Eaglehawk (Pasminco, 1996), Wahratta (CRAE, 1985), Inkerman (BHP, 1997), Quondong-Kars (Newcrest, 2002, 2003) and Burta-Curnamona and Wahratta (Mobil Energy, 1981-1982). Rocks encountered in the Wahratta, Eaglehawk, Inkerman and Quondong-Kars drilling programs were sampled and examined petrographically by Crawford and Direen (1998), and samples were also obtained for lithogeochemical study by Crawford (2013).

During 1995, Pasminco drilled holes EHK1, EHK2 and EHK3, all of which inter-

sected basement rocks at 109.6 m, 167 m and 122.5 m respectively. Microdiorite was intersected in both EHK1 and EHK2, however upon re-examination, the rocks are described as cumulate monzogabbros to monzodiorites (Polito 2015). EHK3 intersected intersected alternating andesites and doleritic dykes (Crawford 2013).

CRA drilled three holes at the Wahratta Prospect in 1985, targeting a large magnetic anomaly (Crawford 2013). The first two holes, DD96WA001 and DD96WA002 were lost as a result of hole caving, however the third hole DD96WA003 intersected basement rocks at 821 m. Basement rocks included intermediate volcanic to subvolcanic rocks with microdiorite, monzodiorite, monzonite and syenite intrusives (Polito 2015).

In 1997, BHP drilled eight holes at the Inkerman Prospect targeting magnetic anomalies. Hole IR96003 was the only drill hole that failed to intersect basement rocks, and the other seven holes intersected granodiorite, diorite, schist and rhyolite (Rennison and Rutley 1997).

The Newcrest/Platsearch drilling program of 2001 and 2002 drilled twelve holes in the Quondong district (Polito 2015), with the first eight holes drilled in 2001 and four more holes in 2002. Only NBH004, NBH005, NBH007, NBH009, NBH010, NBH011 and NBH012 were successful at intersecting basement rocks. NBH004 targeted a magnetic ridge and intersected microdiorite from 111.8 m to end of hole (EOH) at 195.3 m (Bland 2002). NBH005 targeted an ovoid shaped magnetic low and intersected shale from 142.3 m to 155.0 m, andesite porphyry from 155.0 m to 159.85 m, shale from 159.85 m to 163.0 m, and then diorite to the EOH at 186.8 m (Bland 2002). NBH007 targeted an irregular magnetic high and was drilled on the peak of the high, intersecting diorite from 120.4 m to EOH at 155.85m (Bland 2002). NBH009 and NBH010 were designed to test the Kudgee magnetic anomaly, with NBH009 intersecting basement rocks of metabasalt and metagabbro,

and NBH010 intersecting granodiorite (Bland 2003). NBH011 intersected andesite porphyry and diorite from 238 m to EOH at 279.2 m (Polito 2015), and NBH012 intersected fine-grained olivine basalt from 214.0 m to EOH at 225.3 m (Bland 2003).

In 2013, Anglo American Exploration Australia completed a review of all open file exploration data for the Loch Lilly-Kars, involving re-sampling for petrological (Crawford 2015) and geochemical reassessment, as well as U-Pb age dating of zircon and titanite and Ar-Ar age determination of biotite alteration (Archibald 2015). Data are presented in various exploration reports for the different tenements, including EL8197 for the Quondong area, EL8198 for the overlapping area between Quondong and Eaglehawk, EL8199 for Eaglehawk and EL8200 for Netley and Kudgee.

1.2.3 Adelaide Fold Belt

South Australia contains the greatest exposure of the Delamerian Orogen (Foden et al., 2020), with the effects of Delamerian deformation best exposed in the Adelaide Fold Belt (AFB). The AFB extends 1100 km from the Peake and Denison Inliers to the western tip of Kangaroo Island (Foden et al., 2006) and contains outcrops of mafic and felsic intrusive igneous suites (Foden et al., 2020), with folded sedimentary and meta-sedimentary sequences.

The early Cambrian Normanville Group sedimentary sequence of the AFB hosts the basaltic lava flows of the Truro Volcanics dated at 522 ±2 Ma (Foden et al., 2020). The Truro Volcanics have been described as a suite of anorogenic style alkali basalts and are overlain by the clastic-rich Kanmantoo Group, considered to be a major change in the Adelaide Fold Belt's depositional history (Jago et al., 2003). In contrast to the alkali Truro Volcanics of the Normanville Group, the Kanmantoo Group hosts intrusive mafic rocks of tholeiitic composition with back arc basin characteristics, described as sills or dykes by Foden et al. (2020). These sedimentary

sequences also host syn- to post-tectonic felsic volcanics and granite suites of Middle Cambrian to Early Ordovician age (Foden et al., 2006), with the Rathjen Gneiss granitic intrusive in the southern AFB, dated at 514 ±4 Ma, providing an important constraint on the timing of the Delamerian Orogen (Foden et al., 1999). This is the oldest known Cambrian granite in the AFB, considered to be pre to early syn-tectonic, effectively marking the beginning of orogenic activity of the Delamerian (Foden et al., 1999).

1.2.4 Glenelg River Complex

The Glenelg River Complex has been considered as an eastern equivalent of the Kanmantoo Group sequence (Crawford et al., 1997). As explained by Foden et al. (2020), the geological history of the Glenelg Complex closely relates to that of the AFB, with similarities of intrusive bodies of tholeiitic metagabbros and calc-alkaline gabbros within the Harvester's Creek greywacke turbidite sequence which has been equated with the Kanmantoo Group (Foden et al., 2020). Additionally and most importantly, Kemp (2003) explains that the Glenelg River Complex diorites have compositional affinities with boninitic lavas. The presence of these boninitic rocks considered to be non-allochthonous (Foden et al., 2006) questions the validity of some early collisional tectonic models (e.g. Crawford and Berry 1992, Foster and Gray 2000, Foster et al., 2005), because boninites are distinctive Mg-rich lavas that typically erupt within the forearc region of arc environments (Kemp 2003).

1.2.5 Mount Stavely Volcanic Complex

Approximately 70 km east of the Glenelg River Complex, The Mount Stavely Volcanic Complex has been described as a volcanic arc comprised of basalts, andesites and dacites, tuffs, and volcaniclastic sediment that have been slightly metamorphosed and vary from 510 to 503 Ma in age (Foden et al., 2020). It has been implied

that the andesites and dacites of Mount Stavely belong to the same suite as the Magdala basalts which outcrop east of Mount Stavely (Foden et al., 2020), because they both share geochemical characteristics of boninites.

1.3 Tectonic Models

1.3.1 East-dipping subduction zone and polarity reversal.

The east-dipping subduction model implies collision of an intra-oceanic arc in the east with the volcanic passive margin of the Gondwanan continent in the west during the mid- Cambrian (Baatar et al., 2019; Crawford and Berry 1992). Following collision, it is suggested that subduction of the passive margin continental crust beneath the oceanic arc terminated eastward subduction (Münker and Crawford 2000), resulting in slab break-off and a polarity reversal with initiation of new west-dipping subduction below the Australian part of the Gondwana margin (Foster et al., 2005) as shown in Figure 1.3.

This model would suggest the occurrence of Cambrian arc rocks with intra-oceanic arc signatures. Intra-oceanic arc system (IOAS) lavas are characteristically sub-alkaline, with basalts and their fractionates as the predominate rock types, however high-Mg andesites and rhyodacitic magmatic products are also known to occur (Stern 2010).

Volcanic front-arc rocks can range from tholeiitic and high-alumina basalts to calc-alkaline andesites (Stern 2010), and typical trace element patterns for these lavas show enrichment in large-ion lithophile elements (LILE) relative to the high field strength elements (HFSE) (Stern 2002). As LILE have greater tendency to be fluid mobilised, it is considered that this pattern exhibited by arc rocks results from the enrichment of the mantle source region by aqueous fluids released during subduction of oceanic crust (Pearce 1982). Further, Stern (2010) explains that IOAS trace

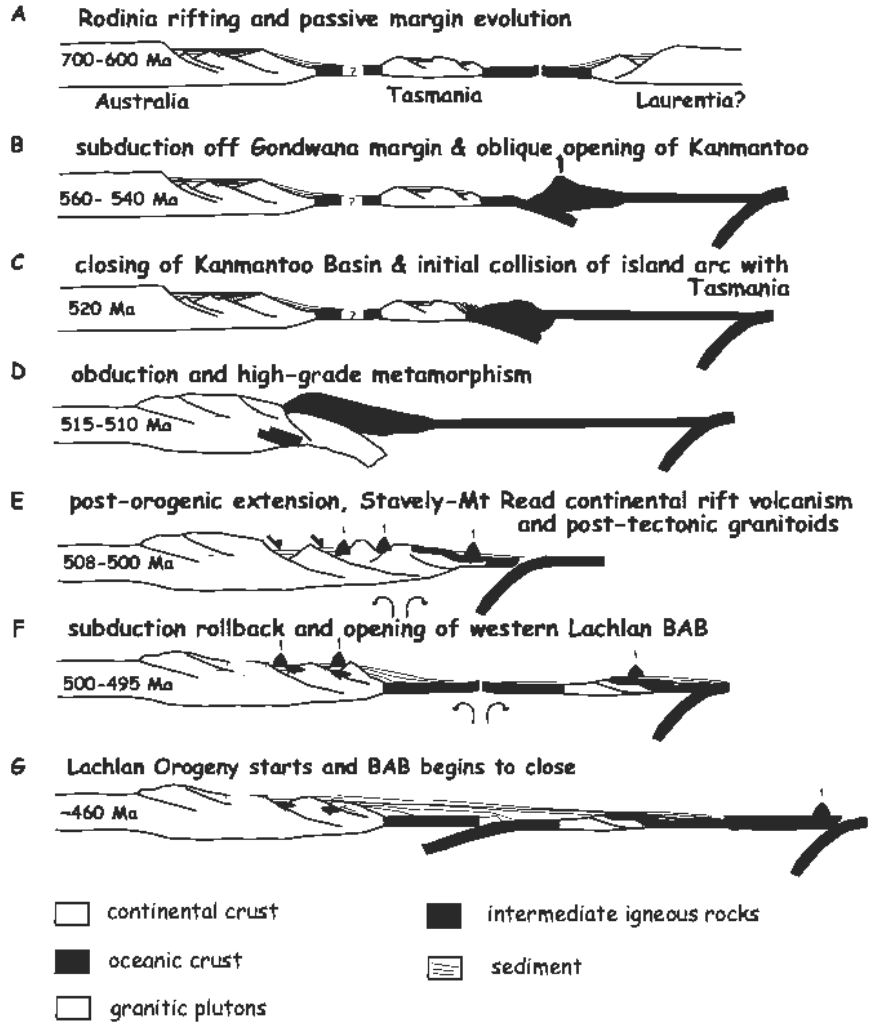

Figure 1.3: Cross-sectional model displaying the evolution of the Gondwana margin throughout the Neoproterozoic and the Silurian. (A) Rifting of Rodinia and development of a passive margin. (B) Initiation of eastward-dipping subduction off the Gondwana margin. (C) Initial collision between an oceanic island arc and Tasmania. (D) Termination of eastward subduction, obduction and peak metamorphism. (E) Extension of the collision zone resulting in continental rift volcanism, and development of west-dipping subduction beneath Australia. (F) Subducting plate rollback resulting in back-arc basin formation, further rifting of the Gondwana margin and arc volcanism. (G) Shortening event and back-arc basin closure. (Sourced from Foster et al., 2005).

element patterns also typically show low contents of Ti, Zr, Nb and heavy rare earth elements (HREE), shown in Figure 1.4, reflecting the greater degree of melt-

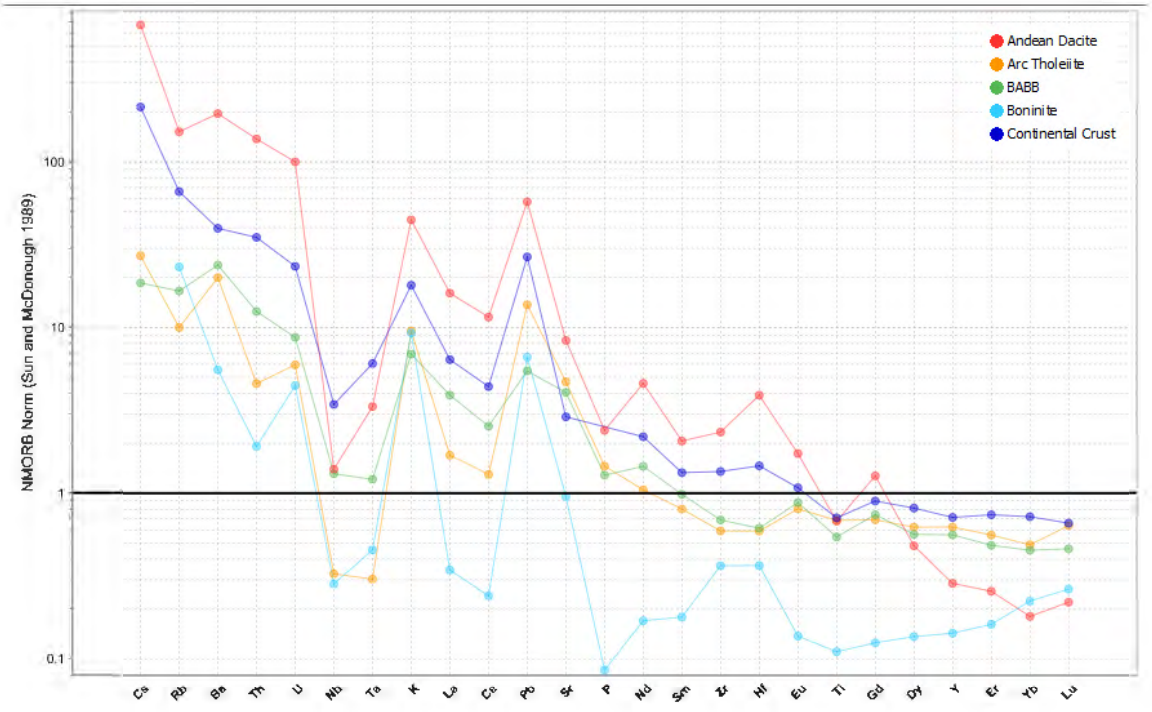

Figure 1.4: Spidergram for typical subduction zone rock types. Normalisation to NMORB and element order after Sun and McDonough (1989). Compatibility of the elements on the horizontal axis increase towards the right of the diagram. Data sourced from Stern (2002).

ing resulting in a depleted mantle source. Tholeiitic basalts dominate back-arc basin (BAB) lavas of IOAS, and are similar in most respects to mid-ocean ridge basalts (MORB) however are typically more hydrous and may range to more arc-like (Stern 2010). Rear-arc volcanoes, common in some intra-oceanic arc settings including the Izu, are generally more enriched and erupt lavas of calc-alkaline and shoshonitic affinity (Stern 2010). Additionally, boninites sometimes form when subduction is initiated and these are characteristic fore-arc rocks of high magnesium content coupled with low calcium and aluminum abundances (Stern et al., 2012). Whilst boninites are not always present in fore-arcs, they are found in the Izu-Bonin-Mariana arc system and represent the uppermost component of the fore-arc volcanic stratigraphy, underlain by tholeiitic basalts (Stern et al., 2012) termed fore-arc basalts by Reagan et al. (2010).

Further research by Greenfield et al. (2011), Foden et al. (2006) and Foden et al. (2020) has suggested the differences in geochemistry observed between the various phases of volcanic activity demonstrate a change from the late Neoproterozoic extension-related volcanism to Cambrian convergence associated with the onset of subduction-related magmatism (Greenfield et al., 2011). This prompted the development a different tectonic model with subduction initiation at the continental passive margin and formation of a west-dipping subduction zone.

1.3.2 West-dipping subduction zone.

Greenfield et al. (2011) suggest that mid-Cambrian volcanic arc magmatism along the East Gondwana margin developed on the continent in response to a west-dipping subduction zone. Volcanic arc development on the continental passive margin is an important constrain on this tectonic model, as this implies a mid-Cambrian tectonic inversion (Foden et al., 2020), whereby a passive margin directly transitions into an active margin.

This interpretation has brought about a new tectonic model, suggested by Greenfield et al. (2011) for the Koonenberry Belt, shown in Figure 1.5. A similar model has recently been proposed by Foden et al. (2020) for the Glenelg River Complex, Mt Stavely Complex and Adelaide Fold Belt, suggesting that the Loch Lilly-Kars area is the link between these two areas. However, as little is known about the basement rocks of the Loch Lily- Kars, the interpretation that this belt is the continuation of the Koonenberry Cambrian sequence (Bittles Tank Volcanics) requires further research to test this hypothesis.

This tectonic model would suggest the occurrence of Cambrian arc rocks with continental arc signatures. Andean style margins or continental volcanic arc systems differ from intra-oceanic arc systems in that the former are built on much thicker and more felsic crust (Stern 2010), therefore, lavas from Andean-type arcs are more

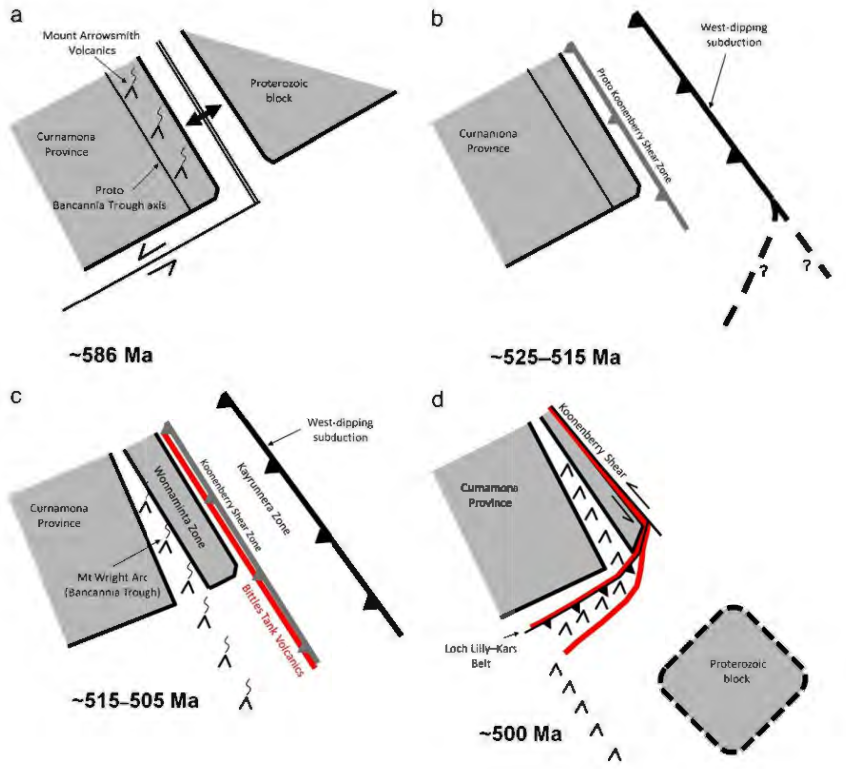

Figure 1.5: Tectonic diagram of the East Gondwana margin alongside the Broken Hill Block (Curnamona Province) throughout the late Neoproterozoic and Cambrian. (a) Passive margin with rift-related volcanics following the separation of Rodinia. (b) Early Cambrian transition from a passive margin to a convergent margin and commencement of west-dipping subduction. (c) Volcanic arc (Mt Wright) development on the continent and extrusion of fore-arc volcanics (shown in red). (d) Termination of arc volcanism and beginning of the Delamerian Orogeny, involving oroclinal folding that possibly resulted in the thrusting of fore-arc volcanics (Bittles Tank Volcanics) over the main arc and against the southern Broken Hill Block margin, forming the Loch Lilly–Kars. (Sourced from Greenfield et al., 2011).

fractionated than those from intra-oceanic arcs (Stern 2002). Spidergrams can again assist in distinguishing between lavas produced from continental and intra-oceanic arc settings, as the continental suites are more enriched in incompatible elements (Fig 1.4), reflecting the more felsic nature of the underlying continental crust (Stern 2002). Additionally, in comparison to intra-oceanic fore-arc basins, continental fore-

arc basins are commonly affected by high sediment flux (Stern et al., 2012) and the igneous infrastructure of the fore-arc is often not exposed (Stern 2002).

Greenfield et al. (2011) provide geochemical evidence for this interpretation, concluding that the calc-alkaline Mount Wright Volcanics have arc affinities of LILE enrichment coupled with depletions in Nb, Ta, Zr and Ti, whilst the tholeiitic basalt-andesite suite have a mixed geochemical signature transitional between arc-like and enriched MORB (E-MORB). The tholeiitic basalts show some characteristics of magmas from enriched mantle sources including the distinct lack of Ti and Zr depletions, however, enrichment in Th and Pb coupled with depletion in Nb are more characteristic of arc-related magmas (Greenfield et al., 2011). Additionally, the sedimentary record supports this interpretation as the presence of the mudstone, siltstone and limestone package of the Gnalta Group as well as the air-fall tuff horizons of similar age and composition to the Mount Wright Volcanics intercalated with mudstone and siltstone of the Ponto Group (Greenfield et al., 2011), suggest a shallow to deep water environment within an arc-type setting.

Geophysical Interpretation of Structural Domains

The Koonenberry Belt can be divided into three structural domains on the basis of aeromagnetic total magnetic intensity and gravity data (Greenfield et al., 2011); the Bancannia Trough, Wonnaminta Zone and the Kayrunnera Zone (Fig 1.6). The Bancannia Trough basement is characterised by a series of high amplitude, long wavelength magnetic anomalies (Johnson and Musgrave, 2012), interpreted to represent an igneous basement of subduction-related continental arc volcanism (Mount Wright Volcanics). To the east of the Bancannia Trough, the Wonnaminta Zone contains shallow magnetic linear features of the Ponto Group rocks (Johnson and Musgrave, 2012), with the Bittles Tank Volcanics providing the dominant magnetic signature (Greenfield et al., 2011).

Similar features to the Bancannia Trough and Wonnaminta Zone are observed in the Menindee Trough and the Loch Lilly-Kars Belt, respectively, forming an approximate 90-degree change in direction at the Grasmere Knee Zone to trend NE-SW (Fig 1.6). The TMI image also shows a second belt of magnetic anomalies, alongside the eastern edge of the Menindee Trough, however these anomalies appear to have deeper sources than the Ponto Group anomalies in the Loch Lilly-Kars Belt.

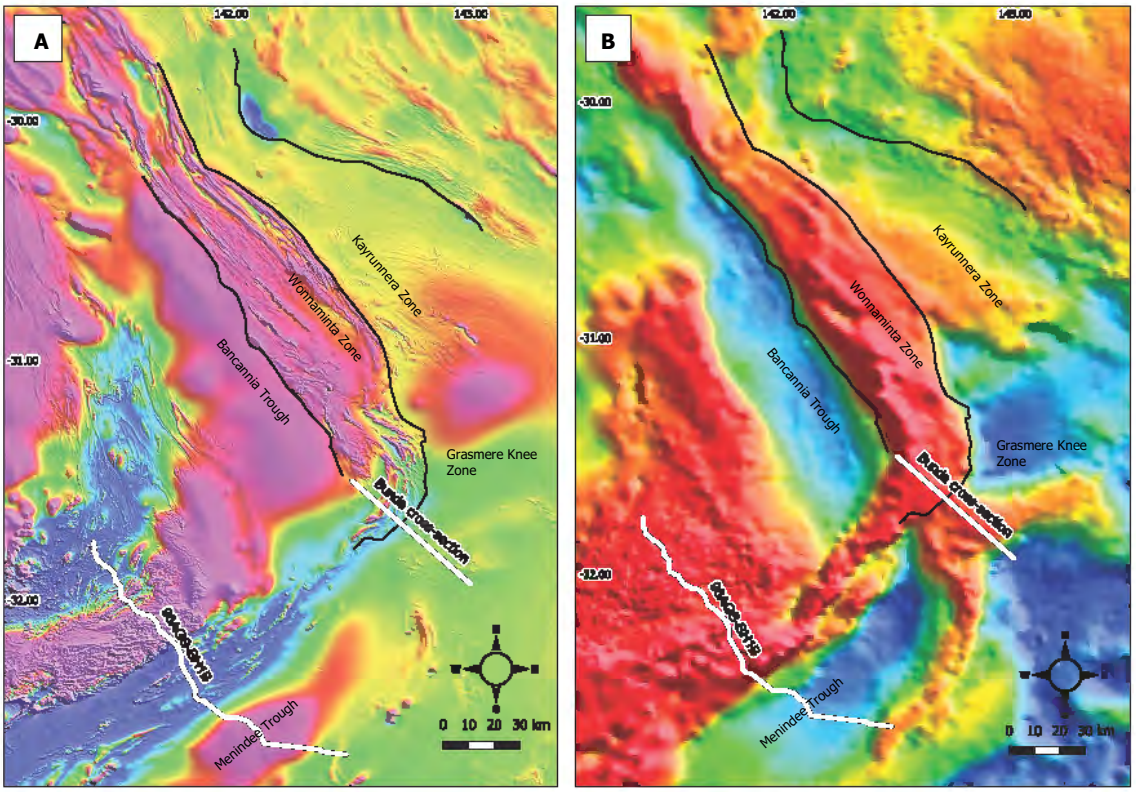

Figure 1.6: TMI (A) and gravity (B) imagery documenting the location of structural domains of the Koonenberry and Loch Lilly-Kars Belts in Western NSW. Locations of the GA seismic line 96AGS-BH1B and the Bunda cross-section are also shown. (TMI and gravity images supplied by GA).

As yet, there is not a geophysically and geologically constrained structural interpretation for the Loch Lilly-Kars Belt. Due to the lack of seismic reflectors in the Geoscience Australia (GA) seismic profile across the Loch Lilly-Kars, this profile has not been interpreted and thus the limited structural knowledge of this area is

based on magnetic and gravity features which correspond to the Ponto Group. A 3D model for the Koonenberry Belt has been produced from geologically constrained inversion of potential field data, via linking a series of 2D geological cross-sections (Musgrave and Dick 2017). The Bunda cross-section at the southern end of the Koonenberry Belt (Fig 1.7) shows the Ponto Group to be thrust to the NW over the Curnamona basement, however, does not directly show the arc features below the Menindee Trough. Therefore, the current interpretation suggests shallow, sub-horizontal westward thrusting (Johnson and Musgrave, 2012) of the Ponto Group from a fore-arc position to the back-arc position in the Loch Lilly-Kars, however this is loosely constrained.

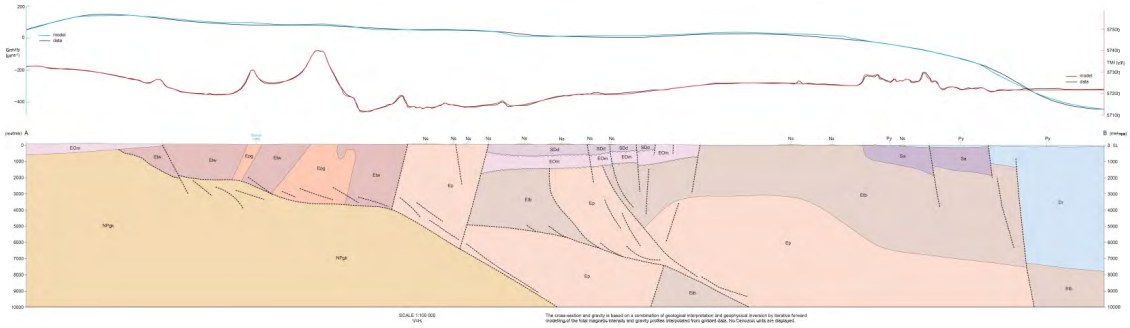

Figure 1.7: Bunda cross-section profile with TMI and gravity profiles. Sourced from Mills and Hicks (2016). NPgk = Kara Formation (Grey Range Group, Neoproterozoic), Etw = Wonnaminta Formation (Teltawongee Group, Cambrian), Etb = Bunker Creek Formation (Teltawongee Group, Cambrian), Epg = Grasmere Formation (Ponto Group, Cambrian), Ep = undifferentiated (Ponto Group, Cambrian), EOm = undifferentiated (Mutawintji Group, Cambro-Ordovician), Sa = Allambie Woolshed Granite (Silurian), SDd = Mount Daubeny Formation (Silurian), Dr = Ravendale Formation (Devonian), Py = Yanna Tank Formation (Permian), Ns = Silcrete (Neogene).

The seismic line across the Loch Lilly-Kars (96AGS-BH1B) shows west dipping reflectors under the Menindee Trough that appear to be interrupted by east dipping reflectors (Fig 1.8 B). This could suggest an analogous westward thrusting of the

Loch Lilly-Kars and the substratum of the Menindee Trough over the Loch Lilly-Kars and against the Curnamona block. There is an absence of horizontal reflectors in the key area of the Loch Lilly-Kars, however linear trends in the TMI and the inversion of geophysical potentials (Johnson and Musgrave, 2012) suggests steeply dipping structures (Fig 1.8 A) which may explain the lack of horizontal reflectors in this section of the seismic profile.

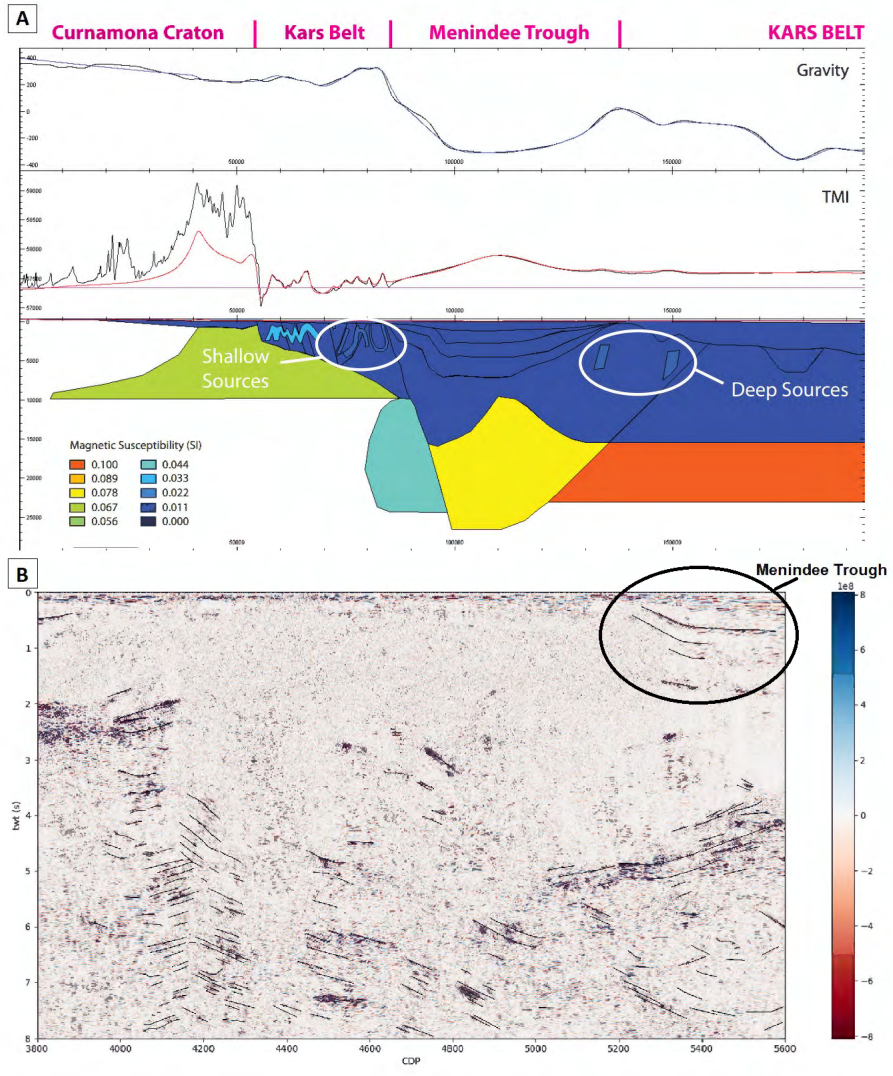

Figure 1.8: (A)Geophysical cross-section of the Loch Lilly-Kars Belt along seismic line 96AGS-BH1B. Sourced from Johnson and Musgrave (2012). (B) Annotated section of 96AGS-BH1B seismic profile (see Appendix 1 for full, unedited 96AGS-BH1B seismic profile). V/H ratio = 2/3, based on CDP = 20 m and an average velocity of 6 km/s.

1.4 Knowledge Gaps

It has been suggested, however as yet to be confirmed, that the Cambrian suites of the Koonenberry, Loch Lilly-Kars, Glenelg River Complex, Mount Stavely Complex and Adelaide Fold Belt belong to the same tectonic regime. Additionally, the polarity of Cambrian subduction is still controversial and as these regions appear to follow a geophysical trend identified from the TMI imagery (Fig. 1.2), similarity in the geochemistry of these volcanic suites will confirm whether there can be a single tectonic model proposed for the Delamerian.

Detailed geochemical analysis of the Mount Wright Volcanics of the Koonenberry Belt by Greenfield et al. (2011) and the Mount Stavely Volcanics in Western Victoria by Foden et al. (2020) have prompted the development of a new model of west-dipping subduction to explain the presence of Cambrian volcanics. This suggests the Loch Lilly-Kars is the link between these areas, however, due to limited drill holes intersecting basement and incomplete structural interpretation, further research is required.

1.5 Aims of this Study

The primary focus of this project is to determine if the geochemistry of the Loch Lilly- Kars Belt volcanics is similar to those in the Koonenberry Belt and if this geochemistry continues along the geophysical trend interpreted from the TMI imagery (Fig. 1.2). Secondly, this project will investigate if there are additional observations supporting the west-dipping subduction model for the Loch Lilly-Kars Belt through combining geochemistry with geochronological and isotopic data to track the geochemical and tectonic evolution. This approach will assist in determining if it is possible to propose a consistent polarity along the belt. Such information will allow tectonic models for the region to be re-evaluated, which will ultimately

assist in developing an improved geodynamic understanding of the evolution of the Delamerian orogenic system in Eastern Australia. Furthermore, understanding the architecture and kinematics of the Tasmanides is fundamental for mineral and resource exploration in Australia.

Chapter 2

Data and Methodology

2.1 Data Accessed

This project builds on a number of previously released results from Greenfield et al. (2011), Baatar et al. (2019) and Foden et al. (2020), with the addition of new data for the Loch Lilly-Kars and Koonenberry Belt.

The studies of Greenfield et al. (2011) were focused on the Koonenberry Belt with the aim of re-evaluating the tectonic setting. Greenfield et al. (2011) has carried out Nd-Sr isotopic analysis and whole rock geochemistry for both drill core and outcrop samples, as well as petrographic analysis of thin sections.

Baatar et al. (2019) have carried out preliminary studies of the Loch Lilly-Kars volcanics which involved collecting samples from drill core for whole rock geochemistry, zircon oxygen isotopic measurements and trace element analysis. As this study primarily concentrated on the prospectivity for porphyry copper mineralisation (Baatar et al., 2019), the intermediate and felsic volcanic rocks were the focus of this study which, due to their composition, are less useful for discriminating tectonic setting. Additionally, the 2015 Annual Exploration Report for exploration license (EL) 8199

from Anglo American has been made publicly available by GSNSW as of the 31st March 2020. This report provides Ar-Ar and laser ablation – inductively coupled plasma – mass spectrometry (LA-ICP-MS) U-Pb dating from Loch Lilly- Kars drill core, and therefore the wealth of existing data for the Loch Lilly-Kars has grown larger. These data has been made available on the NSW Digital Imaging of Geological System (DIGS), an online public archive that allows access to non-confidential reports and other documentary material.

The well-exposed AFB has been extensively studied, with the most recent research of Foden et al. (2020) aiming to develop a more cohesive geochemical analysis of past igneous activity and tectono-magmatic history. Foden et al. (2020) has carried out zircon U-Pb geochronological, whole rock geochemistry and Nd-Sr isotopic analyses for both drill core and outcrop samples from the AFB as well as the Glenelg River Complex and Mount Stavely Volcanic Complex.

2.2 Methods

2.2.1 Remote Sampling

Initially this project involved field work which was scheduled for April 2020 however due to the impacts of COVID-19 and travel restrictions this was unable to occur. An alternate plan was arranged for collecting samples from the Loch Lilly-Kars drill cores at the Broken Hill Drill Core Library remotely. A list was supplied requesting thirteen core samples from seven Loch Lilly-Kars drill holes. Most were sampled, however, there was no core available for one interval requested (sample VP011).

Drill holes sampled for this project include EHK1, EHK2, EHK3 from the Eaglehawk Prospect, drilled by Pasminco in 1995, as well as NBH004, NBH005, NBH009, NBH012 from the Quondong district, drilled by Newcrest in 2001 and 2002. These holes were targeted as they intersect mafic rock units and were used to determine the

tectonic setting on the basis of their geochemical composition. Additionally, there are some discrepancies in ages published by Anglo American (2015) and Baatar et al. (2019), and therefore re-sampling of the same drill core will potentially assist in providing a more cohesive age constraint on these units.

2.2.2 Sample Preparation

Once the core samples were received, they were prepared for geochronology by a series of methods beginning with splitting, crushing, milling and sieving to collect material less than 250 μm. The coarser material was retained and labelled, and the fine material was collected for zircon extraction via standard mineral separation procedures including Wilfley table, Frantz magnetic separator and heavy liquid separation.

Heavy mineral separation of the fine rock powder (< 250 μm) was completed using the Wilfley table method. Using this method, lighter minerals including feldspar and quartz are collected at the lower portion of the table, whilst the heavier minerals such as zircon, magnetite and pyrite are concentrated along the uppermost portion of the table (Chisholm et al., 2014). The collected heavier fraction of the sample was run along the Wilfley table multiple times to reduce the amount of lighter minerals entrained in the flow. The heavy component was then oven dried at 60°C in preparation for magnetic separation. Using a hand magnet, the highly magnetic minerals such as magnetite were removed. The samples were then run through a Frantz Magnetic Separator for further separation, and the separated mineral fractions were collected at intervals between increasing amperage; I = 0.4, 0.8 and 1.2 Amps. Acid digestion was needed for samples that had large amounts of sulfides, to reduce the amount of material for heavy liquid separation.

Heavy liquid separation was performed on the least magnetic fractions of the samples using Lithium Heterotungstate solution (LST). The heavy liquid was heated

in the oven at 70°C before the sample was added and agitated, then returned to the oven to allow the heavy fraction to settle to the bottom and separate from the lighter fraction at the top. Once the sample settled, the vial was submerged in ice cold water to solidify the solution. Using demineralized water, the light and heavy mineral fractions were then washed from the vial into separate funnels lined with filter paper, resulting in the mineral grains collecting on the filter paper. The light mineral fraction was discarded, whilst the heavy fraction was oven dried in preparation for hand picking of zircon under a binocular microscope and then mounted on double-sided tape on glass slides for epoxy resin mounting. Titanite grains were also mounted for samples that contained no zircon. The mounting procedure involved the use of 25 mm diameter Teflon rings which were placed around the sample and filled with epoxy resin. Once the resin hardened, the Teflon rings were removed and the surface of the resin mount was polished to expose the grains and achieve a smooth, flat surface. In total, four mounts were produced; three with zircon grainsets (VP1, VP2, VP3) and one with titanite grainsets (VP4).

In preparation for LA-ICP-MS, the mounts were imaged using a transmitted light (TL) microscope and in cathodoluminescence (CL) using a scanning electron microscope (SEM). Prior to introduction into the SEM (FEI/Philips XL30 SEM with Gatan MiniCL detector), each mount was gold coated to create a conductive surface. CL imaging assisted in identifying the internal grain structure and features, as well as for setting targets for LA-ICP-MS. Secondary electron (SE) and back scatter electron (BSE) imaging was used for the titanite mount. Following imaging, each mount was polished to remove the coating. Spot plans for LA-ICP-MS were completed for each grainset using Inkscape, with a maximum of 40 spots of 30 µm diameter per sample for zircon and a maximum of 50 spots of 50 µm diameter per sample for titanite. Adjustments were made to spot size for titanite samples upon analysis, as explained below.

2.2.3 Zircon Geochronology

Laser ablation split stream (LASS) analysis for zircon was performed at Curtin University. This technique allows for simultaneous analysis of isotopic systems and trace elements from single laser spots (Xie et al., 2018). The zircon samples received LASS-ICP-MS analysis of U-Pb and trace elements, as well as single stream LA-ICP-MS Lu-Hf isotope analyses. Two sessions were performed, the first involved U-Pb, trace elements and Lu-Hf analysis over two days and the second session involved just U-Pb analysis over one day. Detailed methodology is provided below for zircon LASS analysis (C Clark 2021, personal communication, 15 April) and Lu-Hf isotope analysis (C Kirkland 2021, personal communication, 15 April).

Elemental and isotopic composition data were collected using the LASS-ICP-MS housed at the GeoHistory Facility in the John de Laeter Centre at Curtin University. Zircon was ablated using a Resonetics RESOlution M–50A–LR system, incorporating a COMPex 102 193 nm excimer UV laser. Following two cleaning pulses and a 40 s period of background analysis, samples were spot ablated for 35 s at a 10 Hz repetition rate using a 50 μm beam and laser energy at the sample surface of 2.3 J/cm^2. An additional 40 s of baseline was collected after ablation. The sample cell was flushed with ultrahigh purity He (300 mL/min) and N_2 (1.0 mL/min) and high purity Ar was employed as the plasma carrier gas. U–Pb were measured a Nu-Plasma2 HR multi-collector ICP while trace elements were measured using an Agilent 7700s quadrupole ICP-MS, with high-purity Ar as the plasma gas (flow rate 0.98 L min^{-1}). Zircon standard 91500 was used as the primary standard to calculate element concentrations (using ^{90}Zr as an internal standard element, assuming a 43.14% Zr content in zircon) and to correct for instrument drift.

The time-resolved mass spectra were reduced using Iolite and data reduction scheme (DRS) Geochronology 3. Evidence of both lead loss and common lead gain was

Table 2.1: Zircon standard ages and reported ages in the literature.

Standard	Session/Day	n	Age (Ma)	Reported Age (Ma)
91500	1-1	18	1051.7 ± 2.6	1062.4 ± 0.4
				(Wiedenbeck et al., 1995)
	1-2	20	1048.7 ± 2.9	
	2-1	18	1058.2 ± 4.5	
GJ-1	1-1	18	601.8 ± 0.1	601.7 ± 1.4
				(Jackson et al., 2004)
	1-2	20	601.8 ± 0.1	
	2-1	18	601.7 ± 0.6	
Plešovice	1-1	18	340.8 ± 1.6	337.1 ± 0.4
				(Sláma et al., 2008)
	1-2	20	340.7 ± 1.6	
	2-1	18	340.0 ± 3.1	

identified using VizualAge (in Iolite4). Selections of discordant data that showed evidence of common lead gain were common lead corrected. Selections that showed evidence of lead loss were not ^{204}Pb corrected and were excluded from age determination. The primary reference material used for U–Pb dating in this study was zircon standard 91500 (1062.4 ± 0.4 Ma; Wiedenbeck et al., 1995) with secondary standards zircon GJ-1 (601.7 ± 1.4 Ma; Jackson et al., 2004) and Plešovice (337.13 ± 0.37 Ma; Sláma et al., 2008) also used. Analyses were done for the primary and two secondary standards and results are in agreement with the reported values, shown in Table 2.1. Initially, no common lead corrections were deemed necessary during data processing due to low ^{204}Pb counts. Discordant ages with evidence of common lead contamination were corrected post processing to constrain Lu-Hf analyses.

The ablated split for Lu–Hf analysis was measured on a Nu Plasma II multi-collector

Table 2.2: Hafnium standards and reported standard values in the literature.

Standard	Result	Reported Standard Result
91500	0.282328 ± 0.000040	0.282307 ± 58 (Griffin et al., 2007)
		0.2823026 ± 42 (Fisher and Vervoort 2014)
Mud Tank	0.282539 ± 0.000031	0.282522 ± 0.000042 (Griffin et al., 2006)
		0.282523 ± 10 (Gain et al., 2019)
		0.28251860 ± 29 (Fisher and Vervoort 2013)
Plešovice	0.282513 ± 0.000031	0.2824366 ± 28 (Fisher and Vervoort 2013)
GJ-1	0.282053 ± 0.000037	0.282000 ± 6.5 (Fisher and Vervoort 2014)
FC1	0.282210 ± 0.000031	0.2821826 ± 47 (Fisher and Vervoort 2015)

ICP-MS. All isotopes (^{180}Hf, ^{179}Hf, ^{178}Hf, ^{177}Hf, ^{176}Hf, ^{175}Lu, ^{174}Hf, ^{173}Yb, ^{172}Yb and ^{171}Yb) were counted on the Faraday collector array. Time-resolved data were baseline subtracted and reduced using Iolite (data reduction scheme after Woodhead et al., 2004), where ^{176}Yb and ^{176}Lu were removed from the 176 mass signal using ^{176}Yb/^{173}Yb = 0.7962 and ^{176}Lu/^{175}Lu = 0.02655 with an exponential-law mass bias correction assuming ^{172}Yb/^{173}Yb = 1.35274 (Chu et al., 2002). The interference-corrected ^{176}Hf/^{177}Hf was normalized to ^{179}Hf/^{177}Hf = 0.7325 (Patchett and Tatsumoto, 1980) for mass bias correction. Zircon crystals from the Mud Tank carbonatite locality were analysed together with the samples in each session to monitor the accuracy of the results. 91500, Plešovice and GJ-1 zircons were also run as secondary standards. Table 2.2 summarises the Hf isotope measurements made on standard material throughout the analytical session showing that all standards yielded corrected ^{176}Hf/^{177}Hf within uncertainty of their respective reported values.

Terra-Wasserburg Concordia diagrams and weighted mean calculations for zircon U-Pb analyses did not incorporate analyses with >10 % discordance and were plotted using Isoplot and IsoplotR (Vermeesch 2018). Wetherill-type Concordia diagrams

incorporated all data including discordant data and Pb anchored model-1 discordia intercept ages were determined. Emplacement age of samples were calculated by taking the weighted mean average of the youngest concordant population within uncertainty of the youngest concordant analysis (Dickinson and Gehrels 2009).

2.2.4 Titanite Geochronology

Data acquisition for titanite samples was carried out at the Advanced Analytical Centre of James Cook University, using a Photon Machines Analyte G2 193 nm ArF Excimer laser ablation system connected to a Thermo iCAP-RQ ICP-MS. The ablation cell was connected to the iCAP-RQ via Tygon tubing. Ablation was conducted in a HelEx II Active 2-Volume Cell using high-purity He as the carrier gas, which was subsequently mixed with 0.54 L/min Ar and 5 ml/min N2 prior to introduction into the ICP-MS. The ICP-MS was optimized using auto tune on a solution basis. It was tuned further for maximum sensitivity in laser ablation mode using standard glass NIST 610 under robust plasma conditions (U/Th = 1) while maintaining oxide production rates (ThO/Th) to $< 0.3\%$. relative standard deviation (RSD) of U and Th signals of NIST 610 are typically better than 3% when laser fluence was set to 3 J/cm2 at the sample surface with a laser repetition rate and a beam diameter of 5 Hz and 50 µm, respectively.

Conventional spot analyses were used for data acquisition using a laser fluence of 2 J/cm^2. Initially, 85 µm spots were used for most analyses, however 65 µm spots were used for the finer grains of samples VP006 and VP007. Iolite 4 was used to process the raw data (Paton et al., 2011) and as the samples contained common lead, the VizualAge UComPbine data reduction scheme was used (Petrus and Kamber 2012).

IsoplotR was used to plot the U-Pb data using the $^{207}Pb/^{235}U$ and $^{206}Pb/^{238}U$ isotope ratios with a standard error of 2. Lower intercept ages were calculated using the discordia model 1 and plotted on Wetherill type concordia diagrams.

2.2.5 Geochemistry

Existing geochemical data were obtained for most Loch Lilly-Kars and Koonenberry samples, sourced from Baatar et al., (2019) and DIGS. Samples sourced for this project that required geochemical analysis were VP004, VP006, VP010, VP013, PJG0059 and DD89GR05 (95 m). These samples were prepared for geochemical analysis using a tungsten carbide vibratory ring mill, and powdered samples were bagged and sent to Intertek Laboratories, Adelaide, SA for lithogeochemical analyses via Lithium borate fusion inductively coupled plasma atomic emission spectroscopy (ICP-OES) and ICP-MS as well as 4 acid digestion ICP-MS for Nickel (Ni).

All rocks in this analysis have been variably metamorphosed and record lower greenschist to low amphibolite facies assemblages. Most major elements are mobile during metamorphism and therefore determination of the tectonic setting of these samples is based on the least mobile elements such as HFSE and REE, considered to be immobile under most circumstances (Offler et al. 2019).

Spidergrams were used to compare trace element patterns and discrimination diagrams assisted in determining possible tectonic settings. These diagrams were plotted using ioGAS and Microsoft Excel. N-MORB (Sun and McDonough 1989) was the normalising factor for all spidergrams, and mafic and intermediate to felsic samples were plotted separately. To discriminate between mafic and felsic as well as alkaline and sub-alkaline samples, samples were plotted on the Nb/Y vs Zr/TiO2 diagram of Winchester and Floyd (1977). Diagrams of Pearce (2014) and Wood (1980) were used to plot mafic samples only, and Gorton and Schandl (2000) for intermediate to felsic samples. The Ti-V diagram of Shervais (1982) and Zr-Nb-Y diagram of Meschede (1986) were also employed to plot mafic, non calc-alkaline samples.

2.2.6 Sm-Nd Isotopic Analysis

Samples VP004, VP006, VP009, VP012, VP013, PJG0059, PJG0080 and PJG0082 were prepared for isotopic analysis using a tungsten carbide vibratory ring mill. Powdered samples were sent for analysis at the University of Melbourne. Detailed methodology of Sm-Nd isotopic analyses is provided below (R Maas 2021, personal communication, 10 Feb).

Radiogenic isotope compositions (Sm-Nd) were measured by isotope dilution MC-ICPMS, using procedures adapted from Donellan et al. (2019) and Maas et al. (2020). Sample powder (60-70 mg) was weighed into Krogh-type PTFE teflon vessels, spiked with ^{149}Sm-^{150}Nd spike and dissolved in an oven (160°C) using 3:1 HF-HNO_3, conc. HNO_3 and 6M HCl over 4 days. This resulted in clear solutions in all cases. Nd and Sm were extracted and purified using a combination of EICHROM TRU- and LN-resin (Pin et al., 2014). Procedural blanks (<0.1 ng Nd) produced blank corrections that were negligible in all cases.

Sm-Nd isotopic analyses were carried out on a NU Plasma multi-collector inductively coupled plasma mass spectrometer (MC-ICP-MS), with sample uptake via a CETAC Aridus desolvating system and slow-uptake (0.07 ml) PFA nebulizer. Neodymium fractions were re-dissolved in 2% nitric acid running solution and adjusted (60-80 ppb) to yield total Nd signals in the range 15-25V. Data were collected for 30 cycles (30x10 sec) and corrected for instrumental mass bias by internal normalization to ^{146}Nd/^{145}Nd = 2.0719425 (equivalent to the more familiar ^{146}Nd/^{144}Nd = 0.7219, Vance and Thirlwall, 2002), using the exponential law as part of an online iterative spike-stripping/internal normalisation procedure. Final ^{143}Nd/^{144}Nd is reported relative to a value of 0.511860 for the La Jolla Nd isotope standard. Instrumental mass bias in Sm isotope dilution analyses was corrected by internal normalisation to ^{152}Sm/^{147}Sm = 1.78307. Typical in-run precision (2se) for ^{143}Nd/^{144}Nd is

$\sim\pm$0.000012, while the reproducibility of rock and solution standards indicates an external precision of $\pm$0.000030 (2sd). External precision for $^{147}Sm/^{144}Nd$ is $\pm$0.2% (2sd).

Nd isotope result for three USGS rock standards (basalt BCR-2, basalt BHVO-2, andesite AGV-2) analysed over several months in 2020, including the present campaign, yield average $^{143}Nd/^{144}Nd$ of 0.512640$\pm$0.000031, 0.512998$\pm$0.000030 and 0.512795$\pm$0.000036 (2sd, n=30, 23 and 29), respectively, consistent with TIMS and MC-ICPMS reference numbers (e.g., http://georem.mpch-mainz.gwdg.de). A single isotope dilution analysis of the USGS GSP2 granite standard (a Proterozoic LREE-rich A-type granite) yielded 26.05 ppm Sm, 206.2 ppm Nd, $^{147}Sm/^{144}Nd$ = 0.0764 and $^{143}Nd/^{144}Nd$ = 0.511381$\pm$0.000010 (2se), consistent with the TIMS results of Raczek et al. (2000, 2003).

ϵ_{Nd} values ϵ_{Nd}(t) and T_{DM} model ages (where applicable) are calculated using $^{147}Sm/^{144}Nd$ = 0.1960 and $^{143}Nd/^{144}Nd$ = 0.512630 for the modern chondritic mantle (CHUR, Bouvier et al., 2008); a composition of $^{147}Sm/^{144}Nd$ = 0.2129 and $^{143}Nd/^{144}Nd$ = 0.513145 for the model depleted mantle (DM) is used in the calculation of T_{DM}. The Sm decay constant is 6.54 x 10^{-12}/yr.

2.2.7 Petrography

All Loch-Lilly Kars drill core samples as well as some Koonenberry outcrop and drill core samples were prepared for petrographic analysis via creation of thin sections. Thin sections were produced via standard procedures, to 30 µm thickness. In addition, four thin sections from Koonenberry outcrop samples were provided by the GSNSW, coupled with their hand specimens.

Thin sections were examined using a Leica DM750P microscope with a Leica MC170 HD camera to obtain photomicrographs.

Chapter 3

Petrography

Sample locations for this project are displayed in Figure 3.1, and a detailed sample list is provided in Table B.1 (Appendix B). Detailed descriptions for both core samples and thin sections are provided in Appendix C, and a summary of the main petrological features are described below.

All Loch Lilly-Kars and Koonenberry samples have undergone alteration to varying degrees, resulting in assemblages typical of low greenschist to low amphibolite facies, with the former more common. Common alteration assemblages include chlorite-calcite-quartz-epidote-titanite and other alteration minerals such as prehnite and secondary amphiboles are also present. These often occur in veins or replacing magmatic minerals. Deformation features are not often observed in the mafic samples, with the exception of samples from drill hole DD89GR05, which show strong deformation and evidence for shearing, namely, the development of C and S planes defined by fine-grained, low-grade metamorphic minerals. Deformation is manifested as veins, where shear strain is the most well defined, indicating brittle deformation. Additionally, small-scale recumbent folds are observed in the meta-siltstone unit intersected in drill hole NBH005 (sample VP010) and an axial-planar cleavage defined by opaques.

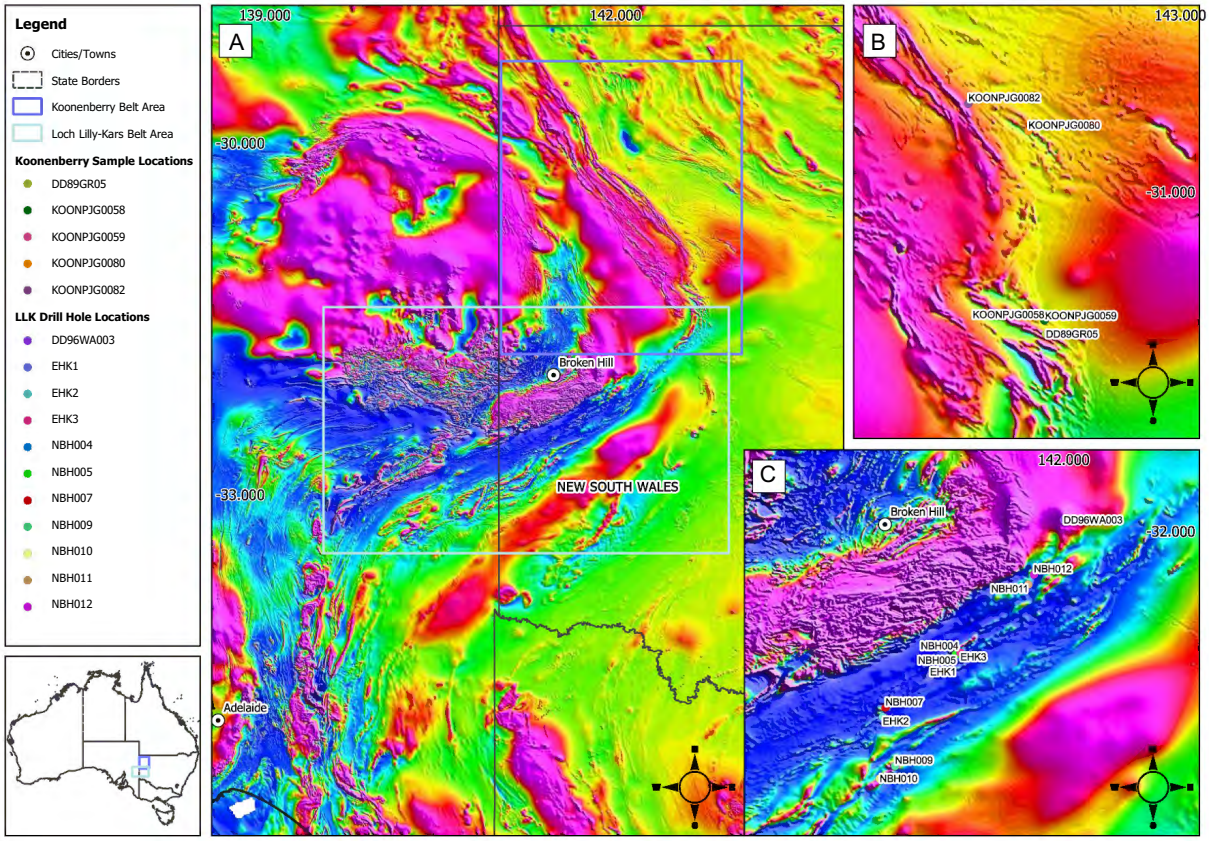

Figure 3.1: Map of Sample Locations superimposed on TMI geophysics base map (TMI image supplied by Geoscience Australia). **A.** Locations of the Koonenberry Belt (blue box) and Loch Lilly-Kars Belt (white box). **B.** Sample locations within the Koonenberry Belt, samples provided by GSNSW. **C.** Sample locations within the Loch Lilly-Kars Belt, remotely sampled from drillcore located at the Broken Hill Core Library.

Chapter 4

Geochemistry

4.1 Introduction

A major aim of this study was to determine if the Loch Lilly-Kars volcanics are geochemically similar to other Cambrian volcanics along trend and if these volcanics record the same tectonic setting.

Geochemical variation diagrams or discrimination diagrams can be used to identify tectonic environments of both ancient and modern igneous rocks (Gorton and Schandl 2000, Pearce 2014, Shervais 1982, Wood 1980). Various immobile element proxies have been identified to represent geological processes such as the Th/Nb proxy for subduction or crustal input, Ti/Yb proxy for plume melting and V/Ti proxy for suprasubduction zone melting (Pearce 2014), and these proxies assist in determining magma type and tectonic setting.

Normalised multi-element diagrams (spidergrams) are an extension of traditional chondrite-normalised REE diagrams (Rollinson 1993), involving plotting of additional trace elements. Trace element patterns show distinct features associated with tectonic settings (Winter 2001), importantly whether there is a depletion or enrich-

ment of particular elements. These peaks and troughs reflect the different behavior of elements and minerals involved during the rock forming process, such as negative Nb anomalies (high Th/Nb) and low Ti which indicate subduction influence (Pearce 2014). They also reflect the composition of the source, importantly whether the source is depleted or enriched, indicated by the presence or absence of Ti, Zr, Nb as well as REE and HFSE anomalies.

4.2 Loch Lilly-Kars

The Zr/TiO_2 and Nb/Y ratios (Fig 4.1) indicate the Loch Lilly-Kars samples are predominantly sub-alkaline to mildly alkaline (Nb/Y = <2). Figure 4.1 shows that the subalkaline samples range from sub-alkaline basalt through to rhyodacite/dacite, and the alkaline samples range from alkali basalt to trachyandesite.

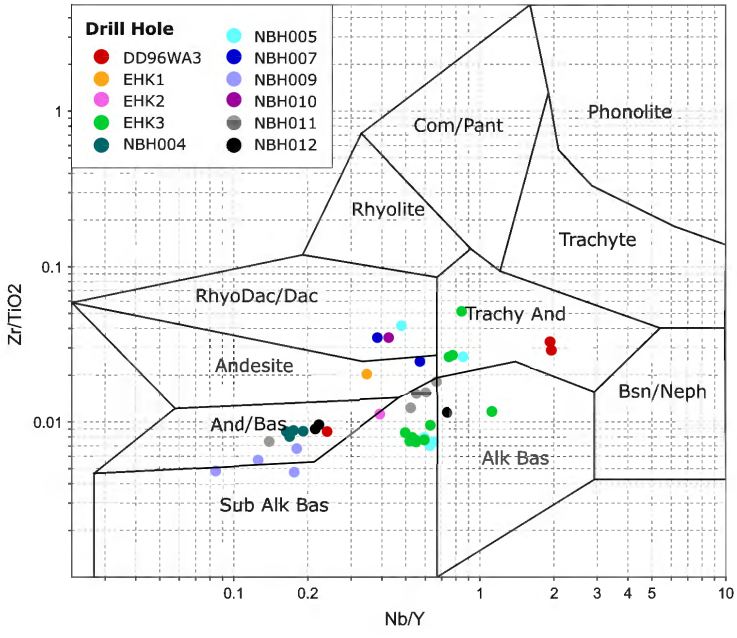

Figure 4.1: Zr/TiO_2 vs Nb/Y discrimination diagram for the Loch Lilly-Kars volcanics (Winchester and Floyd 1977).

Chondrite-normalised patterns (Fig 4.2) reveal that majority of the mafic sub-

alkaline samples are variably LREE enriched, with most having La/Yb_n (chondrite normalised) values that range from 2.75 to 15.3. The mildly alkaline mafic samples from NBH012 and EHK3 are strongly LREE enriched with La/Yb_n values of 12.0 and 11.3, respectively. Samples from drill hole NBH009, however, have La/Yb_n values of 1.01 to 2.65 which are less enriched relative to samples in other drill holes, revealing a distinctively different REE pattern that appears relatively flat (Fig 4.2 F).

NMORB-normalised patterns (Fig 4.3) show that most mafic calc-alkaline samples display continental arc signatures with Nb/Yb values >1 (1.72 to 6.93). The mildly alkaline mafic samples from NBH012 and EHK3 also show continental arc signatures with Nb/Yb values of 7.18 and 12.2, respectively. These alkaline samples plot within the calc-alkaline arc basalt field in Figure 4.7. However, the tholeiitic to transitional samples from drill hole NBH009 (Fig 4.3 F) show intra-oceanic arc signatures with Nb/Yb values closer to 1 (0.76 to 1.67).

Chondrite-normalised patterns reveal that the felsic rocks of the Loch Lilly-Kars are strongly LREE enriched (Fig 4.4) with La/Yb_n values ranging from 13.5 to 38.1. All intermediate to felsic calc-alkaline and mildly alkaline Loch Lilly-Kars samples show high Th/Nb ratios and prominent Ti depletion (Fig 4.5), showing continental arc signatures with Nb/Yb values >1 (3.8 to 19.5).

On the Th/Yb-Nb/Yb diagram of Pearce (2014) shown in Figure 4.6, the LLK mafic suite form an array that plots within the transitional field between oceanic arc and continental arc signatures, extending into the continental arc field. This trend is also observed on the Th-Zr-Nb diagram of Wood (1980) shown in Figure 4.7. All samples plot within the calc-alkaline volcanic arc basalt field (Fig 4.7), however, those samples that appear transitional on Figure 4.6 plot closer to the boundary between arc tholeiites and calc-alkaline basalts in Figure 4.7.

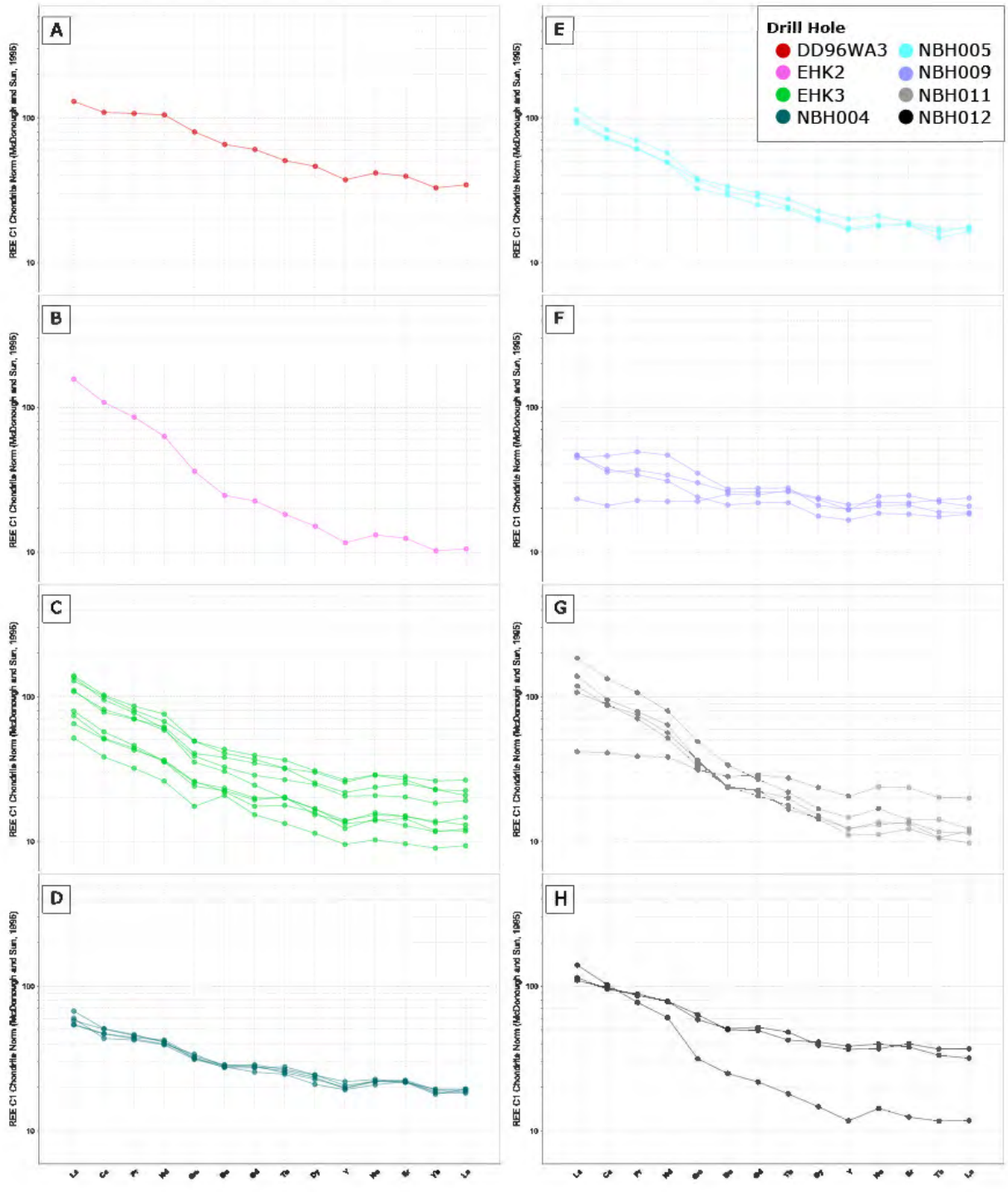

Figure 4.2: Chondrite-normalised REE patterns for mafic rocks of the Loch Lilly-Kars. Normalising values are from Sun and McDonough (1995).

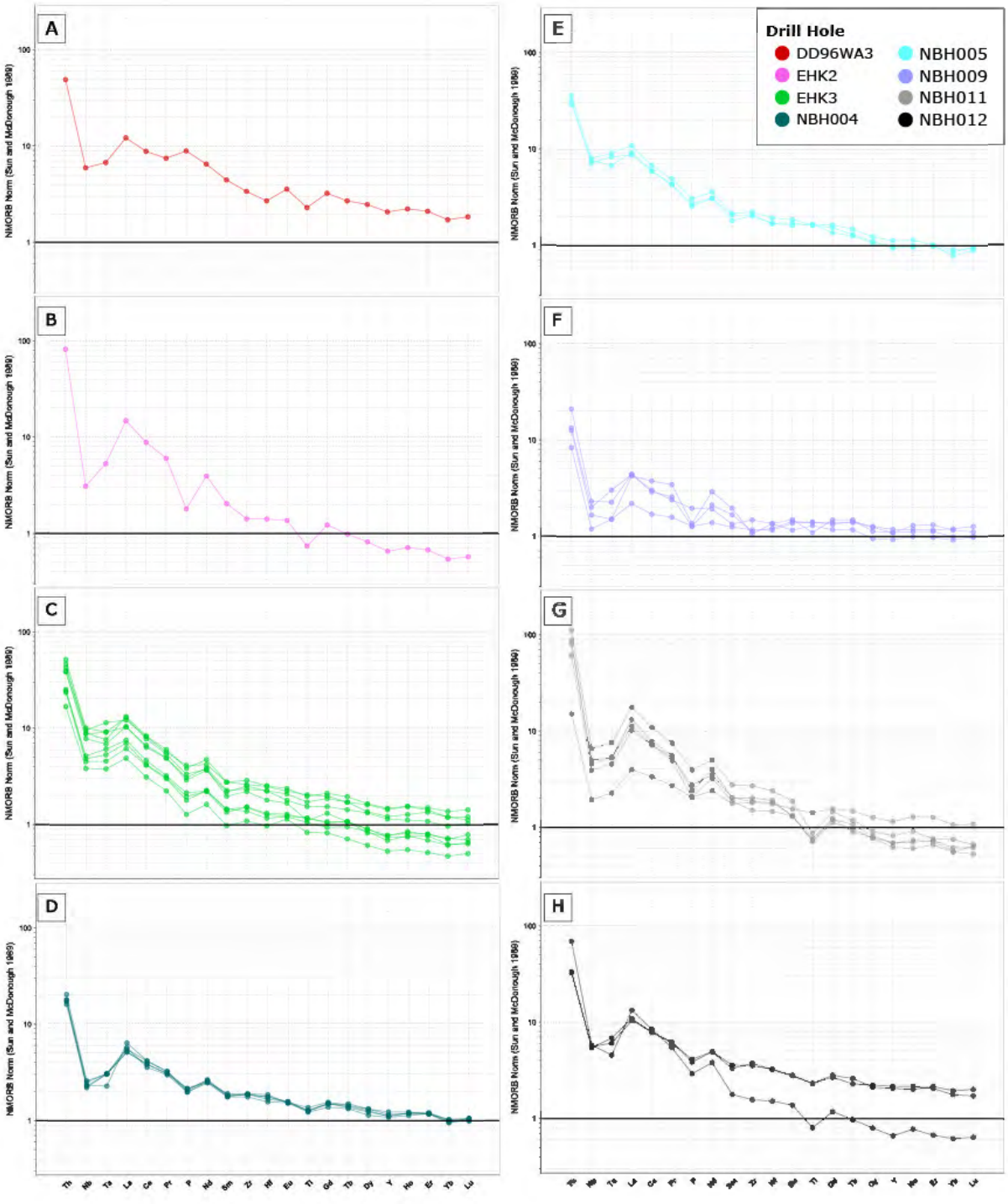

Figure 4.3: NMORB-normalised patterns for mafic rocks of the Loch Lilly-Kars. Normalising values are from Sun and McDonough (1989).

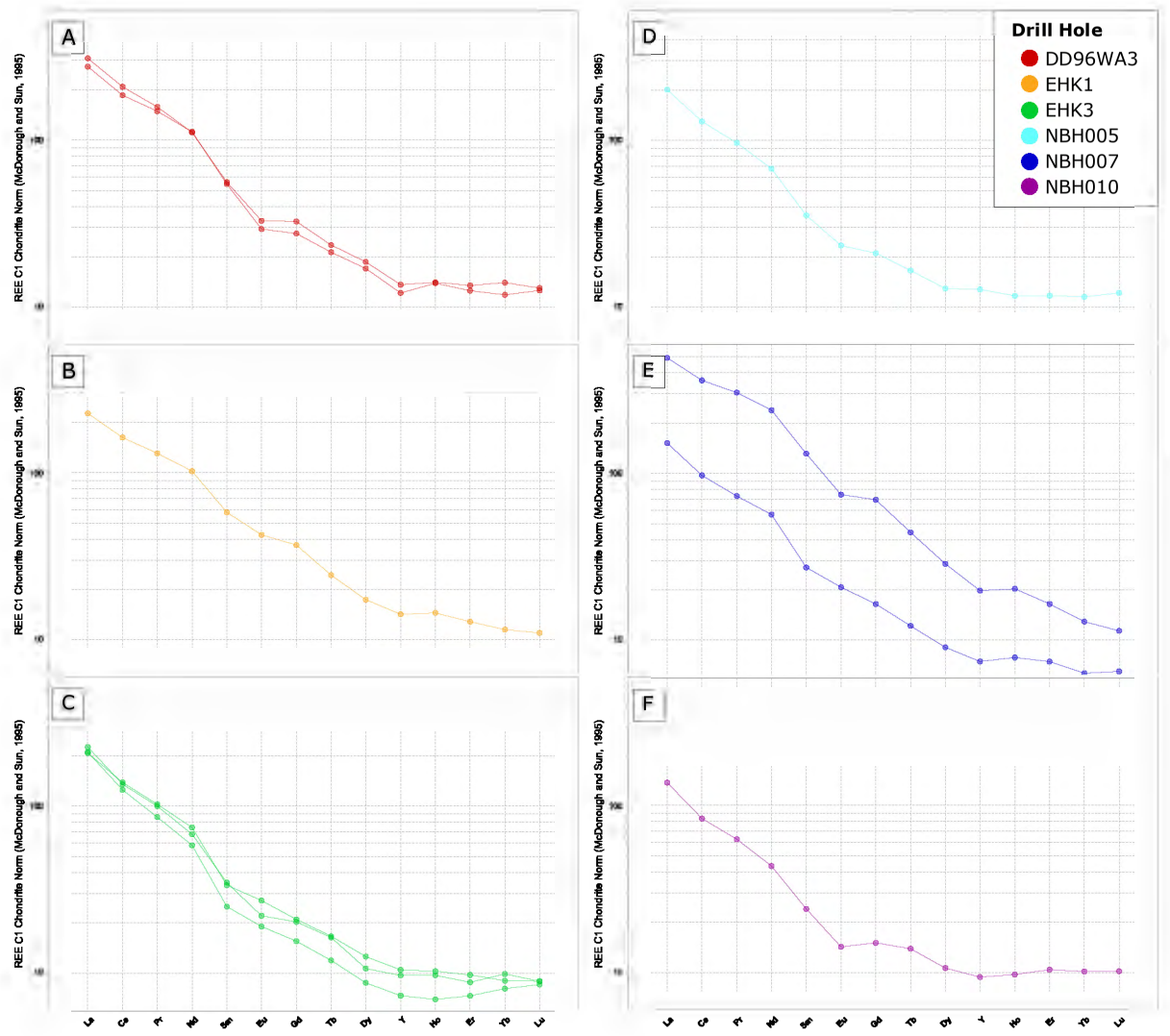

Figure 4.4: Chondrite-normalised REE patterns for intermediate to felsic rocks of the Loch Lilly-Kars. Normalising values are from Sun and McDonough (1995).

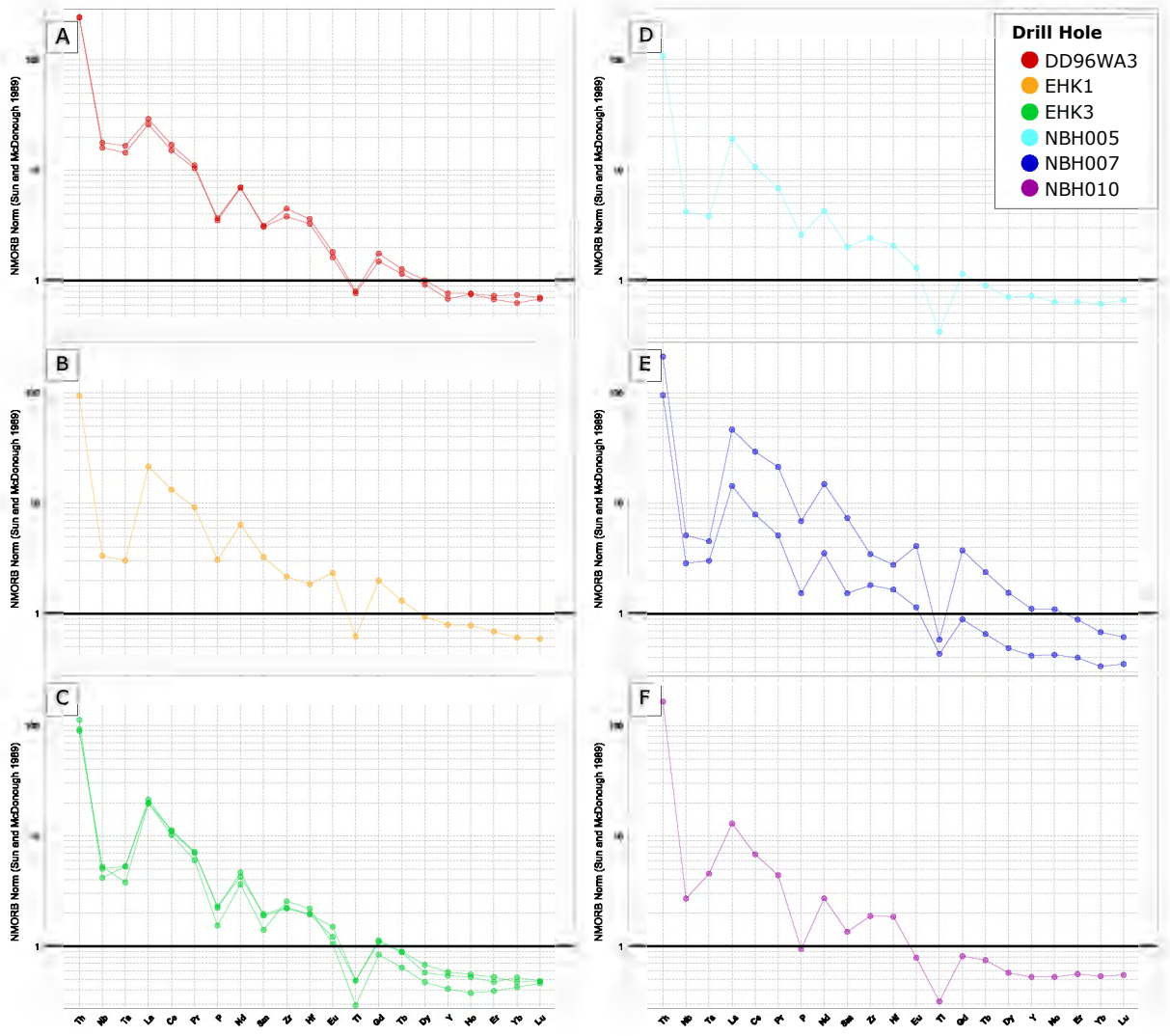

Figure 4.5: NMORB-normalised patterns for intermediate to felsic rocks of the Loch Lilly-Kars. Normalising values are from Sun and McDonough (1989).

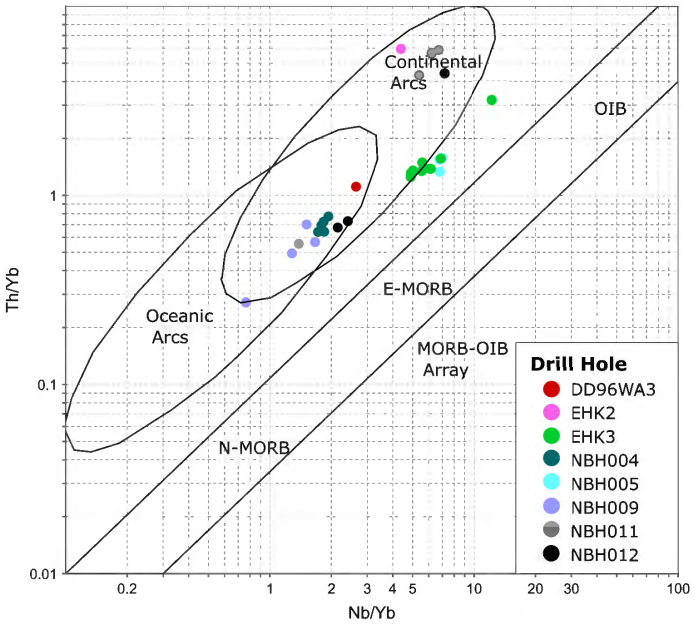

Figure 4.6: Th/Yb vs Nb/Yb discrimination diagram for mafic rocks of the Loch Lilly-Kars (Pearce 2014).

The intermediate to felsic LLK rocks display the same transitional pattern (Fig 4.8) observed within the mafic suite. Samples from drill holes EHK3 and DD96WA3 extend into the active continental margin field with Th/Ta values of 15 to 19, whilst samples from NBH005, NBH007 and NBH010 span the oceanic arc field with Th/Ta values of 22 to 43 (Fig 4.8).

One meta-sedimentary sample (VP010) from drill hole NBH005 shows moderate LREE enrichment (Fig 4.9 A) and has a $(La/Yb)_n$ value of 5.48. The NMORB-normalised pattern for this meta-siltstone (Fig 4.9 B) indicates the source is likely to have been calc-alkaline with a continental arc signature (Nb/Yb value of 7.53).

4.3 Koonenberry

The Zr/TiO_2 and Nb/Y ratios indicate the Koonenberry samples are all sub-alkaline (Nb/Y $\leq$0.2), and plot within the basaltic andesite field (Fig 4.10).

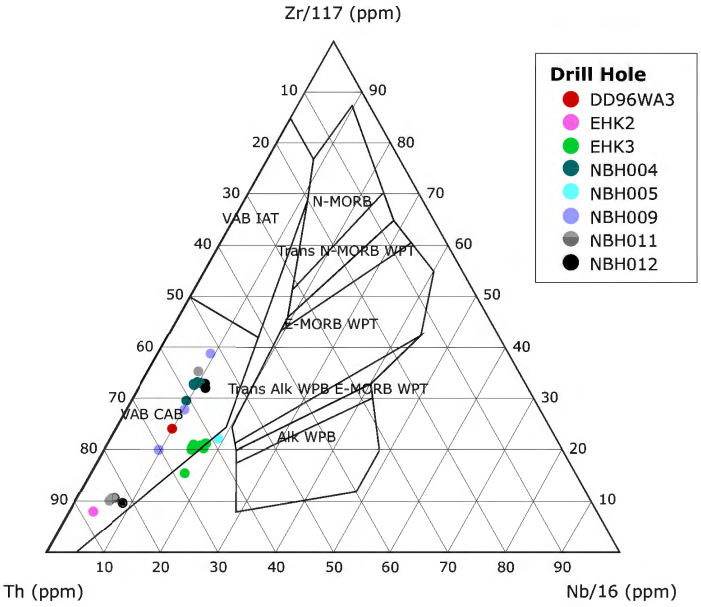

Figure 4.7: Th-Zr-Nb discrimination diagram for mafic rocks of the Loch Lilly-Kars (Wood 1980). Fields: volcanic-arc basalt island-arc tholeiites (VAB IAT), volcanic-arc basalt calc-alkaline basalts (VAB CAB), N-type mid-ocean-ridge basalt (N-MORB), E-type mid-ocean-ridge basalt and within-plate tholeiites (E-MORB WPT), alkaline within-plate basalts (Alk WPB). Transitional zones include Trans N-MORB WPT and Trans Alk WPB E-MORB WPT.

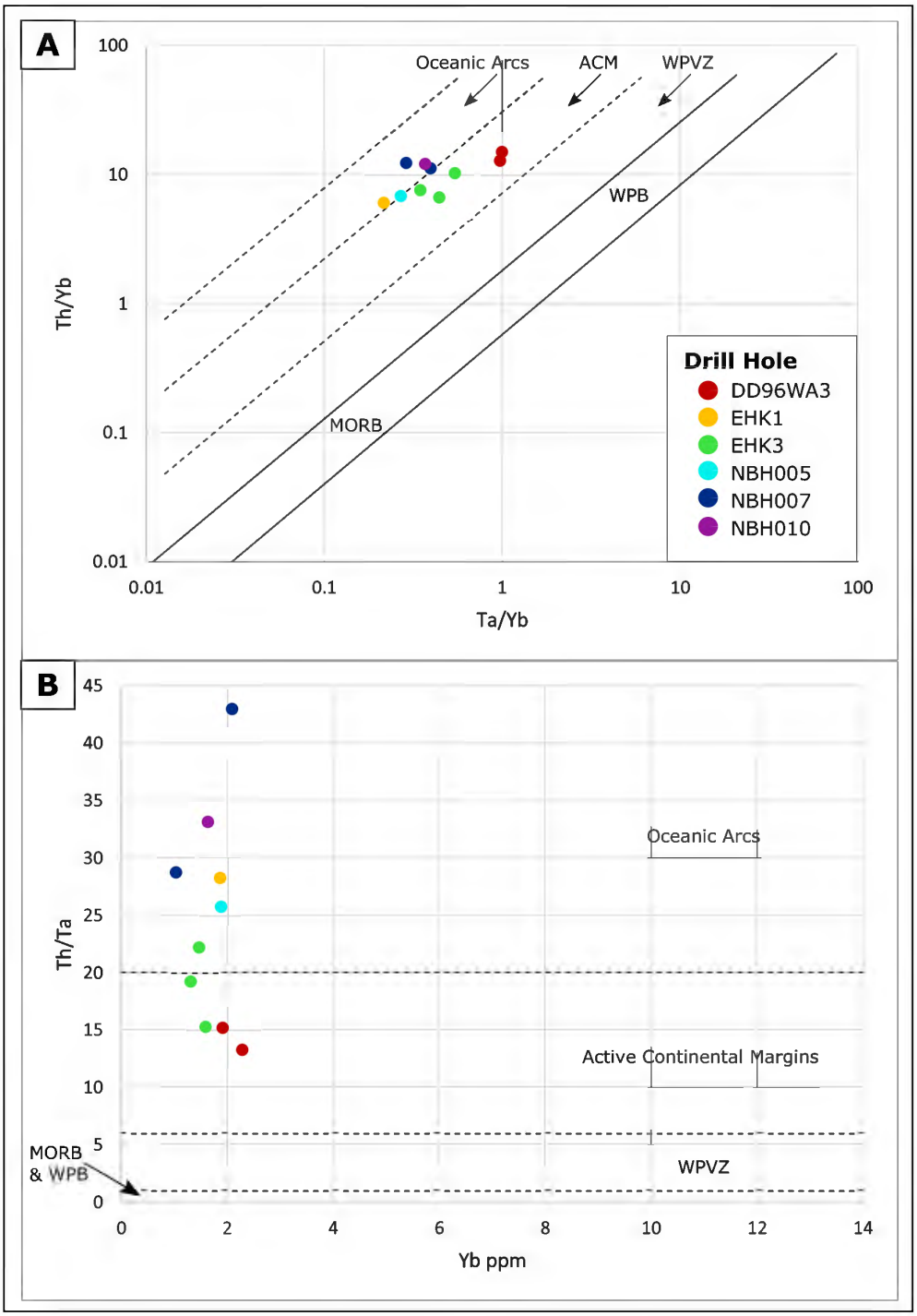

Figure 4.8: Th/Yb vs Ta/Yb (A) and Th/Ta vs Yb (B) discrimination diagrams for intermediate to felsic rocks of the Loch-Lilly Kars (Gordon and Schandl 2000). Fields are oceanic arcs, active continental margins (ACM), within-plate volcanic zones (WPVZ), mid-ocean-ridge basalt (MORB) and within-plate basalt (WPB).

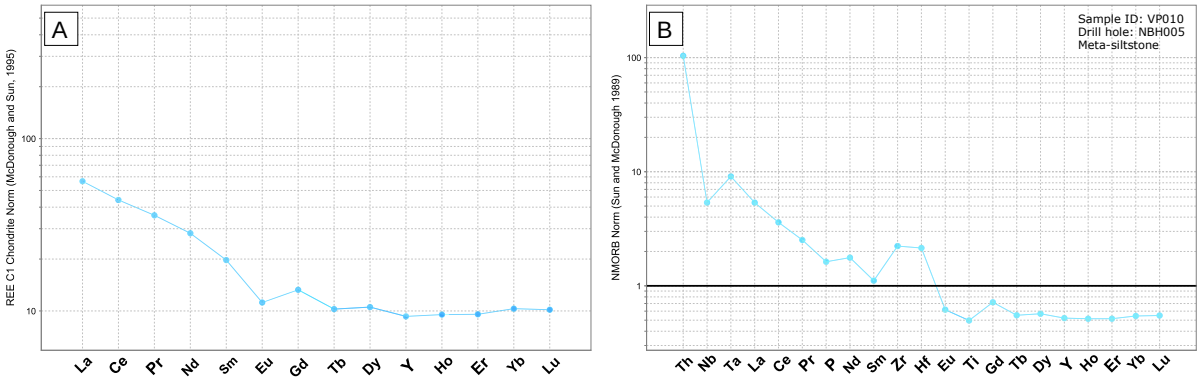

Figure 4.9: (A) Chondrite-normalised pattern for meta-sedimentary sample (VP010) from Loch Lilly-Kars drill hole NBH005. Normalising values are from Sun and McDonough (1995). (B) NMORB-normalised pattern for meta-sedimentary sample (VP010) from Loch Lilly-Kars drill hole NBH005. Normalising values are from Sun and McDonough (1989).

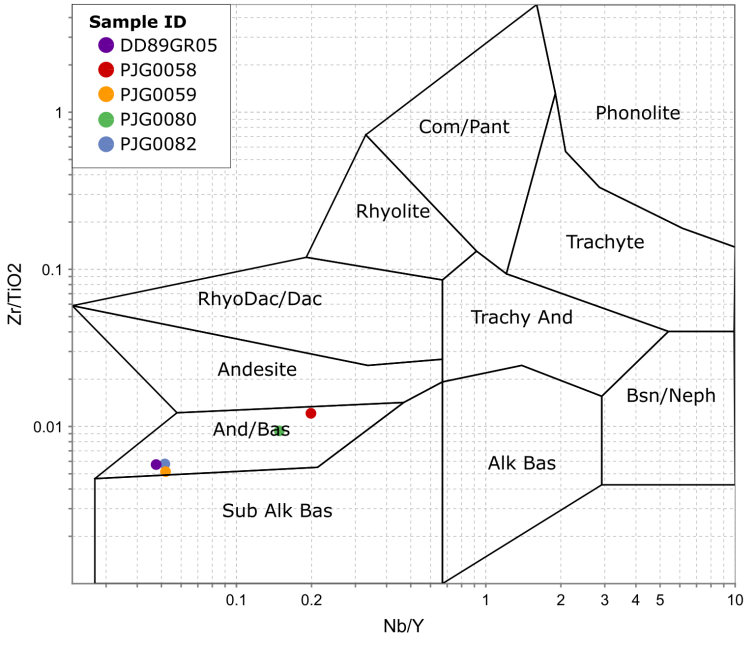

Figure 4.10: Zr/TiO_2 vs Nb/Y discrimination diagram for volcanic rocks of the Koonenberry (Winchester and Floyd 1977).

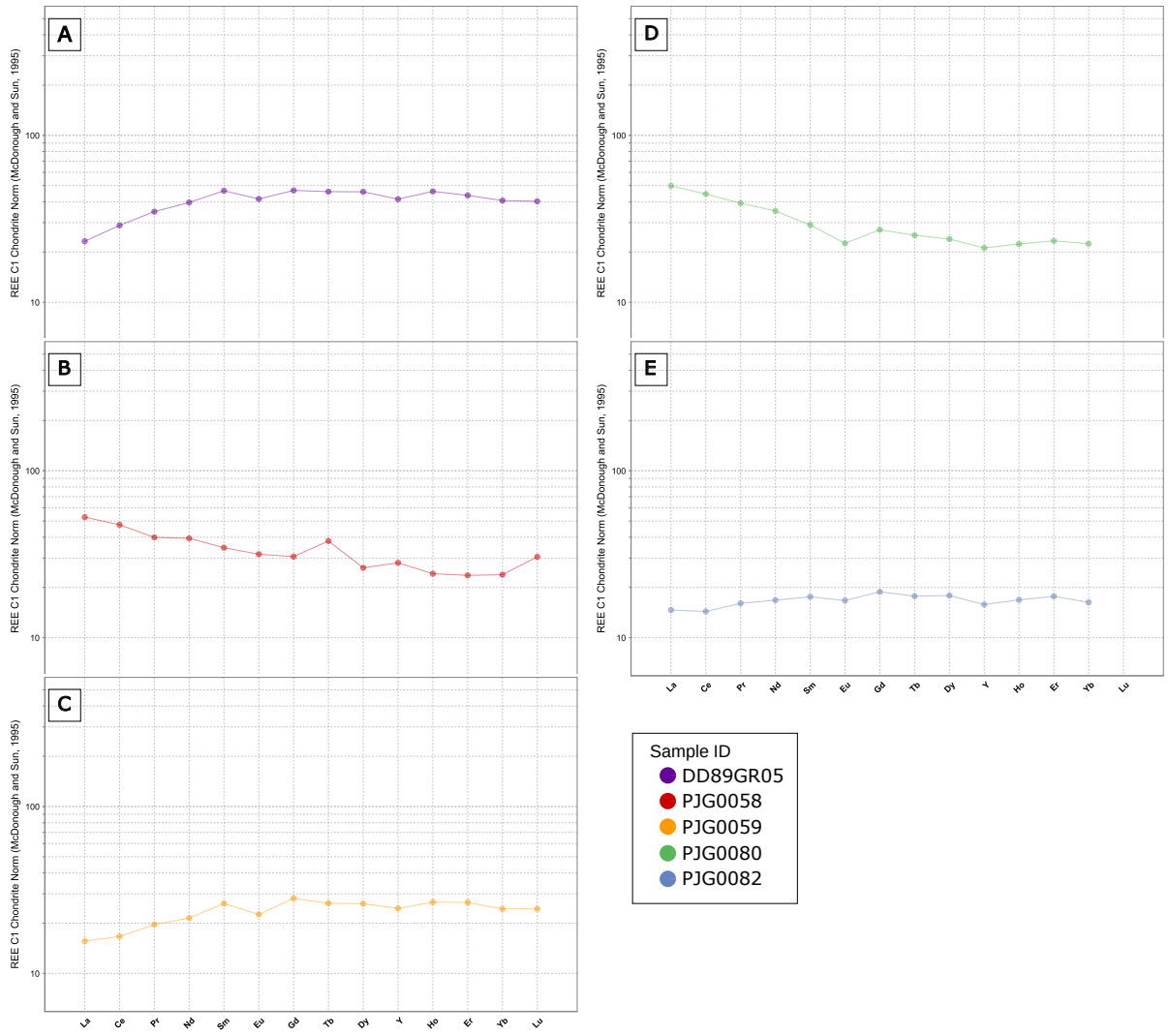

Figure 4.11: Chondrite-normalised REE patterns for mafic rocks of the Koonenberry. Normalising values are from Sun and McDonough (1995).

Chondrite-normalised patterns reveal samples PJG0080 (Fig 4.11 D) and PJG0058 (Fig 4.11 B) are slightly LREE enriched with La/Yb_n values of 2.22 and 2.21, respectively. Samples PJG0059, PJG0082 and DD89GR05 (Fig 4.11 C, E and A, respectively) are slightly depleted in LREE with La/Yb_n values of 0.64, 0.90 and 0.57, respectively.

NMORB-normalised patterns for tholeiitic samples PJG0059 and PJG0082 (Fig 4.12 C and E, respectively) show intra-oceanic arc-like signatures with Nb/Yb values close to 1 (0.51 and 0.49 respectively) and Th enrichment. Additionally, PJG0082

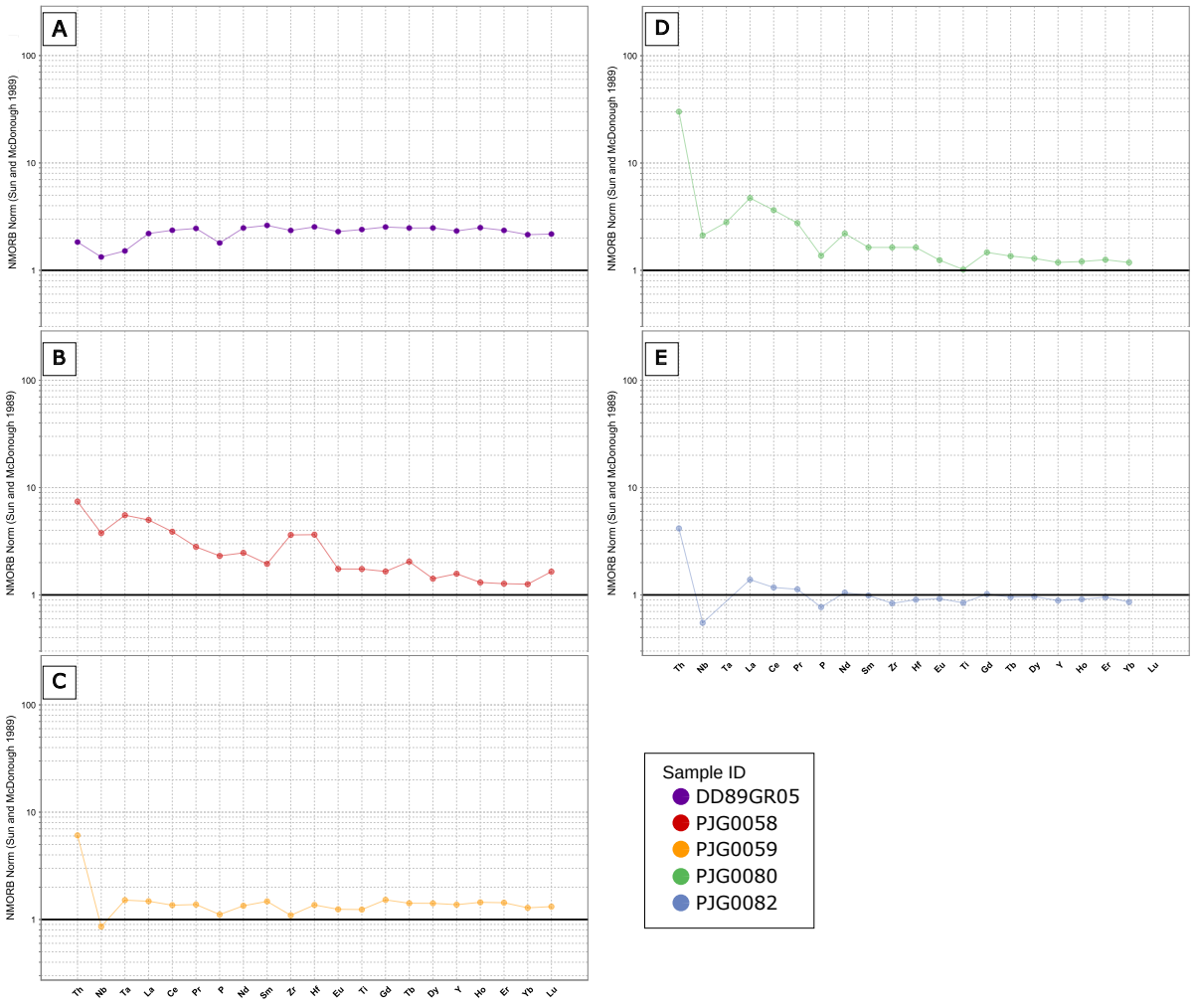

Figure 4.12: NMORB-normalised patterns for mafic rocks of the Koonenberry. Normalising values are from Sun and McDonough (1989).

shows a slight depletion in Ti which is absent in PJG0059, and the Nb depletion in PJG0059 is not as great as typical tholeiitic intra-oceanic arc rocks, making the pattern almost MORB-like. The NMORB-normalised pattern for PJG0080 appears transitional between oceanic and continental arc-like signatures (Fig 4.12 D), with a Nb/Yb ratio slightly greater than 1 (1.37). DD89GR05 and PJG0058 NMORB-normalised patterns (Fig 4.12 A and B, respectively) display relatively flat patterns with no HFSE anomalies. PJG0058 is more enriched than DD89GR05, but both samples are mature back-arc basin or MORB-like.

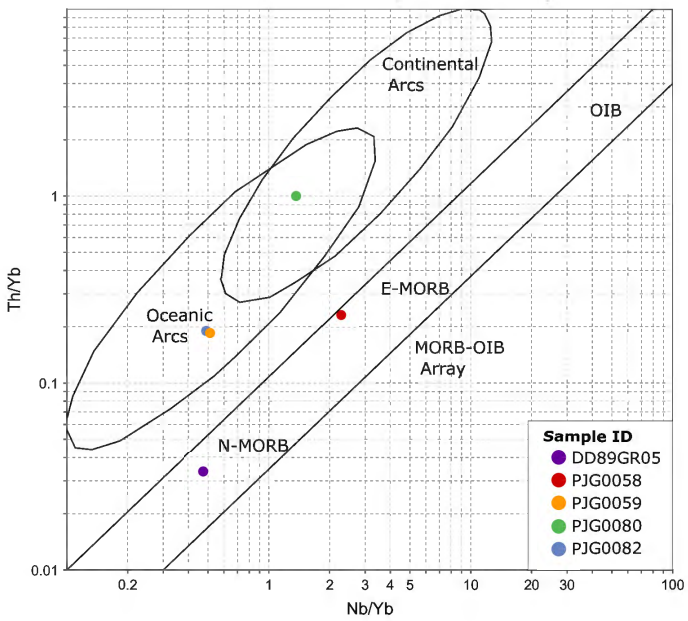

Figure 4.13: Th/Yb vs Nb/Yb discrimination diagram for mafic rocks of the Koonenberry (Pearce 2014).

The range in tectonic settings of the Koonenberry mafic rocks indicated by their NMORB-normalised patterns shown in Figure 4.12 is supported by discrimination diagrams. On the Th/Yb-Nb/Yb diagram of Pearce (2014) shown in Figure 4.13, PJG0059 and PJG0082 plot within the oceanic arc field whereas PJG0080 plots within the transitional field between oceanic and continental arcs. DD89GR05 and PJG0058 plot within the MORB array, with PJG0058 within the E-MORB field (Fig 4.13), reflecting its more enriched nature as indicated in Figure 4.11 B. This is further supported on the Th-Zr-Nb diagram of Wood (1980) shown in Figure 4.14, where PJG0059, PJG0082 and PJG0080 plot in the volcanic-arc basalt field, DD89GR05 plots within th N-MORB field, and PJG0058 plots closer to the transitional field between N-MORB and E-MORB.

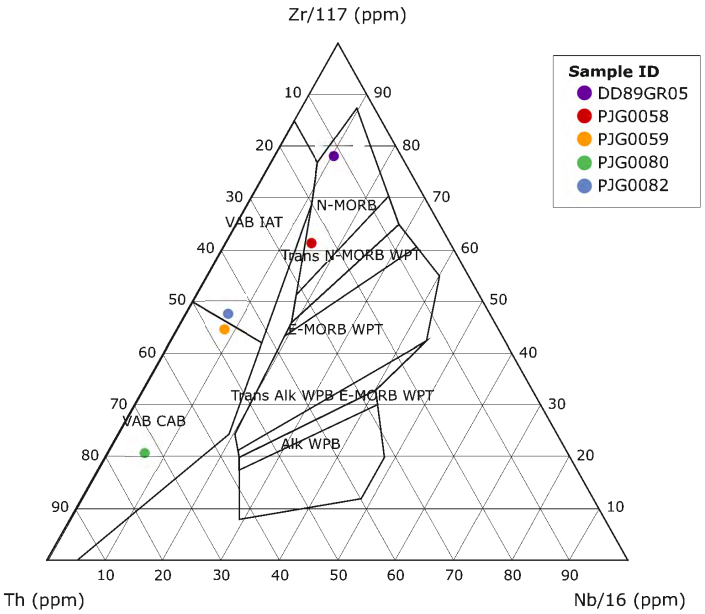

Figure 4.14: Th-Zr-Nb discrimination diagram for mafic rocks of the Koonenberry (Wood 1980). Refer to Figure 4.7 caption for fields.

Chapter 5

Zircon Geochronology

5.1 Introduction

Zircon is variable in external morphology and internal features. Such structures are indicative of the geologic history of the mineral (Corfu et al., 2003) as well as the environment of crystallisation (Belousova et al., 2006), such as temperature and magma composition. As Corfu et al. (2003) explains, acicular needle-shaped zircons are common in sub-volcanic intrusions, gabbros, and high-level granites that have been rapidly crystallised, whereas the more stubby and equant zircon shapes develop within slowly cooled, deep-seated intrusions. Internal zoning patterns, viewed using CL imaging, can assist in distinguishing between igneous oscillatory zoning and metamorphic zoning patterns.

The ability to survive magmatic, metamorphic and erosional processes that destroy most other common minerals, as well as the usefulness as a geochronometer based on the decay of U (and Th) to Pb (Corfu et al., 2003), makes zircon particularly useful for extracting information on the history of the host rock. Additionally, zircon strongly affects the behaviour of many trace elements during magma crystallisation (Belousova et al., 2006), importantly Hf which can be used as a radiogenic isotopic

tracer of crustal and mantle processes.

This section reports morphology, U-Pb ages, Lu-Hf isotope and trace element compositions for zircons separated from five samples from the Loch Lilly-Kars study area and three samples from the Koonenberry study area. These samples were chosen for U-Pb zircon geochronology to provide a better age constraint on the Loch Lilly-Kars as there are some discrepancies between existing ages from Baatar et al. (2019) and unpublished data from the 2015 Annual Exploration Report for EL8199 from Anglo American. These ages are shown in Table 5.1. Additionally, samples from Loch Lilly-Kars drill holes NBH005 and NBH012 as well as samples from outcrop in the Koonenberry Belt were chosen as the age of these units were not known.

Table 5.1: Summary of zircon and titanite U-Pb and Ar-Ar biotite ages for the Loch Lilly-Kars. Data from Baatar et al. (2019) and the 2015 Annual Exploration Report for EL8199 from Anglo American (unpublished).

Drill Hole	Depth (m)	Sample ID	Analysis	Analysis By	Age
EHK1	112.1	AUR101955	U-Pb zircon	Baatar et al. (2019)	392 ± 7 Ma
EHK1	112.1	AUR101955	U-Pb zircon	Anglo American	431.2 ± 3.7 Ma
EHK2	179.8	AUR101956	U-Pb zircon	Anglo American	416 ± 12 Ma
EHK3	144.6	AUR101958	U-Pb titanite	Anglo American	411 ± 9 Ma
EHK3	184.7	AUR101961	U-Pb titanite	Anglo American	426 ± 9 Ma
NBH007	134.25	AUR101934	U-Pb zircon	Baatar et al. (2019)	393 ± 4 Ma

NBH007	134.25	AUR101934	U-Pb zircon	Anglo American	424 ± 5 Ma
NBH009	259.5	AUR101952	U-Pb zircon	Anglo American	506 ± 5 Ma
NBH010	155.9	AUR101946	U-Pb zircon	Baatar et al. (2019)	496 ± 6 Ma
NBH010	155.9 m	AUR101946	U-Pb zircon	Anglo American	508 ± 4 Ma
NBH011	240.5	AUR101940	Ar-Ar biotite	Anglo American	514 ± 4 Ma (plataeu)
DD96WA3	887.1	AUR101988	U-Pb zircon	Anglo American	523 ± 4 Ma
DD96WA3	931	AUR101989	U-Pb titanite	Anglo American	503 ± 8 Ma

5.2 Zircon Morphology

5.2.1 VP001

Zircon grains from sample VP001 are predominantly euhedral, ranging from slender to stubby in shape. Some grains are more rounded and these commonly contain more fractures and inclusions and appear slightly darker in TL. Aspect ratios are commonly 2:1 to 3:1, however, range up to 5:1 for the more elongate crystals. Most grains appear transparent in TL, however appear darker and more brown in colour along the fractures. These areas are likely metamict zones, where the zircon lattice

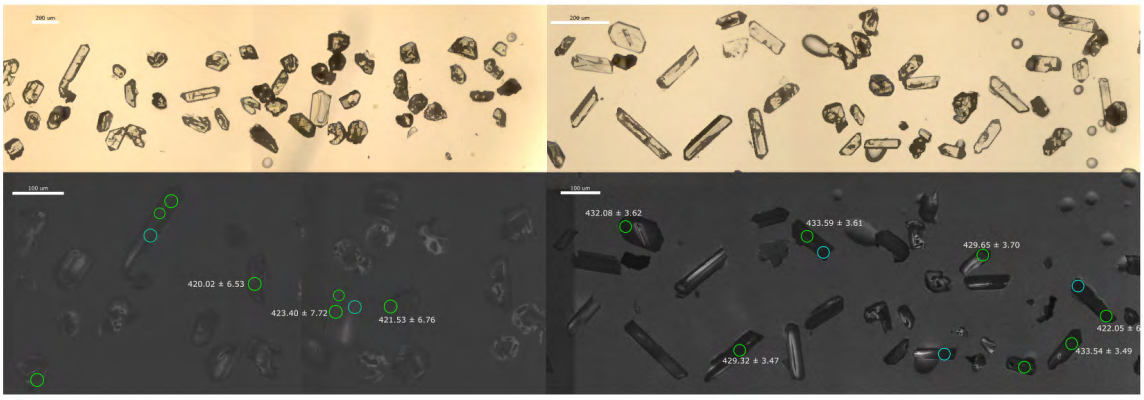

Figure 5.1: Transmitted light (TL) and cathodoluminescence (CL) images of zircon for VP001. Green circles represent targets for U-Pb LA-ICP-MS and blue circles represent targets for Lu-Hf isotope analysis. Concordant ages corresponding to zircon spots are shown.

has suffered radiation damage. In CL, the elongated grains commonly appear homogeneous and show low fluorescence, with some showing broad, ill-defined banding. Rounded grains appear more patchy, with ill-defined concentric zoning.

5.2.2 VP002

Zircon grains from sample VP002 are predominantly euhedral and elongated. Aspect ratios range from 2:1 to 4:1, with 4:1 the most common shape. Grains are mostly transparent to translucent appearing darker and more brown in colour along fractures, likely metamict zones. In CL, most grains show low fluorescence and display homogeneous to il-defined zoning patterns. Some grains show ill-defined concentric zoning of cores.

5.2.3 VP007

A small zircon grainset (<10 grain fragments) was extracted from sample VP007, of which all U-Pb analyses were discordant. Results for this sample are not discussed further.

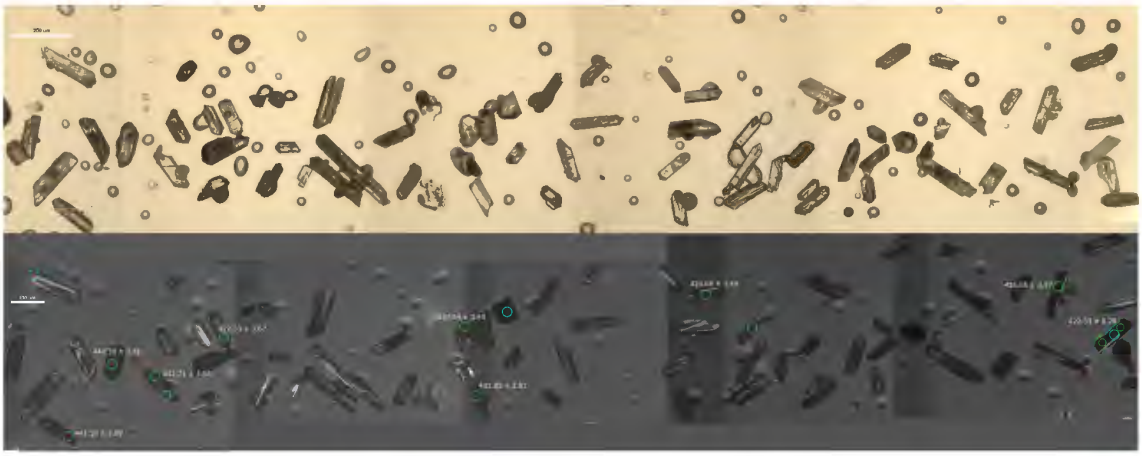

Figure 5.2: TL and CL images of zircon for VP002. Green circles represent targets for U-Pb LA-ICP-MS and blue circles represent targets for Lu-Hf isotope analysis. Concordant ages corresponding to zircon spots are shown.

5.2.4 VP008

Zircon grains from sample VP008 are mostly euhedral grains with aspect ratios of 3:1 to 4:1, with some more rounded grains with aspect ratios of 2:1. Fractures and inclusions are common in the coarser grains, and less common in the finer grained, more euhedral crystals. Grains are predominantly transparent, although some grains display an orange to yellow tint. CL images reveal indistinct zoning patterns with dark, rounded cores and light rims which occasionally show oscillatory zoning for most grains. Sector zoning is also common, and few grains display oscillatory zoning of cores. The more elongate grains appear homogeneous with low fluorescence.

5.2.5 VP012

Zircons were extracted from both felsic (VP012F) and mafic (VP012M) sections of drill core.

The zircon grains from VP012F are mostly euhedral and transparent, with aspect ratios ranging from 2:1 to 3:1. Fractures and inclusions are common. CL imaging reveals complex zoning patterns. Zircon rims appear light and are commonly homo-

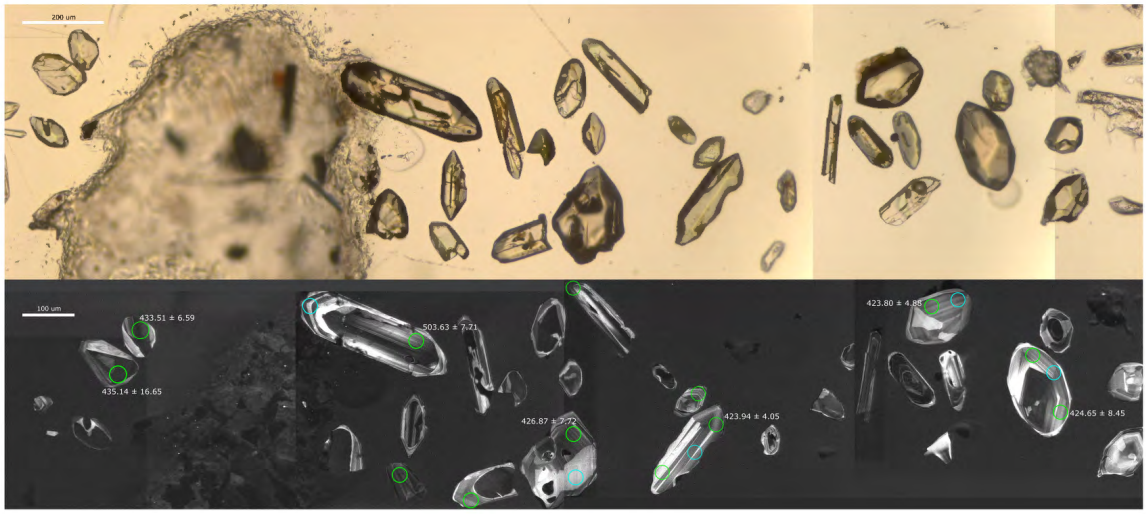

Figure 5.3: TL and CL images of zircon for VP008. Green circles represent targets for U-Pb LA-ICP-MS and blue circles represent targets for Lu-Hf isotope analysis. Concordant ages corresponding to zircon spots are shown.

geneous or show sector zoning. Cores are dark grey to black and are often rounded, displaying patchy or oscillatory zoning.

The mafic sample, VP012M, contains zircon grains ranging in shape from stubby with aspect ratios of 1:1 and 2:1, to moderately elongate with aspect ratios of 3:1. Most grains are transparent with fractures, however, some appear more translucent with a slight grey colour and yellow striations. Inclusions are also present in some grains, commonly within the cores. CL images reveal irregular, patchy domains and sector zoning for most grains. A second type of zoning is observed in the more elongated crystals, with these grains showing homogeneous dark cores with thin, slightly brighter rims.

5.2.6 VP013

One zircon grain was extracted from sample VP013, acicular in shape with an aspect ratio of 5:1.

Figure 5.4: TL and CL images of zircon for VP012F. Green circles represent targets for U-Pb LA-ICP-MS and blue circles represent targets for Lu-Hf isotope analysis. Concordant ages corresponding to zircon spots are shown.

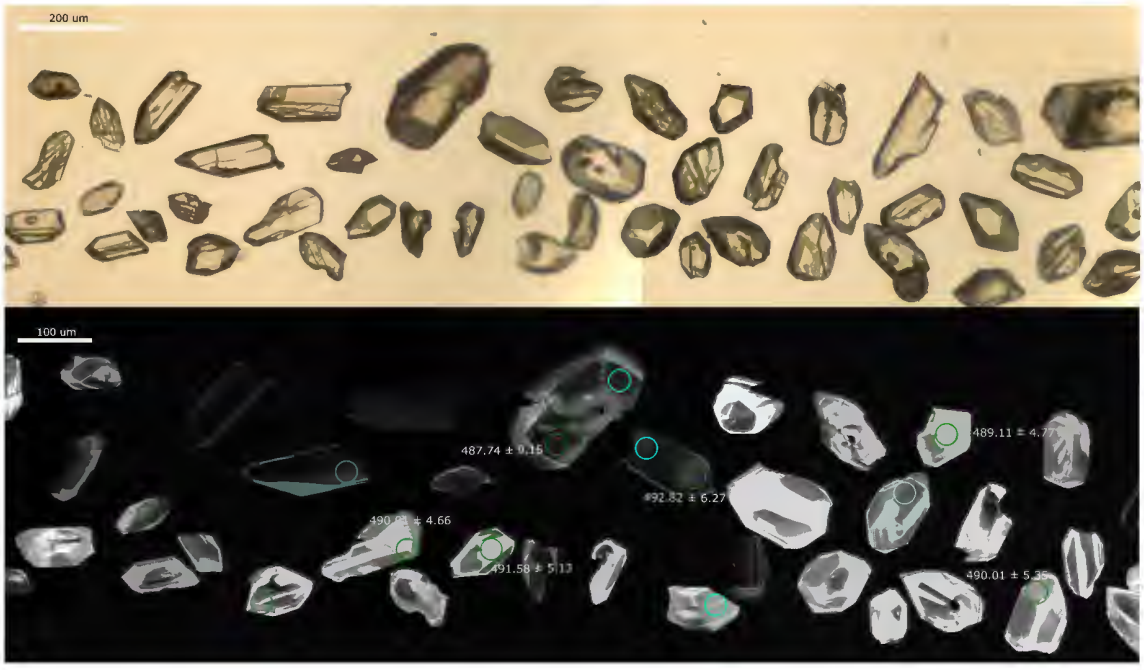

Figure 5.5: TL and CL images of zircon for VP012M. Green circles represent targets for U-Pb LA-ICP-MS and blue circles represent targets for Lu-Hf isotope analysis. Concordant ages corresponding to zircon spots are shown.

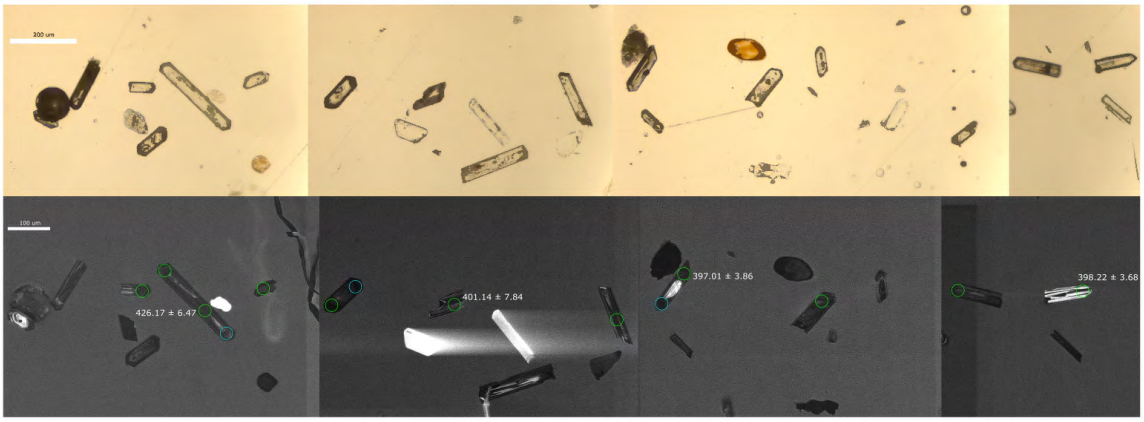

Figure 5.6: TL and CL images of zircon for PJG0059. Green circles represent targets for U-Pb LA-ICP-MS and blue circles represent targets for Lu-Hf isotope analysis. Concordant ages corresponding to zircon spots are shown.

5.2.7 PJG0059

Zircon grains from sample PJG0059 are euhedral and elongated, with aspect ratios commonly 3:1 to 4:1. Most grains are transparent, with some grains showing yellow striations. Grains with multiple fractures have a slight brown colour, likely metamict zones. In CL, grains show concentric zoning with bright cores. Patchy zoning is also common.

5.2.8 PJG0080

Zircon grains from sample PJG0080 range in shape from moderately elongated euhedral to subhedral grains, to more rounded grains with aspect ratios of 1:1 to 2:1. Fractures are very common and grains appear mostly translucent with slight brown to orange colour. Grains with less fractures appear to be either transparent or have grey colourisation with yellow striations. In CL, most grains display ill-defined to broad concentric zoning patterns, with some showing patchy zoning. Few grains show bright oscillatory zoning with dark cores.

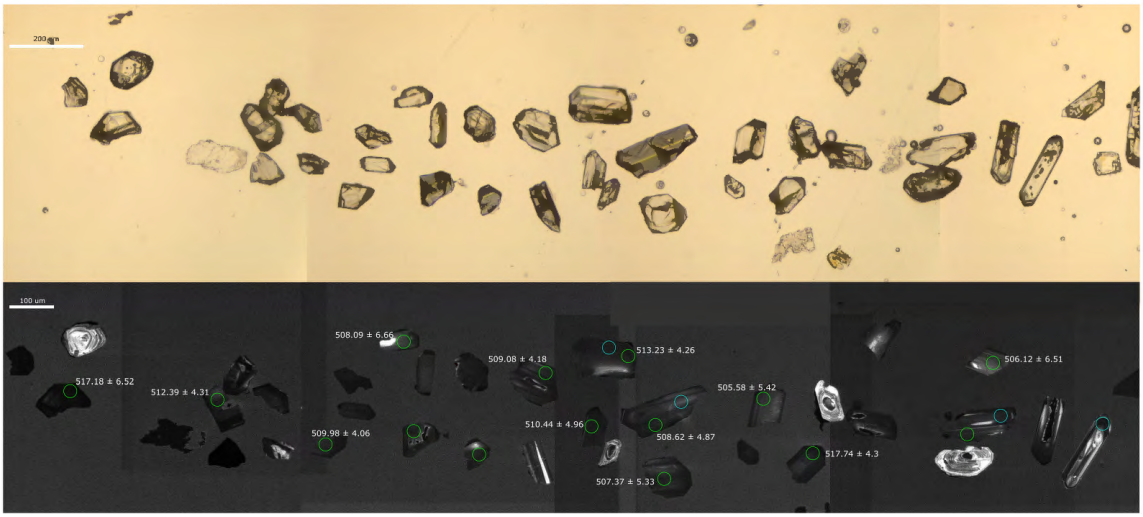

Figure 5.7: TL and CL images of zircon for PJG0080. Green circles represent targets for U-Pb LA-ICP-MS and blue circles represent targets for Lu-Hf isotope analysis. Concordant ages corresponding to zircon spots are shown.

5.2.9 PJG0082

Zircon grains from sample PJG0082 are euhedral to subhedral, with aspect ratios ranging from 1:1 to 2:1. Grains are mostly transparent, with metamict zones along fractures and surrounding inclusions. CL images reveal two types of zoning patterns; concentric zoning is the most common, however, some grains appear dark and homogeneous, exhibiting no obvious zoning patterns or faint banding. Some of the concentric zoned grains show dark, rounded cores that are homogeneous or show patchy zoning.

5.3 Trace Elements

Magmatic and metamorphic zircons can be distinguished by their Th/U ratios (Long et al., 2012), with low Th/U ratios considered indicative of metamorphic zircon (Kirkland et al., 2015). Metamorphic zircons with high Th/U also occur, however, these are associated with high grade metamorphic environments (Kirkland et al., 2015).

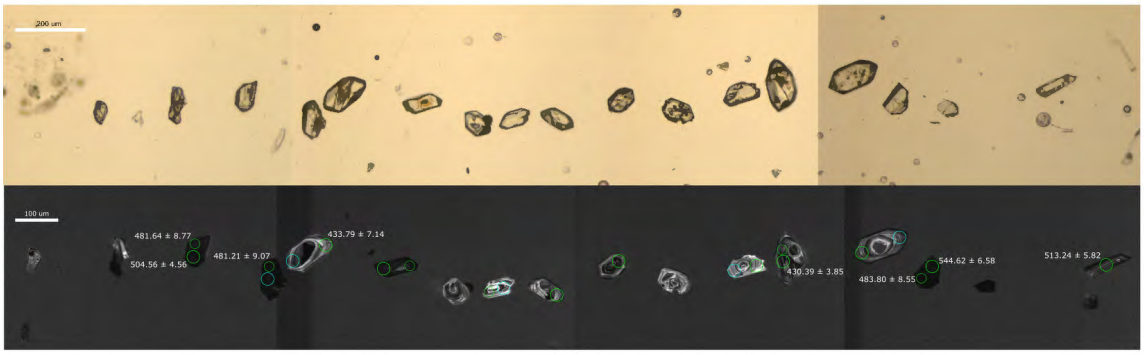

Figure 5.8: TL and CL images of zircon for PJG0082. Green circles represent targets for U-Pb LA-ICP-MS and blue circles represent targets for Lu-Hf isotope analysis. Concordant ages corresponding to zircon spots are shown.

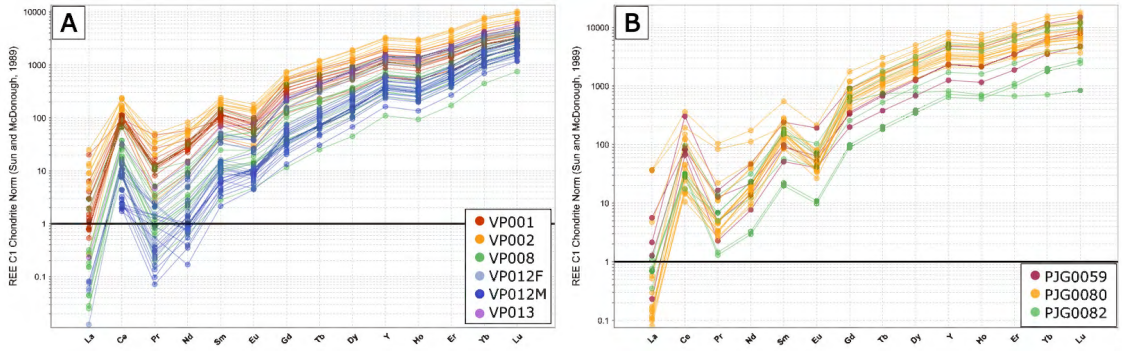

Figure 5.9: Zircon trace element patterns for Loch Lilly-Kars (A) and Koonenberry (B) samples. Normalising values are from Sun and McDonough (1989).

The concordant analyses used in the weighted mean average age for all Loch Lilly-Kars and Koonenberry samples have Th/U ratios > 0.4. These values indicate a magmatic origin for the zircons, as these rocks do not show evidence of high grade metamorphism. Furthermore, chondrite-normalised REE patterns (Fig 5.9) show a steep increase from La to Lu with positive Ce and negative Eu anomalies, typical of unaltered, magmatic zircon (Hoskin and Schaltegger 2003, Hoskin 2004, Long et al., 2012). In some samples such as VP008, VP012M and VP013, the Eu anomaly is less pronounced.

5.4 U-Pb Ages

A brief summary of zircon U-Pb LA-ICP-MS geochronology data and sample details are provided in Table 5.2, followed by detailed descriptions of data characteristics for each sample. Two sessions of zircon U-Pb LA-ICP-MS geochronology data are presented. The data from session two is commonly discordant and has larger errors than data from session one.

Table 5.2: Summary of zircon U-Pb LA-ICP-MS geochronology results.

Sample ID	Drill Hole	Rock Type	Age	MSWD	n
VP001	EHK1	Diorite	423.98 ± 1.23	1.09	17/45
VP002	EHK2	Diorite	423.00 ± 1.51	0.92	10/25
VP008	NBH005	Andesite Porphyry	426.26 ± 1.49	0.96	13/24
VP012F	NBH009	Diorite	490.18 ± 1.64	0.78	11/25
VP012M	NBH009	Gabbro	490.00 ± 1.55	0.98	13/13
PJG0059	Outcrop	Porphyritic Basalt	398.87 ± 3.80	1.80	4/9
PJG0080	Outcrop	Dolerite	509.07 ± 1.17	0.97	25/39
PJG0082	Outcrop	Gabbro	430.25 ± 6.48	1.03	3/6

5.4.1 VP001

440 zircon grains were mounted for VP001. Due to the fine grainsize, 46 spots were analysed in session one and a further 16 spots were added for the follow up session (session two). 40 of 46 analyses from session one were concordant and the results are presented in Figure 5.10 A. The youngest analysis (VP001b-7.d) is 90% concordant with an age of 418.37 ± 8.03 Ma and is within uncertainty of the youngest cluster included in the weighted mean average. Two concordant analyses from session two have been included in the combined weighted mean average age, shown in Figure 5.10 B as 423.98 ± 1.23 Ma, with a statistically robust MSWD of 1.09. All data

from session two including discordant analyses are presented in Figure 5.10 C, with two analyses removed due to suspected lead loss and two included but greyed out due to inheritance. Figure 5.10 D shows the combined analyses from session one and two. Of the session one discordant data, two analyses have been removed from the Concordia plot (Fig 5.10 D) due to suspected lead loss and 13 analyses have been included but greyed out due to inheritance.

Projection back to the concordia returns Pb anchored model-1 discordia intercept ages of 425.67 ± 2.72 Ma (Fig 5.10 C), and 426.95 ± 1.51 Ma (Fig 5.10 D). These ages are within error of the age determined from the combined weighted mean average age of concordant data shown in Figure 5.10 B.

Interpretation

The combined weighted mean average age of 423.98 ± 1.23 Ma is the inferred emplacement age for this diorite intrusive. Zircon grains are elongate and display ill-defined to patchy zoning, consistent with patterns observed in zircons from intermediate to mafic melts (Corfu et al. 2003; Hoskin 2000), and trace element REE patterns are consistent with those observed in magmatic zircons (Fig 5.9).

5.4.2 VP002

275 zircon grains were mounted for VP002. Due to the fine grainsize, 32 spots were analysed in session one and a further 19 spots were added for the follow up session (session two). 22 of 32 analyses from session one were concordant and the results are presented in Figure 5.11 A. The youngest analysis (VP002b-13.d) is 90% concordant with an age of 419.50 ± 7.48 Ma and is within uncertainty of the youngest cluster included in the weighted mean average. Two concordant analysis from session two have been included in the combined weighted mean average age, shown in Figure 5.11 B as 423 ± 1.51 Ma, with a statistically robust MSWD of 0.92. All data

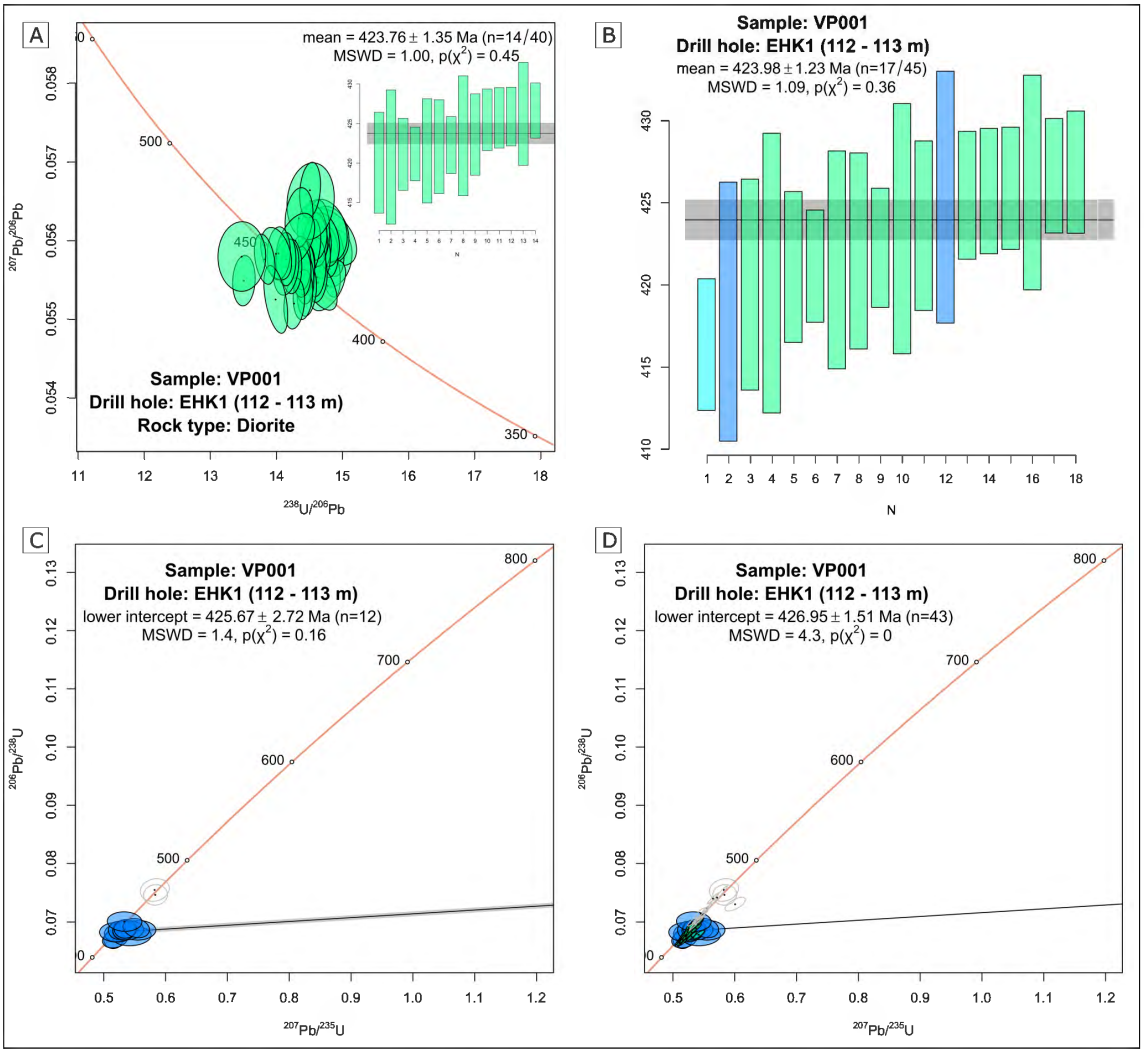

Figure 5.10: (A) Tera–Wasserburg Concordia diagram for VP001. Inset of the weighted mean average age. Data from session one. (B) Combined weighted mean average age of concordant data from both sessions. (C) Wetherill-type Concordia diagram for VP001, with Model-1 intercept age presented. Concordant and discordant data included from session two. (D) Combined Wetherill-type Concordia diagram for VP001, with Model-1 intercept age presented. Concordant and discordant data included from both sessions. Green represents analyses from session one, dark blue represents analyses from session two, and light blue represents outliers. Ages inferred to be inheritance are presented on Concordia diagrams in grey.

from session two including discordant analyses are presented in Figure 5.11 C, with 11 analyses removed due to suspected lead loss. Figure 5.11 D shows the combined analyses from session one and two. Of the session one discordant data, eight analyses have been removed from the Concordia plot (Fig 5.11 D) due to suspected lead loss and one analysis has been included but greyed out due to inheritance.

Projection back to the concordia returns Pb anchored model-1 discordia intercept ages of 421.55 ± 4.76 Ma (Fig 5.11 C), and 425.86 ± 2.46 Ma (Fig 5.11 D). These ages are within error of the age determined from the combined weighted mean average age of concordant data shown in Figure 5.11 B.

Interpretation

The combined weighted mean average age of 423 ± 1.51 Ma is the inferred emplacement age for this diorite intrusive. Zircons mounted from this sample are morphologically similar to VP001, and considered to represent a magmatic population. This is supported by the trace element REE patterns which indicate a magmatic origin (Fig 5.9).

5.4.3 VP008

149 zircon grains were mounted for VP008. 46 spots were analysed in session one and a further 22 spots were added for the follow up session (session two). 23 of 46 analyses from session one were concordant and the results are presented in Figure 5.12 A. The youngest analysis (VP008(#2)-03-1) is 93% concordant with an age of 423.68 ± 6.33 Ma and is within uncertainty of the youngest cluster included in the weighted mean average. One concordant analysis from session two has been included in the combined weighted mean average age, shown in Figure 5.12 B as 426.26 ± 1.49 Ma, with a statistically robust MSWD of 0.96. All data from session two including discordant analyses are presented in Figure 5.12 C, with seven analyses removed due

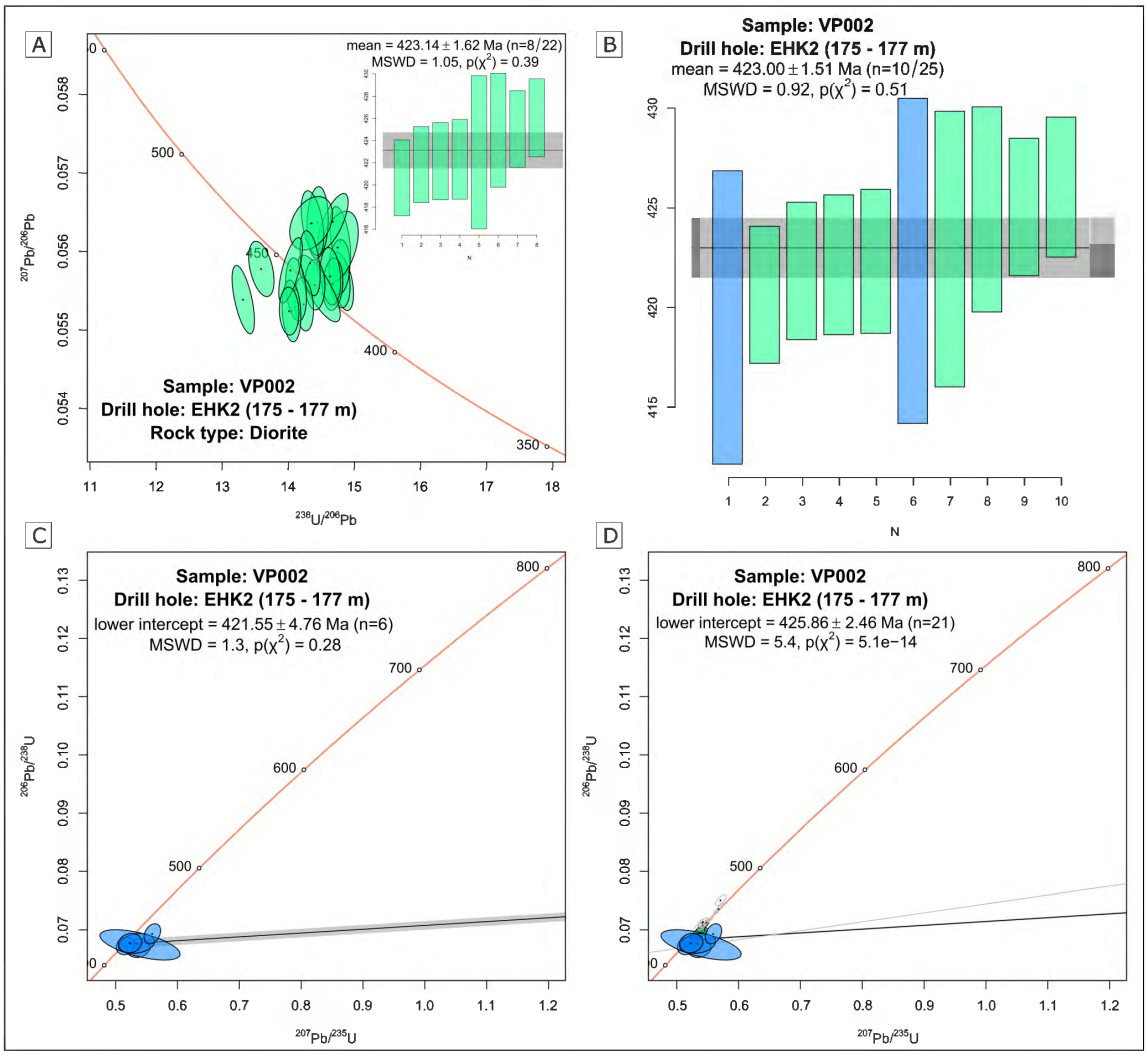

Figure 5.11: (A) Tera–Wasserburg Concordia diagram for VP002. Inset of the weighted mean average age. Concordant data from session one only. (B) Combined weighted mean average age of concordant data from both sessions. (C) Wetherill-type Concordia diagram for VP002, with Model-1 intercept age presented. Concordant and discordant data included from session two. (D) Combined Wetherill-type Concordia diagram for VP002, with Model-1 intercept age presented. Concordant and discordant data included from both sessions. Green represents analyses from session one and dark blue represents analyses from session two. Ages inferred to be inheritance are presented on Concordia diagrams in grey.

to suspected lead loss and six analyses included but greyed out due to inheritance. Figure 5.12 D shows the combined analyses from session one and two. Of the session one discordant data, seven analyses have been removed from the Concordia plot (Fig 5.12 D) due to suspected lead loss and one analysis has been included but greyed out due to inheritance.

Projection back to the concordia returns Pb anchored model-1 discordia intercept ages of 423.91 ± 6.53 Ma (Fig 5.12 C), and 426.29 ± 2.22 Ma (Fig 5.12 D). These ages are within error of the age determined from the combined weighted mean average age of concordant data shown in Figure 5.12 B.

Interpretation

Most spots for U-Pb LA-ICP-MS were placed on the outer growth domains of zircon grains that exhibit oscillatory zoning patterns or elongate grains that appear dark and homogeneous. The weighted mean average age determined from the youngest population within error of the youngest concordant analysis reveals an age of 426.26 ± 1.49 Ma. This is the inferred emplacement age for this andesite porphyry.

Two spots, one placed on a rounded core showing ill-defined zoning and the other placed on a rounded grain showing sector zoning, reveal older ages of 503.63 ± 7.71 Ma and 503.08 ± 4.57 Ma. These are considered to be inherited components from a Delamerian aged source.

5.4.4 VP012

VP012F

148 zircon grains were mounted for VP012F. 32 spots were analysed in session one, and a further 25 spots were added for the follow up session (session two). 25 of 32 analyses from session one were concordant and the results are presented in Figure

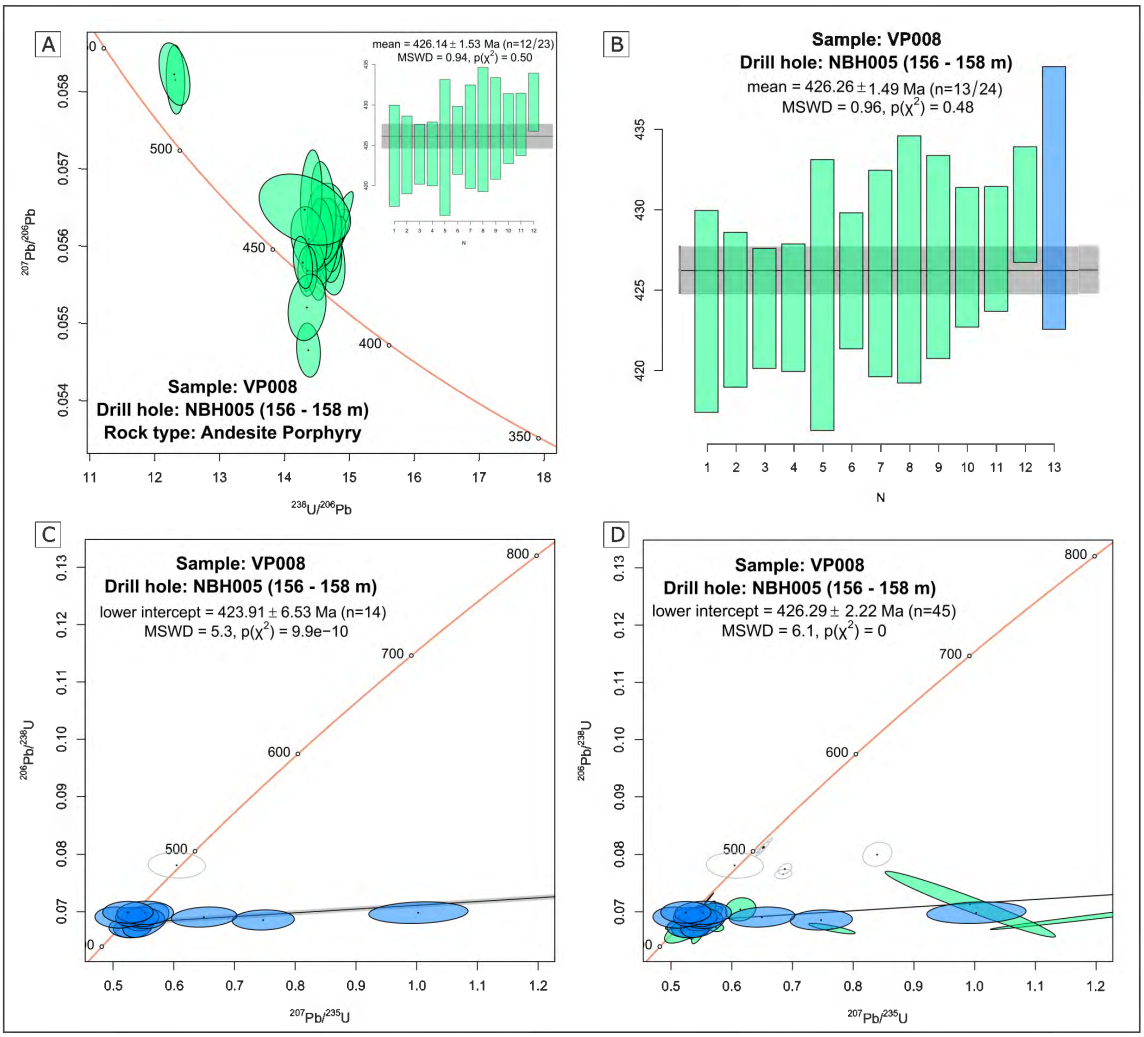

Figure 5.12: (A) Tera–Wasserburg Concordia diagram for VP008. Inset of the weighted mean average age. Concordant data from session one only. (B) Combined weighted mean average age of concordant data from both sessions. (C) Wetherill-type Concordia diagram for VP008, with Model-1 intercept age presented. Concordant and discordant data included from session two. (D) Combined Wetherill-type Concordia diagram for VP008, with Model-1 intercept age presented. Concordant and discordant data included from both sessions. Green represents analyses from session one and dark blue represents analyses from session two. Ages inferred to be inheritance are presented on Concordia diagrams in grey.

5.13 A. The youngest analysis (VP012F-11-1) is 90% concordant with an age of 486.49 ± 6.47 Ma and is within uncertainty of the youngest cluster included in the weighted mean average. The weighted mean average age is shown in Figure 5.13 B as 490.18 ± 1.64 Ma, with a MSWD of 0.78, suggesting parts of the data population may be missing. The analyses from session two were all discordant and the results are presented in Figure 5.13 C, with one analysis removed due to suspected lead loss and one analysis included but greyed out due to inheritance. Figure 5.13 D shows the combined analyses from session one and two. Of the session one discordant data, four analyses have been removed from the Concordia plot (Fig 5.13 D) due to lead loss and one analysis has been included but greyed out due to inheritance.

Projection back to the concordia returns Pb anchored model-1 discordia intercept ages of 503.38 ± 3.31 Ma (Fig 5.13 C), and 496.10 ± 2.04 Ma (Fig 5.13 D). This supports the age determined from the weighted mean average age of 490.18 ± 1.64 Ma, determined from concordant data from session one (Fig 5.13 B).

VP012M

117 zircon grains were mounted for VP012M and 28 spots were analysed in session one. A further 22 spots added for the follow up session (session two). 13 of 28 analyses from session one were concordant and the results are presented in Figure 5.14 A. The youngest analysis (VP012M-09-1) is 91% concordant with an age of 486.16 ± 4.33 Ma and is within uncertainty of the youngest cluster included in the weighted mean average. The weighted mean average age of the 13 concordant analyses is shown in Figure 5.14 B as 490 ± 1.55 Ma, with a statistically robust MSWD of 0.98. All analyses from session two were discordant and the results are presented in Figure 5.14 C, with one analysis included but greyed out due to inheritance. Figure 5.14 D shows the combined analyses from session one and two. Of the session one discordant data, 11 analyses have been removed from the Concordia plot (Fig 5.14

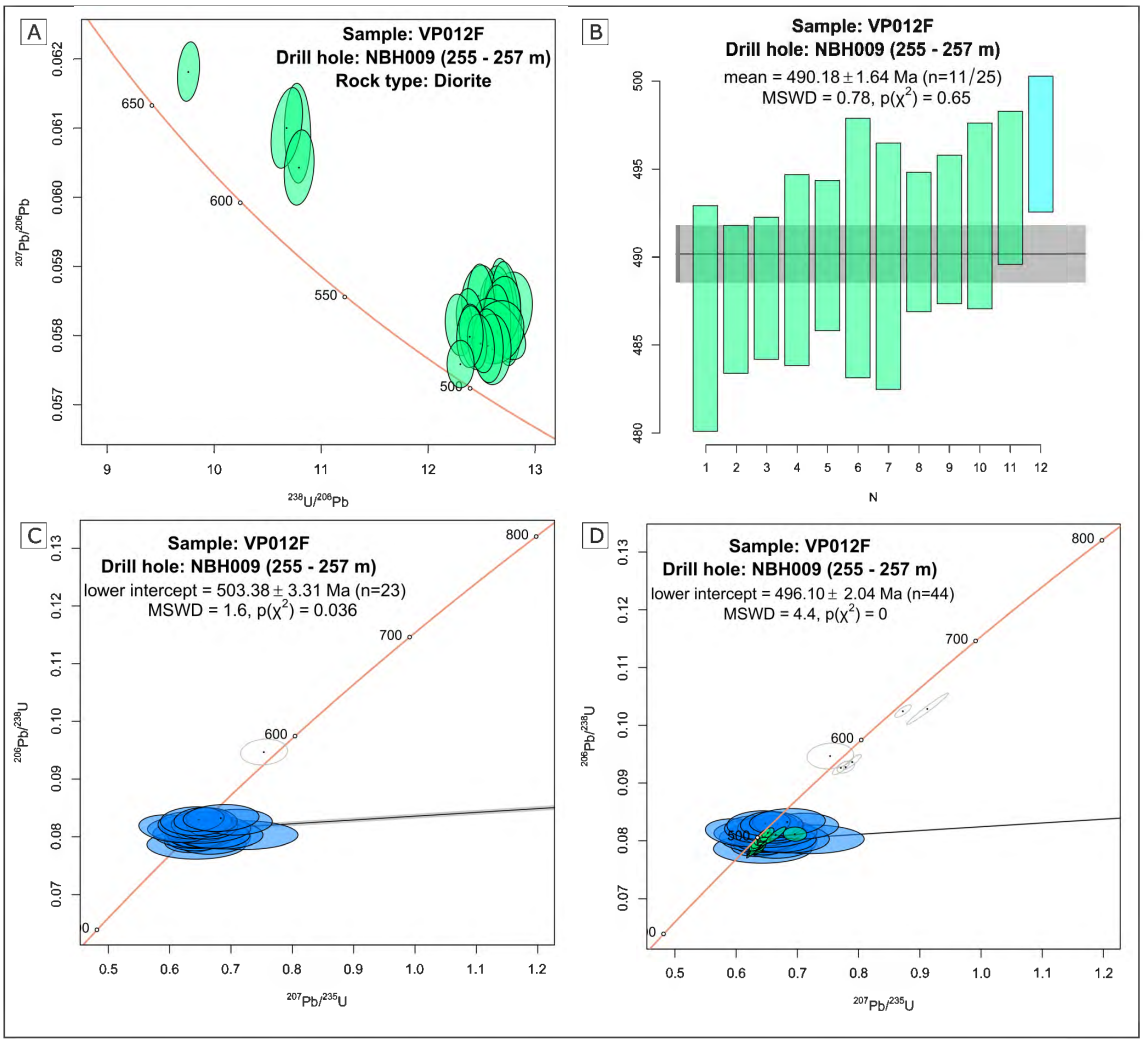

Figure 5.13: (A) Tera–Wasserburg Concordia diagram for VP012F. Data from session one. (B) Weighted mean average age of concordant data from session one. (C) Wetherill-type Concordia diagram for VP012F, with Model-1 intercept age presented. Concordant and discordant data included from session two. (D) Combined Wetherill-type Concordia diagram for VP012F, with Model-1 intercept age presented. Concordant and discordant data included from both sessions. Green represents analyses from session one, dark blue represents analyses from session two, and light blue represents outliers. Ages inferred to be inheritance are presented on Concordia diagrams in grey.

D) due to suspected lead loss.

Projection back to the concordia returns Pb anchored model-1 discordia intercept ages of 501.42 ± 4.79 Ma (Fig 5.14 C), and 490.40 ± 2.15 Ma (Fig 5.14 D). This supports the age determined from the weighted mean average age of 490 ± 1.55 Ma, determined from concordant data from session one (Fig 5.14 B).

Interpretation

Samples VP012F and VP012M represent diorite and gabbro that were likely comagmatic. The weighted mean average age for VP012F (490.18 ± 1.64 Ma; Fig 5.13 B) and VP012M (490 ± 1.55 Ma; Fig 5.14 B) are within error, and the combined weighted mean average age (not shown) is 490 ± 1.06 Ma. The euhedral zircon shape and trace element REE patterns are suggestive of magmatic origin (Fig 5.9), and therefore this age is inferred to represent the emplacement age.

VP012F has an inherited component of Neoproterozoic age that is not observed in VP012M. Spots placed on rounded grains showing ill-defined zoning or dark, rounded cores in VP012F reveal concordant ages ranging from 571.12 ± 5.80 Ma to 906.65 ± 7.3 Ma. There is also a much older concordant age of 2262.52 ± 16.80 Ma, from a spot on a dark, rounded core with ill-defined zoning.

5.4.5 VP013

One zircon grain was mounted for VP013. Three spots on this grain were analysed in session one, with only one spot returning a concordant analysis, returning an age of 386.18 ± 6.98 Ma.

Although the zircon is euhedral and acicular, characteristic of zircon grains from basaltic rocks, this age is likely an insignificant result and will therefore not be discussed further.

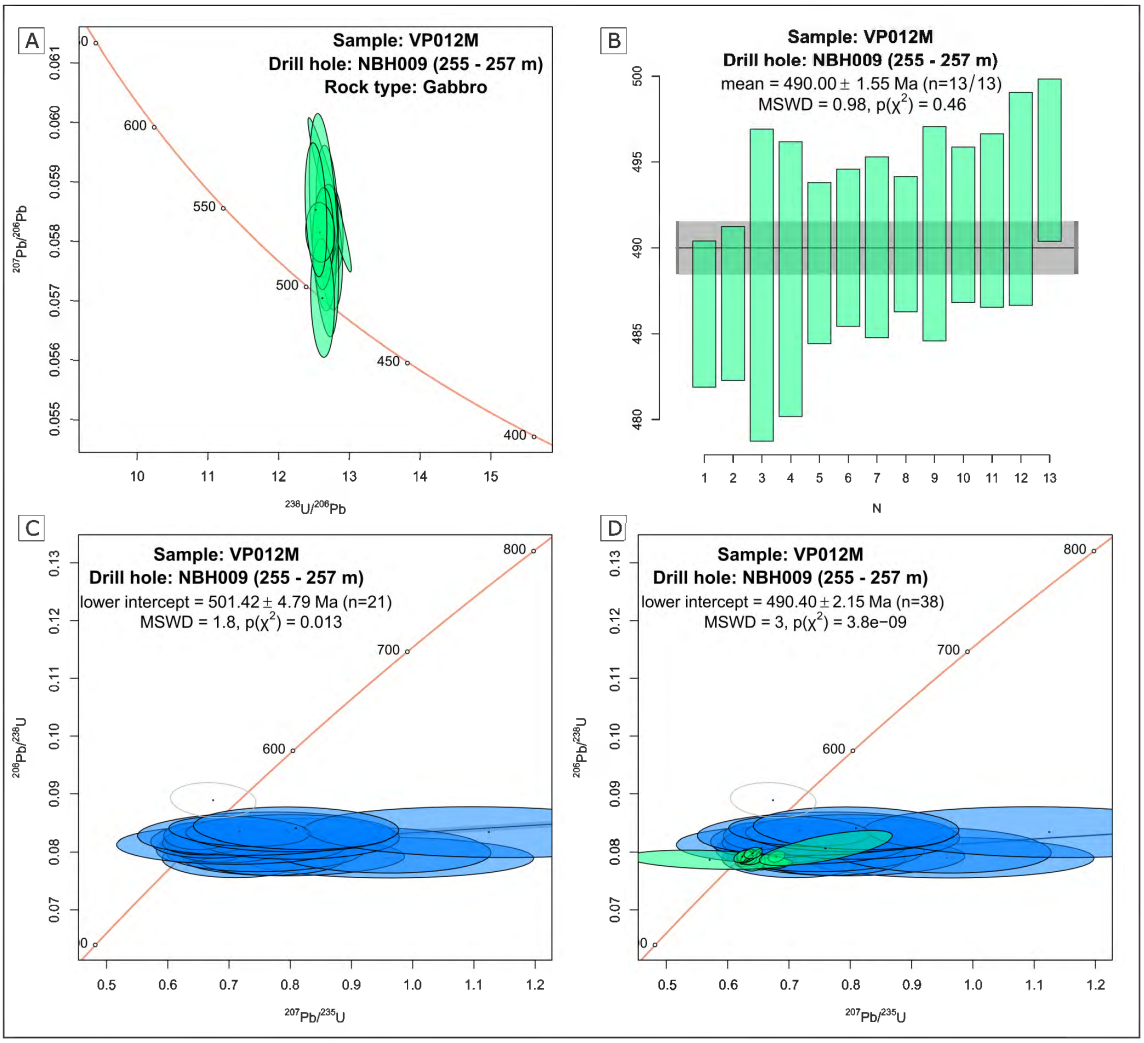

Figure 5.14: (A) Tera–Wasserburg Concordia diagram for VP012M. Concordant data from session one only. (B) Weighted mean average age of concordant data from session one. (C) Wetherill-type Concordia diagram for VP012M, with Model-1 intercept age presented. Concordant and discordant data included from session two. (D) Combined Wetherill-type Concordia diagram for VP012M, with Model-1 intercept age presented. Concordant and discordant data included from both sessions. Green represents analyses from session one and dark blue represents analyses from session two. Ages inferred to be inheritance are presented on Concordia diagrams in grey.

5.4.6 PJG0059

76 zircon grains and grain fragments were mounted for PJG0059. 32 spots were analysed in session one and a further 15 spots were added for the follow up session (session two). Eight of 32 analyses from session one were concordant and the results are presented in Figure 5.15 A. The youngest analysis (PJG0059-L2-17-1) is 90% concordant with an age of 397.01 ± 3.86 Ma and is within uncertainty of the youngest cluster included in the weighted mean average. One concordant analysis from session two has been included in the combined weighted mean average age, shown in Figure 5.15 B as 398.87 ± 3.80 Ma. All data from session two including discordant analyses are presented in Figure 5.15 C, with six analyses removed due to suspected lead loss. Figure 5.15 D shows the combined analyses from session one and two. Of the session one discordant data, ten analyses have been removed from the Concordia plot (Fig 5.12 D) due to suspected lead loss and two analyses have been included but greyed out due to inheritance.

Projection back to the concordia returns Pb anchored model-1 discordia intercept ages of 399.29 ± 5.87 Ma (Fig 5.15 C), and 400.70 ± 3.42 Ma (Fig 5.15 D). These ages are within error of the age determined from the combined weighted mean average age of concordant data shown in Figure 5.15 B.

Interpretation

The phyric nature of this sample and large grainset support the presence of zircon, and the euhedral grain shape and zoning patterns are suggestive of a magmatic origin. Therefore, the combined weighted mean average age of 398.87 ± 3.80 Ma is inferred to be the emplacement age.

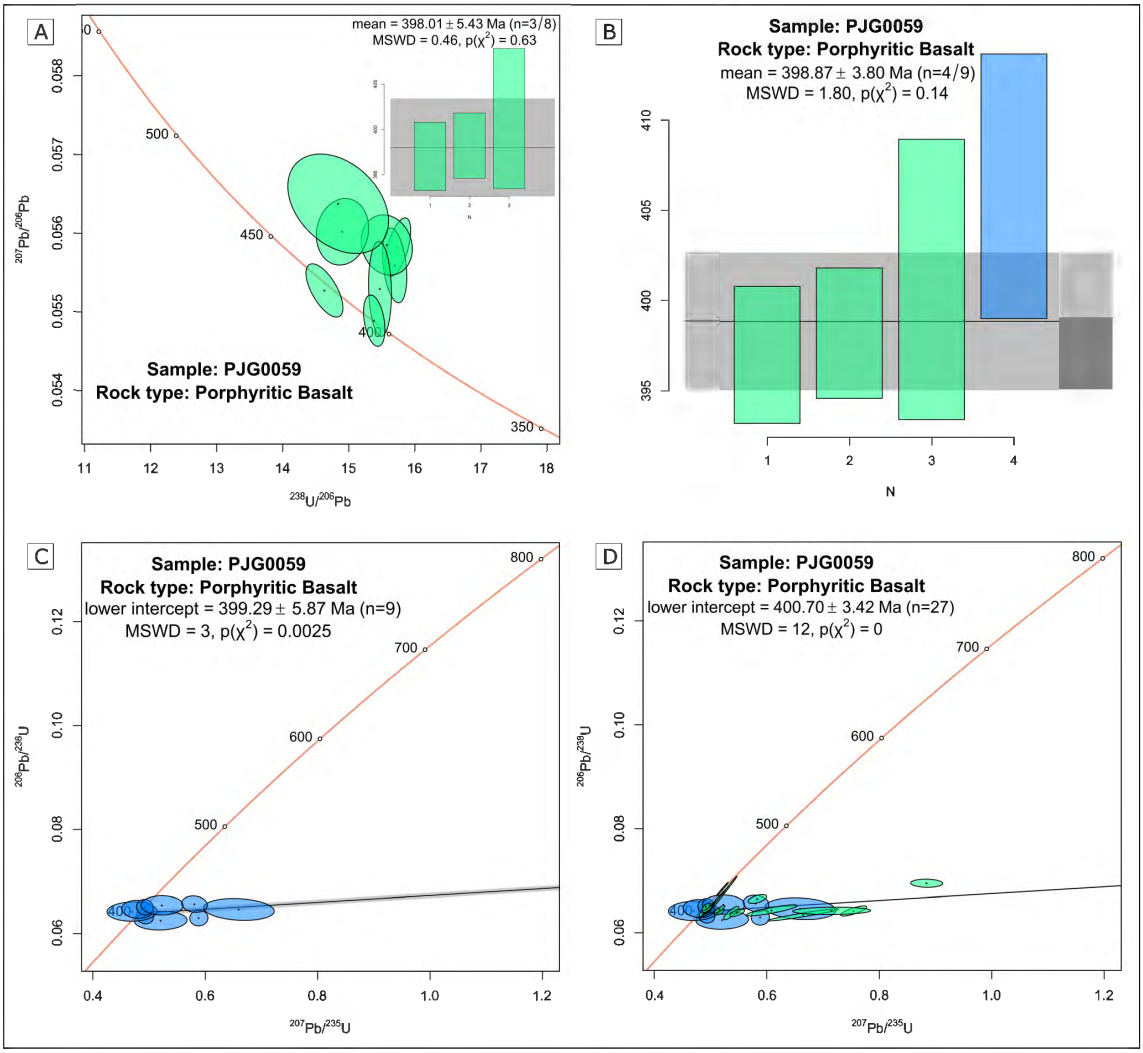

Figure 5.15: (A) Tera–Wasserburg Concordia diagram for PJG0059. Inset of the weighted mean average age. Concordant data from session one only. (B) Combined weighted mean average age of concordant data from both sessions. (C) Wetherill-type Concordia diagram for PJG0059, with Model-1 intercept age presented. Concordant and discordant data included from session two. (D) Combined Wetherill-type Concordia diagram for PJG0059, with Model-1 intercept age presented. Concordant and discordant data included from both sessions. Green represents analyses from session one and dark blue represents analyses from session two. Ages inferred to be inheritance are presented on Concordia diagrams in grey.

5.4.7 PJG0080

115 zircon grains and grain fragments were mounted for PJG0080. 35 spots were analysed in session one and a further 24 spots were added for the follow up session (session two). 27 of 35 analyses from session one were concordant and the results are presented in Figure 5.16 A. 13 of 24 analyses from session two were concordant and the results are presented in Figure 5.16 B. The youngest analysis (PJG0080b-8.d) is 91% concordant with an age of 498.30 ± 9.88 Ma and is within uncertainty of the youngest cluster included in the weighted mean average. The combined weighted mean average age of concordant data from both sessions is presented in Figure 5.16 C, shown as 509.07 ± 1.17 Ma, with a statistically robust MSWD of 0.97. Figure 5.16 D shows the combined analyses from session one and two. Of the session one discordant data, five analyses have been removed from the Concordia plot (Fig 5.16 D) due to suspected lead loss and one analysis has been included but greyed out due to inheritance. Of the session two discordant data, seven analyses have been removed from the Concordia plot (Fig 5.16 D) due to suspected lead loss and two analyses has been included but greyed out due to inheritance.

Projection back to the concordia returns an Pb anchored model-1 discordia intercept age of 509.82 ± 2.03 Ma (Fig 5.16 D). This is within error and supports the age determined from the combined weighted mean average age of concordant data shown in Figure 5.16 B.

Interpretation

The euhedral grain shape, zoning patterns and trace element REE patterns (Fig 5.9) are suggestive of magmatic origin. Therefore, the combined weighted mean average age (Fig 5.16) of 509.07 ± 1.17 Ma is inferred to be the emplacement age.

Older concordant ages from session one range from 512.39 ± 4.31 Ma to 526.40 ± 7.71 Ma and correspond to more rounded or fragmented grains. These ages were

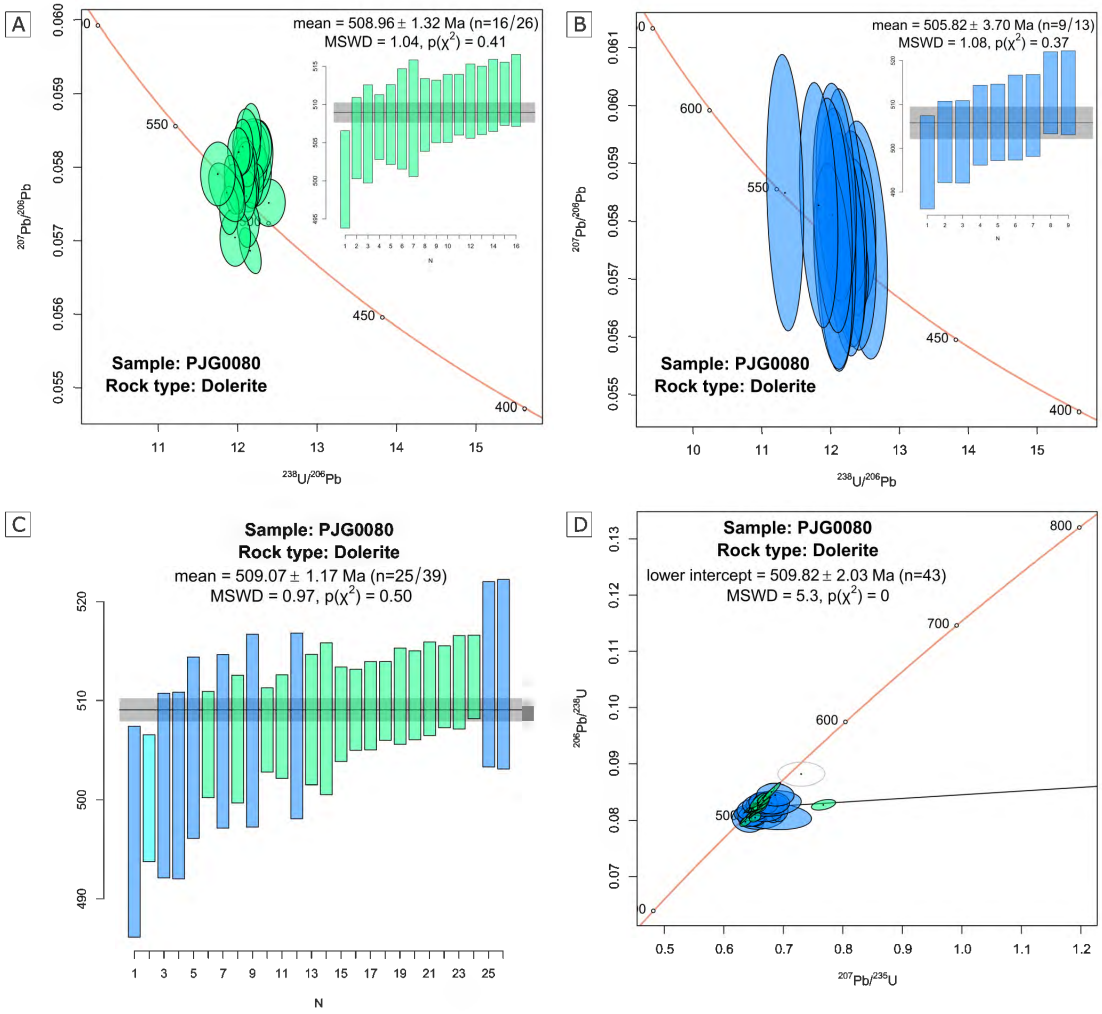

Figure 5.16: (A) Tera–Wasserburg Concordia diagram for PJG0080. Inset of the weighted mean average age. Concordant data from session one only. (B) Tera–Wasserburg Concordia diagram for PJG0080. Inset of the weighted mean average age. Concordant data from session two only. (C) Combined weighted mean average age of concordant data from both sessions. (D) Combined Wetherill-type Concordia diagram for PJG0080, with Model-1 intercept age presented. Concordant and discordant data included from both sessions. Green represents analyses from session one, dark blue represents analyses from session two, and light blue represents outliers. Ages inferred to be inheritance are presented on Concordia diagrams in grey.

not used in the weighted mean average and are considered to represent an inherited component.

5.4.8 PJG0082

17 zircon grains and grain fragments were mounted for PJG0082. 11 spots were analysed in session one and a further seven spots were added for the follow up session (session two). Six of 11 analyses from session one were concordant and the results are presented in Figure 5.17 A. The youngest analysis (PJG0082-11b) is 96% concordant with an age of 426.87 ± 6.50 Ma and is within uncertainty of the youngest cluster included in the weighted mean average. The weighted mean average age is shown in Figure 5.17 B as 430.25 ± 6.48 Ma, with a statistically robust MSWD of 1.03. Three analyses from session two were also concordant, however returned older ages of 481.21 ± 9.07 Ma, 481.64 ± 8.77 Ma and 483.80 ± 8.55 Ma. These analyses have been included in the combined Concordia plot shown in Figure 5.17 C.

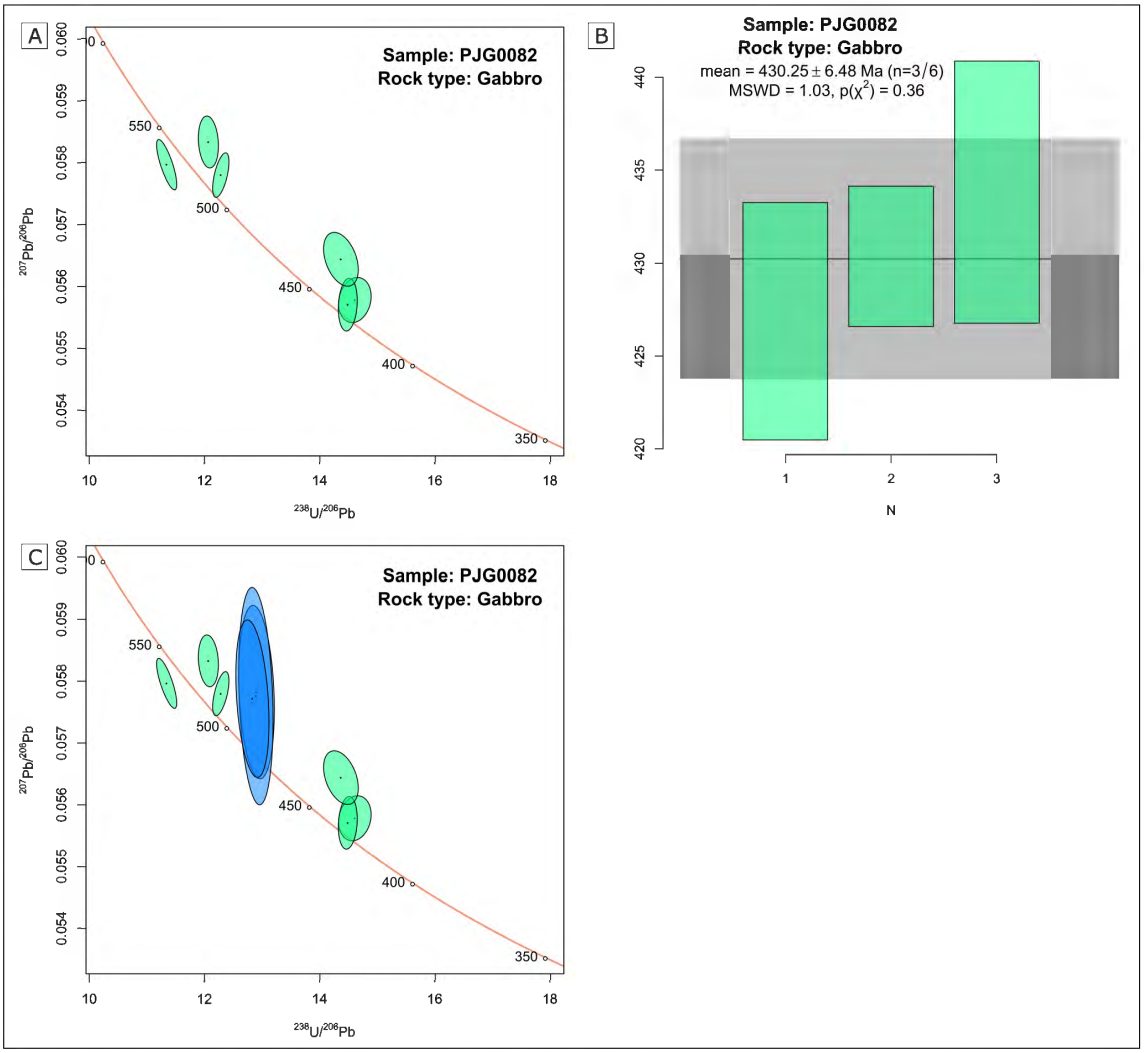

Figure 5.17: (A) Tera–Wasserburg Concordia diagram for PJG0082. Concordant data from session one only. (B) Weighted mean average age of concordant data for PJG0082 from session one. (C) Combined Tera–Wasserburg Concordia diagram for PJG0082. Data included from both sessions. Green represents analyses from session one and dark blue represents analyses from session two.

Interpretation

The concordant 426.87 ± 6.50 Ma to 433.79 ± 7.14 Ma ages used to obtain the weighted mean average age of 430.25 ± 6.48 Ma correspond to spots on concentric growth domains, often surrounding rounded, homogeneous or patchy zoned cores. This is inferred to be the emplacement age or at least represents a maximum age

for the unit. The limited sized grainset, including an inherited component, and presence within a rock type unlikely to crystallize zircon may suggest that this grainset represents zircons entrained in the melt due to walk rock assimilation during emplacement (Miller et al., 2007).

Older concordant ages from session one range from 504.56 ± 4.55 Ma to 544.62 ± 6.58 Ma. These ages correspond to spots on dark homogeneous grains and are considered to represent an inherited component. The 481.21 ± 9.07 Ma to 483.84 ± 8.55 Ma ages obtained from the three concordant analyses from session two contradict the ages obtained from the more reliable data from session one. Furthermore, the spots for session two were placed near areas of metamic radiation damage and therefore have likely experienced open system behaviour. Thus, it is likely that these analyses have suffered lead loss and, despite being concordant, do not represent the true age of the inherited zircon grains.

Trace element patterns (discussed further in Section 5.3) for both groups of zircons display magmatic patterns, suggesting the older zircon component has been inherited from a Delamerian aged source.

5.5 Lu-Hf Isotope Signatures

Results are presented in Figure 5.18. Where possible, the Lu-Hf has been constrained by concordant U-Pb ages from the same zircon grain or common lead corrected ages. If the age has suffered lead loss and was unsuitable for correction, the inferred emplacement age has been used.

Two similar isotopic arrays are present, one at 500 - 510 Ma and the other at 400 - 420 Ma. The arrays display a spread of mantle-like and crustal ϵHf values at the same time, likely reflecting a mixing array of mantle and crustal source components. This range in values is best observed in PJG0080 which varies from 15.4 to -7.8.

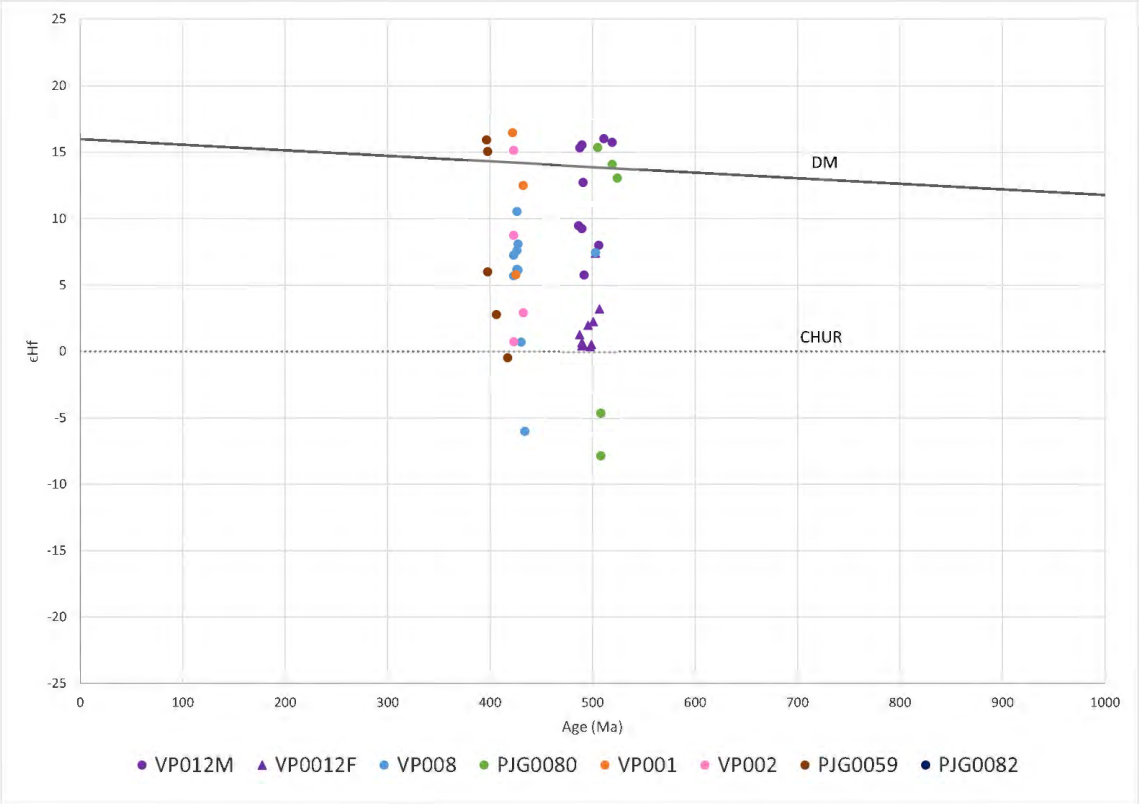

Figure 5.18: ϵHf values of igneous rocks of the Loch Lilly-Kars and Koonenberry. Loch Lilly-Kars drill core samples include VP001, VP002, VP008, VP012F and VP012M. Koonenberry outcrop samples include PJG0059, PJG0080 and PJG0082.

Chapter 6

Sm-Nd Isotopic Analysis

6.1 Introduction

Samarium (Sm) and neodymium (Nd) are rare earth elements and the immobility of these elements provides a relatively robust chronometer with respect to alteration and low-grade metamorphism. ^{147}Sm decays via α-decay to ^{143}Nd, with a half-life of 106 Ga (DePaolo 1988). Partial melting of the mantle removes more Nd than Sm, depleting the mantle in the daughter isotope (Winter 2001). This results in depleted mantle showing higher ^{143}Nd/^{144}Nd ratios with time in comparison to enriched mantle which will show lower Sm/Nd ratios, resulting in generation of smaller quantities of ^{143}Nd (Winter 2001).

The epsilon Nd notation (ϵNd) was introduced by DePaolo and Wasserburg (1976) to express the degree of Nd enrichment, as the differences in Nd isotope ratios are very small. Winter (2001) explains that positive ϵNd values have higher ^{143}Nd and are considered depleted with respect to the Chondritic Uniform Reserve (CHUR) standard, whereas negative ϵNd values have lower ^{143}Nd and are considered enriched. Therefore, positive ϵNd values indicate the rock was dervied from a depleted mantle source, and negative ϵNd values indicate the rock was derived from an enriched

mantle or crustal source that has been enriched overtime (Winter 2001).

6.2 Sm-Nd Isotopes

Sm and Nd isotopic compositions are presented in Table 6.1. ϵNd values range from -0.6 to 8.0, reflecting a range from crustal-like to depleted mantle values.

Table 6.1: Summary of Sm-Nd results for Loch Lily-Kars and Koonenberry samples.

Sample	Geology	ϵNd (now)	Age (Ga)	T	Initial $^{143}Nd/^{144}Nd$	TDM1 (Ga)	ϵNd
VP004	Gabbro	-1.2	0.43		0.512191	1.13	2.1
VP006	Basalt	1.4	0.43		0.512258	1.26	3.4
VP009	Diorite	-0.6	0.43		0.512230	1.04	2.9
VP012	Gabbro	9.7	0.49		0.512409	-0.25	8.0
VP013	Basalt	0.5	0.52		0.512149	1.17	3.6
PJG0059	Porphyritic basalt	8.9	0.40		0.512501	-0.77	7.5
PJG0080	Dolerite	-3.7	0.51		0.511901	2.15	-1.6
PJG0082	Gabbro	7.8	0.43		0.512433	12.44	6.9

Chapter 7

Titanite Geochronology

7.1 Introduction

Common in calc-silicate rocks, metamorphosed igneous rocks, and calc-alkaline plutons (Kohn et al., 2018), titanite is a useful mineral for U-Pb dating due to its relatively high U, Th and Pb contents (Sun et al., 2012). However, as titanite commonly accommodates common Pb in its crystal structure, common-Pb correction is often necessary before an age can be calculated (Chew et al., 2014; Kohn et al., 2018).

This section reports morphology and U-Pb ages for titanite separated from 4 rocks from the Loch Lilly-Kars study area. These samples were initially chosen for zircon separation, however, this was unsuccessful and instead the separation yielded large quantities of titanite grains. All titanite samples in this analysis contained common lead, therefore the data was discordant and required common lead correction (see methods) before plotting.

7.2 Titanite Morphology

Titanite was separated successfully from samples VP003 and VP004 from drill hole EHK3, as well as samples VP006 and VP007 from drill hole NBH004. Two main groups of titanite grains show distinctive differences in grainsize and morphology. These groups are the coarse-grained, darker orange-brown coloured grains from VP003 and VP004, and the finer-grained, lighter coloured grains from VP006 and VP007. In thin section, titanite appears in association with other alteration products (Fig 7.1) and is variable in grainsize and shape.

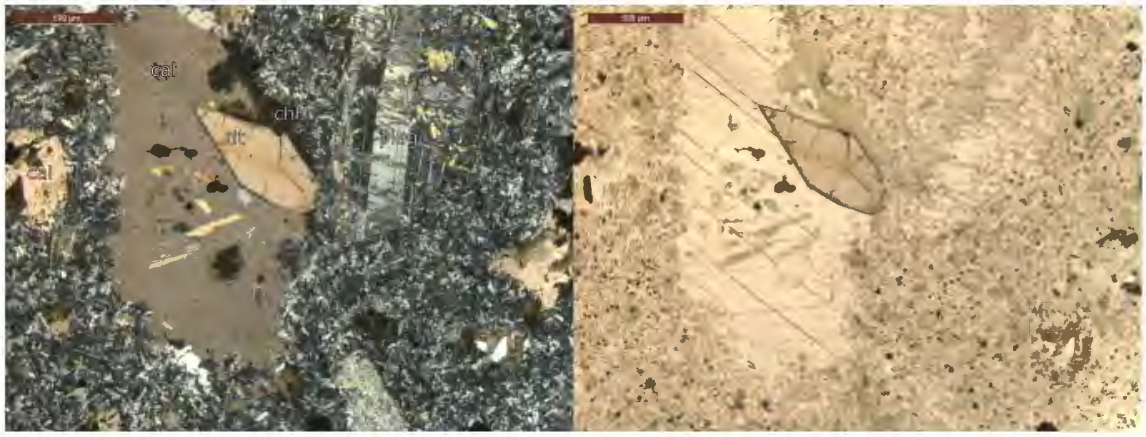

Figure 7.1: Crossed-polars image (left) and plane-polarised light image (right) of thin section VP003-02, showing alteration assemblage of titanite, calcite and chlorite.

7.2.1 VP003 and VP004

Titanite grains occur as coarse, orange to brown, wedge-shaped grains that range from 200 to 350 µm and appear translucent (Figures 7.2 and 7.3 A). Titanite grains display a bright, consistent response from BSE imaging, whilst inclusions and intergrowths appear darker (Fig 7.2 and 7.3 B).

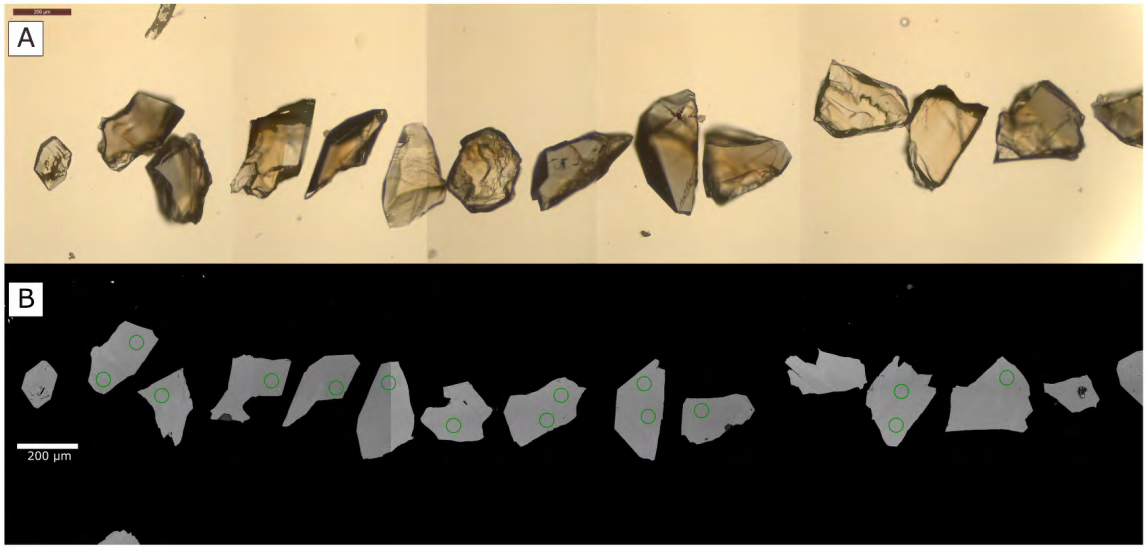

Figure 7.2: Transmitted light (TL; A) and backscattered-electron (BSE; B) images of titanite grains from VP003. Green circles represent targets for U-Pb LA-ICP-MS.

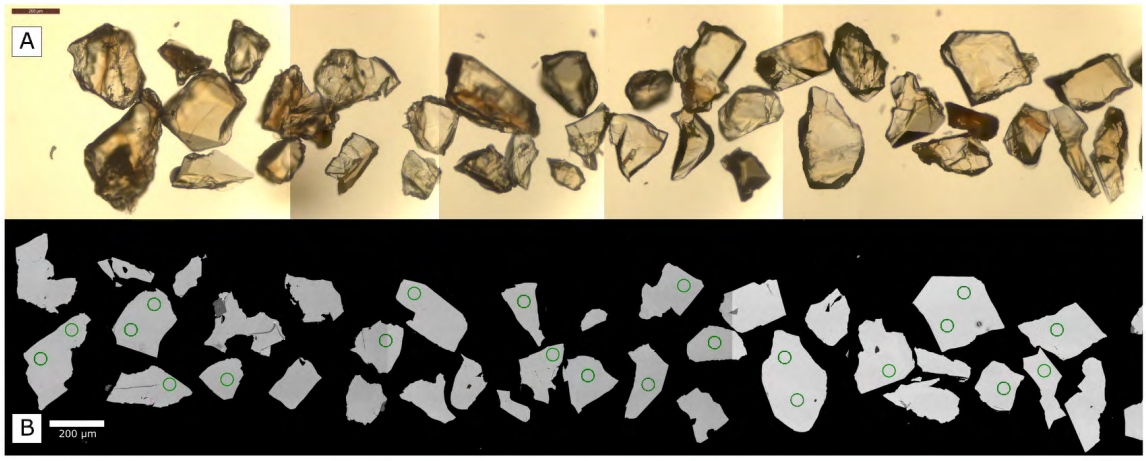

Figure 7.3: TL (A) and BSE (B) images of titanite grains from VP004. Green circles represent targets for U-Pb LA-ICP-MS.

7.2.2 VP006 and VP007

Titanite grains are finer-grained than those separated from VP003 and VP004, most commonly ranging from 100 to 180 µm with some finer grains that are <100 µm. Grains also appear more grey in colour rather than orange-brown (Figures 7.4 and 7.5 A). BSE imaging reveals inclusions are more common in VP006 and VP007 than

VP003 and VP004 (Figures 7.4 and 7.5 B). These inclusions are dark and contrast to the white response of the titanite grains in BSE.

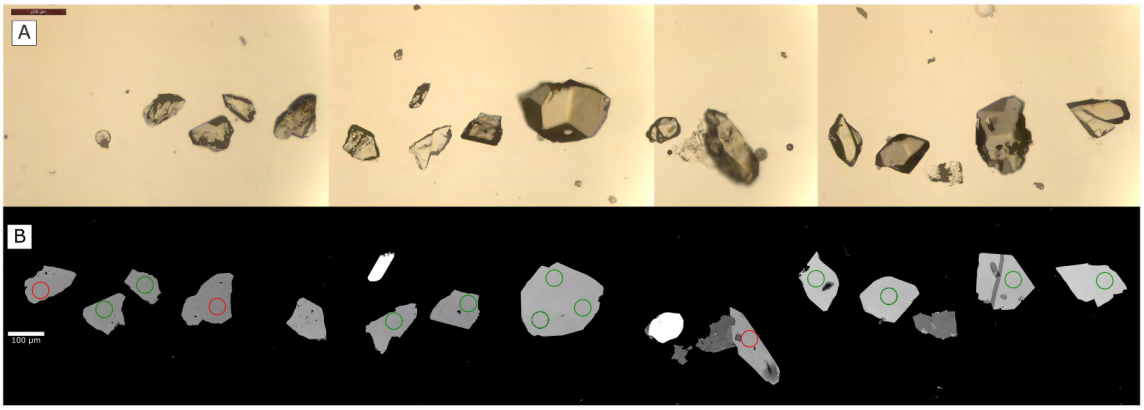

Figure 7.4: TL (A) and BSE (B) images of titanite grains from VP006. Green circles represent preferred targets for U-Pb LA-ICP-MS. Red circles represent targets for U-Pb LA-ICP-MS that are close to fractures or inclusions.

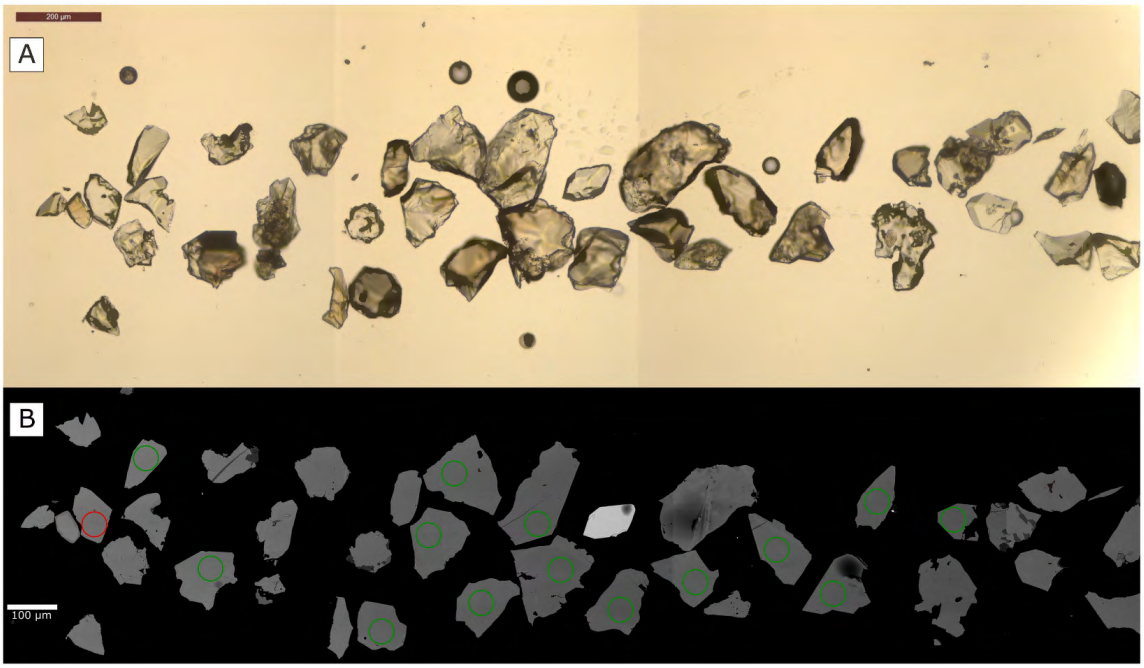

Figure 7.5: TL (A) and BSE (B) images of titanite grains from VP007. Green circles represent preferred targets for U-Pb LA-ICP-MS. Red circles represent targets for U-Pb LA-ICP-MS that are close to fractures or inclusions.

7.3 U-Pb Ages

A summary of sample details and U-Pb LA-ICP-MS geochronology results are provided in Table 7.1, and Wetherill-type Concordia diagrams are shown below (Figures 7.6, 7.7, 7.8).

Sample ID	Rock Type	Age	MSWD	n
VP003	Andesite	426.57 ± 2.32	2.1	40
VP004	Gabbro	422.74 ± 2.40	0.82	40
VP006 & VP007	Basalt	416.98 ± 3.64	0.71	28

Table 7.1: Summary of titanite U-Pb LA-ICP-MS results. Note the mean squared weighted deviation (MSWD) for VP003 is greater than 1, therefore the results are less reliable than those from VP004 and VP006 and VP007. Ages are Pb anchored model-1 discordia intercept ages.

7.3.1 VP003

A total of 146 grains were mounted for VP003, and 40 spots were analysed. The results of the analyses are presented in Figure 7.6 A, with the lower-intercept age shown as 426.57 ± 2.32 Ma.

7.3.2 VP004

A total of 76 grains were mounted for VP004, and 40 spots were analysed. The results of the analyses and lower-intercept age of 422 ± 2.40 Ma are presented in Figure 7.7.

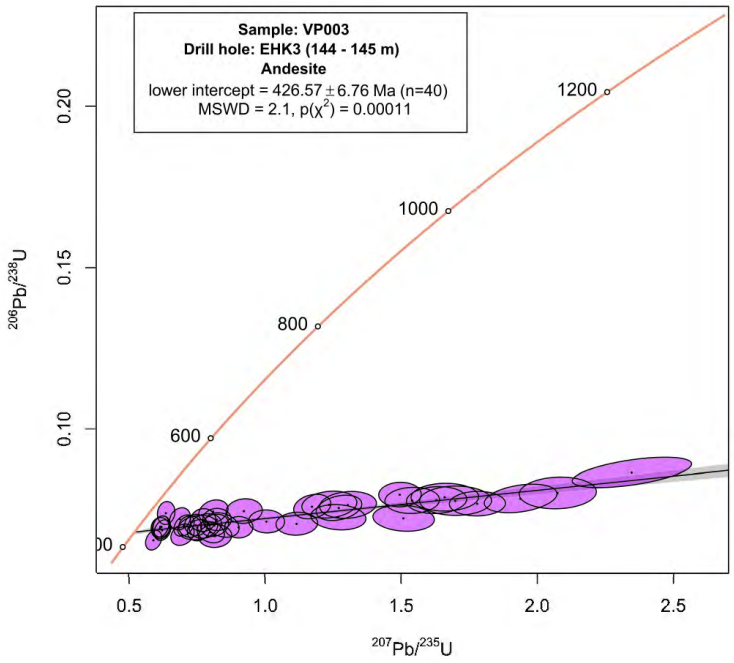

Figure 7.6: Wetherill-type Concordia diagram for VP003.

7.3.3 VP006 and VP007

A total of 15 grains were mounted for VP006, and 56 grains for VP007. Due to the fine grainsize, fractures and inclusions, only 8 spots were analysed for VP006 and 14 for VP007. The combined lower-intercept age has been determined for VP006 and VP007 as these samples are from the same unit, sampled at different intervals, and is shown in Figure 7.8.

7.4 Interpretation

The titanite data provide information on the post emplacement history of the Loch Lilly-Kars. Titanite in these samples is secondary and associated with alteration assemblages, therefore ages obtained from these samples are likely to represent later deformation or burial metamorphic events rather than emplacement age.

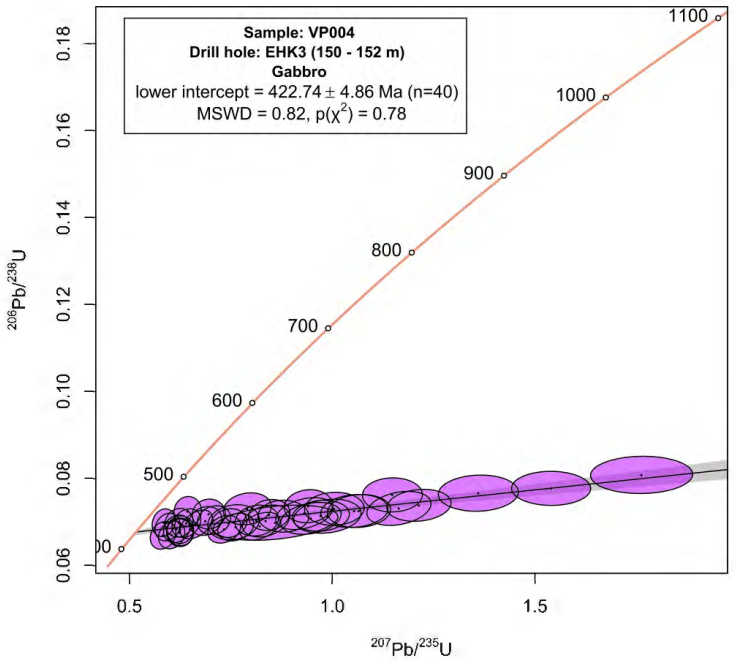

Figure 7.7: Wetherill-type Concordia diagram for VP004.

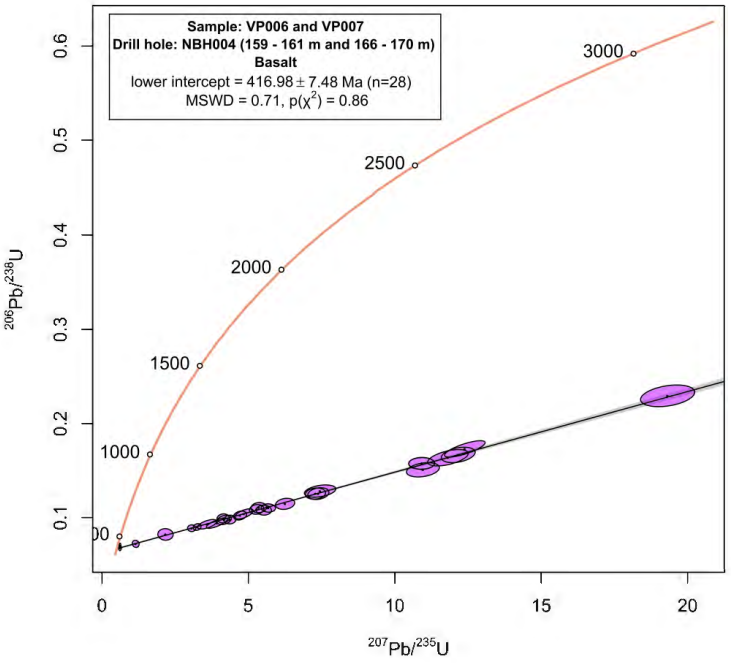

Figure 7.8: Wetherill-type Concordia diagram for VP006 and VP007.

Chapter 8

Discussion

8.1 Interpretation of Loch Lilly-Kars Geochemistry

Through combining geochronological and geochemical data, it is evident that the Loch Lilly-Kars (LLK) records multiple episodes of magmatism. This supports the finding of Baatar et al. (2019) in identifying two main periods of magmatic intrusive activity across the LLK; Cambrian emplacement of the Netley Granodiorite (drill hole NBH010) and intrusions of fine-grained quartz monzonite (drill hole NBH007) and microdiorite suites (drill holes EHK1 and EHK2) of Devonian age.

U-Pb zircon ages for Loch Lilly-Kars (LLK) samples revealed only one sample of Delamerian age; VP012 at ∼490 Ma. There are a number of existing ages for other Delamerian rocks in the LLK, outlined in Table 5.1, and this group is discussed further below in Section 8.1.1.

U-Pb titanite ages obtained for samples from EHK3 and NBH004 likely represent deformation or burial metamorphic events rather than emplacement age. A weak S1 cleavage axial-planar to small-scale recumbent folding within the thin meta-siltstone horizon intersected in drill hole NBH005 has been suggested to be related

to deformation events (Rankin 2014). It is therefore more likely that the titanite ages represent deformation events rather than burial metamorphism, however this interpretation is limited as this meta-siltstone is the only visibly deformed unit intersected within the surrounding LLK sequence. These samples have been grouped into the Late Silurian to Devonian (Siluro-Devonian) rocks of the LLK on the basis of geochemistry and proximity to the samples from EHK1, EHK2 and NBH005 that returned zircon U-Pb ages of 423 - 426 Ma. These are discussed further below in Section 8.1.2.

8.1.1 Delamerian

The NMORB-normalised patterns shown in Figures 4.3 and 4.5, reveal that the Delamerian (520 to 490 Ma) samples from drill holes DD96WA3, NBH010, NBH011 and NBH012 display calc-alkaline continental arc signatures with high Th, Nb and Ti depletion, whilst the samples from NBH009 show tholeiitic to transitional intra-oceanic arc signatures.

Existing SHRIMP I age dating of a coarse-grained monzodiorite intersected in DD96WA3 resulted in age determinations of 505 ± 5 Ma, 519 ± 5 Ma and 521 ± 5 Ma (Greenfield et al., 2011). This age is supported by the results presented in the unpublished Anglo American Exploration Report EL8199 (2015), with a zircon age of 523 ± 4 Ma for a monzodiorite from 887.1 m downhole. Greenfield et al. (2011) correlated the monzodiorite samples from DD96WA3 to the Mount Wright Volcanics with respect to age and geochemistry. The samples Greenfield et al. (2011) used to correlate DD96WA3 to Mount Wright are alkaline and have Nb/Y ratios that range from 0.72 to 1.49. However, the Mount Wright volcanics span the subalkaline field and have Nb/Y ratios of 0.10 to 0.99, therefore it appears they cannot be directly correlated. The calc-alkaline basaltic samples from drill hole NBH011 are geochemically similar to the calc-alkaline dolerite sample from

DD96WA3 (Fig 4.3 G and A), showing high Th/Nb ratios, LILE enrichment and Ti depletion. However, NBH011 is geochronologically unconstrained apart from one Ar-Ar age of 514 ± 4 Ma (Archibald 2015). As this age represents the maximum age of biotite alteration, it is inferred that the emplacement age of the rock is older than 514 ± 4 Ma, and therefore likely belongs to the Delamerian arc sequence in the LLK. Additionally, samples from NBH012 (Fig 4.3 H) also share similar geochemical features to NBH011 and DD96WA3, and although unconstrained, NBH012 lies on the same magnetic feature as NBH011 (Fig 3.1), suggesting this may also belong to the same arc sequence. Furthermore, samples from all three drill holes plot within the calc-alkaline arc basalt field, shown in Figure 4.7, and extend into the continental arc field on the Th/Yb-Nb-Yb diagram of Pearce (2014; Fig 4.6). This supports the interpretation that these samples formed in a continental arc setting during the Delamerian.

Tholeiitic to transitional gabbro and diorite samples from drill hole NBH009 are comagmatic, with an emplacement age of 490 ± 1.06 Ma. These samples show similar N-MORB normalised patterns (Fig 4.3 F)to the Bittles Tank Volcanics (BTV) of the Koonenberry (Fig 8.3), discussed further below in Section 8.2. This similarity in geochemistry may indicate the continuation of the BTV sequence into the LLK, however, the age of 490 ± 1.06 Ma is slightly younger than the inferred age of ∼510 Ma for the BTV. This age suggests these are likely not the direct correlatives of the BTV, and rather, a more appropriate correlation would be the volcanics within the younger sequences of the Nuntherungie and Kayrunnera basins. The Netley Granodiorite intersected in drill hole NBH010, situated on the same high magnetic anomaly as NBH009, has been dated at 496 ± 6 Ma and 508 ± 4 Ma (refer to Table 5.1), suggesting bimodal magmatism occured during the final stages of the Delamerian in the LLK. This is consistent with the abrupt transition from syntectonic S- and I-type granite production to a bimodal magmatic association of

mafic intrusions and felsic granites of S- and A-type affinities observed within the Adelaide Fold Belt (Foden et al., 2002).

8.1.2 Late Silurian to Early Devonian

The Late Silurian to Early Devonian intrusive rocks of the LLK occur along strike from the Delamerian arc rocks (NBH011 and NBH012). These include the diorite intrusives intercepted in drill holes EHK1 and EHK2 dated at 423.98 ± 1.23 Ma and 423 ± 1.51 Ma, andesite porphyry in NBH005 dated at 426.26 ± 1.49 Ma, as well as the andesite and gabbro in EHK3 and basalt in NBH004 inferred to be of similar age based on U-Pb titanite ages.

NMORB-normalised patterns shown in Figures 4.3 and 4.5, reveal that this younger sequence of intrusives show continental arc signatures with similarities to the Delamerian arc rocks. However, during the Late Silurian to Early Devonian, it is unlikely to have a continental arc setting within the LLK, as by this time the arc system had migrated further east.

Calc-alkaline, subduction-influenced arc geochemistry can also occur in post-orogenic back-arc basins (BAB) and rift-related settings, retaining the subduction signature of earlier activity within the area (Hack et al., 2018). This is observed within the Silurian Honeysuckle beds (HSB, Dadd 1998) and the Devonian Comerong Volcanics (Dadd 2011) of the Lachlan Orogen, as well as the Early Devonian Warraweena Volcanics of the Thomson Orogen (Hack et al., 2018). Samples from these areas are plotted against the Siluro-Devonian rocks of the LLK (Fig 8.1), showing similar trends and mostly plotting within the transitional field between oceanic and continental arc as well as just below the continental arc field. LLK rocks from drill holes EHK3 and NBH005 also trend from calc-alkaline to alkaline compositions (Fig 4.1). This association is observed in the Warraweena Volcanics (Hack et al., 2018) and the Louth Volcanics (Dwyer et al., 2018), providing further evidence the Siluro-

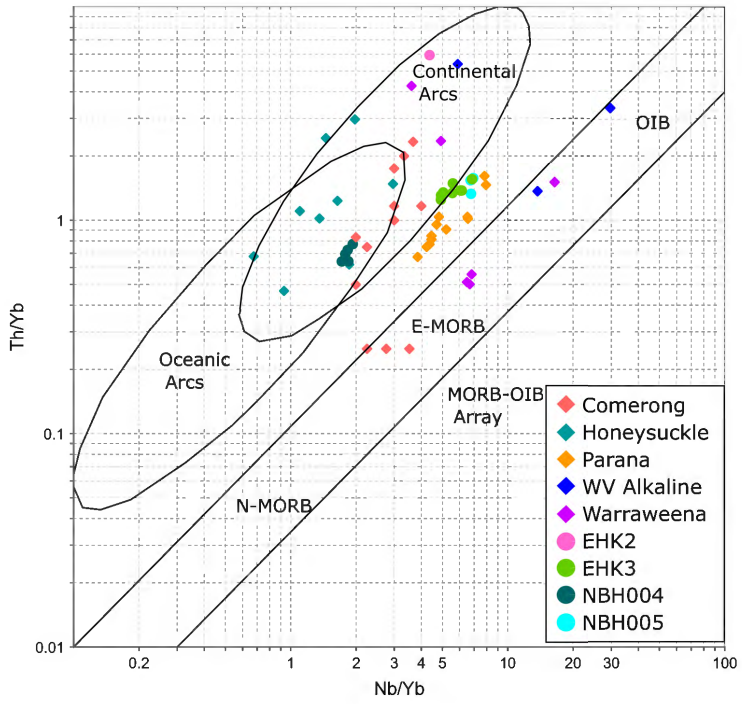

Figure 8.1: Th/Yb vs Nb/Yb discrimination diagram of Pearce (2014) comparing the Siluro-Devonian LLK with other rift-related suites in the Lachlan and Thomson Orogens. Samples from the Parana continental flood basalts have also been plotted for comparison. Data sourced from Dadd (1998), Dadd (2011), Vickery (2008), Peate et al. (1988).

Devonian LLK may be related to rifting and that the alkaline rocks may be related to later stage activity. Thus, through comparison with Siluro-Devonian rocks from other well-studied rift-related sequences within the Lachlan and Thomson Orogens (Figure 8.1), it can be suggested that the Siluro-Devonian rocks of the LLK reflect a continental rift sequence. The Siluro-Devonian LLK samples retain an arc signature with high Th/Nb ratios, possibly derived from crustal assimilation.

Furthermore, a rift-related setting in this area at ~430 Ma is not uncommon. The Mount Daubeny basin in the Koonenberry Belt is a pull-apart basin which opened as a result of dextral transpression in the Late Silurian to Devonian, involving sedimentation of the Mount Daubeny Formation accompanied by calc-alkaline magmatism of the Wertago Volcanics (Greenfield et al., 2010). The Wertago Volcanics are dacite-

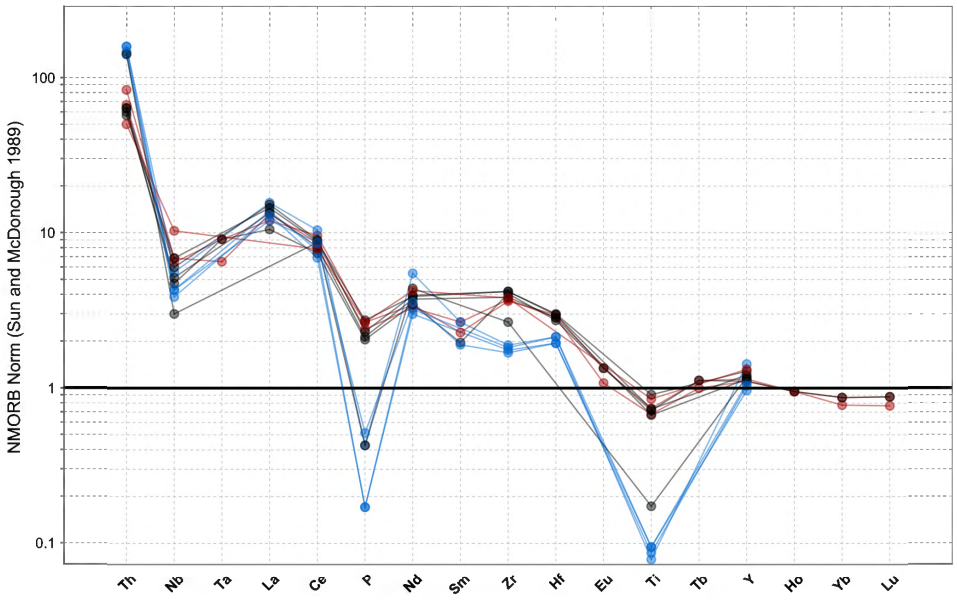

Figure 8.2: NMORB-normalised patterns for the Wertago Volcanics. Data sourced from Greenfield et al. (2011). Blue patterns represent rhyolite samples, red patterns represent andesite and black patterns represent dacite. Normalising values are from Sun and McDonough (1989).

rhyolite intrusives with continental calc-alkaline affinities, and have U-Pb ages of 414.2 ± 2.7 Ma and 417.7 ± 1.9 Ma (Greenfield et al., 2010, Black 2005, Black 2006). These intrusives cross-cut the Mount Daubeny Formation and an andesitic lava flow dated at 425 ± 7 Ma is intercalated with the basal conglomeratic Gnaltaknoko Member of the Mount Daubney Formation (Greenfield et al., 2010, Black 2007). Additionally, the Wertago Volcanics also retain a continental arc signature (Fig 8.2), showing strong Th enrichment accompanied by Nb depletion and Nb/Yb ratios >1.

8.2 Interpretation of the Koonenberry Geochemistry

The Koonenberry samples analysed in this study (PJG0058, PJG0059, PJG0080, PJG0082 and DD89GR05) were interpreted to belong to the BTV in the field how-

ever U-Pb dating, geochemistry and isotopic analysis has revealed they are quite distinct.

The BTV are mafic extrusive and intrusive igneous rocks within the Ponto Group, intercalated with air-fall tuff horizons, siltstone and mudstone (Greenfield et al., 2011), with geochemistry reflecting a tectonic setting of oceanic intra-plate rifting most likely within a back-arc environment (Fig 8.3, Greenfield et al., 2010). The BTV are inferred to be of Cambrian age, constrained by tuff ages of 508 ± 3.2 Ma, 512 ± 3.1 Ma and 511.7 ± 3.5 Ma (Greenfield at el., 2011). Greenfield et al. (2010) group the Nuntherungie dolerites and Kayrunnera gabbros within the BTV, however Johnson et al. (2016) identifies these as individual, younger sequences using biostratigraphic age constraints. Sample PJG0067 (Dywer and Gilmore 2017) is an interesting and significant sample attributed to the BTV, showing a distinctly different geochemical pattern (Fig 8.3) that is much more depleted than the BTV with Th below detection limits. This pegmatitic gabbro also has a U-Pb zircon age of 535 ± 4 Ma, making it older than the inferred age of the BTV and the Mount Wright arc. This older age combined with the absence of Th makes it difficult to place into context, and may represent an earlier phase of extension-related magmatism with a highly depleted mantle source (Dywer and Gilmore 2017) not observed elsewhere in the Koonenberry.

With an age of 509.07 ± 1.17 Ma, PJG0080 is the only Koonenberry sample from this study likely to belong to the BTV. PJG0080 displays an arc signature transitional between intra-oceanic and continental (Fig 4.12 D), displaying close similarities to the Nuntherungie dolerite (Fig 8.3). This sample is situated east of the Koonenberry fault and in the same location as the Nuntherungie Dolerite. Until now, rocks eastward of this fault have been ∼500-490 Ma (J Greenfield 2021, personal communication, 26 April), and on the basis of geochemistry and outcrop location, PJG0080 and the Nuntherungie Dolerite may be correlated and therefore provide an

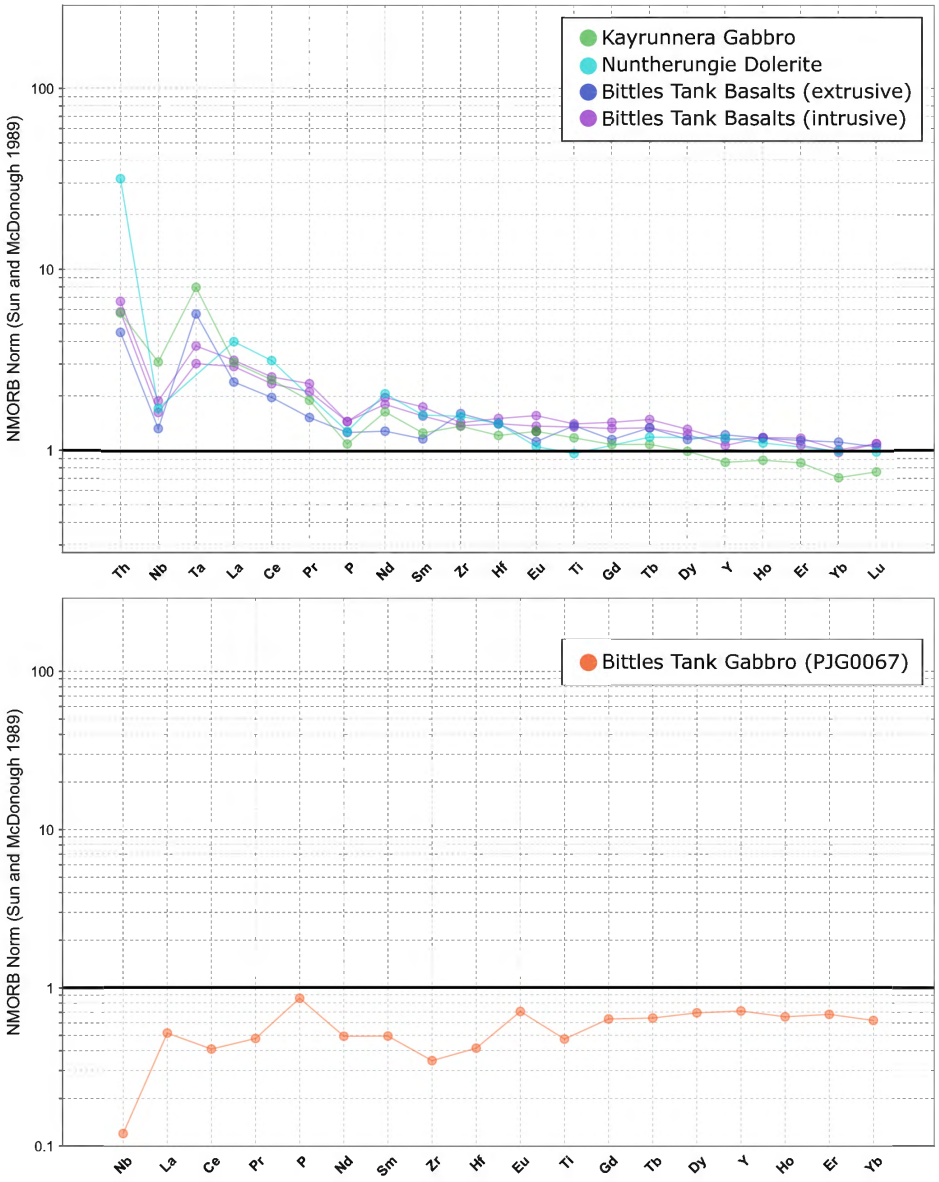

Figure 8.3: NMORB-normalised patterns for the Bittles Tank Volcanics, Nuntherungie Dolerite and Kayrunnera Gabbro. Data sourced from Greenfield et al. (2011) and Dywer and Gilmore (2017). Normalising values are from Sun and McDonough (1989).

age constraint of 509.07 ± 1.17 Ma for this unit. Other members of the BTV show similar trace element patterns however are not as enriched in Th (Fig 8.3), and as no direct dating has been done on members of the BTV, it is difficult to compare these samples along the belt and place in geodynamic context.

Samples PJG0058 and DD89GR05 display MORB-like patterns (Fig 4.12 A and B), and PJG0059 and PJG0082 display tholeiitic intra-oceanic arc-like patterns (Fig 4.12 C and D), both distinct from the NMORB-normalised patterns of the BTV (Fig 8.3). In addition to differences in geochemistry, the U-Pb zircon ages of the Koonenberry samples analysed in this study are younger than the inferred Cambrian age for the BTV.

As discussed above in Section 8.1.2, the Mount Daubeny Basin contains intermediate to felsic calc-alkaline intrusive rocks and extrusive lava flows of Late Silurian to Early Devonian age. Greenfield et al. (2010) note the absence of mafic rocks in this basin, however, the location of PJG0082 proximal to the basin and an age of 430.25 ± 6.48 Ma, which is within error of the age obtained for an andesitic lava flow within the Gnaltaknoko Member, suggests that PJG0082 may be a tholeiitic, mafic end-member of rift-related magmatism within the Mount Daubeny Basin. The difference in geochemistry observed between PJG0082 and the Wertago Volcanics may be due to the former picking up a more depleted source component of subduction influenced crust.

Sample PJG0059 displays a more MORB-like pattern than PJG0082 however still retains a subduction signature, showing Th enrichment and a slight Nb depletion (Fig 4.12 C). With an age of 398.87 ± 3.80 Ma, emplacement of this porphyritic basalt may have been related to a terminal phase of mafic magmatism, similar to what Kemp (2009) observes in the Lachlan Orogen, however more far-field. These intraplate-like basalts show more mantle-like isotope signatures and have

been inferred to have intruded after crustal thicking, emplaced as a result of intra-continental rifting behind the nascent New England Orogen intra-oceanic arc (Kemp 2009). Furthermore, PJG0058 is in the same location as PJG0059 which is considered to be a porphyritic variant of PJG0058, (Fig 3.1) and shows an E-MORB-like geochemistry. No zircon U-Pb dating was completed for PJG0058 (Fig 4.12 B), however, it is inferred to be contemporaneous with PJG0059. DD89GR05 is also proximal to PJG0058 and PJG0059, located in the Grasmere Knee Zone, and shows N-MORB-like geochemistry (Fig 4.12 A). However, unlike PJG0058 and PJG0059, this sample shows strong deformation (refer to Appendix C.0.18), and therefore may be related to an older orogenic event, possibly the Delamerian.

8.3 Correlation with the Adelaide Fold Belt, Glenelg River Complex and Mount Stavely Complex

The geochemistry and isotopic character (discussed further below in Section 8.4) of the southern Delamerian (Adelaide Fold Belt, Glenelg and Mount Stavely) differs from that of the northern Delamerian (Koonenberry and Loch Lilly-Kars), perhaps due to different mantle sources and basement architecture.

A major difference in the southern Delamerian basement is the presence of extended continental crust behind the arc, the Adelaide Fold Belt (AFB). During subduction, melt passing through the continental crust would likely result in the more crustal-like and evolved isotopic signatures observed in the rocks of the southern Delamerian (Figure 8.5). The Koonenberry Belt, however, is built on the edge of the Curnamona Craton with the Grey Range Group containing the Kara Formation and Mount Arrowsmith Volcanics rift sequence underlying it. Sediments from the Grey Range Group contain a minor 600 Ma and two major 1.0 and 1.3 Ga major detrital zircon populations (Johnson et al., 2016). This indicates the sequence had a mixture of

ancient cratonic and crustal components of Ediacaran age and may explain the mixed geochemical and isotopic signatures observed in the Koonenberry Belt sequences (Greenfield et al., 2010). Therefore it is likely that the differences observed in the geochemical and isotopic data between the southern and norther Delamerian can be attributed to differences in basement composition and geometry.

A major difference in geochemistry between the southern and northern Delamerian is the presence of boninite-like magmatism in the south (Glenelg and Mount Stavely). Whilst boninites are absent from the proposed forearc sequence of the Ponto Group in the Koonenberry Belt, common ages seen in the south and north of 510 - 505 Ma could represent coeval magmatism to the FAB/boninites in the south and support Greenfield et al. (2011) suggestion that the BTV are part of this continual forearc sequence. Cratonic derived detritus and detrital zircons of Ediacaran ages within the Teltawongee and Ponto groups of the Koonenberry Belt are at odds with this interpretation (Johnson et al., 2016). An Andean-style continental arc should form a significant barrier to the transport of such detritus (Johnson et al., 2016; Pastor-Galan et al., 2021), and detritus shed off the continental arc into the proposed forearc basin should contain distinctive clastic/lithic components and detrital zircon populations, of which are lacking in the syn-Delamerian basin sequences (Johnson et al., 2016). Thus, it is plausible that the Mount Wright Arc was not a major topographic feature usually associated with a continental arc and may have been more sub-aerial to sub-volcanic in extent as is suggested by Johnson et al. (2016). Therefore, the Mount Wright Arc could still represent continental arc magmatism, equivalent to arc rocks of Mount Stavely, with the BTV in a fore-arc position equivalent to the sequence in the southern Delamerian. It is also possible that boninites are not seen in the north due to the timing and speed of forearc retreat in the different regions, in that a rapid extensional regime in the southern Delamerian allowed for upwelling of a greater volume of hot mantle material resulting in

a very high temperature supra-subduction zone setting known to produce boninites (R Musgrave 2021, personal communication, 10 May). Another possibility is that they have not been sampled due to limited outcrop exposure and biased sampling in drillcore.

In the AFB, ^{40}Ar-^{39}Ar and Rb-Sr ages of detrital mica and ^{40}Ar-^{39}Ar cooling ages cluster at the age of termination of Delamerian deformation (∼503-490 Ma; Turner et al., 1996). The change to post-tectonic bimodal, mantle-derived magmatism involving mafic intrusions and A-type granites reflects the cessation of orogenesis, indicating this stage of magmatism was associated with new mantle influx (Foden et al., 2002, 2006). Whilst A-type granites are not observed in the northern Delamerian, post-tectonic extensional related mafic magmatism is, indicated by the gabbros from LLK drill hole NBH009. As indicated above in Section 8.1.1, these samples show geochemical similarities to the BTV of the Koonenberry Belt, however with a younger age of 490 obtained from this study and possible mingling with a more felsic component (diorites within NBH009 and the Netley Granodiorite within NBH010), it may be more appropriate to correlate to the Black Hill gabbroic complex in the AFB. The Black Hill gabbroic complex consists of layered gabbroic rocks that yield a Sm-Nd isochron age of 489 ± 39 Ma (Turner 1996) and show similar geochemical patterns of LREE enrichment, Th enrichment and negative Nb anomalies (Fig 8.4). Furthermore, this mafic sequence intruded with the Mannum Granite, part of the Padthaway A-type granite suite, that contains numerous mafic enclaves indicative of mingling between mafic magma and granite magma during intrusion (Turner and Foden 1996). The post-tectonic A-types in the south are isotopically more crustal-like than the LLK equivalents but this could also be attributed to the presence of the extended continental crust in the south and absence in the north. This crustal component would likely influence the geochemistry and make direct correlation difficult.

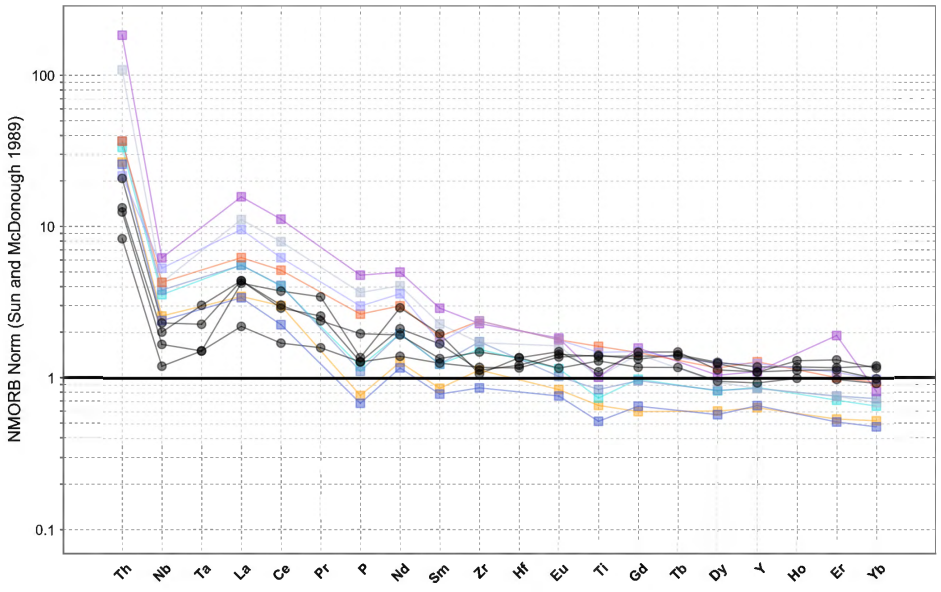

Figure 8.4: NMORB-normalised patterns for the Black Hill gabbroic complex (data sourced from Turner 1996) compared to gabbro and diorite samples from Loch Lilly-Kars drill hole NBH009. Loch Lilly-Kars samples are shown in black, coloured patterns are Black Hill samples (samples 879-11-1035, 876-11-1081, 876-19-1278, 876-19-635, 876-4-201, 876-7-510, BHN-II, MG-10). Normalising values are from Sun and McDonough (1989).

Another similarity observed between the southern and northern Delamerian is the presence of syn-tectonic granites, notably the Rathjen Gneiss in the AFB (Foden et al., 1999) and the Williams Peak Granite in the Koonenberry Belt (Greenfield et al., 2010). The granites are of the same age, 514 ± 5 Ma (Foden et al., 1999) and 515.1 ± 2.7 Ma (Black 2007), and show strong deformation associated with the Delamerian Orogeny.

8.4 Sm-Nd and Lu-Hf Isotopes

Whole rock Nd and zircon Hf isotope compositions of the Tasmanides from Cambrian to Late Silurian/Early Devonian age are presented in Figure 8.5 and Figure 8.6. The data forms two covariant arrays that display a spread of mantle-like and crustal values, as well as trends towards increasingly juvenile isotope compositions following compressional events of the Delamerian and Benambran Orogenies.

The whole rock Nd and zircon Hf isotopic data obtained from this study display the same trends, however the Hf data show a greater spread of values within a sample whereas ϵNd shows the average of the sample. Hf data can therefore show crystallisation and mixing history of components of the rock as zircon isotope tracer information has the ability to distinguish juvenile contributions to felsic igneous suites (Kemp et al., 2007, 2009). High positive values reflect mantle components, whereas lower positive and negative values reflect crustal components. Sample VP012 from Loch Lilly-Kars (LLK) drill hole NBH009 demonstrates this, as the Hf isotope data (Fig 8.6) show a range of high positive values extending above the depleted mantle line for the mafic (VP012M) fraction of the sample to lower values for the more felsic (VP012F) fraction. This reflects the comagmatic nature of the gabbro and diorite at that time. However, in Figure 8.5, VP012M sits above the depleted mantle line, reflecting the whole rock average value for the sample and not exhibiting

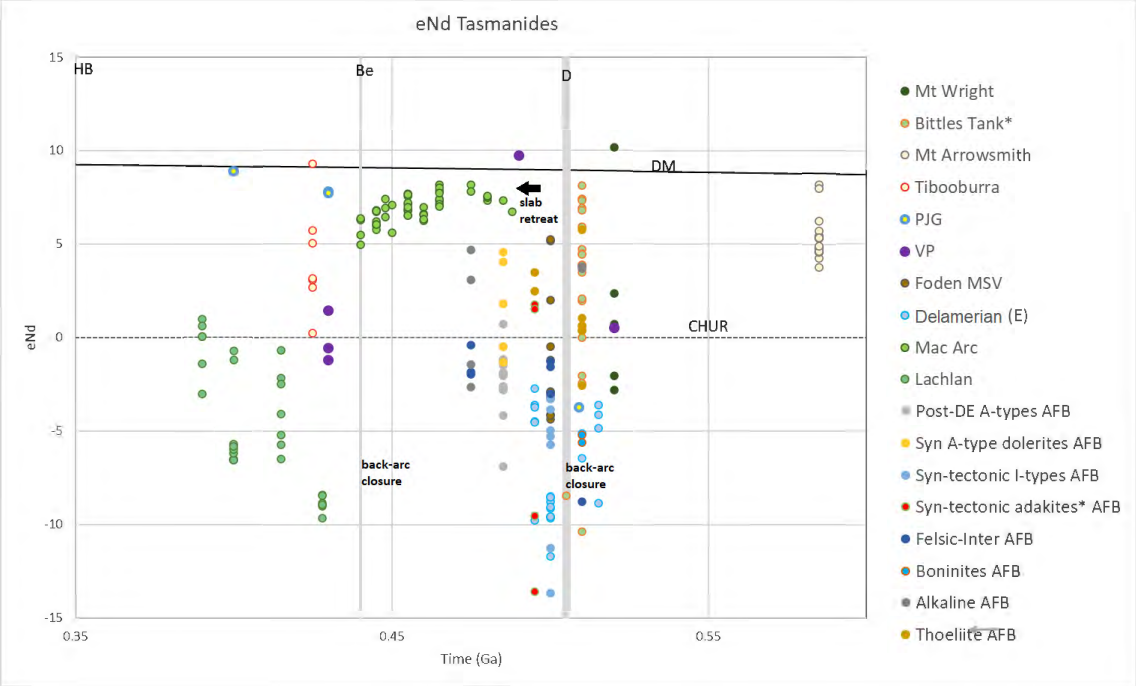

Figure 8.5: ϵNd values of igneous rocks of the Delamerian and Lachlan Orogens. Data for Mt Arrowsmith, Mt Wright, Bittles Tank and Tibooburra sourced from Greenfield et al. (2011). Data for PJG and VP sourced from this study. Data for Mt Stavely Volcanics (MSV) and Adelaide Fold Belt (AFB) suites from Foden et al. (2020). Data for Delamerian (E), Macquarie Arc and Lachlan Orogen sourced from Kemp (2009). The shaded time slices correspond to major contractional episodes, as follows: HB, Hunter–Bowen; Be, Benambran (early phase); D, Delamerian.

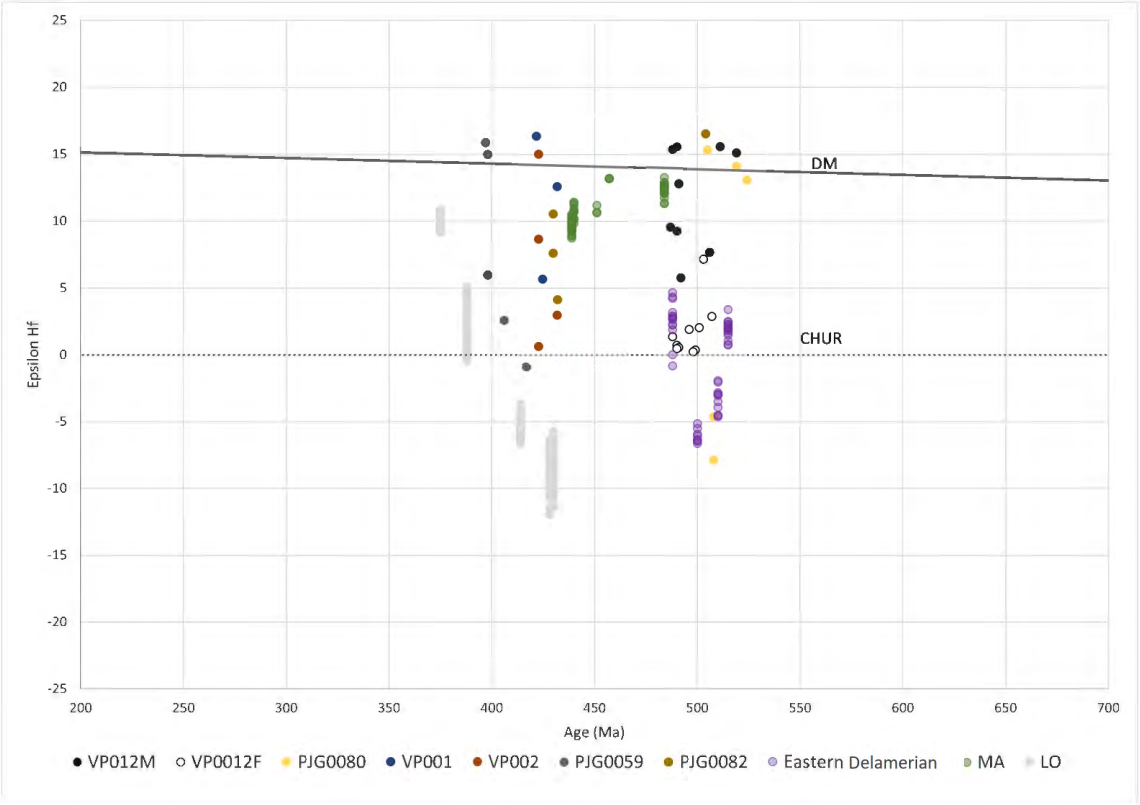

Figure 8.6: ϵHf values of igneous rocks of this study (LLK samples VP001, VP002, VP008, VP012M, VP012F and Koonenberry samples PJG0059, PJG0080, PJG0082) compared to values for the Eastern Delamerian, Macquarie Arc (MA) and Lachlan Orogen (LO), data sourced from Kemp (2009).

the compositional variation displayed by the Hf data.

As observed in Figure 8.5, the Bittles Tank Volcanics (BTV) isotopic array show a wide range in values suggestive of a crust-mantle mix between two compositionally distinct end members. The more juvenile end-member of the BTV is more mantle-like than the Macquarie Arc (Fig 8.5) and show extremely high positive ϵNd values. In effort to determine the type of subduction system setting, samples from the northern Delamerian were compared to potential analogues in the Izu-Bonin arc (Ishizuka et al., 2020; Straub et al., 2010; Yogodzinski et al., 2018) and Lau Basin back-arc (Nebel and Arculus 2015). Fore-arc sequences within the Izu-Bonin arc share similar high positive ϵNd/ϵHf trends with the mantle-like/juvenile component in the northern Delamerian, however, samples within and across the Lau Basin also shared these high positive trends. As intra-oceanic systems without continental basement it is unsurprising that they trend towards more juvenile values and therefore may not be a suitable analogue to the northern Delamerian system.

A more appropriate comparison was made between the southern Delamerian and the South Kitakami fore-arc in Tohoku, Japan (Pastor-Galan et al., 2021). The South Kitakami fore-arc, located at the northern end of the Japanese archipelago, is floored by continental basement and includes a thick Paleozoic to Mesozoic forearc sequence (Pastor-Galan et al., 2021). Cambrian to Silurian intrusives outcrop within this region and detailed detrital and magmatic zircon U-Pb and Lu-Hf data provide an interesting comparison to what is observed within the northern Delamerian. Zircon populations with ages $>$ 1500 Ma are interpreted to be derived from a cratonic crustal source, likely the South China Craton, and return entirely negative eHf values. $\sim$1000 and $\sim$600 Ma zircon populations display mixed patterns which are interpreted to represent a mixing between newly extracted mantle material and this cratonic crustal source, and this mixing array displays broad similarities to what is observed in the northern Delamerian. In the South Kitakami forearc, younger zircon

populations reveal that the arc acts as a barrier to the fore-arc, limiting a major influx of the older cratonic derived populations. This is reflected in the zircon ages and ϵHf values, but initially this was not the case and might provide a reasonable comparison to northern Delamerian.

Further investigation uncovered similar trends within isotopic studies on the Gawler Craton in South Australia. In this study the crustal end member is interpreted to represent upper crustal material which is reworked and buried to the mid to lower crust where it contributes to melt generation (Reid and Payne 2017). The juvenile mantle component is considered to be mantle derived and likely produced in a continental rift or extensional continental magmatic arc setting. A similar scenario is envisaged for the northern Delamerian that sees a mixing between a crustal end member and mantle end member in an extension dominated tectonic setting. A continental, extensional dominated, magmatic arc setting as proposed by previous workers (Foden et al., 2020; Greenfield et al., 2011; Johnson et al., 2016) fits the isotopic trends observed in the northern Delamerian, involving subduction initiation followed by rollback and eastward retreat. This would have resulted in relocation of the Mount Wright Arc to an extensional back-arc position and melting of underplated calc-alkaline material to produce continued CAB magmatism to ∼506 Ma (Johnson et al., 2016), therefore it is reasonable to suggest underplating in the fore-arc region has contributed to the anomalous geochemistry of the BTV.

The juvenile to evolved array with extreme juvenile values observed in Gawler Craton is considered to have a relationship with major crustal scale faults (Reid and Payne 2017). The Koonenberry Fault, located between the Wonnaminta and Kayrunnera Zones of the Koonenberry Belt, may represent a similar crustal scale fault to what is observed within the Gawler Craton, possibly providing the conduit for this juvenile mantle dominated material during extensional events in the northern Delamerian. Reactivation of this fault system during the Silurian and a mixing

between the Delamerian crust and an influx of new mantle derived material would explain the trends from low positive to high positive ϵHf within this sequence. This is supported by the spread of mantle-like and crustal ϵHf values for the Late Silurian to Early Devonian LLK and Koonenberry samples mirroring the samples of Delamerian age (Fig 8.6), without the high negative values seen in the BTV which reflect the cratonic crustal source. Additionally, the zircons from VP008 and PJG0082 show inherited cores of Delamerian age surrounded by younger growth domains, indicating the potential incorporation of a Delamerian component.

Furthermore, the Siluro-Devonian LLK and Koonenberry samples show more mantle-like values than the Lachlan at that time (Fig 8.6), displaying a return to more juvenile isotope compositions after the Benambran Orogeny much more rapidly than is observed in the Lachlan. This rapid progression to more mantle like compositions has been observed in rift settings in the Southern Thomson Orogen (Hack et al., 2018) and Tumut Trough (Batch 2021). Hotter drier melting conditions and different basement architecture has likely attributed to this change, as does its close relationship to a reactivated crustal scale fault.

Interestingly, the southern Delamerian data (Adelaide Fold Belt suites, MSV and East Delamerian) do not show high positive values like the BTV and LLK data (Fig 8.5 and Fig 8.6), and the samples with the highest ϵNd values are the MSV boninites (Fig 8.5). Further, the southern Delamerian data follows a similar pattern to what is observed in the Lachlan Orogen (Kemp 2009) but is more compressed towards negative crustal-like values, indicating significant contribution of the ancient cratonic crustal component is present. This difference in values between the northern (BTV and LLK) and southern Delamerian suggests there is a difference in source characteristics for the two regions, likely linked to differences in basement architecture and tectonic setting. A major contributing factor, as discussed previously in Section 8.3, is the presence of extended continental crust behind the arc in the south

and the absence of this in the north. Additionally, the differences observed could be attributed to melt generation under more hydrous conditions or due to increased water flux melting (Collins et al., 2020). Under these conditions, higher proportion of the crustal component could be incorporated during melt generation in the AFB.

Chapter 9

Conclusions and Recommendations for Future Work

An important aim of this study was to determine if the geochemistry of the Loch Lilly-Kars is similar to other areas of the Delamerian Orogen and confirm if this belt is the continuation of the Bittles Tank Volcanics and Mount Wright Arc sequences of the Koonenberry Belt. Whilst there are geochemical and geochronological similarities between rocks of the Loch Lilly-Kars and Koonenberry Belts, the geodynamic context of this region still largely remains unresolved. The apparent fore-arc setting of the Bittles Tank Volcanics and continuation into the Loch Lilly-Kars remains ambiguous as the geochemical patterns observed are not consistent with those of common fore-arc environments, and instead display arc/back-arc to MORB affinities.

Despite some similarities such as syn-tectonic granites and post-tectonic extensional related mafic magmatism, the geochemistry of the northern (Koonenberry and Loch Lilly-Kars) and southern (Adelaide Fold Belt, Glenelg and Mount Stavely) Delamerian differs, and the Bittles Tank Volcanics signature is not observed in the southern Delamerian. ϵNd and ϵHf isotopic evidence suggests there are differences in mantle

sources for these regions, which may explain the variation observed in the geochemistry. The northern Delamerian data shows mixing between a juvenile mantle and crustal source, whereas the southern Delamerian data shows significant contribution of the ancient cratonic crustal component. This study suggests that these differences may be attributed to differences in basement architecture and tectonic setting and discusses the South Kitakami fore-arc and the Gawler Craton as a potential analogues to explain the isotopic trends of the northern Delamerian.

The U-Pb zircon results for the Loch Lilly-Kars samples of this study returned mostly Late Silurian to Early Devonian ages, supporting the finding of Baatar et al. (2019) that the Loch Lilly-Kars Belt records a late Silurian to Devonian intrusive event. The Koonenberry samples analysed as part of this project also mostly returned U-Pb zircon results of Siluro-Devonian age. These samples were originally inferred to belong to the Bittles Tank Volcanics based on field observations, however the age and geochemistry indicates they do not belong to this sequence and are more likely the result of extensional related magmatism resulting from the opening of pull-apart basins. The ϵNd and ϵHf isotopic data of the Siluro-Devonian aged samples show a spread of mantle-like and crustal values, and are more mantle-like than the Lachlan Orogen at that time. A significant observation from this study is that the progression to mantle-like compositions following the Benambran Orogeny has occurred much earlier in the Loch Lilly-Kars and Koonenberry rift sequences than observed anywhere else in the Tasmanides.

Recommendations for future work include direct age dating for members of the Bittles Tank Volcanics as this may assist in providing a greater understanding of the geodynamic setting of the Koonenberry Belt. Furthermore, limited trace element datasets made comparisons between regions difficult and therefore further geochemical analysis is recommended. Further isotopic analysis on the more felsic samples of the Loch Lilly-Kars is also recommended, as this study focused on the mafic units.

Chapter 10

References

ARCHIBALD, D. A. (2015). Report on 40Ar/39Ar step-heating Analyses of Two Rocks with Biotite Alteration , Loch Lilly Tenement , W NSW for Anglo-American Exploration (Perth). (Report GS2016/0061). Geological Survey of NSW (unpublished).

BAATAR, B., PARRA-AVILA, L. A., FIORENTINI, M. L., POLITO, P., & CRAWFORD, A. J. (2020). Porphyry Cu fertility of the Loch Lilly-Kars Belt, Western New South Wales, Australia. Australian Journal of Earth Sciences, 67(1), 75–87.

BATCH, T. (2021). Investigations into the geology of the Tumut Trough, Lachlan Orogen, NSW: Implications for mineral prospectivity. Honours thesis. University of Newcastle.

BELOUSOVA, E. A., GRIFFIN, W. L., O'REILLY, S. Y., & FISHER, N. I. (2002). Igneous zircon: Trace element composition as an indicator of source rock type. Contributions to Mineralogy and Petrology, 143(5), 602–622.

BLACK, L. P. (2005). SHRIMP U-Pb zircon ages obtained during 2004/05 for the NSW Geological Survey. 1–22.

BLACK, L. P. (2006). SHRIMP U-Pb zircon ages obtained during 2005/06 for NSW Geological Survey projects. 1–37.

BLACK, L. P. (2007). SHRIMP U-Pb zircon ages obtained during 2006/07 for NSW Geological Survey projects.

BLAND, M. (2002). Annual Report for Exploration Licences 5478, 5515, 5528 and 5816 "Broken Hill Porphyry Project" for the period 27 April 2001 to 26 April 2002. (Report GS2002/886). Geological Survey of NSW.

BLAND, M. (2003). Annual Report for Exploration Licences 5478 and 5515 "Broken Hill Porphyry Project" for the period 27 April 2002 to 26 April 2003. (Report GS2003/278). Geological Survey of NSW.

BOUVIER, A., VERVOORT, J., AND PATCHETT, J. P. (2008) The Lu-Hf and Sm-Nd isotopic composition of CHUR: Constraints from unequilibrated chondrites and implications for the bulk composition of terrestrial planets. Earth and Planetary Science Letters, 272, 48-57.

CHEW, D. M., PETRUS, J. A., AND KAMBER, B. S. (2014). U-Pb LA-ICPMS dating using accessory mineral standards with variable common Pb. Chemical Geology, 363, 185–199.

CHISHOLM, E.-K., SIRCOMBE, K., AND DIBUGNARA, D. (2014). Handbook of Geochronology Mineral Separation Laboratory Techniques. In GeoCat 78527.

CHU, N. C., TAYLOR, R. N., CHAVAGNAC, V., NESBITT, R. W., BOELLA, R. M., MILTON, J. A., GERMAN, C. R., BAYON, G., & BURTON, K. (2002). Hf isotope ratio analysis using multi-collector inductively coupled plasma mass spectrometry: An evaluation of isobaric interference corrections. Journal of Analytical Atomic Spectrometry, 17(12), 1567–1574.

COLLINS, W. J., MURPHY, J. B., JOHNSON, T. E., & HUANG, H. Q. (2020).

Critical role of water in the formation of continental crust. Nature Geoscience, 13(5), 331–338.

CORFU, F., HANCHAR, J. M., HOSKIN, P. W. O., & KINNY, P. (2003). Atlas of zircon textures. Reviews in Mineralogy & Geochemistry, 469–500.

CRAWFORD, A. J. (2013). Exploration Proposal. Loch Lilly-Kars Trend, W NSW for Anglo American Exploration. (Report GS2014/1815). Geological Survey of NSW (unpublished).

CRAWFORD, A. J. (2015). Petrographic Report. 21 Rocks from the Loch Lilly for Anglo-American Exploration. (Report GS2016/0061). Geological Survey of NSW (unpublished).

CRAWFORD, A. J., & BERRY, R. F. (1992). Tectonic implications of Late Proterozoic-Early Palaeozoic igneous rock associations in western Tasmania. Tectonophysics, 214(1–4), 37–56.

CRAWFORD, A.J., STEVENS, B.P.J., FANNING, M. (1997). Geochemistry and tectonic setting of some Neoproterozoic and Early Cambrian volcanics in western New South Wales. Australian Journal of Earth Sciences, 44 (6), 831–852.

DADD, K. A. (1998). Incipient backarc magmatism in the Silurian Tumut Trough, New South Wales: An ancient analogue of the early Lau Basin. Australian Journal of Earth Sciences, 45, 109–121.

DADD, K. A. (2011). Extension related volcanism in the Middle to Late Devonian of the Lachlan Orogen: Geochemistry of mafic rocks in the Comerong Volcanics. Australian Journal of Earth Sciences, 58, 209–222.

DE PAOLO, D.J. (1988). Neodymium Isotope Geochemistry: an introduction. Springer-Verlag, Berlin. Heidelberg. 20.

DEPAOLO, D, J., & WASSERBURG, G.J. (1976) Nd Isotopic Variations and Pet-

rogenetic Models. Geophysical Research Letter, 3, 249 252.

DICKINSON, W. R., & GEHRELS, G. E. (2009). Use of U-Pb ages of detrital zircons to infer maximum depositional ages of strata: A test against a Colorado Plateau Mesozoic database. Earth and Planetary Science Letters, 288(1–2), 115–125.

DIREEN, N.G. & CRAWFORD, A.J. (1998). Evidence for the timing of continental breakup and volcanic passive margin formation, southeast Gondwana: an actualistic perspective. In: Bird, R.T. (ed.) The Assembly and Breakup of Rodinia. Geological Society of Australia Abstracts, 50, 24–28.

DIREEN, N. G., & CRAWFORD, A. J. (2003). The Tasman Line: Where is it, what is it, and is it Australia's Rodinian breakup boundary? Australian Journal of Earth Sciences, 50(4), 491–502.

DONNELLAN, N., CAMACHO, A., MAAS, R., PRICE, R. C. (2019) Mantle upwelling or plume activity on the periphery of the Warakurna LIP: evidence from the geochemistry and petrogenesis of the Alcurra Dolerite in the Eastern Musgrave Province. Journal of Petrology, 60, 301-328.

DWYER, R. C., & GILMORE, P. J. (2017). New geochronology in the Koonenberry Belt, far western NSW. (Report GS2017/0557). Geological Survey of NSW.

DWYER, R. C., COLLINS, W. J., HACK, A. C., HEGARTY, R., HUANG, H.-Q. (2018). Age and tectonic significance of the Louth volcanics: Implications for the evolution of the Tasmanides of eastern Australia. Australian Journal of Earth Sciences, 65, 1049–1069.

FISHER, C. M., VERVOORT, J. D., & DUFRANE, S. A. (2014). Accurate Hf isotope determinations of complex zircons using the "laser ablation split stream" method. Geochemistry, Geophysics, Geosystems, 15(1), 121–139.

FODEN, J. D., ELBURG, M. A., TURNER, S. P., SANDIFORD, M., O'CALLAGHAN,

J., & MITCHELL, S. (2002). Granite production in the Delamerian Orogen, South Australia. Journal of the Geological Society, 159(5), 557–575.

FODEN, J., SANDIFORD, M., DOUGHERTY-PAGE, J., & WILLIAMS, I. (1999). Geochemistry and geochronology of the Rathjen Gneiss: Implications for the early tectonic evolution of the Delamerian Orogen. Australian Journal of Earth Sciences, 46(3), 377–389.

FODEN, J., ELBURG, M. A., DOUGHERTY-PAGE, J., & BURTT, A. (2006). The timing and duration of the Delamerian orogeny: Correlation with the Ross Orogen and implications for Gondwana assembly. Journal of Geology, 114(2), 189–210.

FODEN, J., ELBURG, M., TURNER, S., CLARK, C., BLADES, M. L., COX, G., COLLINS, A. S., WOLFF, K., GEORGE, C. (2020). Cambro-Ordovician magmatism in the Delamerian orogeny: Implications for tectonic development of the southern Gondwanan margin. Gondwana Research, 81, 490–521.

FOSTER, D. A., & GRAY, D. R. (2000). Evolution and Structure of the Lachlan Fold Belt (Orogen) of Eastern Australia. Annual Review of Earth and Planetary Sciences, 28(1), 47–80.

FOSTER, D. A., GRAY, D. R., & SPAGGIARI, C. (2005). Timing of subduction and exhumation along the Cambrian East Gondwana margin, and the formation of Paleozoic backarc basins. GSA Bulletin, 117(1–2), 105–116.

GORTON, M. P., & SHANDL, E. S. (2000). From continents to island arcs: A geochemical index of tectonic setting for arc-related and within-plate felsic to intermediate volcanic rocks. Canadian Mineralogist, 38(5), 1065–1073.

GRIFFIN, W. L., PEARSON, N. J., BELOUSOVA, E. A., & SAEED, A. (2006). Comment: Hf-isotope heterogeneity in zircon 91500. Chemical Geology, 233(3–4), 358–363.

GRIFFIN, W. L., PEARSON, N. J., BELOUSOVA, E. A., & SAEED, A. (2007). Reply to "Comment to short-communication 'Comment: Hf-isotope heterogeneity in zircon 91500" by W.L. Griffin, N.J. Pearson, E.A. Belousova and A. Saeed (Chemical Geology 233 (2006) 358-363)" by F. Corfu." Chemical Geology, 244(1–2), 354–356.

GREENFIELD, J. E., GILMORE, P. J., & MILLS, K. J. (2010). Explanatory notes for the Koonenberry Belt geological maps. Geological Survey of New South Wales. Bulletin 35.

GREENFIELD, J. E., MUSGRAVE, R. J., BRUCE, M. C., GILMORE, P. J., & MILLS, K. J. (2011). The Mount Wright Arc: A Cambrian subduction system developed on the continental margin of East Gondwana, Koonenberry Belt, eastern Australia. Gondwana Research, 19(3), 650–669.

HACK, A. C., DWYER, R. C., PHILLIPS, G., WHALAN, S., & HUANG, H. Q. (2018). The age and tectonic significance of the Warraweena Volcanics and related rocks, southern Thomson Orogen. Australian Journal of Earth Sciences, 65(7–8), 1071–1096.

ISHIZUKA, O., TAYLOR, R. N., UMINO, S., & KANAYAMA, K. (2020). Geochemical evolution of arc and slab following subduction initiation: A record from the Bonin islands, Japan. Journal of Petrology, 61(5).

JACKSON, S. E., PEARSON, N. J., GRIFFIN, W. L., & BELOUSOVA, E. A. (2004). The application of laser ablation-inductively coupled plasma-mass spectrometry to in situ U-Pb zircon geochronology. Chemical Geology, 211(1–2), 47–69.

JAGO, J. B., GUM, J. C., BURTT, A. C., & HAINES, P. W. (2003). Stratigraphy of the Kanmantoo Group: A critical element of the Adelaide Fold Belt and the Palaeo-Pacific plate margin, Eastern Gondwana. Australian Journal of Earth Sciences, 50(3), 343–363.

JOHNSON, E. L., PHILLIPS, G., & ALLEN, C. M. (2016). Ediacaran–Cambrian basin evolution in the Koonenberry Belt (eastern Australia): Implications for the geodynamics of the Delamerian Orogen. Gondwana Research, 37, 266–284.

JOHNSON, E., & MUSGRAVE, R. (2012). Potential-field interpretation of the Kars Belt, western NSW. ASEG Extended Abstracts, 2012(1), 1–3.

KEMP, A. I. S. (2003). Plutonic boninite-like rocks in an anatectic setting: Tectonic implications for the Delamerian orogen in southeastern Australia. Geology, 31(4), 371–374.

KEMP, A. I. S., HAWKESWORTH, C. J., FOSTER, G. L., PATERSON, B. A., WOODHEAD, J. D., HERGT, J. M., GRAY, C. M., WHITEHOUSE, M. (2007). Magmatic and crustal differentiation history of granitic rocks from Hf–O isotopes in zircon. Science, 315, 980–983.

KEMP, A. I. S., HAWKESWORTH, C. J., COLLINS, W. J., GRAY, C. M., & BLEVIN, P. L. (2009). Isotopic evidence for rapid continental growth in an extensional accretionary orogen: The Tasmanides, eastern Australia. Earth and Planetary Science Letters, 284(3–4), 455–466.

KIRKLAND, C. L., SMITHIES, R. H., TAYLOR, R. J. M., EVANS, N., & MCDONALD, B. (2015). Zircon Th/U ratios in magmatic environs. Lithos, 212–215, 397–414.

KOHN, M. J., ENGI, M., LANARI, P. (2018). Petrochronology: Methods and Applications. Reviews in Mineralogy and Geochemistry. 83.

LONG, X., SUN, M., YUAN, C., KRÖNER, A., & HU, A. (2012). Zircon REE patterns and geochemical characteristics of Paleoproterozoic anatectic granite in the northern Tarim Craton, NW China: Implications for the reconstruction of the Columbia supercontinent. Precambrian Research, 222–223, 474–487.

MAAS, R,. APUKHTINA, O., KAMENETSKY, V., EHRIG, K., SPRUNG, P., MÜNKER, C. (2020) Carbonates at the supergiant Olympic Dam Cu-U-Au-Ag deposit, South Australia. Part 2: Sm-Nd, Lu-Hf and Sr-Pb isotope constraints on the chronology of carbonate deposition. Ore Geology Reviews.

MESCHEDE, M. (1986). A method of discriminating between different types of mid-ocean ridge basalts and continental tholeiites with the Nb1bZr1bY diagram. Chemical Geology, 56(3–4), 207–218.

MILLER, J. S., MATZEL, J. E. P., MILLER, C. F., BURGESS, S. D., & MILLER, R. B. (2007). Zircon growth and recycling during the assembly of large, composite arc plutons. Journal of Volcanology and Geothermal Research, 167(1–4), 282–299.

MILLS, K.J. AND HICKS, M.G. 2016. Bunda 1:100,000 Geological Sheet 7434. Second Edition. Geological Survey of New South Wales, Maitland.

MÜNKER, C., & CRAWFORD, A. J. (2000). Cambrian arc evolution along the se gondwana active margin: A synthesis from Tasmania-New Zealand-Australia-Antarctica correlations. Tectonics, 19(3), 415–432.

MUSGRAVE, R. J.; DICK, S. (2017). A 3D model for the Koonenberry Belt from geologically constrained inversion of potential field data. Quarterly Notes No 149 (1). Geological Survey of NSW.

NEBEL, O., & ARCULUS, R. J. (2015). Selective ingress of a Samoan plume component into the northern Lau backarc basin. Nature Communications, 6, 1–7.

OFFLER, R., ZWINGMANN, H., FODEN, J., SUTHERLAND, F. L., & GRAHAM, I. T. (2019). Age and composition of dykes emplaced before and during the opening of the Tasman Sea—source implications. Australian Journal of Earth Sciences, 66(8), 1129–1144.

PASTOR-GALÁN, D., SPENCER, C. J., FURUKAWA, T., & TSUJIMORI, T.

(2021). Evidence for crustal removal, tectonic erosion and flare-ups from the Japanese evolving forearc sediment provenance. Earth and Planetary Science Letters, 564.

PATCHETT, P. J., & TATSUMOTO, M. (1980). A routine high-precision method for Lu-Hf isotope geochemistry and chronology. Contributions to Mineralogy and Petrology, 75(3), 263–267.

PATON, C., HELLSTROM, J., PAUL, B., WOODHEAD, J., & HERGT, J. (2011). Iolite: Freeware for the visualisation and processing of mass spectrometric data. Journal of Analytical Atomic Spectrometry, 26(12), 2508–2518.

PEARCE, J. A. (1982). Trace elements characteristics of lavas from destructive plate margins.

PEARCE, J. A. (2014). Immobile element fingerprinting of ophiolites. Elements, 10(2), 101–108.

PEATE D. W., MANTOVANI M. S. M., HAWKESWORTH C.J. (1988) Geochemical stratigraphy of Parana continental flood basalts: a contribution from borehole samples. In Piccirillo EM, Melfi AJ (eds) The Mesozoic flood volcanism of the Parana basin: petrogenetic and geophysical aspects. IAG-USP press: 14-24

PETRUS, J. A., & KAMBER, B. S. (2012). VizualAge: A Novel Approach to Laser Ablation ICP-MS U-Pb Geochronology Data Reduction. Geostandards and Geoanalytical Research, 36(3), 247–270.

PIN, C., GANNOUN, A., & DUPONT, A. (2014) Rapid, simultaneous separation of Sr, Pb and Nd by extraction chromatography prior to isotope ratios determination by TIMS and MC-ICP-MS. Journal of Analytical Atomic Spectrometry, 29, 1858-1870.

POLITO, P. (2015). Annual report for Loch-Lilly EL8199 for the period 6 November 2014 to 5 November 2015. Anglo American Exploration Pty Ltd (Report

GS2016/0061). Geological Survey of NSW (unpublished).

PROFETA, L., DUCEA, M. N., CHAPMAN, J. B., PATERSON, S. R., GONZALES, S. M. H., KIRSCH, M., PETRESCU, L., & DECELLES, P. G. (2015). Quantifying crustal thickness over time in magmatic arcs. Scientific Reports, 5, 1–7.

RACZEK, I., STOLL, B., HOFMANN, A. W., & JOCHUM, K. P. (2000) High-precision trace element data for the USGS reference materials BCR-1, BCR-2, BHVO-1, BHVO-2, AGC-1, AGV-2, DTS-1, DTS-2, GSP-1 and GSP-2 by ID-TIMS and MIC-SSMS. Geostandards Newsletter, 25, 77-86.

RACZEK, I., JOCHUM, K. P., & HOFMANN, A. W. (2003) Neodymium and strontium isotope data for USGS reference materials BCR-1, BCR-2, BHVO-1, BHVO-2, AGV-1, AGV-2, GSP-1, GSP-2 and eight MPI-DING reference glasses. Geostandards Newsletter, 27, 173-179.

RANKIN, L. R. (2014). Structural Setting and Porphyry Potential of the Loch Lilly – Kars Belt, Western NSW. Geointerp Confidential Report 2014/01 for Anglo American Exploration Australia. (Report GS2014/1815). Geological Survey of NSW (unpublished).

REAGAN, M. K., ISHIZUKA, O., STERN, R. J., KELLEY, K. A., OHARA, Y., BLICHERT-TOFT, J., BLOOMER, S. H., CASH, J., FRYER, P., HANAN, B. B., HICKEY-VARGAS, R., ISHII, T., KIMURA, J. I., PEATE, D. W., ROWE, M. C., WOODS, M. (2010). Fore-arc basalts and subduction initiation in the Izu-Bonin-Mariana system. Geochemistry, Geophysics, Geosystems, 11(3), 1–17.

REID, A. J., & PAYNE, J. L. (2017). Magmatic zircon Lu–Hf isotopic record of juvenile addition and crustal reworking in the Gawler Craton, Australia. Lithos, 292–293, 294–306.

RENNISON, M. W., & RUTLEY, A. J. (1997). First annual exploration report for the period ended 16 June 1997 for EL5038, Inkerman, Koonenberry Project, NSW. BHP Minerals Pty Ltd (Report GS1997/437). Geological Survey of NSW (unpublished).

ROLLINSON, H. (1993). Using Geochemical Data: Evolution, Presentation, Interpretation. Longman Scientific and Technical Press. 26. ROSENBAUM, G. (2018). The Tasmanides: Phanerozoic Tectonic Evolution of Eastern Australia. Annual Review of Earth and Planetary Sciences, 46(June), 291–325.

SHERVAIS, J. W. (1982). TiV plots and the petrogenesis of modern and ophiolitic lavas. Earth and Planetary Science Letters, 59(1), 101–118.

SLÁMA, J., KOŠLER, J., CONDON, D. J., CROWLEY, J. L., GERDES, A., HANCHAR, J. M., HORSTWOOD, M. S. A., MORRIS, G. A., NASDALA, L., NORBERG, N., SCHALTEGGER, U., SCHOENE, B., TUBRETT, M. N., WHITEHOUSE, M. J. (2008). Plešovice zircon - A new natural reference material for U-Pb and Hf isotopic microanalysis. Chemical Geology, 249(1–2), 1–35.

STRAUB, S. M., GOLDSTEIN, S. L., CLASS, C., SCHMIDT, A., & GOMEZ-TUENA, A. (2010). Slab and mantle controls on the Sr-Nd-Pb-Hf isotope evolution of the Post 42 Ma Izu-Bonin volcanic arc. Journal of Petrology, 51(5), 993–1026.

STERN, R. J., REAGAN, M., ISHIZUKA, O., OHARA, Y., & WHATTAM, S. (2012). To understand subduction initiation, study forearc crust: To understand forearc crust, study ophiolites. Lithosphere, 4(6), 469–483.

STERN, R. J. (2002). Subduction zones. Reviews of Geophysics, 40(4), 3-1-3–38.

STERN, R. J. (2010). The anatomy and ontogeny of modern intra-oceanic arc systems. Geological Society Special Publication, 338, 7–34.

SUN, J. F., YANG, J. H., WU, F. Y., XIE, L. W., YANG, Y. H., LIU, Z. C., &

LI, X. H. (2012). In situ U-Pb dating of titanite by LA-ICPMS. Chinese Science Bulletin, 57(20), 2506–2516.

SUN, S. S., & MCDONOUGH, W. F. (1989). Chemical and isotopic systematics of oceanic basalts: Implications for mantle composition and processes. Geological Society Special Publication, 42(1), 313–345.

SUN, S. S., & MCDONOUGH, W. F. (1995). The composition of the Earth. Chemical Geology, 120(3–4), 223–253.

TURNER, S. P. (1996). Petrogenesis of the late-Delamerian gabbroic complex at Black Hill, South Australia: Implications for convective thinning of the lithospheric mantle. Mineralogy and Petrology, 56(1), 51–89.

TURNER, S., & FODEN, J. (1996). Magma mingling in late-Delamerian A-type granites at Mannum, South Australia. Mineralogy and Petrology, 56(3), 147–169.

TURNER, S., KELLEY, S., VANDENBERG, A., FODEN, J., SANDIFORD, M., FLOTTMANN, T. (1996). Source of the Lachlan fold belt flysch linked to convective removal of the lithospheric mantle and rapid exhumation of the Delamerian-Ross fold belt. Geology, 24, 941–944.

VANCE, D., & THIRLWALL, M. F. (2002) An assessment of mass discrimination in MC-ICPMS using Nd isotopes. Chemical Geology, 185, 227-240.

VERMEESCH, P. (2018). IsoplotR: A free and open toolbox for geochronology. Geoscience Frontiers, 9(5), 1479–1493.

VICKERY, N. (2008). Petrology and geochemistry of samples selected from drillholes in the Louth–Bourke area. Maitland NSW: Geological Survey of NSW. GS2008/0730 (unpublished).

WIEDENBECK, M., ALLÉ, P., CORFU, F., GRIFFIN, W. L., MEIER, M., OBERLI, F., QUADT, A. VON, RODDICK, J. C., SPIEGEL, W. (1995). Three Natural Zir-

con Standards for U-Th-Pb, Lu-Hf, Trace Element and Ree Analyses. Geostandards Newsletter, 19(1), 1–23.

WINCHESTER, J. A., & FLOYD, P. A. (1977). Geochemical discrimination of different magma series and their differentiation products using immobile elements. Chemical Geology, 20(C), 325–343.

WINTER, J. D. (2001). An Introduction to Igneous and Metamorphic Petrology. Prentice Hall, New Jersey.

WOOD, D.A. (1980). The application of a Th-Hf-Ta diagram to problems of tectonomagmatic classification and to establishing the nature of crustal contamination of basaltic lavas of the British Tertiary Volcanic Province. Earth and Planetary Science Letters 50, 11-30.

WOODHEAD, J., HERGT, J., SHELLEY, M., EGGINS, S., & KEMP, R. (2004). Zircon Hf-isotope analysis with an excimer laser, depth profiling, ablation of complex geometries, and concomitant age estimation. Chemical Geology, 209(1–2), 121–135.

XIE, L. W., EVANS, N. J., YANG, Y. H., HUANG, C., & YANG, J. H. (2018). U-Th-Pb geochronology and simultaneous analysis of multiple isotope systems in geological samples by LA-MC-ICP-MS. Journal of Analytical Atomic Spectrometry, 33(10), 1600–1615.

YOGODZINSKI, G. M., BIZIMIS, M., HICKEY-VARGAS, R., MCCARTHY, A., HOCKING, B. D., SAVOV, I. P., ISHIZUKA, O., ARCULUS, R. (2018). Implications of Eocene-age Philippine Sea and forearc basalts for initiation and early history of the Izu-Bonin-Mariana arc. Geochimica et Cosmochimica Acta, 228, 136–156.

Appendix A

Seismic Line

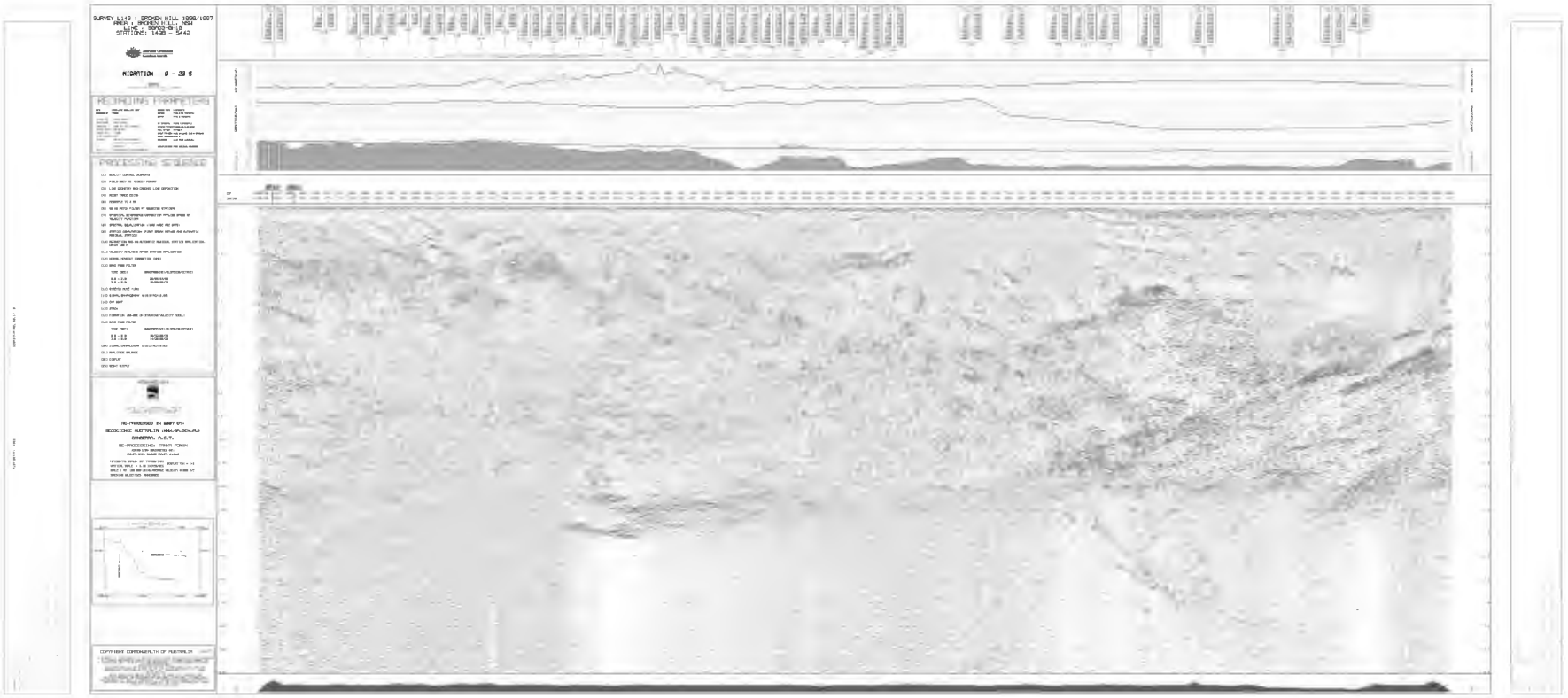

Figure A.1: Seismic line 96AGS-BH1B, sourced from Geoscience Australia (GA).

Appendix B

Sample List

Table B.1: List of samples for this project

Sample ID	Sampled From	Depth (m)	Longitutde	Latitude	Sampled By	Rock Type	Sample Purpose
VP001	EHK1	112 - 113	141.603759	-32.428569	This study	Diorite	Geochronology, Thin section
VP002	EHK2	175 - 177	141.463550	-32.549413	This study	Diorite	Geochronology, Thin section
VP003	EHK3	144 - 145	141.693742	-32.358824	This study	Andesite	Geochronology, Thin section
VP004	EHK3	150 - 152	141.693742	-32.358824	This study	Gabbro	Geochronology, Thin section, Geochemistry, Sm-Nd
VP005	EHK3	146 - 147	141.693742	-32.358824	This study	Margin between andesite and gabbro	Thin section
VP006	NBH004	159 - 161	141.688010	-32.351432	This study	Basalt	Geochronology, Thin section, Geochemistry, Sm-Nd
VP007	NBH004	166 - 170	141.688010	-32.351432	This study	Basalt	Geochronology, Thin section
VP008	NBH005	156 - 158	141.680234	-32.364563	This study	Andesite porphyry	Geochronology, Thin section

VP009	NBH005	170 - 172	141.680234	-32.364563	This study	Diorite	Thin section, Sm-Nd
VP010	NBH005	160 - 162	141.680234	-32.364563	This study	Meta-siltstone	Thin section, Geochemistry
VP012	NBH009	255 - 257	141.499821	-32.694301	This study	Gabbro with dioritic pods	Geochronology, Thin section, Sm-Nd
VP013	NBH012	218 - 220.5	141.911797	-32.128042	This study	Basalt	Geochronology, Thin section, Geochemistry, Sm-Nd
PJG0058	Blue Tank Well	-	142.712036	-31.271700	PJG, Kyle Hughes, Glen Phillips 2015	Basalt	Thin section, Geochemistry
PJG0059	Blue Tank Well	-	142.713125	-31.270909	PJG, Kyle Hughes, Glen Phillips 2015	Porphyritic basalt	Geochronology, Thin section, Geochemistry, Sm-Nd
PJG0080	East of Koonenberry Fault	-	142.678310	-30.871638	PJG, Kyle Hughes, Glen Phillips 2015	Dolerite	Geochronology, Thin section, Geochemistry, Sm-Nd
PJG0082	West of Koonenberry Fault	-	142.551245	-30.813723	PJG, Kyle Hughes, Glen Phillips 2015	Gabbro	Geochronology, Thin section, Geochemistry, Sm-Nd
DD89GR05-83.5	DD89GR05	83.5	142.715476	-31.300839	PJG, Kyle Hughes, Glen Phillips 2015	Meta-igneous rock	Thin section
DD89GR05-95	DD89GR05	95	142.715476	-31.300839	PJG, Kyle Hughes, Glen Phillips 2015	Basalt	Geochemistry, Thin section

Appendix C

Sample Descriptions

C.0.1 VP001

Sampled from drill hole EHK1 at 112 - 113 m depth.

Core Description

Medium-grained, dark grey to black in colour with a slight porphyritic texture. Black, sub-rounded phenocrysts (3 mm) within finer groundmass of shiny black and grey/white grains. Similar to VP002 described below, however finer-grained and less porphyritic.

Thin Section Description

Plagioclase and clinopyroxene phenocrysts are dominant, ranging in grainsize from 0.5 to 2 mm and 0.5 to 1 mm respectively. Plagioclase shows strong core to rim zoning and appears largely fresh with minimal alteration. Uralisation of clinopyroxene to amphibole-dominated assemblages is common, mainly to green hornblende and in some cases a mix of secondary amphiboles. Brown biotite and interstital quartz also present. Zircon observed in biotite and opaques are common throughout.

Figure C.1: Core sample VP001 from LLK drill hole EHK1.

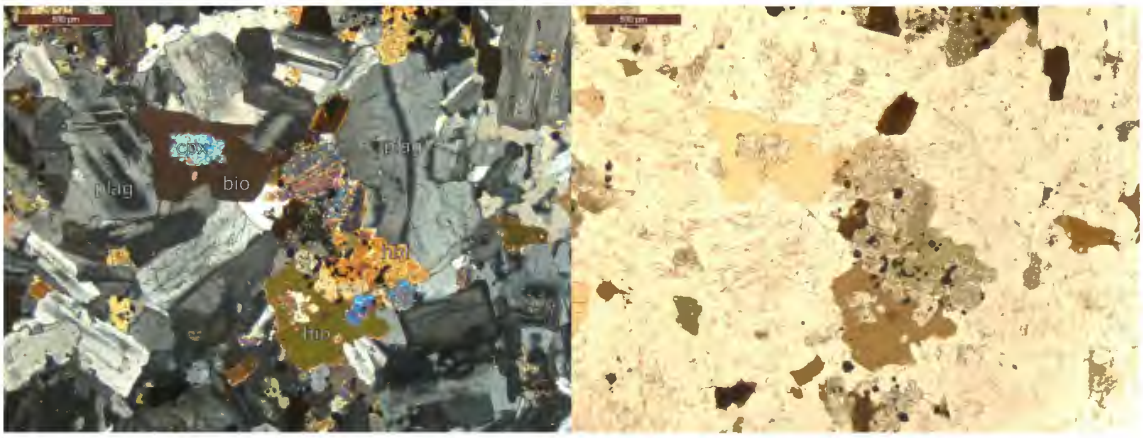

Figure C.2: Crossed-polars (left) and plane-polarised light (right) images of thin section VP001 showing plagioclase, clinopyroxene cores surrounded by biotite, and biotite and hornblende overgrowing clinopyroxene.

C.0.2 VP002

Sampled from drill hole EHK2 at 175 - 177 m depth.

Core Description

Medium to coarse grained diorite, medium/dark grey to black in colour with a "salt and pepper" appearance and porphyritic texture. Coarse (2 to 5 mm), black, sub-angular to sub-rounded hornblende or pyroxene grains and coarse (3 to 4 mm) clear, lath shaped plagioclase grains within a finer groundmass of shiny, black and cream-white sub-rounded grains. Some phenocrysts appear to have been infilled/replaced with sulphides, leaving behind a coarse (approx. 4 mm) dark gold coloured centre within thin black halo, possibly magnetite. Sulphide veining also present and radial mesh of cream-white fibrous grains, possibly secondary alteration. Lighter coloured areas surrounding veins appear pink-orange in colour, possibly fluid alteration. Large enclave (4 cm) of more mafic material.

Thin Section Description

Clinopyroxene occurs as phenocrysts, displaying twinning and commonly overgrown by hornblende and biotite. Plagioclase occurs as interstitial clusters of fine, lath-shaped, interlocking grains approximately 0.5 to 1 mm in length, as well as coarser grains approximately 2.5 to 3 mm. Plagioclase shows zoning and is altered, and mymekite is also present along some grain boundaries. Alteration phases include sericite in plagioclase and uralisation of clinopyroxene as well as minor titanite and calcite.

Mafic enclave displays distinct change in grainsize to a finer matrix of plagioclase peppered with opaques, fine hornblende and biotite grains (<0.5 mm).

Figure C.3: Core sample VP002 from LLK drill hole EHK2.

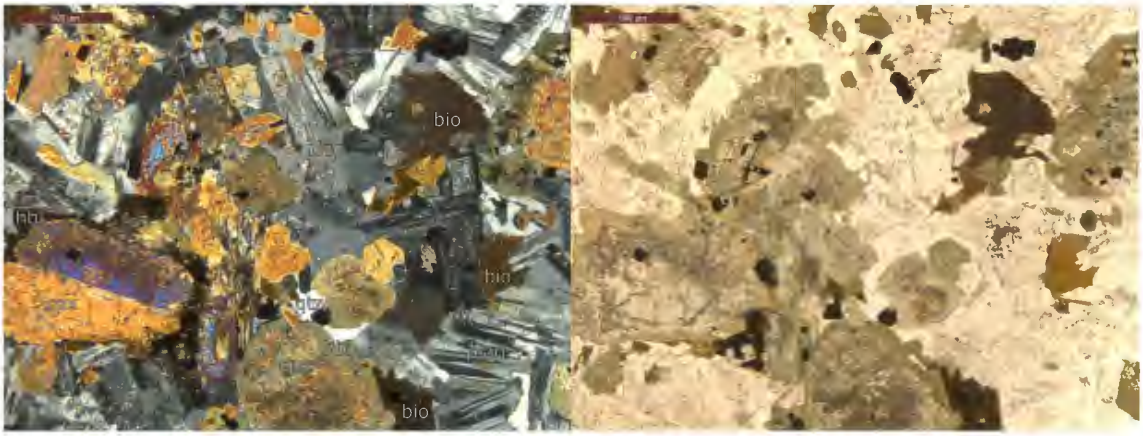

Figure C.4: Crossed-polars (left) and plane-polarised light (right) images of thin section VP002 showing clinopyroxene, plagioclase, hornblende and biotite. The clinopyroxene phenocryst on the left shows twinning.

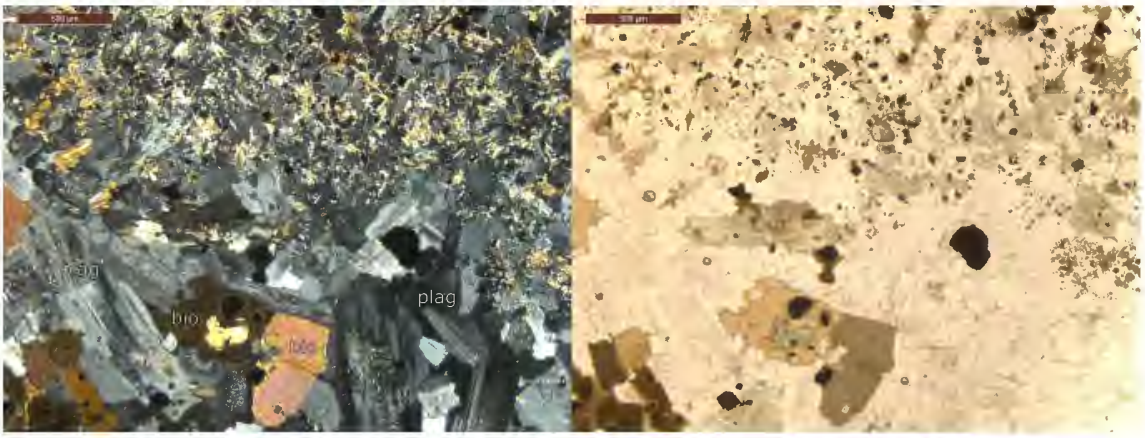

Figure C.5: Crossed-polars (left) and plane-polarised light (right) images of thin section VP002-02 showing the change in grainsize between the enclave (top) and the diorite (bottom).

C.0.3 VP003

Sampled from drill hole EHK3 at 144 - 145 m depth.

Core Description

Fine to medium grained, light to dark grey with porphyritic texture and a coarse (3 cm) black, glassy enclave of more mafic material. Black, sub-rounded to angular shaped phenocrysts range in grainsize from 2 to 5 mm. White/cream coloured phenocrysts from 2 to 3 mm are also present and appear more tabular to blocky in shape. Fine grained, light grey groundmass with finer black grains (>1 mm), and finer material surrounding margin of the enclave.

Thin Section Description

Euhedral, lath-shaped plagioclase phenocrysts range in grainsize, mainly 1 to 3.5 mm, and are strongly altered and zoned. Clinopyroxene phenocrysts have been almost entirely replaced by brown hornblende (0.5 to 1.5 mm) and altered to chlorite and calcite. Fine-grained groundmass consisting of mostly plagioclase and opaques.

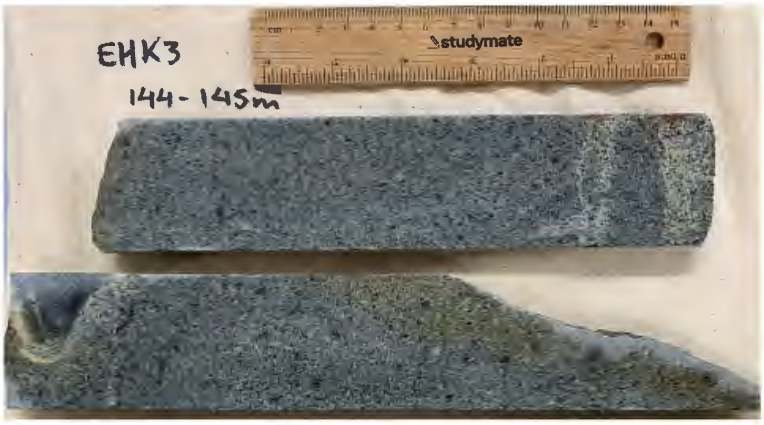

Figure C.6: Core sample VP003 from LLK drill hole EHK3.

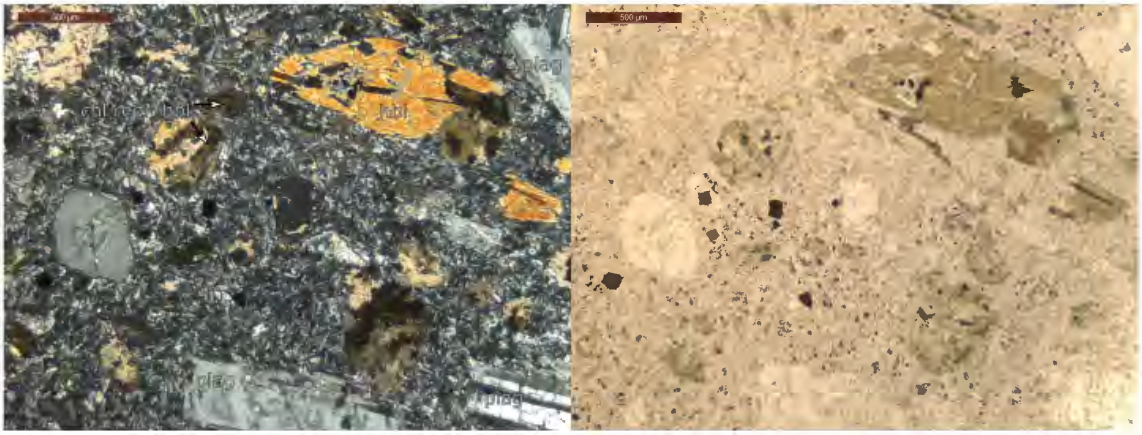

Figure C.7: Crossed-polars (left) and plane-polarised light (right) images of thin section VP003 showing hornblende and plagioclase phenocrysts within a fine-grained groundmass. Chlorite replacing hornblende is also shown.

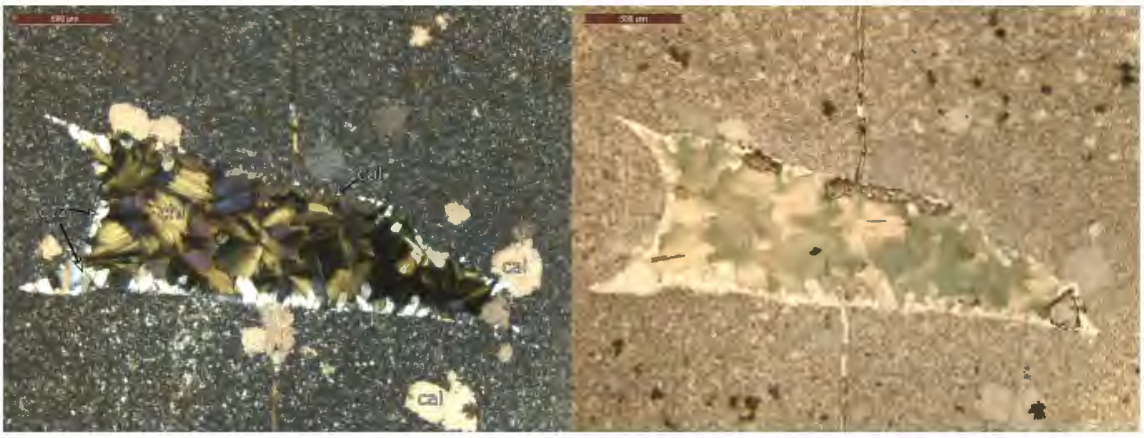

Figure C.8: Crossed-polars (left) and plane-polarised light (right) images of thin section VP003 showing a phenocryst within the enclave entirely replaced by chlorite, rimmed by calcite and quartz.

Medium-grained (1.5 mm) rhomb-shaped sphene (titanite) grains are commonly surrounded by calcite, chlorite and quartz. These alteration assemblages are common, ranging in grainsize up to 2 mm, and are typical of greenschist facies metamorphism.

Fine-grained enclave has an aphanitic texture and contains a calcite vein with cross-cutting chlorite veins as well as inclusions of euhedral grains entirely replaced by alteration assemblages. Phenocrysts are finer grained surrounding the enclave.

C.0.4 VP004

Sampled from drill hole EHK3 at 150 - 152 m depth.

Core Description

This rock is dark grey to black and mostly fine-grained. Slightly coarser black grains (1 to 2 mm) stand out from the finer-grained groundmass. Sulfide veining and pyrite common. Larger veins (3 mm width) appear green in colour, whereas thin veins (¡1mm width) are more cream to white.

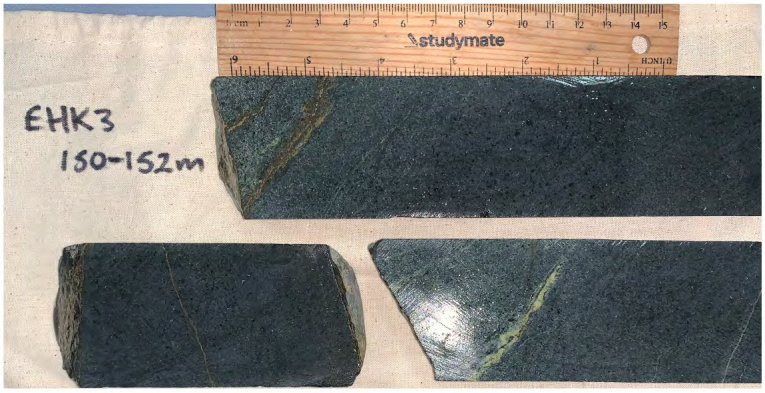

Figure C.9: Core sample VP004 from LLK drill hole EHK3.

Thin Section Description

Primary mafic phases include clinopyroxene, plagioclase and opaques. Clinopyroxene phenocrysts range in grainsize from 0.5 to 1.5 mm and are overgrown by secondary amphibole along the edges of grains. Some clinopyroxene grains show strong core to rim zoning. Plagioclase is strongly altered and secondary, mix-layered clays are present within plagioclase grains, a common feature in low grade metamorphic rocks.

The turquoise-blue secondary amphibole is also common with secondary biotite aggregates. The presence of secondary amphiboles and fine-grained secondary biotite indicates this fine-grained gabbro has experienced lower amphibolite facies.

C.0.5 VP005

Sampled from drill hole EHK3 at 146 - 147 m depth.

Core Description

This core sample the contact between VP003 (andesite) and VP004 (gabbro). Distinct change in grainsize and colour is suggestive of a chilled margin.

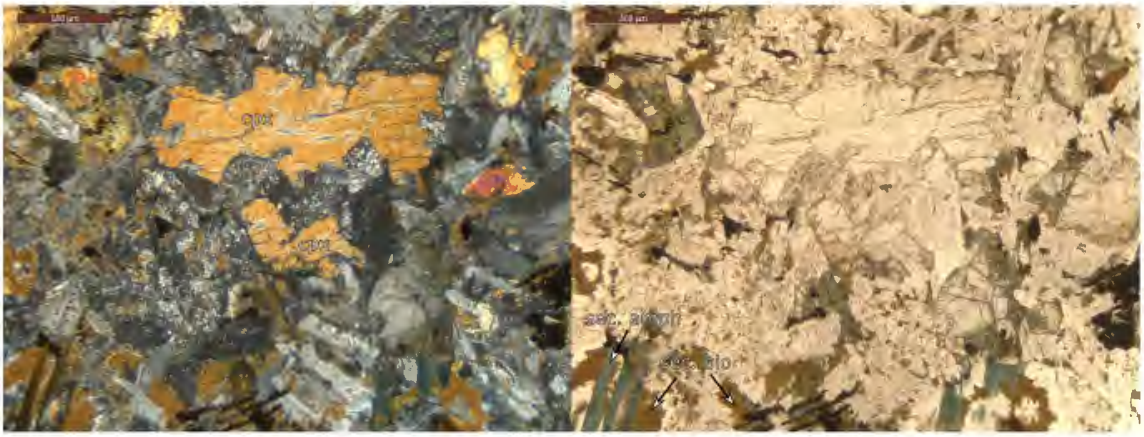

Figure C.10: Crossed-polars (left) and plane-polarised light (right) images of thin section VP004 showing clinopyroxene phenocrysts, secondary amphiboles and secondary biotite.

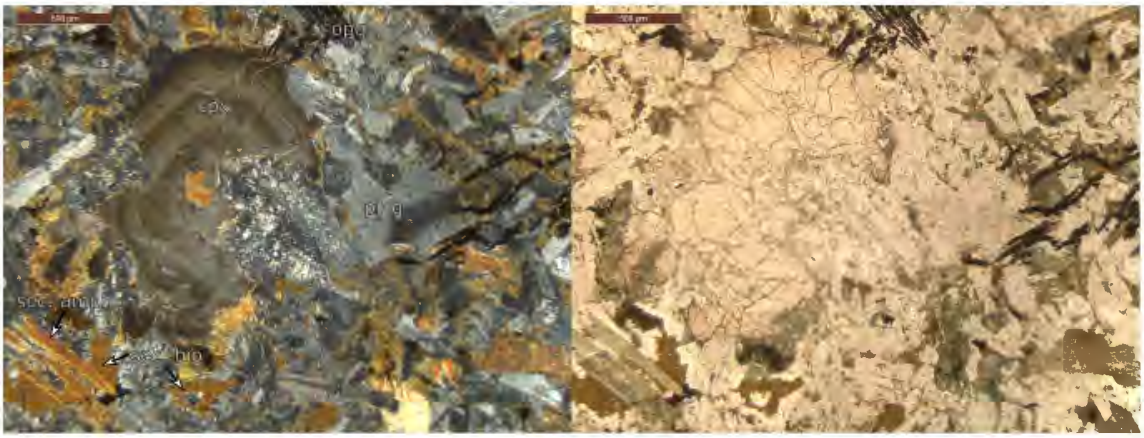

Figure C.11: Crossed-polars (left) and plane-polarised light (right) images of thin section VP004 showing zoned core of a clinopyroxene phenocryst.

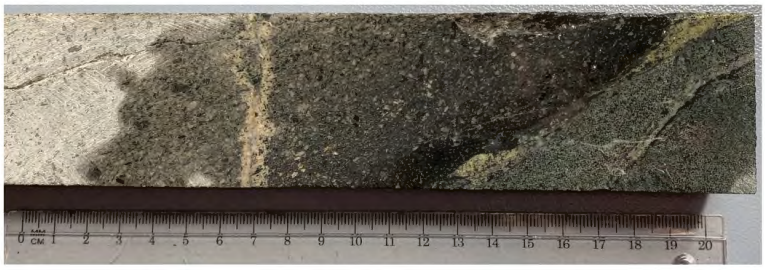

Figure C.12: Core sample VP005 from LLK drill hole EHK3.

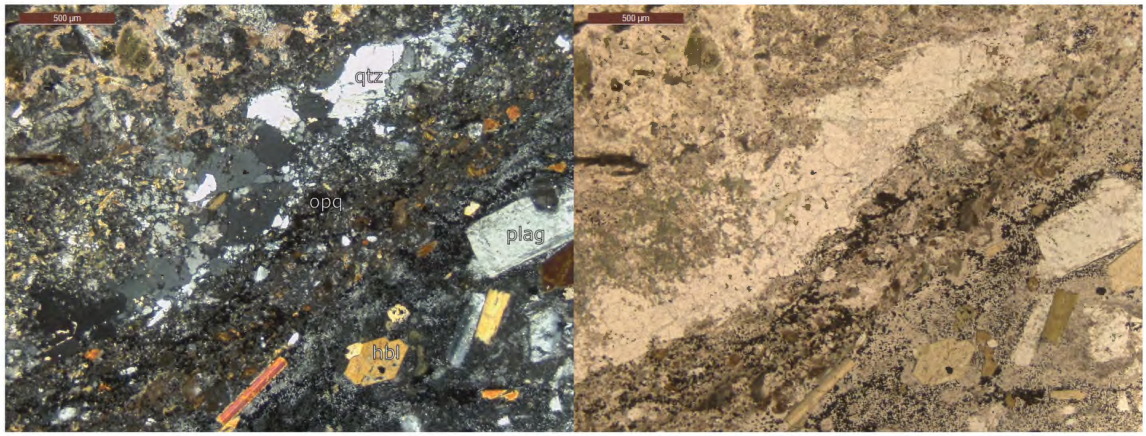

Figure C.13: Crossed-polars (left) and plane-polarised light (right) images of thin section VP005 showing chilled margin defined by opaques, quartz and finer-grained phenocrysts.

Thin Section Description

A narrow chilled margin is present within the andesite, marked by change in grain-size, and indicates the andesite intruded later than the gabbro. Margin is defined by opaques, quartz and fine-grained minerals.

C.0.6 VP006

Sampled from drill hole NBH004 at 159 - 161 m depth.

Core Description

This rock is a dark grey to black, generally fine-grained basalt however some intervals appear to be more medium-grained. Sulfide veining and alteration observed throughout.

Figure C.14: Core sample VP006 from LLK drill hole NBH004.

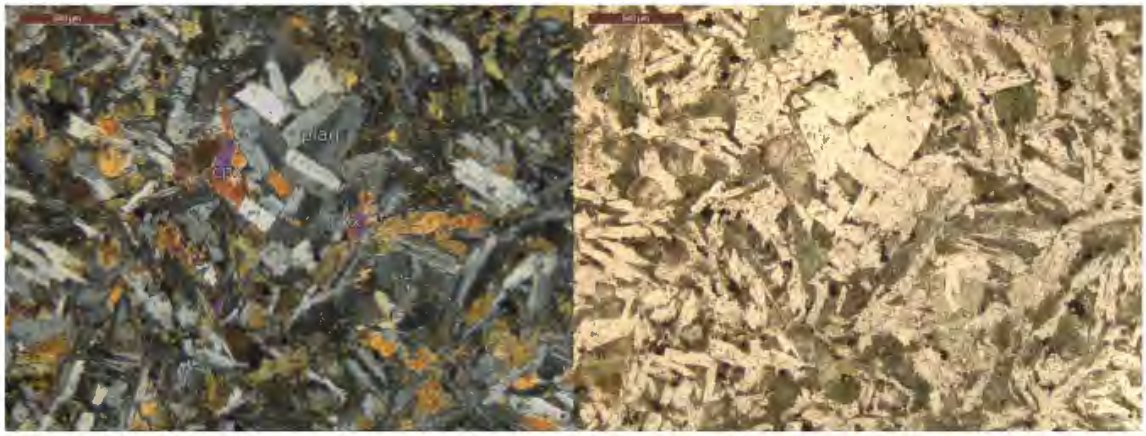

Figure C.15: Crossed-polars (left) and plane-polarised light (right) images of thin section VP006 showing plagioclase and altered clinopyroxene phenocrysts.

Thin Section Description

Fine-grained basalt with interlocking plagioclase laths and clinopyroxene grains (commonly <0.5 mm) that have experienced quartz-biotite-actinolite alteration. Opaques are present throughout, as well as secondary turquoise-blue amphibole and secondary brown biotite.

C.0.7 VP007

Sampled from drill hole NBH004 at 166 - 170 m depth.

Figure C.16: Core sample VP007 from LLK drill hole NBH004.

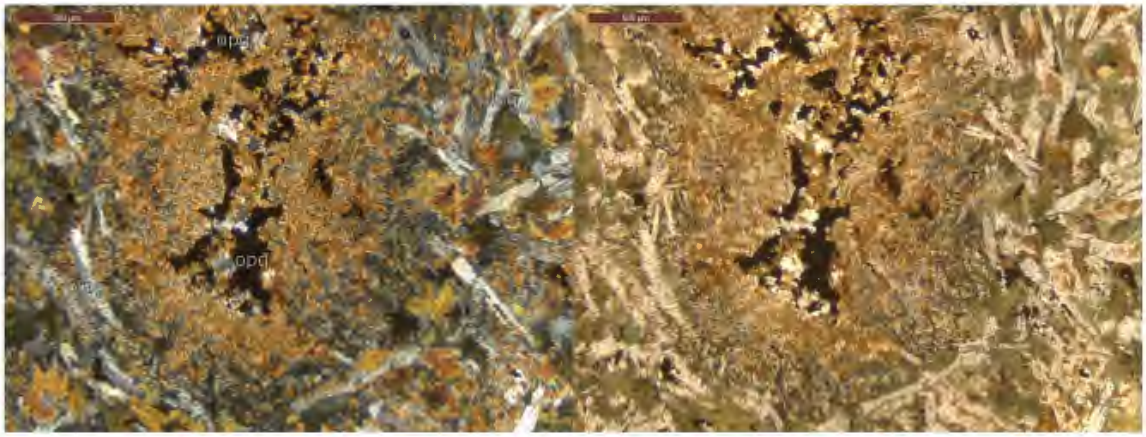

Figure C.17: Crossed-polars (left) and plane-polarised light (right) images of thin section VP007 showing opaques surrounded by alteration products.

Core Description

Dark grey to black, fine-grained basalt with some intervals appearing more medium-grained and lighter in colour due to greater alteration. Overall, this sample appears strongly altered, disseminated opaques with white halos.

Thin Section Description

Similar mineralogy and texture to VP006, however, more strongly altered. Unidentified orange to red, slightly pleochroic alteration product throughout and occurs with secondary blue-green amphibole. Opaques surrounded by this alteration assemblage.

Figure C.18: Core sample VP008 from LLK drill hole NBH005.

C.0.8 VP008

Sampled from drill hole NBH005 at 156 - 158 m depth.

Core Description

Brown to grey coloured andesite with a porphyritic texture. Black sub-rounded and pinkish-white tabular grains (commonly 2 to 3 mm) stand out from the finer-grained brown groundmass. Patches of coarse red/orange (up to 5 mm) and green (2 to 3 mm) grains are also observed, possibly alteration products.

Thin Section Description

Plagioclase and hornblende phenocrysts within a fine-grained groundmass of plagioclase and clay minerals. Plagioclase phenocrysts range in grainsize from 0.5 to 2.5 mm and are altered. Hornblende has been replaced with aggregates of chlorite, epidote and opaques.

C.0.9 VP009

Sampled from drill hole NBH005 at 170 - 172 m depth.

Figure C.19: Crossed-polars (left) and plane-polarised light (right) images of thin section VP008 showing altered plagioclase phenocrysts within a fine-grained groundmass.

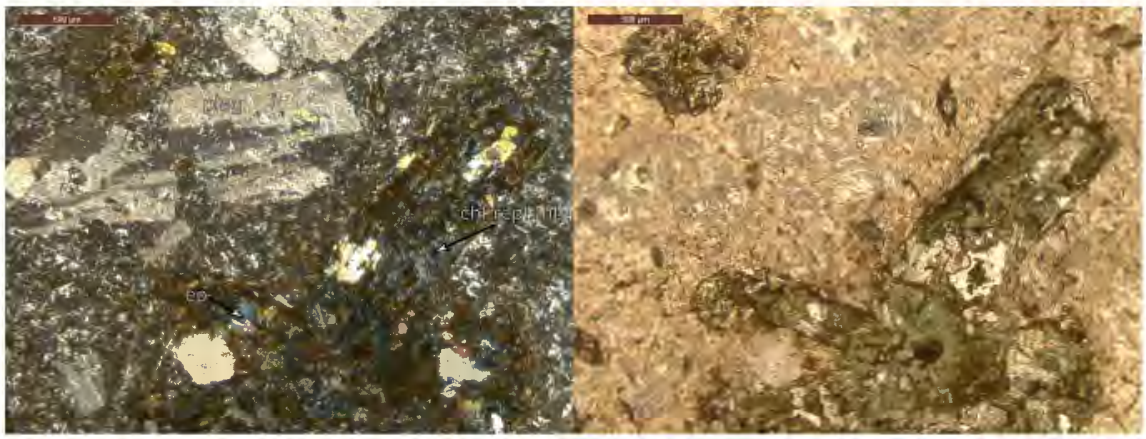

Figure C.20: Crossed-polars (left) and plane-polarised light (right) images of thin section VP008 showing altered plagioclase and hornblende phenocrysts.

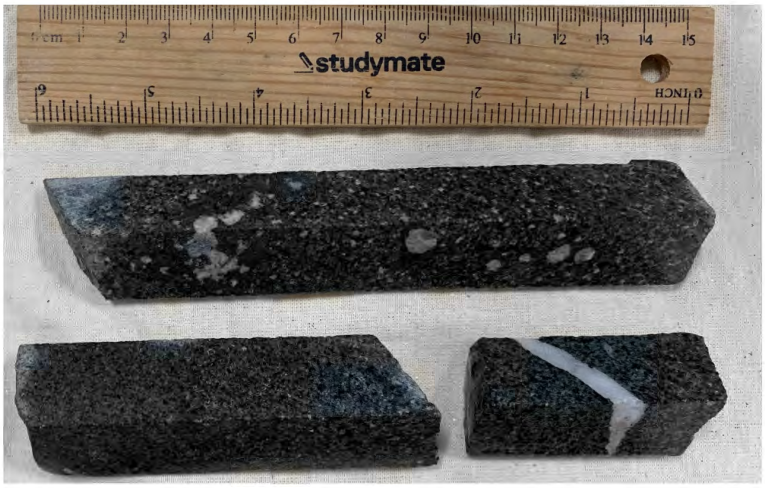

Figure C.21: Core sample VP009 from LLK drill hole NBH005.

Core Description

This rock is a medium-grained, dark grey to black diorite with porphyritic texture in some areas. Slight "salt and pepper" appearance with some more rounded and coarser (up to 5 mm) white/light grey grains throughout and a large white vein (possibly quartz or calcite).

Thin Section Description

Predominantly interlocking, altered plagioclase laths and clinopyroxene grains with coarse patches of chlorite, calcite and quartz alteration assemblages throughout. Clinopyroxene has been totally replaced by mix-layered clay

Coarse patches of prehnite commonly associated with calcite and quartz, appears clear in PPL with low relief and has first order yellow to pink birefringence and exhibits fan-like extinction. Opaques common throughout slide.

C.0.10 VP010

Sampled from drill hole NBH005 at 160 - 161 m depth.

Figure C.22: Crossed-polars (left) and plane-polarised light (right) images of thin section VP009 showing coarse-grained secondary prehnite, altered plagioclase and altered clinopyroxene.

Core Description

Thin siltstone horizon exhibiting layering 0.5 to 1 mm thick with angular inclusions of black medium-grained material (1 to 3 mm). Small-scale recumbent folding is observed in this core interval.

Thin Section Description

This rock is fine-grained and dominated by quartz, including interlocking quartz in groundmass that has been recrystallised as well as polycrystalline quartz veins. Mudclasts and psammo-pelitic layers are also present, as well as sandy layers however these are less common. Bedding is the dominant layering observed, however cleavage is also visible and forms an anastomosing texture that is defined by opaques.

Angular quartz grains and clasts suggests the source was local. White mica is observed to be orientated in two directions and the sedimentary fabric is dominant, indicating this rock has experienced low strain.

Figure C.23: Core sample VP010 from LLK drill hole NBH005.

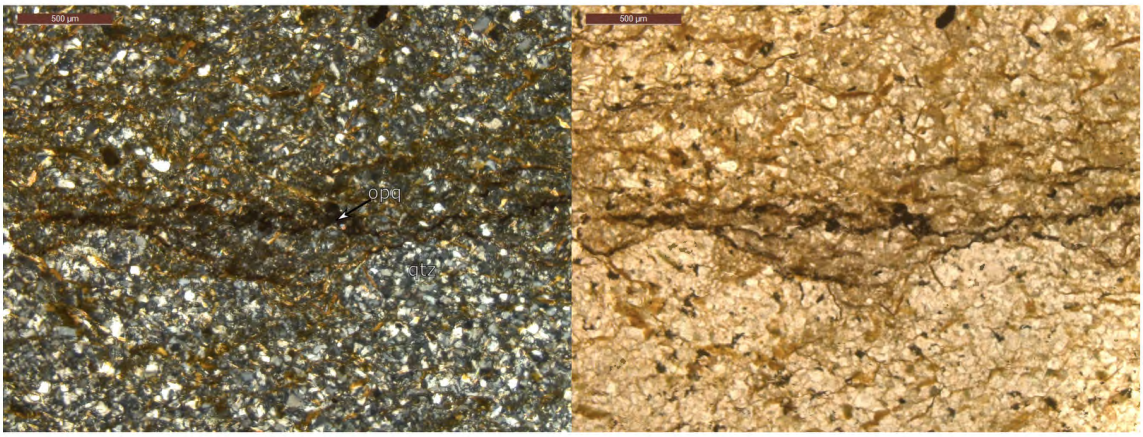

Figure C.24: Crossed-polars (left) and plane-polarised light (right) images of thin section VP010 showing fine-grained quartz groundmass with opaques defining cleavage.

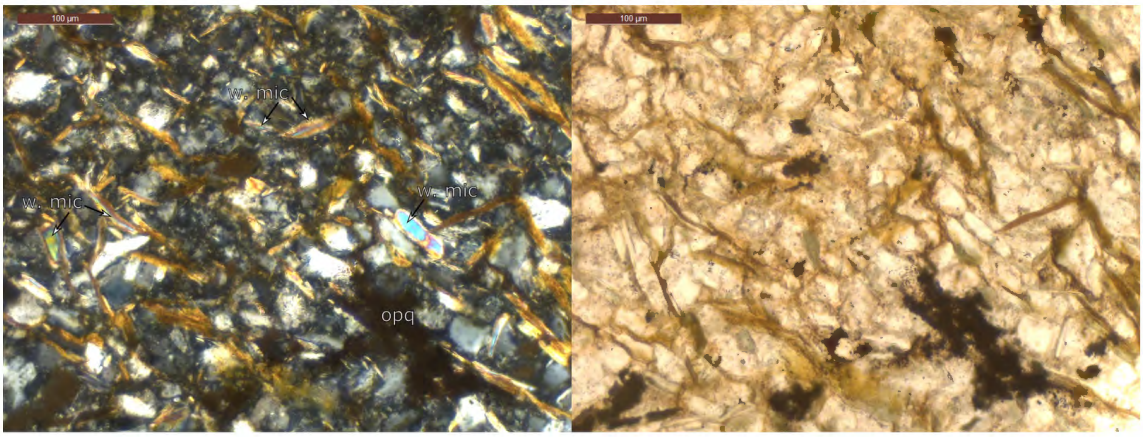

Figure C.25: Crossed-polars (left) and plane-polarised light (right) images of thin section VP010 showing white mica orientated in two directions.

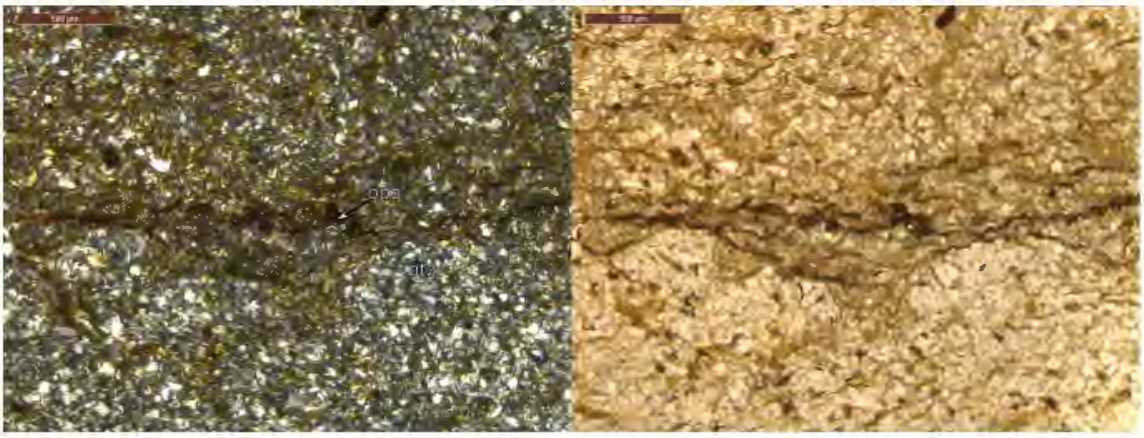

Figure C.26: Crossed-polars (left) and plane-polarised light (right) images of thin section VP010 showing mud-clast.

C.0.11 VP012

Sampled from drill hole NBH009 at 255 - 257 m depth.

Core Description

Medium-grained, dark grey to black with pods of coarser, more felsic material with a black and white spotted appearance. There is no distinct contact observed between the mafic and felsic areas. Sulfide veining is observed.

Thin Section Description

This core sample is texturally and compositionally variable, ranging from gabbro to diorite. Patches of coarse-grained poikolitic, khaki-brown hornblende enclosing orthopyroxene, clinopyroxene and plagioclase are common. Interstitial quartz is present in the more plagioclase dominant areas that contain little or no hornblende or biotite. Opaques are present throughout all textural domains. Zircon observed within hornblende.

Some areas appear relatively fresh with minimal alteration, whilst other areas show chlorite replacing brown biotite and muscovite-sericite alteration of plagioclase.

Figure C.27: Core sample VP012 from LLK drill hole NBH009.

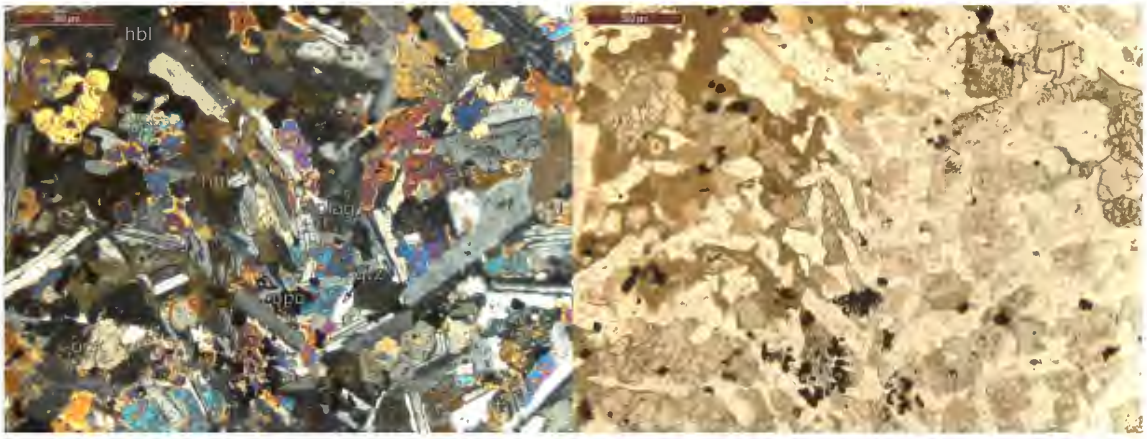

Figure C.28: Crossed-polars (left) and plane-polarised light (right) images of thin section VP012 showing a fresh, relatively unaltered gabbroic section. Clinopyroxene grains are commonly overgrown or enclosed by hornblende.

Chlorite and epidote are also commonly observed in the groundmass. Cross-cutting vein defined by opaques and prehnite. There are layers of finer grained material including quartz and interstitial chlorite and within these areas, the mafic minerals are more altered.

C.0.12 VP013

Sampled from drill hole NBH012 at 218 - 220.5 m.

Core Description

Greenish-black, fine-grained basalt with an aphanitic texture.

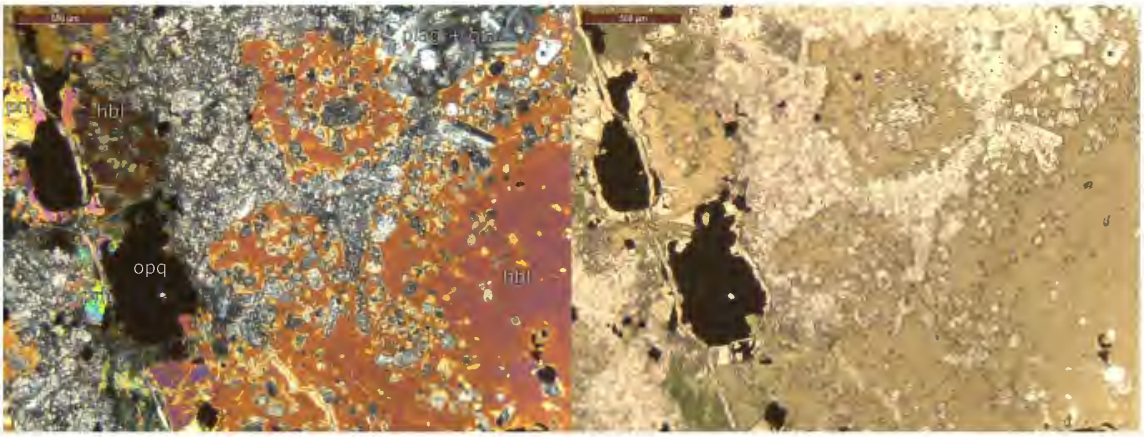

Figure C.29: Crossed-polars (left) and plane-polarised light (right) images of thin section VP012-02 showing poikolitic hornblende phenocryst and vein defined by opaques and prehnite.

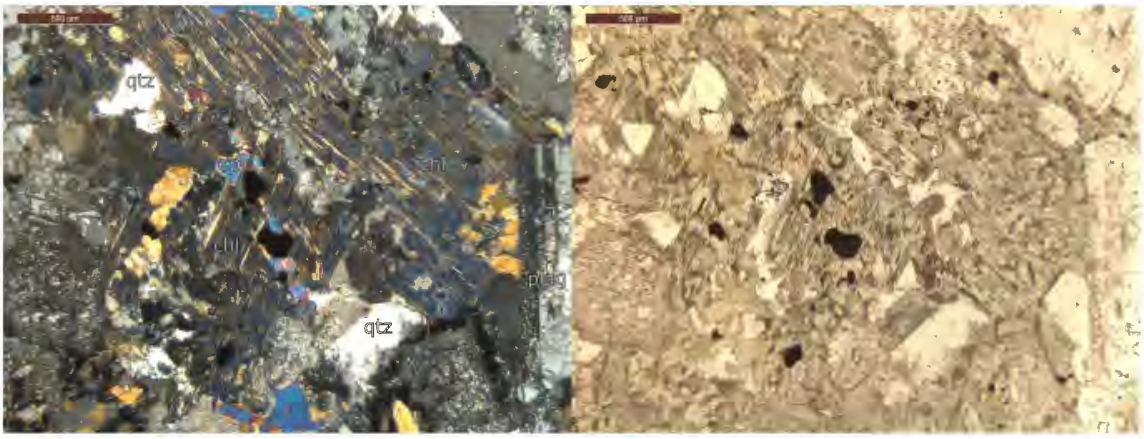

Figure C.30: Crossed-polars (left) and plane-polarised light (right) images of thin section VP012-03 showing chlorite and epidote in groundmass.

Figure C.31: Core sample VP013 from LLK drill hole NBH012.

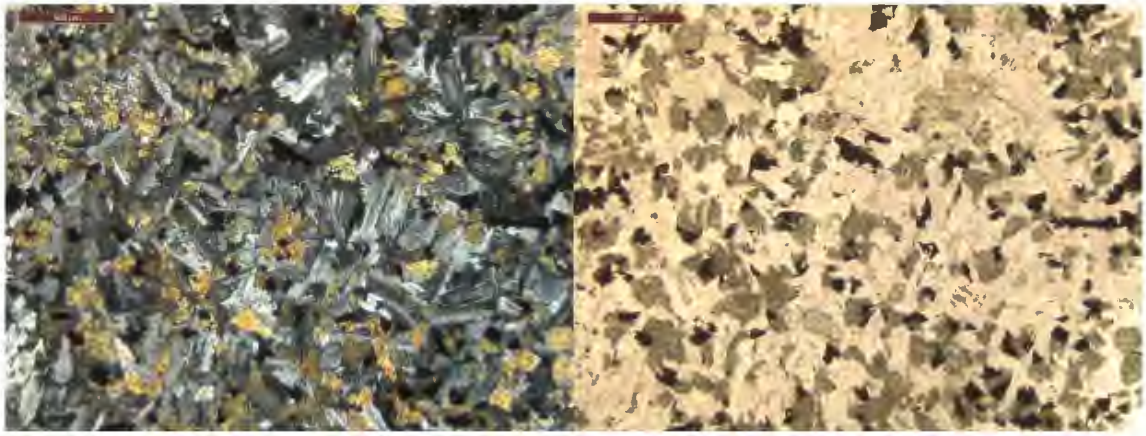

Figure C.32: Crossed-polars (left) and plane-polarised light (right) images of thin section VP013 showing plagioclase and fine-grained, altered clinopyroxene.

Thin Section Description

Dominated by plagioclase, altered clinopyroxene phenocrysts, opaques and apatite. Plagioclase grains are commonly 0.5 to 1 mm, and all other minerals are finer-grained. Minor biotite is present that has mostly been chloritized. Aggregates of high relief mineral with high birefringence, difficult to identify to due lack of shape and alteration.

C.0.13 PJG0058

This sample was supplied by the GSNSW.

Figure C.33: Koonenberry outcrop sample PJG0058.

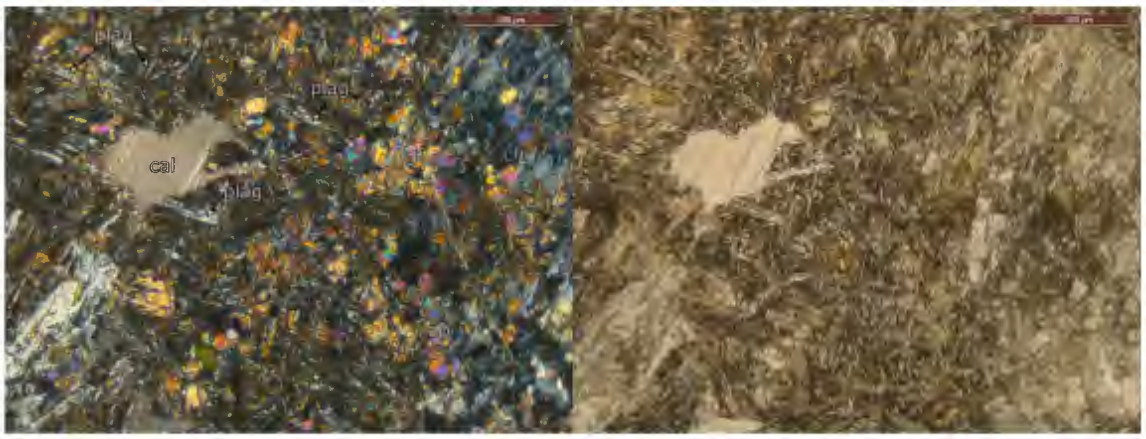

Figure C.34: Crossed-polars (left) and plane-polarised light (right) images of thin section PJG0058 showing chlorite, epidote and calcite alteration.

Hand Specimen Description

Fine-grained, dark bluish-grey rock with weathered surface. White, lustrous grains approximately 1 mm or finer observed throughout.

Thin Section Description

Fine-grained groundmass of interlocking laths of plagioclase, suggests this was rapidly cooled. Mafic mineral likely clinopyroxene, however difficult to determine due to chlorite alteration rimmed by coarse, crystalline epidote. Fractures are present, filled with alteration products. Alteration assemblage of calcite, chlorite and epidote. Anhedral, coarse-grained calcite grains (2 to 3 mm) are common.

Figure C.35: Koonenberry outcrop sample PJG0059.

C.0.14 PJG0059

This sample was supplied by the GSNSW.

Hand Specimen Description

Dark-grey, mostly fine-grained rock with a porphyritic texture. Coarser white grains (3 mm) stand out from the fine-grained blue-grey groundmass. Surface is weathered in some places.

Thin Section Description

Very strongly altered and difficult to determine mafic mineral phases. Relics of clinopyroxene phenocrysts throughout the slide, quite fine-grained (commonly 0.5 mm). Chlorite and epidote replace much of the groundmass, and interstitial quartz (mostly >0.5 mm) is common.

C.0.15 PJG0080

This sample and thin section were supplied by the GSNSW.

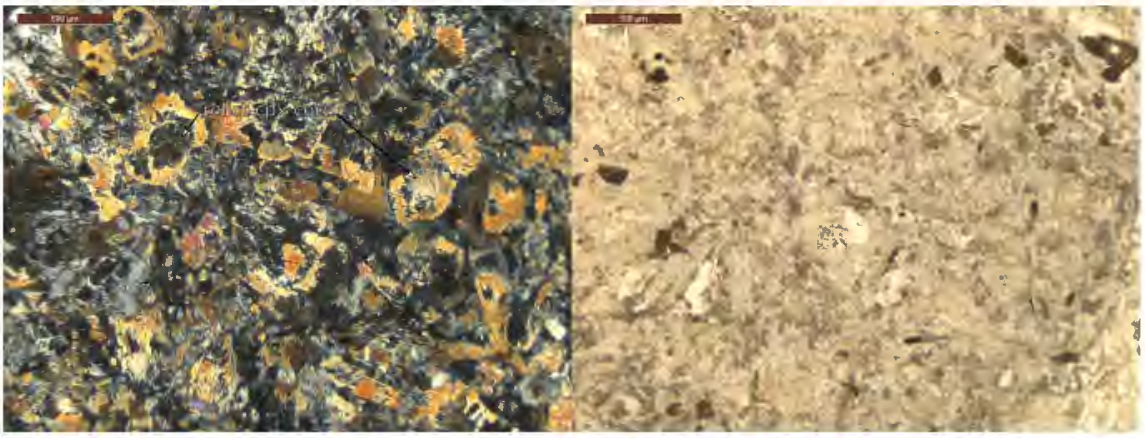

Figure C.36: Crossed-polars (left) and plane-polarised light (right) images of thin section PJG0059 showing relict clinopyroxene cores within groundmass largely replaced with chlorite.

Hand Specimen Description

Rock consists of mostly even sized, fine-medium grains (0.5 - 1 mm) with some slightly larger phenocrysts up to approximately 3 mm. Grains do not appear oriented. Phenocrysts are usually clear with a lustrous appearance and are tabular shaped, likely plagioclase. Finer grains consist of black, shiny grains and grey, dull grains. Leucocratic pod of dark pink-grey appearance, consisting of shiny grains throughout as well as dull creamy-white grains. Felsic material is aplite like.

Thin Section Description

Plagioclase phenocrysts are quite altered and occasionally exhibit zoning, ranging from coarse laths (up to 3 mm) to finer grained interlocking grains. Clinopyroxene phenocrysts are commonly altered to green hornblende and vary in grainsize from 0.5 to 1.5 mm. Quartz shows undulose extinction and form optically continuous grains surrounding plagioclase.

The leucocratic pod is composed of mostly quartz and myrmekite with fine clusters of chlorite and calcite as well as coarser grains from the host rock included along

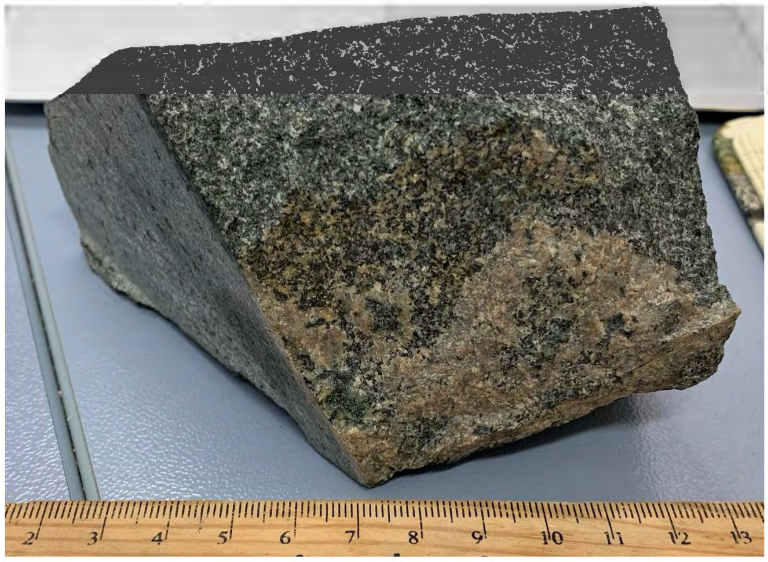

Figure C.37: Koonenberry outcrop sample PJG0080.

the boundary. Fine zircons are present within this pod as well as apatite.

C.0.16 PJG0082

This sample and thin section were supplied by the GSNSW.

Hand Specimen Description

Similar appearance to PJG0080, however much coarser-grained. Coarse creamy-white grains range from 2 mm up to 5 mm grainsize.

Thin Section Description

Very coarse-grained, resembling gabbro rather than dolerite. Mafic minerals include coarse-grained clinopyroxene phenocrysts (mostly 2.5 to 5mm) that have been variably altered, opaques, hornblende, as well as plagioclase which is extensively altered. Seconday epidote and actinolite is present, as well as secondary fine-grained white mica.

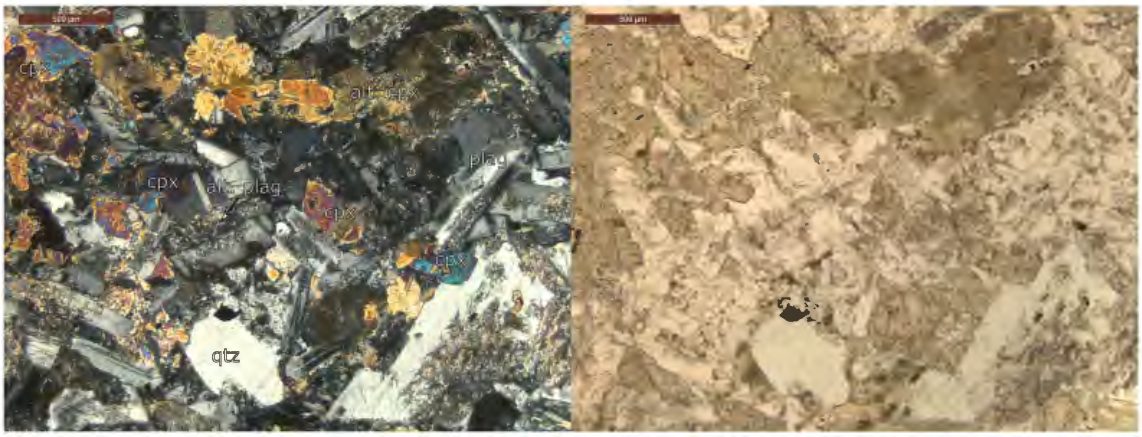

Figure C.38: Crossed-polars (left) and plane-polarised light (right) images of thin section PJG0080 showing altered plagioclase and clinopyroxene grains.

Figure C.39: Koonenberry outcrop sample PJG0082.

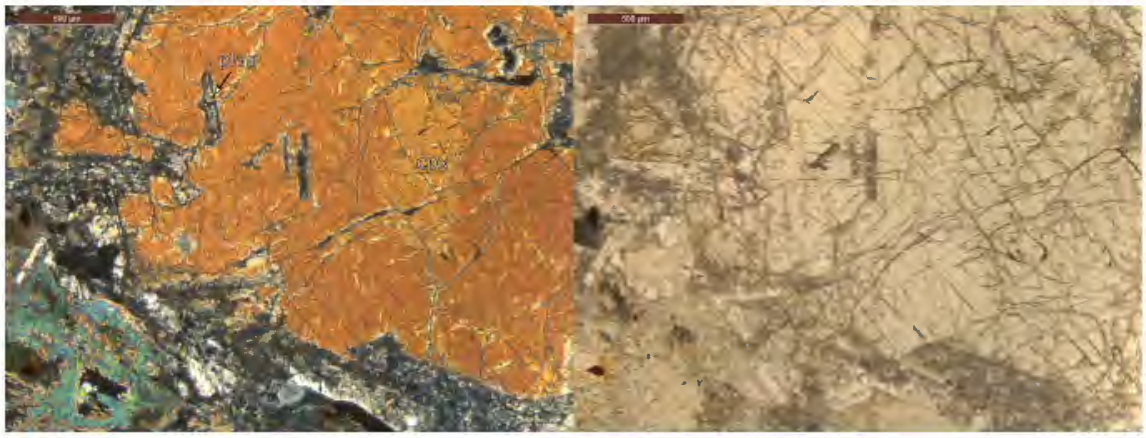

Figure C.40: Crossed-polars (left) and plane-polarised light (right) images of thin section PJG0082 showing coarse-grained clinopyroxene phenocryst enclosing plagioclase laths.

C.0.17 DD89GR05 - 83.5 m

This sample was supplied by the GSNSW.

Core Description

This core sample has a layered appearance of fine-grained black layers with lighter greenish-blue layers. Layering varies in width and is not consistent. Alteration is present, both gold and green in colour.

Thin Section Description

This rock is strongly deformed with metamorphic minerals defining deformation fabrics. There is a distinct layering present defined by opaque minerals, chlorite, quartz and others. Calcite and quartz veining cross-cuts the layering. Kinematic shear zones are also observed. The flow layering indicates this rock is not fragmental and tuffaceous, and was once a mafic rock that has now been metamorphosed. Mafic minerals have largely been replaced by low greenschist facies minerals.

Figure C.41: Core sample DD89GR05-83.5 from Koonenberry drill hole DD89GR05.

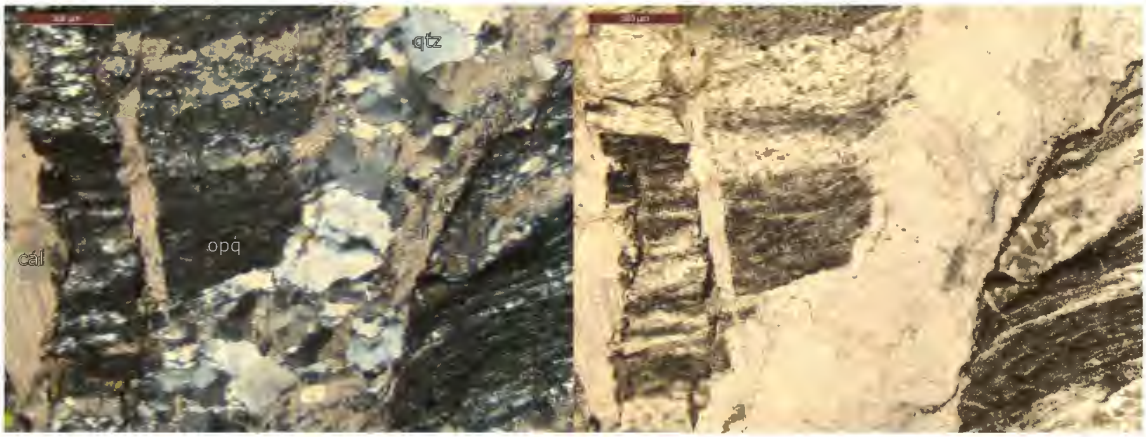

Figure C.42: Crossed-polars (left) and plane-polarised light (right) images of thin section DD89GR05-83.5 showing chlorite and quartz veining cross-cutting the layering defined by opaques.

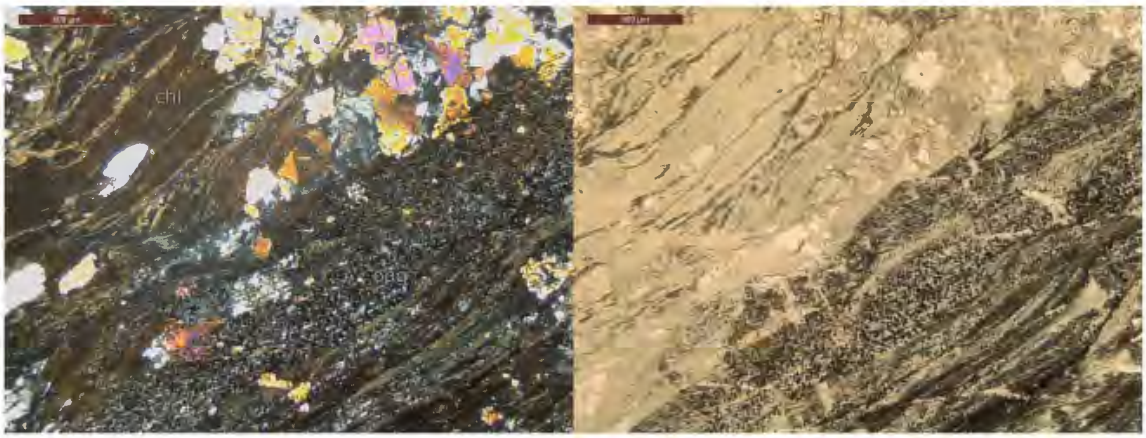

Figure C.43: Crossed-polars (left) and plane-polarised light (right) images of thin section DD89GR05-83.5 showing layering defined by opaques and chlorite.

C.0.18 DD89GR05 - 95 m

This sample was supplied by the GSNSW.

Core Description

Massive, aphanitic texture with a large vein (2 cm thick). Alteration present along contact between vein and host rock appearing dark brown-red in colour, and alteration throughout rock appearing green in colour, possibly along fractures or fine veins.

Thin Section Description

The large vein observed in this core sample is composed of mostly quartz and calcite with chlorite alteration along the edge of the vein. There is also another alteration mineral along the edge of the vein, appearing red-brown in PPL and fine-grained. Shear strain is very well defined along the vein by the red-brown alteration mineral, and shows distinct S-C fabrics that are also observed throughout the host rock.

The host rock is fine-grained with primary plagioclase, opaques, secondary chlorite and fine-grained aggregates of epidote. Two fabrics are observed in the host rock at acute angles to each other, defined by fine-grained, low-grade metamorphic minerals. There appears to be a chloritised zone within the host rock, alongside the vein, that is peppered with opaques and epidote. Strong deformation and shear strain is observed throughout the host rock, indicated by the presence of two fabrics at acute angles, mostly defined by fine-grained, low-grade metamorphic minerals.

Figure C.44: Core sample DD89GR05-95 from Koonenberry drill hole DD89GR05.

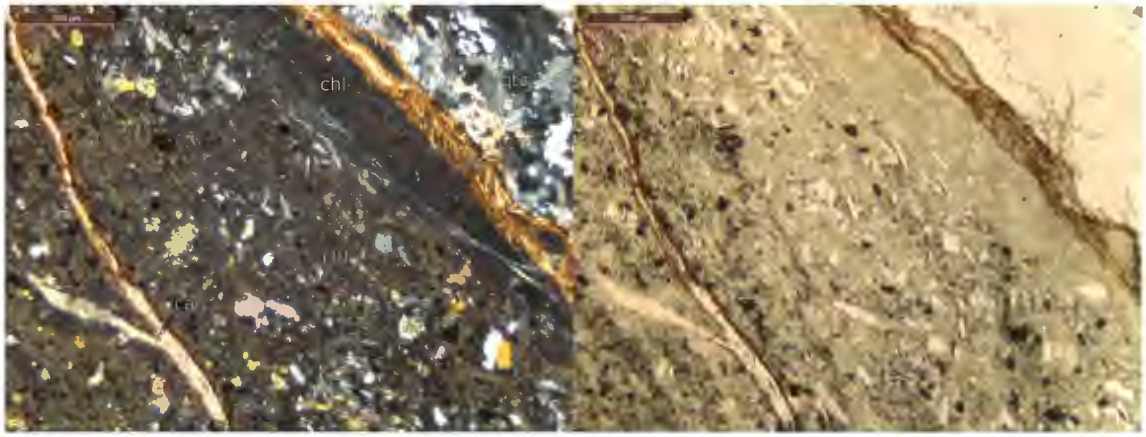

Figure C.45: Crossed-polars (left) and plane-polarised light (right) images of thin section DD89GR05-95 showing chlorite alteration and another alteration mineral (red-brown in colour) along the edge of the vein.

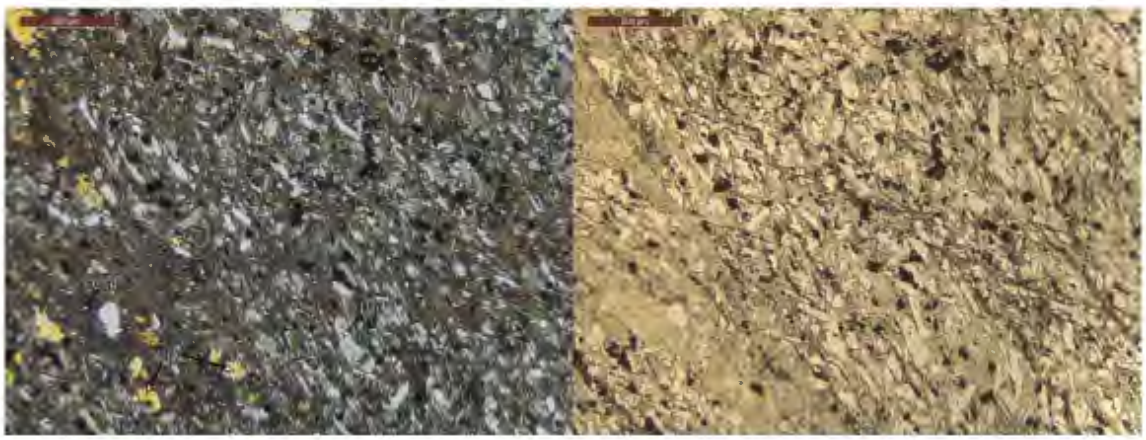

Figure C.46: Crossed-polars (left) and plane-polarised light (right) images of thin section DD89GR05-95 showing plagioclase, chlorite, epidote and opaques within the host rock.

Appendix D

Geochemistry Data

Table D.1: Raw geochemistry data for LLK samples analysed as part of this project.

		Sample ID	AUR101924	AUR101926	AUR101928	AUR101933	AUR101934	AUR101935
		Drill Hole	NBH004	NBH004	NBH004	NBH004	NBH007	NBH007
Element	Units	Detection						
SiO2	%	0.01	50.75	51.16	50.88	47.62	63	55.09
TiO2	%	0.01	1.59	1.63	1.59	1.55	0.55	0.74
Al2O3	%	0.01	14.64	15.59	14.48	14.32	15.67	14.2
Fe2O3	%	0.04	9.37	9.9	9.2	9.34	4.74	7.52
MnO	%	0.01	0.24	0.19	0.23	0.29	0.06	0.12
MgO	%	0.01	5.07	5.49	4.33	5.11	2.86	6.3
CaO	%	0.01	11.37	8.07	12.85	14.06	4.63	7.45
Na2O	%	0.01	4.75	5.73	4.66	4.2	4.24	3.8
K2O	%	0.01	0.26	0.39	0.25	0.24	2.07	1.53
P2O5	%	0.01	0.24	0.25	0.23	0.23	0.18	0.81
LOI	%	-5.1	1.5	1.4	1.1	2.8	1.7	2
Total	%		97.363991	97.43299	97.800991	96.049991	97.538995	96.841992
Sc	ppm	1	33	35	33	33	10	18

V	ppm	8	245	257	243	250	79	151
Ni	ppm	0.01	28	34	24	35	40	84
Ga	ppm	0.5	20.1	17.2	18.8	17.8	19.6	18.5
Rb	ppm	0.1	6.4	11.9	6.5	7.3	55.3	41.2
Sr	ppm	0.5	205.5	187.2	249.2	262	712.8	1107.3
Cs	ppm	0.1	0.5	1	1.3	1.6	1.3	0.9
Ba	ppm	1	154	134	211	289	813	666
W	ppm	0.5	1	0.8	0.8	1.1	0.25	0.25
Sn	ppm	1	3	3	3	3	1	2
Th	ppm	0.2	2.4	2.1	2.1	1.9	11.5	25.8
U	ppm	0.1	0.6	0.7	0.8	0.6	2.1	5.5
Nb	ppm	0.1	6	5.3	5.4	5.1	6.7	12
Ta	ppm	0.1	0.4	0.4	0.3	0.4	0.4	0.6
Zr	ppm	0.1	137.1	139.9	138.7	129.8	134.4	257.3
Hf	ppm	0.1	3.6	3.8	3.4	3.2	3.4	5.7
Y	ppm	0.1	31.4	32.4	30.9	30.3	11.7	31.1
La	ppm	0.1	12.8	13.6	15.8	14.1	36	116.8

Ce	ppm	0.1	28.7	30.8	31	26.6	59.6	221.3
Pr	ppm	0.02	4.08	4.21	4.27	3.92	6.79	28.3
Nd	ppm	0.3	19.3	18.8	18.7	17.9	25.9	109.4
Sm	ppm	0.05	4.84	4.73	4.66	4.61	4.04	19.42
Eu	ppm	0.02	1.61	1.54	1.6	1.56	1.17	4.2
Gd	ppm	0.05	5.58	5.43	5.48	5.07	3.28	13.84
Tb	ppm	0.01	0.91	1	0.94	0.89	0.44	1.6
Dy	ppm	0.05	5.6	6	5.76	5.17	2.23	7.06
Ho	ppm	0.02	1.21	1.2	1.2	1.14	0.43	1.11
Er	ppm	0.03	3.59	3.48	3.52	3.51	1.19	2.64
Tm	ppm	0.01	0.48	0.46	0.49	0.48	0.14	0.35
Yb	ppm	0.05	3.1	2.89	3.02	2.96	1.02	2.08
Lu	ppm	0.01	0.47	0.48	0.46	0.45	0.16	0.28
Mo	ppm	0.1	0.7	0.8	1.2	2	0.3	0.3
Cu	ppm	0.1	39	19.6	44.4	40.4	17.5	36
Pb	ppm	0.1	20.1	16.5	29.4	33.9	6.8	7.7
Zn	ppm	1	155	160	150	211	53	73

As	ppm	1	0.5	0.5	0.5	0.5	0.5	0.5
Cd	ppm	0.1	0.5	0.3	0.6	0.5	0.05	0.1
Sb	ppm	0.1	0.4	0.2	0.6	0.3	0.05	0.2
Bi	ppm	0.1	0.3	0.2	0.3	0.2	0.05	0.1
Ag	ppm	0.1	0.2	0.05	0.1	0.2	0.05	0.05
Co	ppm	1	30.6	28.5	22	27.2	14.5	26.3
		Sample ID	AUR101936	AUR101937	AUR101938	AUR101939	AUR101940	AUR101942
		Drill Hole	NBH005	NBH005	NBH005	NBH005	NBH011	NBH011
Element	Units	Detection						
SiO2	%	0.01	62.4	46.08	47.04	45.19	55.21	54.14
TiO2	%	0.01	0.43	2.09	2.07	2.13	0.97	0.91
Al2O3	%	0.01	16.75	15.85	15.86	15.43	16.01	14.26
Fe2O3	%	0.04	5.39	11.84	11.75	11.53	9.71	8.39
MnO	%	0.01	0.06	0.17	0.18	0.17	0.12	0.15
MgO	%	0.01	2.22	7.61	6.54	6.11	5.28	6
CaO	%	0.01	2.32	5.4	7.49	11.68	5.85	8.81
Na2O	%	0.01	5.51	4.61	4.43	3.23	3.3	4.68

K2O	%	0.01	2.03	0.53	0.46	0.03	1.62	0.56
P2O5	%	0.01	0.3	0.36	0.32	0.3	0.28	0.32
LOI	%	-5.1	2.3	5.2	3.6	4	1.3	1.5
Total	%		96.875995	93.370988	94.982988	94.661988	97.43899	97.434992
Sc	ppm	1	7	27	28	29	27	26
V	ppm	8	60	259	258	272	224	208
Ni	ppm	0.01	24	61	72	61	138	150
Ga	ppm	0.5	19.6	21.1	21.9	21.1	20.6	13.3
Rb	ppm	0.1	57.8	12.2	9.6	1.3	75.4	15.2
Sr	ppm	0.5	637	366.4	415.1	146.9	526.6	546.2
Cs	ppm	0.1	2	0.8	0.6	0.9	4.9	0.3
Ba	ppm	1	820	366	510	31	565	276
W	ppm	0.5	1.1	0.6	0.25	0.5	1.1	1.1
Sn	ppm	1	2	2	2	2	2	3
Th	ppm	0.2	12.9	4.3	3.5	3.8	10.6	9.6
U	ppm	0.1	3	0.9	0.7	0.7	2.4	2.2
Nb	ppm	0.1	9.7	18.8	17.8	16.7	11.6	10.6

Ta	ppm	0.1	0.5	1.2	0.9	1.1	0.7	0.7
Zr	ppm	0.1	178.3	166	154.6	150.4	149.3	137.3
Hf	ppm	0.1	4.2	4	3.5	3.5	3.9	3.7
Y	ppm	0.1	20.1	31.7	27.5	26.7	19.2	19.2
La	ppm	0.1	47.6	27.2	23	21.9	32.9	28.1
Ce	ppm	0.1	79.5	51	45	44.3	58.5	53.5
Pr	ppm	0.02	8.96	6.52	5.73	5.67	7.33	6.97
Nd	ppm	0.3	30.9	26.3	22.7	22.7	29.2	25.7
Sm	ppm	0.05	5.26	5.68	5.52	4.83	5.31	5.35
Eu	ppm	0.02	1.32	1.91	1.76	1.66	1.32	1.35
Gd	ppm	0.05	4.2	6.05	5.7	5.03	4.52	4.44
Tb	ppm	0.01	0.6	1	0.88	0.85	0.6	0.72
Dy	ppm	0.05	3.19	5.65	5.04	4.88	3.57	3.69
Ho	ppm	0.02	0.64	1.16	1.01	0.98	0.71	0.74
Er	ppm	0.03	1.88	3.05	2.95	2.96	2.17	2.12
Tm	ppm	0.01	0.27	0.45	0.42	0.35	0.3	0.29
Yb	ppm	0.05	1.86	2.79	2.63	2.41	1.87	1.71

Lu	ppm	0.01	0.3	0.43	0.44	0.41	0.28	0.29
Mo	ppm	0.1	1	0.4	0.4	0.8	0.5	0.9
Cu	ppm	0.1	8.8	46.3	29.6	43.1	11.7	3.9
Pb	ppm	0.1	13.9	4.1	4.1	4.2	4.9	5.4
Zn	ppm	1	66	105	88	92	42	44
As	ppm	1	0.5	0.5	0.5	0.5	1	3
Cd	ppm	0.1	0.2	0.1	0.05	0.4	0.05	0.05
Sb	ppm	0.1	0.3	0.05	0.05	0.3	0.2	1.1
Bi	ppm	0.1	0.2	0.05	0.05	0.05	0.05	0.05
Ag	ppm	0.1	0.1	0.1	0.1	0.05	0.05	0.05
Co	ppm	1	29.4	36.9	37.7	35.2	38	33.1

		Sample ID	AUR101943	AUR101944	AUR101945	AUR101946	AUR101947	AUR101949
		Drill Hole	NBH011	NBH011	NBH011	NBH010	NBH009	NBH009
Element	Units	Detection						
SiO2	%	0.01	55.81	51.64	49.13	68.69	47.41	48.69
TiO2	%	0.01	1.1	0.91	1.8	0.4	1.8	1.65
Al2O3	%	0.01	18.48	14.84	14.83	14.55	13.51	14.46

Fe2O3	%	0.04	8.07	10.49	12.17	3.88	15.88	13.76
MnO	%	0.01	0.04	0.13	0.19	0.09	0.26	0.24
MgO	%	0.01	2.26	7.17	6.46	1.43	6.84	6.77
CaO	%	0.01	4.37	7.14	10.02	2.89	10.98	9.46
Na2O	%	0.01	4.15	4.56	3.29	3.12	1.94	2.33
K2O	%	0.01	3.95	0.87	0.56	3.42	0.54	0.51
P2O5	%	0.01	0.46	0.24	0.24	0.11	0.15	0.23
LOI	%	-5.1	0.9	1.7	1.1	1.2	0.5	1.7
Total	%		97.888992	97.01499	97.497988	98.195996	97.729984	96.743986
Sc	ppm	1	17	35	40	7	48	39
V	ppm	8	228	212	297	69	360	324
Ni	ppm	0.01	32	125	30	0.005	26	47
Ga	ppm	0.5	22.2	14.9	20.5	15.9	19.1	18.2
Rb	ppm	0.1	112.9	29.2	24.5	147.3	24.7	19.5
Sr	ppm	0.5	614.4	537.4	313.5	346	215.1	281.4
Cs	ppm	0.1	2.8	0.5	2.1	7	4.4	6.6
Ba	ppm	1	1632	321	177	518	83	121

W	ppm	0.5	1.4	1	0.25	0.25	0.25	0.25
Sn	ppm	1	3	3	2	2	2	2
Th	ppm	0.2	13.4	7.3	1.8	19.9	1	1.6
U	ppm	0.1	2.8	1.2	0.4	2.4	0.2	0.3
Nb	ppm	0.1	15.3	9.1	4.5	6.3	2.8	4.7
Ta	ppm	0.1	1	0.6	0.3	0.6	0.2	0.4
Zr	ppm	0.1	199.7	111.2	133.4	139.1	87.4	110.3
Hf	ppm	0.1	4.9	3	3.6	3.8	2.4	2.8
Y	ppm	0.1	22.9	17.4	32.2	14.7	33.3	26.1
La	ppm	0.1	44	25.4	9.9	32.4	5.5	11
Ce	ppm	0.1	81.8	54	25.1	51.1	12.8	22.8
Pr	ppm	0.02	9.89	6.51	3.59	5.82	2.1	3.16
Nd	ppm	0.3	36.5	23.6	17.5	19.8	10.2	14.1
Sm	ppm	0.05	7.25	4.9	4.63	3.55	3.31	3.55
Eu	ppm	0.02	1.9	1.34	1.58	0.8	1.41	1.19
Gd	ppm	0.05	5.33	4.11	5.74	2.99	4.92	4.35
Tb	ppm	0.01	0.79	0.64	0.99	0.5	0.96	0.79

Dy	ppm	0.05	4.12	3.5	5.78	2.61	5.8	4.35
Ho	ppm	0.02	0.92	0.61	1.3	0.53	1.2	1.01
Er	ppm	0.03	2.25	1.95	3.76	1.66	3.49	2.92
Tm	ppm	0.01	0.35	0.26	0.52	0.24	0.51	0.38
Yb	ppm	0.05	2.28	1.69	3.24	1.63	3.68	2.82
Lu	ppm	0.01	0.3	0.24	0.49	0.25	0.58	0.45
Mo	ppm	0.1	0.6	0.3	0.2	0.05	0.05	0.3
Cu	ppm	0.1	3.8	5.2	66.3	2.7	50.3	56.8
Pb	ppm	0.1	5.1	2.5	7.1	10.4	4	6.3
Zn	ppm	1	21	58	92	43	117	128
As	ppm	1	2	1	0.5	0.5	0.5	0.5
Cd	ppm	0.1	0.1	0.05	0.05	0.05	0.2	0.05
Sb	ppm	0.1	0.4	0.5	0.2	0.2	0.7	0.4
Bi	ppm	0.1	0.05	0.05	0.05	0.05	0.05	0.05
Ag	ppm	0.1	0.05	0.05	0.2	0.05	0.05	0.05
Co	ppm	1	24.7	32.5	41.8	9.1	49.8	39.1
		Sample ID	AUR101950	AUR101951	AUR101953	AUR101954	AUR101955	AUR101956

Element	Units	Drill Hole Detection	NBH009	NBH009	NBH012	NBH012	EHK1	EHK2
SiO2	%	0.01	45.86	48.28	49.74	48.44	56.52	56.76
TiO2	%	0.01	1.4	1.77	2.91	1.01	0.79	0.94
Al2O3	%	0.01	14.91	13.76	14.2	15.83	15.32	16.08
Fe2O3	%	0.04	12.81	15.4	14.3	10.23	7.12	7.67
MnO	%	0.01	0.2	0.25	0.39	0.17	0.12	0.11
MgO	%	0.01	9.09	6.43	4.2	7.5	5.65	4.71
CaO	%	0.01	10.2	9.96	7.55	9.66	6.98	6.52
Na2O	%	0.01	2.21	2	3.61	2.67	3.66	3.76
K2O	%	0.01	0.96	0.59	0.72	0.79	2.29	1.84
P2O5	%	0.01	0.16	0.15	0.45	0.34	0.36	0.21
LOI	%	-5.1	1.8	1.2	1.6	3	0.8	1.1
Total	%		96.552987	97.055985	96.642986	95.67399	98.136993	97.845992
Sc	ppm	1	39	45	38	34	18	19
V	ppm	8	406	366	413	301	145	157
Ni	ppm	0.01	92	31	18	125	76	24

Ga	ppm	0.5	18.5	22.4	24.9	18.6	21	21
Rb	ppm	0.1	42.3	30.1	25.5	23.3	63.3	50.5
Sr	ppm	0.5	357.4	264.4	339	575.2	961.7	883.5
Cs	ppm	0.1	5.3	8.5	2	1.8	1.7	1.4
Ba	ppm	1	142	129	225	454	818	516
W	ppm	0.5	0.25	1.1	0.9	1.1	0.5	0.25
Sn	ppm	1	2	3	3	2	2	2
Th	ppm	0.2	1.5	2.5	4	8.3	11.3	9.8
U	ppm	0.1	0.4	0.8	0.9	1.7	3.3	1.9
Nb	ppm	0.1	3.9	5.4	12.7	13.5	7.8	7.2
Ta	ppm	0.1	0.2	0.3	0.9	0.6	0.4	0.7
Zr	ppm	0.1	79.1	83.7	276.1	115.7	160.3	104.9
Hf	ppm	0.1	2.8	2.5	6.6	3.1	3.8	2.9
Y	ppm	0.1	30.9	30.7	57.5	18.4	22.3	18.3
La	ppm	0.1	10.6	11	27.2	33.2	53.7	37.1
Ce	ppm	0.1	28.2	21.8	58.2	62.8	99.6	66.3
Pr	ppm	0.02	4.55	3.4	8.22	7.17	12.13	7.95

Nd	ppm	0.3	21.3	15.5	35.8	27.7	46.7	28.8
Sm	ppm	0.05	5.17	4.44	8.7	4.66	8.57	5.36
Eu	ppm	0.02	1.53	1.47	2.86	1.4	2.39	1.39
Gd	ppm	0.05	5.48	5.16	10.34	4.33	7.34	4.5
Tb	ppm	0.01	1	0.94	1.74	0.65	0.88	0.66
Dy	ppm	0.05	5.17	5.69	9.6	3.61	4.27	3.72
Ho	ppm	0.02	1.14	1.32	2.02	0.78	0.79	0.72
Er	ppm	0.03	3.37	3.93	6.39	1.99	2.05	2
Tm	ppm	0.01	0.47	0.52	0.89	0.29	0.26	0.29
Yb	ppm	0.05	3.03	3.56	5.91	1.88	1.85	1.65
Lu	ppm	0.01	0.46	0.51	0.91	0.29	0.27	0.26
Mo	ppm	0.1	0.05	0.1	0.8	0.6	1.4	0.6
Cu	ppm	0.1	64.8	73.3	156.2	544.6	87.8	22.5
Pb	ppm	0.1	3.3	5.5	5.7	14.6	13.5	9.4
Zn	ppm	1	97	132	108	161	73	68
As	ppm	1	0.5	1	2	1	0.5	0.5
Cd	ppm	0.1	0.1	0.1	1	0.9	0.1	0.2

Sb	ppm	0.1	0.1	0.8	0.4	0.3	0.2	1.4
Bi	ppm	0.1	0.05	0.05	0.05	0.05	0.1	0.05
Ag	ppm	0.1	0.05	0.05	0.1	0.2	0.1	0.1
Co	ppm	1	45.6	56.2	47.1	37.7	28.6	21.8

		Sample ID	AUR101957	AUR101958	AUR101959	AUR101961	AUR101962	AUR101963
		Drill Hole	EHK3	EHK3	EHK3	EHK3	EHK3	EHK3
Element	Units	Detection						
SiO2	%	0.01	49.46	60.14	48.48	60.27	47.1	65.9
TiO2	%	0.01	2.5	0.62	2.18	0.62	1.48	0.37
Al2O3	%	0.01	16.49	16.15	15.71	16.21	17	16.7
Fe2O3	%	0.04	11.45	4.93	11.4	5.49	10.46	3.5
MnO	%	0.01	0.21	0.06	0.17	0.05	0.18	0.04
MgO	%	0.01	4.57	2.7	6.93	2.79	7.65	1.4
CaO	%	0.01	9.06	5.31	9.79	4.86	11.78	3.49
Na2O	%	0.01	3.93	5.65	2.97	5.62	2.29	4.96
K2O	%	0.01	1.03	0.36	0.97	0.8	0.26	2.15
P2O5	%	0.01	0.45	0.27	0.36	0.26	0.25	0.18

LOI	%	-5.1	0.6	3.6	0.8	2.8	1.3	1
Total	%		98.018989	95.706995	97.850989	96.429995	97.42999	98.344996
Sc	ppm	1	36	9	39	9	25	4
V	ppm	8	318	89	305	92	201	43
Ni	ppm	0.01	27	28	52	26	76	9
Ga	ppm	0.5	25	17.7	20.2	17.3	21.3	18.1
Rb	ppm	0.1	31.3	10.4	30.9	25.8	9.5	51.4
Sr	ppm	0.5	425.4	736.2	393.9	758.9	662.7	810.8
Cs	ppm	0.1	1.6	0.6	1.4	1	1.5	1.2
Ba	ppm	1	250	306	215	416	210	956
W	ppm	0.5	0.9	0.9	0.9	0.6	0.7	0.7
Sn	ppm	1	2	2	2	2	2	1
Th	ppm	0.2	5.5	10.7	4.6	11.1	2.9	13.5
U	ppm	0.1	1.1	2.2	1.1	3.7	0.6	3.7
Nb	ppm	0.1	20.7	11.8	18.1	12.3	12	9.7
Ta	ppm	0.1	1	0.7	0.9	0.5	0.8	0.7
Zr	ppm	0.1	213.1	166.3	173.4	162.2	113.3	189.6

Hf	ppm	0.1	5.2	4	4.6	4	2.7	4.5
Y	ppm	0.1	41.6	15.2	34.1	16.4	21.9	11.5
La	ppm	0.1	32.7	53.4	25.9	49.2	18.7	49.8
Ce	ppm	0.1	62.2	82.7	47.5	84.9	34.8	76.6
Pr	ppm	0.02	7.92	9.26	6.44	9.49	4.24	7.96
Nd	ppm	0.3	34.4	31	28.1	34	16.3	26.6
Sm	ppm	0.05	7.26	5.15	5.98	4.97	3.78	3.7
Eu	ppm	0.02	2.42	1.24	2.13	1.53	1.31	1.07
Gd	ppm	0.05	7.79	4.03	6.89	4.17	3.96	3.09
Tb	ppm	0.01	1.31	0.59	1.15	0.6	0.72	0.43
Dy	ppm	0.05	7.54	2.62	6.24	3.09	4.1	2.15
Ho	ppm	0.02	1.57	0.53	1.29	0.56	0.83	0.38
Er	ppm	0.03	4.47	1.41	4.01	1.56	2.4	1.17
Tm	ppm	0.01	0.6	0.21	0.55	0.22	0.32	0.2
Yb	ppm	0.05	4.2	1.59	3.68	1.45	2.16	1.3
Lu	ppm	0.01	0.65	0.22	0.51	0.22	0.36	0.21
Mo	ppm	0.1	0.8	0.2	0.5	1.1	1	1.6

Cu	ppm	0.1	33	7.2	18.1	1.7	29.8	27.9
Pb	ppm	0.1	7.4	9.6	4.6	8.7	6.2	10.7
Zn	ppm	1	73	42	85	40	75	33
As	ppm	1	0.5	0.5	0.5	0.5	0.5	0.5
Cd	ppm	0.1	0.2	0.05	0.2	0.05	0.2	0.1
Sb	ppm	0.1	0.5	0.6	2	0.3	0.9	0.1
Bi	ppm	0.1	0.05	0.05	0.05	0.05	0.05	0.05
Ag	ppm	0.1	0.1	0.05	0.05	0.05	0.05	0.05
Co	ppm	1	41.1	7.9	32.6	6.1	36.5	7.4

		Sample ID	AUR101964	AUR101965	AUR101966	AUR101967	AUR101968	AUR101988
		Drill Hole	EHK3	EHK3	EHK3	EHK3	EHK3	DD96WA3
Element	Units	Detection						
SiO2	%	0.01	45.01	45.09	48.19	48.25	49.06	56.16
TiO2	%	0.01	1.49	1.34	1.06	1.96	1.41	0.97
Al2O3	%	0.01	12.49	14.62	13.04	16.36	16.89	16.79
Fe2O3	%	0.04	14.06	12.45	11.65	11.87	9.78	5.98
MnO	%	0.01	0.2	0.18	0.21	0.17	0.15	0.09

MgO	%	0.01	13.39	11.93	10.32	7.1	7.36	3.47
CaO	%	0.01	7.77	8.28	10.98	8.63	9.07	7.02
Na2O	%	0.01	1.3	1.89	2.09	3.29	2.93	6.19
K2O	%	0.01	0.67	0.6	0.09	0.9	1.27	1.16
P2O5	%	0.01	0.23	0.21	0.15	0.34	0.39	0.43
LOI	%	-5.1	3.2	3	1.9	0.8	1.3	1.4
Total	%		95.258986	95.385988	96.646988	97.698988	97.34799	97.669994
Sc	ppm	1	27	23	18	27	23	15
V	ppm	8	219	189	153	247	188	179
Ni	ppm	0.01	211	182	136	89	85	24
Ga	ppm	0.5	15.4	15.3	14.3	21	19.2	19.8
Rb	ppm	0.1	26	33	2.4	23.7	27.7	56.4
Sr	ppm	0.5	184.6	369	440	411.5	514.7	998.9
Cs	ppm	0.1	3.3	3.3	0.2	2.8	2.6	0.7
Ba	ppm	1	152	163	105	233	317	311
W	ppm	0.5	0.25	0.5	36.9	0.7	0.8	2
Sn	ppm	1	1	0.5	1	1	1	3

Th	ppm	0.2	3	2.8	2	4.6	6.1	28.9
U	ppm	0.1	0.6	0.5	0.4	1.1	1.3	6.4
Nb	ppm	0.1	11.2	10.5	8.9	20.2	23.3	37.3
Ta	ppm	0.1	0.7	0.6	0.5	1.2	1.2	1.9
Zr	ppm	0.1	112.3	102.2	81.3	186	163.6	281.3
Hf	ppm	0.1	2.6	2.4	2	4.6	3.7	6.7
Y	ppm	0.1	21.6	19.3	15	32.2	20.8	19.1
La	ppm	0.1	17.4	15.3	12.2	25.5	31.9	65
Ce	ppm	0.1	31.5	31	23.4	49.6	57.8	113.3
Pr	ppm	0.02	4.07	3.95	2.96	6.52	7.12	13.77
Nd	ppm	0.3	16.1	16.6	11.9	26.7	27.4	51.1
Sm	ppm	0.05	3.56	3.83	2.58	5.73	5.2	8.07
Eu	ppm	0.02	1.26	1.24	1.17	1.83	1.71	1.65
Gd	ppm	0.05	3.85	3.47	3.04	5.68	4.85	5.49
Tb	ppm	0.01	0.73	0.64	0.48	0.96	0.72	0.77
Dy	ppm	0.05	3.76	3.9	2.8	6.06	4.14	4.19
Ho	ppm	0.02	0.86	0.78	0.56	1.13	0.76	0.76

Er	ppm	0.03	2.37	2.06	1.54	3.24	2.3	2.01	
Tm	ppm	0.01	0.31	0.31	0.22	0.44	0.32	0.3	
Yb	ppm	0.05	2.22	1.88	1.45	2.95	1.91	1.91	
Lu	ppm	0.01	0.32	0.3	0.23	0.47	0.29	0.31	
Mo	ppm	0.1	0.4	0.7	0.3	0.8	0.4	1.4	
Cu	ppm	0.1	32.3	11.5	97.4	18.4	17.2	29	
Pb	ppm	0.1	3.2	2.9	3.2	3.4	4	12.5	
Zn	ppm	1	97	70	65	67	64	31	
As	ppm	1	0.5	3	3	2	2	5	
Cd	ppm	0.1	0.05	0.05	0.05	0.2	0.05	0.05	
Sb	ppm	0.1	0.6	0.5	0.3	0.5	0.6	1.1	
Bi	ppm	0.1	0.05	0.05	0.05	0.05	0.05	0.1	
Ag	ppm	0.1	0.05	0.05	0.05	0.05	0.05	0.05	
Co	ppm	1	69.8	61.3	54.7	40	40.4	17.2	
		Sample ID	AUR101990	AUR101992		VP004	VP006	VP010	VP013
		Drill Hole	DD96WA3	DD96WA3		EHK3	NBH004	NBH005	NBH012
Element	Units	Detection			Detection				

SiO2	%	0.01	55.12	50.12	0.03	50.02	50.93	69.12	50.15
TiO2	%	0.01	1.01	2.95	0.02	2.59	1.73	0.63	2.94
Al2O3	%	0.01	16.7	13.32	0.02	16.74	15.86	12.85	14.42
Fe2O3	%	0.04	7.72	14.21	0.02	10.97	8.53	5.94	13.59
MnO	%	0.01	0.13	0.28	0.02	0.18	0.25	0.04	0.22
MgO	%	0.01	3.47	3.91	0.02	3.85	4.91	2.44	4.17
CaO	%	0.01	5.94	7.22	0.02	9.02	10.64	0.43	7.54
Na2O	%	0.01	3.99	3.72	0.02	4.07	5.38	3.68	3.73
K2O	%	0.01	3.87	1.35	0.02	1.17	0.23	1.57	0.5
P2O5	%	0.01	0.41	1.05	0.03	0.48	0.25	0.19	0.48
LOI	%	-5.1	1.2	1.6	0.01	0.52	0.57	2.7	1.51
Total	%		97.594992	96.712986					
Sc	ppm	1	17	30	10	39	41	11	42
V	ppm	8	205	221	10	332	268	95	414
Ni	ppm	0.01	31	9	1	18	44	58	20
Ga	ppm	0.5	20.5	18.7	0.1	22.1	19.4	18.6	24.3
Rb	ppm	0.1	134.2	43.5	0.1	38.3	4.4	60.1	14.7

Sr	ppm	0.5	956	444.7	0.2	406.4	175.7	140.8	330.8
Cs	ppm	0.1	2.7	1.8	0.05	1.13	0.86	3.38	1.09
Ba	ppm	1	944	268	0.5	248.8	182.5	379.2	241.4
W	ppm	0.5	1.2	0.25	1	163	116	79	124
Sn	ppm	1	2	2	1	2	2	4	3
Th	ppm	0.2	29.3	5.9	0.05	5.04	2.02	12.45	3.92
U	ppm	0.1	6.7	1	0.05	0.87	0.49	1.89	0.8
Nb	ppm	0.1	41.3	14	0.1	22.1	5.8	12.5	12.9
Ta	ppm	0.1	2.2	0.9	0.1	1.5	0.4	1.2	0.8
Zr	ppm	0.1	332.1	253.3	1	193	138	165	262
Hf	ppm	0.1	7.4	5.6	0.1	5.1	3.6	4.4	6.6
Y	ppm	0.1	21.4	58.8	0.5	40.2	34.4	14.6	60.4
La	ppm	0.1	72.8	30.7	0.2	30.2	12.7	13.4	26
Ce	ppm	0.1	127.3	66.8	0.5	61.2	28.5	27	59.8
Pr	ppm	0.02	14.61	9.95	0.05	7.42	4	3.33	8
Nd	ppm	0.3	50.6	47.9	0.1	30.6	18.1	12.9	36
Sm	ppm	0.05	8.27	11.83	0.05	7.26	5	2.92	9.41

Eu	ppm	0.02	1.85	3.69	0.05	2.28	1.57	0.63	2.81
Gd	ppm	0.05	6.48	12.06	0.05	7.32	5.69	2.64	9.84
Tb	ppm	0.01	0.85	1.83	0.02	1.15	0.96	0.37	1.53
Dy	ppm	0.05	4.59	11.41	0.05	7.36	5.98	2.59	10.1
Ho	ppm	0.02	0.77	2.28	0.02	1.56	1.24	0.52	2.17
Er	ppm	0.03	2.16	6.34	0.05	4.25	3.47	1.53	6.08
Tm	ppm	0.01	0.31	0.85	0.05	0.62	0.5	0.24	0.86
Yb	ppm	0.05	2.26	5.31	0.05	3.65	3.14	1.66	5.36
Lu	ppm	0.01	0.32	0.85	0.02	0.55	0.48	0.25	0.78
Mo	ppm	0.1	2.3	1.3					
Cu	ppm	0.1	40.8	24.1					
Pb	ppm	0.1	20.9	7.7					
Zn	ppm	1	59	106					
As	ppm	1	2	4					
Cd	ppm	0.1	0.05	0.05					
Sb	ppm	0.1	0.3	0.4					
Bi	ppm	0.1	0.05	0.05					

Ag	ppm	0.1	0.05	0.05
Co	ppm	1	16.7	26.4

Table D.2: Raw geochemistry data for Koonenberry samples analysed as part of this project.

		Sample ID	PJG0080	PJG0082		PJG0058		PJG0059	DD89GR05
Element	Units	Detection			Detection		Detection		
Al2O3	%	0.2	14	15.9	0.02	14.5	0.02	14.71	14.55
As	ppm	0.6	1.7	1.2	5				
Ba	ppm	1.4	167	354	7	137	0.5	123.3	35.9
Be	ppm	2			0.02	0.23			
CaO	%	0.01	10	11.8	0.02	9.9	0.02	9.73	7.03
Ce	ppm	0.1	27.3	8.8	0.01	29.1	0.5	10.2	17.7
Cl	ppm	50	115	83					
Co	ppm	0.5	69.7	64	2	55			
Cr	ppm	3.5	142	424	6	55	20	160	107
Cs	ppm	0.2	0.36	0.93	0.1	0.1	0.05	0.2	1.36
Cu	ppm	1.5	57.7	58.9	1	75			
Dy	ppm	0.5	5.88	4.4	0.02	6.45	0.05	6.44	11.29
Er	ppm	0.1	3.73	2.83	0.05	3.78	0.05	4.26	6.99
Eu	ppm	0.1	1.27	0.94	0.02	1.78	0.05	1.27	2.34

F	ppm	50	328	192					
Fe2O3	%	0.04	11.5	10.5	0.02	11.9	0.02	12.55	19.54
FeO	%	0.01	6.85	6.76	0.2	3.7			
Ga	ppm	0.3	16.8	14.7	0.1	22	0.1	18.3	23.2
Gd	ppm	0.1	5.41	3.75	0.05	6.09	0.05	5.61	9.31
Ge	ppm	0.3	1.57	1.47	0.2	1.2			
Hf	ppm	0.2	3.35	1.85	0.01	7.47	0.1	2.8	5.2
Ho	ppm	0.1	1.22	0.92	0.02	1.32	0.02	1.46	2.52
K2O	%	0.05	0.64	0.54	0.02	0.36	0.02	0.59	0.33
La	ppm	0.2	11.8	3.47	0.01	12.5	0.2	3.7	5.5
Li					0.1	7			
LOI	%	0.001	2.21	2.52	0	2.66	0.01	2.83	3.9
Lu	ppm	1			0.02	0.75	0.02	0.6	0.99
MgO	%	0.05	6.24	8.29	0.05	5.2	0.02	6.27	6.23
Na2O	%	0.05	2.54	2.21	0.05	3.88	0.02	2.36	2.64
Nb	ppm	0.2	4.93	1.28	0.03	8.77	0.1	2	3.1
Nd	ppm	0.2	16.1	7.67	0.02	18	0.1	9.8	18.1

Ni	ppm	8	45.1	90	2	43	1	61	55
P2O5	%	0.01	0.16	0.09	0.02	0.27	0.03	0.13	0.21
Pb		0.5	4.11	3.56	0.05	1.18			
Pr	ppm	0.1	3.64	1.49	0.05	3.7	0.05	1.82	3.24
Rb	ppm	1	18.8	22.3	0.1	5.7	0.1	14.9	10.5
S	%						0.01	0.03	0.04
Sb		0.9			0.5	0.9			
Sc	ppm	0.5	41.2	40.1	0.2	50.5	10	44	58
Se		10	10		4				
SiO2	%	0.1	52.6	48.5	0.02	48.9	0.03	48.14	42.23
Sm	ppm	1	4.3	2.6	0.02	5.12	0.05	3.88	6.89
Sn	ppm	0.5	1.6	0.7	0.6	2	1	0.5	2
SO3		0.1	0.2						
Sr	ppm	1	141	145	0.4	220	0.2	108.4	147.3
Ta	ppm	0.1	0.37		0.03	0.73	0.1	0.2	0.2
Tb	ppm	0.1	0.91	0.64	0.02	1.37	0.02	0.95	1.66
Th	ppm	0.1	3.61	0.5	0.001	0.89	0.05	0.73	0.22

TiO2	%	0.01	1.29	1.07	0.02	2.21	0.02	1.57	3.04
Tm	ppm				0.05	0.47	0.05	0.62	1.03
U	ppm	0.1	0.56	0.1	0.5		0.05	0.2	0.18
V	ppm	1	266	251	5	349	10	319	579
W	ppm				0.1	68.8	1	86	19
Y	ppm	0.2	33.2	24.8	0.02	44.1	0.5	38.5	65.1
Yb	ppm	0.2	3.61	2.62	0.05	3.84	0.05	3.92	6.55
Zn	ppm	4	81.3	84.6	2	104			
Zr	ppm	0.5	121	61.8	0.1	268	1	81	174

Appendix E

Geochronology Data

Table E.1: Raw zircon geochronology data from session one.

Sample	$^{207}Pb/^{235}U$	$\pm 2\sigma$	$^{207}Pb/^{206}Pb$	$\pm 2\sigma$	$^{206}Pb/^{238}U$	$\pm 2\sigma$	Date(Ma)	$\pm 2\sigma$(Ma)	Conc(%)
VP008-01 - 1	0.5312	0.0095	0.0564	0.0003	0.0683	0.0011	426.0	6.5	90.9
VP008-03 - 1	0.5745	0.0101	0.0620	0.0009	0.0673	0.0006	419.6	3.5	62.7
VP008-05 - 1	0.9927	0.1147	0.0751	0.0429	0.0713	0.0047	448.1	11.4	27.6
VP008-06 - 1	0.5434	0.0220	0.0565	0.0004	0.0699	0.0028	435.1	16.7	92.6
VP008-07 - 1	0.5370	0.0094	0.0561	0.0003	0.0696	0.0011	433.5	6.6	95.3
VP008-09 - 1	0.6533	0.0112	0.0582	0.0003	0.0813	0.0013	503.6	7.7	93.8
VP008-10 - 1	0.8399	0.0198	0.1004	0.0034	0.0613	0.0012	383.3	7.1	23.8

VP008-11 - 1	0.6877	0.0090	0.0644	0.0005	0.0775	0.0008	481.1	4.6	64.0
VP008-12 - 1	0.5320	0.0337	0.0560	0.0003	0.0685	0.0013	426.9	7.7	94.5
VP008-14 - 1	0.5453	0.0123	0.0588	0.0006	0.0673	0.0017	420.0	10.3	75.4
VP008-15 - 1	0.5539	0.0163	0.0589	0.0011	0.0681	0.0031	431.1	13.0	80.3
VP008-17 - 1	0.5262	0.0074	0.0561	0.0004	0.0680	0.0007	423.9	4.1	92.4
VP008-18 - 1	0.8397	0.0197	0.0775	0.0027	0.0800	0.0017	496.1	10.0	44.9
VP008-20 - 1	0.5455	0.0086	0.0635	0.0006	0.0624	0.0009	389.9	5.7	54.1
VP008-21 - 1	0.5364	0.0385	0.0608	0.0095	0.0678	0.0027	429.7	7.9	95.2

VP008-22 - 1	0.5434	0.0084	0.0567	0.0005	0.0694	0.0007	432.5	3.9	90.8
VP008-23 - 1	0.5342	0.0083	0.0565	0.0005	0.0685	0.0007	427.1	4.4	90.5
VP008-24 - 1	0.5228	0.0076	0.0558	0.0004	0.0680	0.0008	423.8	4.9	95.6
VP008-26 - 1	0.6144	0.0207	0.0631	0.0012	0.0704	0.0017	438.6	9.9	61.8
VP008-28 - 1	0.5340	0.0174	0.0561	0.0005	0.0681	0.0014	424.6	8.5	92.5
VP008-29 - 1	0.5360	0.0110	0.0631	0.0008	0.0621	0.0013	388.2	7.8	54.4
VP008-30 - 1	0.5688	0.0131	0.0611	0.0014	0.0684	0.0020	426.5	11.9	67.6
VP008-31 - 1	0.5298	0.0086	0.0562	0.0004	0.0685	0.0011	427.1	6.4	92.7

VP008-33 - 1	0.5288	0.0092	0.0560	0.0004	0.0683	0.0007	425.6	4.3	94.8
VP008-35 - 1	0.6512	0.0085	0.0582	0.0004	0.0812	0.0008	503.1	4.6	93.8
VP012M-01-1	0.7600	0.0887	0.0643	0.0038	0.0807	0.0025	499.7	14.5	65.8
VP012M-02 - 1	0.6803	0.0380	0.0641	0.0025	0.0764	0.0021	474.2	12.4	60.3
VP012M-03 - 1	0.6470	0.0168	0.0605	0.0010	0.0770	0.0012	478.1	7.1	77.7
VP012M-04 - 1	0.6969	0.0190	0.0665	0.0011	0.0761	0.0011	472.6	6.8	57.3
VP012M-05 - 1	0.5711	0.1099	0.0601	0.0067	0.0787	0.0014	488.1	8.1	90.0
VP012M-06 - 1	0.6561	0.0098	0.0623	0.0006	0.0767	0.0012	476.1	6.9	69.9

VP012M-07 - 1	0.6472	0.0104	0.0608	0.0007	0.0773	0.0014	480.0	8.4	76.3
VP012M-08 - 1	0.6190	0.0118	0.0606	0.0006	0.0737	0.0011	458.2	6.4	73.7
VP012M-09 - 1	0.6296	0.0095	0.0582	0.0006	0.0783	0.0007	486.2	4.3	91.0
VP012M-10 - 1	0.6573	0.0135	0.0616	0.0010	0.0775	0.0009	481.1	5.1	73.5
VP012M-11 - 1	0.6208	0.0132	0.0609	0.0008	0.0740	0.0014	460.4	8.3	73.2
VP012M-12 - 1	0.6415	0.0122	0.0585	0.0009	0.0798	0.0008	495.1	4.8	90.7
VP012M-13 - 1	0.6757	0.0197	0.0625	0.0016	0.0781	0.0008	484.7	5.0	71.4
VP012M-14 - 1	0.6789	0.0236	0.0652	0.0015	0.0755	0.0012	469.0	7.2	61.1

VP012M-16 - 1	0.6297	0.0111	0.0578	0.0008	0.0790	0.0008	490.0	4.7	94.9
VP012M-17 - 1	0.6244	0.0117	0.0571	0.0008	0.0792	0.0009	491.6	5.1	100.8
VP012M-18 - 1	0.6377	0.0193	0.0588	0.0011	0.0786	0.0015	487.7	9.2	91.8
VP012M-21 - 1	0.6406	0.0124	0.0582	0.0004	0.0795	0.0011	492.8	6.3	92.3
VP012M-24 - 1	0.6334	0.0112	0.0585	0.0009	0.0788	0.0008	489.1	4.8	90.2
VP012M-25 - 1	0.6330	0.0107	0.0582	0.0006	0.0790	0.0009	490.0	5.4	92.0
VP012M-26 - 1	0.6317	0.0077	0.0579	0.0003	0.0790	0.0007	490.2	4.0	93.2
VP012M-28 - 1	0.6260	0.0105	0.0577	0.0007	0.0784	0.0008	486.8	4.6	94.5

VP012M-29 - 1	0.6636	0.0128	0.0618	0.0009	0.0780	0.0009	484.3	5.5	73.1
VP012M-30 - 1	0.6347	0.0109	0.0580	0.0007	0.0792	0.0008	491.3	4.6	93.2
VP012M-33 - 1	0.6286	0.0132	0.0615	0.0006	0.0743	0.0012	462.2	7.0	70.7
VP012M-34 - 1	0.6799	0.0111	0.0622	0.0008	0.0792	0.0008	491.5	4.7	72.2
VP012M-35 - 1	0.7200	0.0260	0.0674	0.0017	0.0766	0.0010	475.9	5.8	56.2
VP012M-36 - 1	0.6355	0.0165	0.0583	0.0015	0.0791	0.0011	490.8	6.3	92.3
VP012F-02 - 1	0.6256	0.0090	0.0598	0.0005	0.0760	0.0009	472.0	5.4	79.4
VP012F-03 - 1	0.8727	0.0109	0.0618	0.0003	0.1025	0.0009	628.8	5.2	94.4

VP012F-04 - 1	0.6330	0.0096	0.0581	0.0004	0.0789	0.0012	490.8	6.4	92.3
VP012F-05 - 1	0.6252	0.0104	0.0591	0.0005	0.0770	0.0010	478.1	6.0	84.4
VP012F-06 - 1	1.4709	0.0178	0.0706	0.0003	0.1510	0.0013	906.6	7.3	96.0
VP012F-07 - 1	0.6437	0.0081	0.0580	0.0004	0.0805	0.0007	499.2	4.1	94.6
VP012F-09 - 1	0.7714	0.0115	0.0604	0.0004	0.0926	0.0010	571.1	5.8	92.5
VP012F-10 - 1	0.6333	0.0098	0.0578	0.0004	0.0794	0.0009	492.3	5.4	93.8
VP012F-11 - 1	0.6296	0.0104	0.0584	0.0005	0.0784	0.0011	486.5	6.5	89.9
VP012F-13 - 1	8.2904	0.0987	0.1430	0.0006	0.4205	0.0037	2,262.5	16.8	100.0

VP012F-14 - 1	0.6347	0.0085	0.0579	0.0004	0.0796	0.0007	493.9	4.4	94.6
VP012F-15 - 1	0.6649	0.0134	0.0595	0.0005	0.0810	0.0011	502.1	6.8	86.3
VP012F-17 - 1	0.6521	0.0081	0.0582	0.0004	0.0814	0.0007	504.3	4.2	94.5
VP012F-18 - 1	0.6318	0.0095	0.0583	0.0006	0.0786	0.0007	487.6	4.3	90.4
VP012F-19 - 1	0.6461	0.0088	0.0586	0.0004	0.0802	0.0008	497.2	5.0	90.4
VP012F-20 - 1	0.6321	0.0122	0.0580	0.0004	0.0791	0.0013	490.5	7.5	92.5
VP012F-22 - 1	0.9126	0.0279	0.0642	0.0007	0.1028	0.0022	630.9	13.1	84.8
VP012F-23 - 1	0.6325	0.0094	0.0598	0.0005	0.0767	0.0009	476.3	5.4	80.4

VP012F-25 - 1	0.6456	0.0077	0.0576	0.0003	0.0813	0.0007	503.8	4.1	98.2
VP012F-26 - 1	0.6962	0.0157	0.0617	0.0008	0.0812	0.0010	503.0	6.0	76.9
VP012F-27 - 1	0.7792	0.0116	0.0609	0.0006	0.0928	0.0009	571.9	5.1	90.2
VP012F-28 - 1	0.7898	0.0120	0.0610	0.0005	0.0936	0.0011	577.0	6.2	90.6
VP012F-29 - 1	0.6218	0.0094	0.0610	0.0005	0.0739	0.0009	459.7	5.5	72.1
VP012F-30 - 1	0.6453	0.0088	0.0584	0.0005	0.0801	0.0007	496.4	4.1	91.2
VP012F-31 - 1	0.6483	0.0080	0.0582	0.0004	0.0807	0.0007	500.4	4.0	93.1
VP012F-32 - 1	0.6372	0.0090	0.0584	0.0005	0.0790	0.0007	490.1	4.3	90.2

VP012F-34 - 1	0.6389	0.0087	0.0585	0.0004	0.0792	0.0007	491.6	4.3	90.0
VP012F-35 - 1	0.6452	0.0081	0.0580	0.0004	0.0807	0.0007	500.4	3.9	94.8
VP012F-36 - 1	0.6388	0.0077	0.0579	0.0003	0.0800	0.0007	496.4	3.9	94.7
VP012F-39 - 1	0.6331	0.0093	0.0584	0.0006	0.0787	0.0007	488.2	4.1	90.2
VP012F-40 - 1	0.6349	0.0087	0.0582	0.0005	0.0791	0.0007	490.9	4.0	91.9
VP012F-42 - 1	0.6326	0.0101	0.0583	0.0004	0.0789	0.0009	489.2	5.5	90.6
VP001-01 - 1	0.5148	0.0068	0.0560	0.0004	0.0667	0.0007	416.4	4.1	92.3
VP001-02 - 1	0.5286	0.0065	0.0560	0.0003	0.0685	0.0006	426.9	3.8	94.5

VP001-03 - 1	0.5351	0.0119	0.0565	0.0004	0.0689	0.0014	429.4	8.3	91.2
VP001-04 - 1	0.5212	0.0113	0.0560	0.0003	0.0674	0.0014	420.7	8.6	92.8
VP001-05 - 1	1.8597	0.8422	0.0608	0.0010	0.2042	0.0863	1,016.9	351.9	162.7
VP001-06 - 1	0.4933	0.0081	0.0561	0.0003	0.0638	0.0010	398.4	5.8	87.6
VP001-07 - 1	0.5189	0.0071	0.0559	0.0003	0.0675	0.0008	421.1	4.7	94.1
VP001-08 - 1	0.5185	0.0117	0.0573	0.0006	0.0654	0.0010	408.5	6.1	82.0
VP001-10 - 1	0.5557	0.0069	0.0558	0.0003	0.0723	0.0007	450.3	4.0	101.9
VP001-11 - 1	0.5139	0.0085	0.0558	0.0003	0.0673	0.0011	420.0	6.5	95.0

VP001-12 - 1	0.5251	0.0123	0.0561	0.0003	0.0679	0.0013	423.4	7.7	92.8
VP001-14 - 1	0.5212	0.0093	0.0561	0.0003	0.0676	0.0011	421.5	6.8	92.8
VP002-01 - 1	0.5223	0.0099	0.0652	0.0031	0.0597	0.0025	373.9	15.3	50.1
VP002-03 - 1	0.5195	0.0101	0.0560	0.0004	0.0676	0.0011	421.5	6.6	93.3
VP002-04 - 1	0.5409	0.0070	0.0564	0.0003	0.0696	0.0007	433.8	4.1	93.2
VP002-06 - 1	0.5279	0.0089	0.0555	0.0003	0.0691	0.0012	430.8	7.5	99.6
VP002-07 - 1	0.8036	0.0590	0.0879	0.0048	0.0654	0.0011	408.1	6.9	30.8
VP002-08 - 1	1.8718	5.8872	0.6149	0.0792	0.0532	0.0901	435.5	366.5	11.3

VP002-09 - 1	0.5221	0.0089	0.0564	0.0003	0.0673	0.0010	420.0	5.7	90.1
VP002-10 - 1	7.7853	4.5981	0.1200	0.0041	0.4714	0.2742	2,078.7	799.8	107.2
VP002-11 - 1	0.4880	0.0115	0.0693	0.0025	0.0523	0.0026	328.2	16.0	36.8
PJG0080-L1-01 - 1	0.6436	0.0083	0.0569	0.0003	0.0822	0.0008	509.5	4.6	105.0
PJG0080-L1-02 - 1	0.6559	0.0083	0.0578	0.0003	0.0825	0.0008	511.2	4.8	98.2
PJG0080-L1-02b	0.6803	0.0121	0.0579	0.0004	0.0851	0.0013	526.4	7.7	100.2
PJG0080-L1-03 - 1	0.6391	0.0100	0.0575	0.0003	0.0807	0.0011	500.2	6.5	98.0

PJG0080-L1-04 - 1	0.0299	0.0347	1.2379	0.0052	0.0034	0.0038	20.7	23.3	4.1
PJG0080-L1-06 - 1	0.6403	0.1154	0.0573	0.0004	0.0814	0.0145	502.3	88.5	100.0
PJG0080-L1-08 - 1	0.6746	0.0293	0.0606	0.0009	0.0814	0.0043	504.0	25.7	80.8
PJG0080-L1-10 - 1	3.0549	0.1475	0.2501	0.0074	0.0880	0.0019	543.8	11.1	17.1
PJG0080-L1-11 - 1	0.6551	0.0079	0.0582	0.0003	0.0818	0.0007	507.0	4.3	94.7
PJG0080-L1-11b	0.6567	0.0080	0.0576	0.0003	0.0826	0.0007	511.4	4.2	99.5

PJG0080-L2-01 - 1	0.6570	0.0105	0.0570	0.0003	0.0835	0.0011	517.2	6.5	104.3
PJG0080-L2-02 - 1	0.6596	0.0084	0.0579	0.0003	0.0827	0.0007	512.4	4.3	97.5
PJG0080-L2-02b	0.6714	0.0115	0.0577	0.0003	0.0843	0.0013	521.6	8.0	101.2
PJG0080-L2-03 - 1	0.6554	0.0078	0.0578	0.0003	0.0823	0.0007	510.0	4.1	97.8
PJG0080-L2-03b	0.6672	0.0080	0.0578	0.0003	0.0836	0.0007	517.8	4.2	99.6
PJG0080-L2-04 - 1	0.6577	0.0103	0.0582	0.0003	0.0820	0.0011	508.1	6.7	94.5

PJG0080-L2-05 - 1	0.7675	0.0166	0.0672	0.0012	0.0828	0.0008	512.7	4.6	61.3
PJG0080-L2-06 - 1	0.6529	0.0078	0.0588	0.0003	0.0805	0.0007	499.3	4.0	89.5
PJG0080-L2-07 - 1	0.6623	0.0081	0.0585	0.0003	0.0822	0.0007	509.1	4.2	93.1
PJG0080-L2-08 - 1	0.6626	0.0086	0.0584	0.0003	0.0824	0.0008	510.4	5.0	93.9
PJG0080-L2-10 - 1	0.6664	0.0081	0.0583	0.0003	0.0829	0.0007	513.2	4.3	95.2

PJG0080-L2-11 - 1	0.6545	0.0087	0.0577	0.0003	0.0821	0.0008	508.6	4.9	98.2
PJG0080-L2-13 - 1	0.6541	0.0090	0.0580	0.0003	0.0819	0.0009	507.4	5.3	96.2
PJG0080-L2-14 - 1	0.6479	0.0084	0.0578	0.0003	0.0816	0.0009	505.6	5.4	96.7
PJG0080-L2-15 - 1	0.6657	0.0080	0.0577	0.0003	0.0836	0.0007	517.7	4.3	100.1
PJG0080-L2-16 - 1	0.6535	0.0095	0.0581	0.0004	0.0817	0.0011	506.1	6.5	94.8

PJG0080-L2-17 - 1	0.6432	0.0113	0.0628	0.0008	0.0746	0.0014	463.7	8.3	66.2
PJG0080-L2-21 - 1	0.6575	0.0128	0.0582	0.0003	0.0820	0.0013	508.2	7.8	94.5
PJG0080-L2-21b	0.6366	0.0082	0.0577	0.0004	0.0798	0.0007	494.9	4.2	95.6
PJG0080-L2-23 - 1	0.6637	0.0083	0.0581	0.0003	0.0826	0.0008	511.8	4.8	96.3
PJG0080-L2-24 - 1	0.6659	0.0078	0.0574	0.0003	0.0841	0.0007	520.3	4.2	102.8
PJG0080-L2-25 - 1	0.6486	0.0098	0.0611	0.0005	0.0771	0.0012	478.8	7.4	74.7

PJG0080-L2-27 - 1	0.6507	0.0081	0.0572	0.0003	0.0824	0.0008	510.5	4.6	102.3
PJG0080-L2-29 - 1	0.6903	0.0089	0.0637	0.0006	0.0786	0.0008	487.7	4.8	66.9
PJG0082-01 - 1	0.6497	0.0086	0.0578	0.0003	0.0814	0.0008	504.6	4.6	96.9
PJG0082-04 - 1	0.5415	0.0097	0.0564	0.0004	0.0696	0.0012	433.8	7.1	92.6
PJG0082-05 - 1	0.6862	0.0142	0.0617	0.0009	0.0804	0.0008	498.5	4.7	75.5
PJG0082-07 - 1	0.4898	0.0087	0.0687	0.0013	0.0518	0.0007	325.7	4.3	37.0
PJG0082-08 - 1	0.5414	0.0230	0.0612	0.0020	0.0633	0.0006	395.4	3.8	62.9

PJG0082-10 - 1	0.4918	0.0069	0.0604	0.0007	0.0592	0.0009	370.8	5.5	60.4
PJG0082-11b	0.5257	0.0096	0.0558	0.0003	0.0685	0.0011	426.9	6.5	96.5
PJG0082-11 - 1	0.5313	0.0071	0.0557	0.0003	0.0690	0.0006	430.4	3.9	97.9
PJG0082-12 - 1	0.6866	0.0250	0.0833	0.0038	0.0602	0.0009	376.7	5.8	30.2
PJG0082-14 - 1	0.7044	0.0096	0.0580	0.0003	0.0882	0.0011	544.6	6.6	103.3
PJG0082-15 - 1	0.6674	0.0098	0.0583	0.0003	0.0829	0.0010	513.2	5.8	94.9
PJG0059-L1-02 - 1	0.4913	0.0119	0.0593	0.0005	0.0602	0.0012	376.5	7.1	65.2

PJG0059-L1-03 - 1	0.5220	0.0207	0.0564	0.0005	0.0674	0.0028	420.3	16.9	90.3
PJG0059-L1-06 - 1	0.4931	0.0072	0.0553	0.0005	0.0646	0.0006	403.8	3.6	95.7
PJG0059-L1-07 - 1	0.5833	0.0134	0.0638	0.0011	0.0665	0.0007	414.9	4.2	57.2
PJG0059-L1-08 - 1	0.7154	0.0568	0.0806	0.0063	0.0642	0.0006	401.3	3.5	36.8
PJG0059-L1-09 - 1	0.7743	0.0430	0.0951	0.0063	0.0605	0.0013	378.6	8.2	26.7

PJG0059-L1-11 - 1	0.5475	0.0107	0.0622	0.0009	0.0638	0.0006	398.9	3.5	59.1
PJG0059-L1-12 - 1	0.4645	0.0095	0.0793	0.0016	0.0428	0.0012	270.1	7.6	23.1
PJG0059-L1-13 - 1	0.7545	0.0189	0.0852	0.0014	0.0642	0.0008	401.1	4.8	30.5
PJG0059-L1-15 - 1	0.5163	0.0078	0.0581	0.0005	0.0645	0.0006	402.9	3.6	76.0
PJG0059-L1-16 - 1	1.0621	0.0814	0.1686	0.0149	0.0466	0.0009	293.4	5.6	12.1

PJG0059-L1-17 - 1	0.5173	0.0128	0.0560	0.0003	0.0671	0.0015	418.6	8.8	92.6
PJG0059-L1-19 - 1	1.8767	0.0617	0.1835	0.0061	0.0743	0.0009	462.3	5.6	17.3
PJG0059-L1-21 - 1	-0.1596	1.4772	0.0768	0.0067	0.0293	0.1177	415.2	393.0	38.5
PJG0059-L1-22 - 1	0.6649	0.0515	0.0756	0.0048	0.0634	0.0010	396.5	5.8	38.2
PJG0059-L1-23 - 1	1.6284	0.1273	0.1575	0.0098	0.0734	0.0017	456.5	10.0	19.5

PJG0059-L1-24 - 1	0.4878	0.0063	0.0556	0.0004	0.0637	0.0006	398.2	3.7	91.6
PJG0059-L1-25 - 1	0.4931	0.0084	0.0765	0.0022	0.0477	0.0019	299.9	11.7	27.5
PJG0059-L2-01 - 1	0.5369	0.0110	0.0615	0.0007	0.0638	0.0011	398.6	6.4	61.0
PJG0059-L2-02 - 1	0.5708	0.1131	0.0566	0.0004	0.0670	0.0077	395.4	13.3	83.0
PJG0059-L2-03 - 1	0.5210	0.0085	0.0553	0.0003	0.0683	0.0011	426.2	6.5	101.0

PJG0059-L2-05 - 1	-2.2779	0.9864	1.0609	0.0944	-0.0063	0.0088	-32.0	51.7	-6.3
PJG0059-L2-06 - 1	0.5146	0.0076	0.0584	0.0006	0.0641	0.0005	400.5	3.2	73.6
PJG0059-L2-09 - 1	0.4944	0.0116	0.0559	0.0003	0.0642	0.0013	401.1	7.8	89.7
PJG0059-L2-10 - 1	0.4771	0.0060	0.0577	0.0004	0.0599	0.0008	374.7	4.7	72.4
PJG0059-L2-11 - 1	0.4921	0.0058	0.0549	0.0003	0.0650	0.0006	406.0	3.4	99.9

PJG0059-L2-12 - 1	0.8843	0.0233	0.0928	0.0024	0.0695	0.0006	433.1	3.8	29.5
PJG0059-L2-14 - 1	0.6514	0.0155	0.0790	0.0022	0.0601	0.0016	376.1	9.9	32.4
PJG0059-L2-15 - 1	-0.0014	0.0001	1.1575	0.0050	0.0000	0.0000	-0.1	0.0	0.0
PJG0059-L2-17 - 1	0.4881	0.0067	0.0558	0.0003	0.0635	0.0006	397.0	3.9	89.4
PJG0059-L2-18 - 1	0.6090	0.0370	0.0681	0.0034	0.0643	0.0009	401.8	5.3	48.9
VP013-01 - 1	0.4725	0.0066	0.0563	0.0003	0.0609	0.0006	380.8	3.5	82.3

VP013-03 - 1	0.4723	0.0102	0.0554	0.0003	0.0617	0.0012	386.2	7.0	90.2
VP013-04 - 1	0.4884	0.0070	0.0566	0.0003	0.0625	0.0007	391.0	3.9	82.5
VP007-01 - 1	0.5291	0.0076	0.0581	0.0004	0.0659	0.0008	411.2	5.0	77.4
VP007-02 - 1	0.5518	0.0094	0.0613	0.0006	0.0649	0.0009	405.6	5.7	62.7
VP007-04 - 1	0.6275	0.0153	0.0610	0.0013	0.0745	0.0014	463.1	8.1	73.0
VP007-06 - 1	0.6068	0.0126	0.0594	0.0005	0.0741	0.0015	460.8	9.3	79.7
VP007-07 - 1	9.1517	0.2506	0.4893	0.0054	0.1361	0.0031	822.2	17.2	19.5
VP007-08 - 1	0.7024	0.0135	0.0782	0.0012	0.0650	0.0007	406.0	4.4	35.4

VP007-09 - 1	0.9220	0.0206	0.1038	0.0014	0.0645	0.0007	402.8	4.4	23.9
VP008(2)-01 - 1	0.6848	0.0115	0.0647	0.0008	0.0766	0.0007	475.7	4.0	62.4
VP008(2)-02 - 1	0.5423	0.0083	0.0600	0.0006	0.0654	0.0006	408.3	3.5	67.8
VP008(2)-03 - 1	0.5256	0.0098	0.0561	0.0003	0.0679	0.0011	423.7	6.3	93.3
VP008(2)-04 - 1	0.5245	0.0070	0.0547	0.0003	0.0696	0.0007	433.7	4.4	109.2
VP008(2)-05 - 1	0.5492	0.0335	0.0623	0.0010	0.0620	0.0022	387.8	13.7	57.2
VP008(2)-06 - 1	0.5359	0.0100	0.0552	0.0004	0.0697	0.0012	435.6	6.4	102.9
VP008(2)-08 - 1	0.5424	0.0099	0.0605	0.0006	0.0648	0.0008	404.8	4.8	65.3

VP008(2)-09 - 1	0.7650	0.0312	0.0832	0.0038	0.0671	0.0008	418.4	4.5	34.2
VP008(2)-11 - 1	0.5350	0.0064	0.0557	0.0003	0.0697	0.0006	434.2	3.6	99.0
VP008(2)-12 - 1	0.5302	0.0065	0.0557	0.0003	0.0690	0.0006	430.4	3.7	98.1
VP008(2)-13 - 1	25.3388	0.7573	0.6590	0.0053	0.2798	0.0067	1,589.2	33.7	34.7
VP008(2)-15 - 1	0.5232	0.0066	0.0559	0.0003	0.0680	0.0006	423.9	3.8	95.0
VP008(2)-16 - 1	2.8140	0.1432	0.2513	0.0091	0.0806	0.0014	499.3	8.4	15.7
VP008(2)-17 - 1	0.5377	0.0064	0.0558	0.0003	0.0700	0.0006	436.2	3.6	98.5
VP008(2)-18 - 1	0.5558	0.0081	0.0588	0.0006	0.0687	0.0006	428.1	3.6	77.1

VP008(2)-19 - 1	1.1333	2.0156	0.0890	0.0085	0.0774	0.1028	699.1	177.6	55.5
VP008(2)-20 - 1	1.2691	0.1992	0.1231	0.0141	0.0700	0.0026	436.1	15.4	24.4
VP008(2)-21 - 1	0.7153	0.0178	0.0798	0.0022	0.0652	0.0007	407.1	4.4	34.5
VP008(2)-22 - 1	0.5306	0.0068	0.0562	0.0003	0.0686	0.0007	427.6	4.0	93.0
VP008(2)-24 - 1	0.5299	0.0072	0.0572	0.0003	0.0673	0.0007	420.0	4.1	84.6
VP008(2)-25 - 1	0.5335	0.0102	0.0570	0.0017	0.0685	0.0015	427.2	9.2	92.4
VP001-L2-01 - 1	0.5206	0.0063	0.0559	0.0003	0.0677	0.0006	422.3	3.7	94.7

VP001-L2-02 - 1	0.5237	0.0063	0.0555	0.0003	0.0684	0.0006	426.7	3.5	98.6
VP001-L2-03 - 1	0.5318	0.0065	0.0552	0.0003	0.0701	0.0006	436.6	3.8	104.1
VP001-L2-03b	0.5452	0.0071	0.0553	0.0004	0.0715	0.0008	445.0	4.5	105.7
VP001-L2-05 - 1	0.5294	0.0063	0.0553	0.0003	0.0694	0.0006	432.7	3.5	102.1
VP001-L2-06 - 1	0.5255	0.0066	0.0559	0.0003	0.0682	0.0007	425.5	4.0	94.7
VP001-L2-07 - 1	0.5477	0.0073	0.0558	0.0003	0.0713	0.0007	443.7	4.4	99.7

VP001-L2-07b	0.5717	0.0135	0.0558	0.0004	0.0742	0.0016	461.4	9.8	104.1
VP001-L2-08 - 1	0.5435	0.0067	0.0558	0.0003	0.0707	0.0006	440.4	3.7	99.7
VP001-L208b	0.5391	0.0103	0.0560	0.0003	0.0700	0.0012	436.0	7.0	96.6
VP001-L2-09 - 1	0.5186	0.0062	0.0556	0.0003	0.0675	0.0006	421.2	3.5	96.4
VP001-L2-10 - 1	0.5259	0.0067	0.0559	0.0003	0.0683	0.0006	425.7	3.9	95.4
VP001-L2-12 - 1	0.5498	0.0086	0.0558	0.0003	0.0714	0.0010	444.8	5.8	100.0

VP001-L1-01 - 1	0.6009	0.0136	0.0594	0.0007	0.0731	0.0010	454.6	5.8	78.8
VP001-L1-02 - 1	0.5316	0.0064	0.0557	0.0003	0.0693	0.0006	432.1	3.6	98.5
VP001-L1-03 - 1	0.5310	0.0064	0.0559	0.0003	0.0689	0.0006	429.3	3.5	95.8
VP001-L1-04 - 1	0.5330	0.0064	0.0556	0.0003	0.0696	0.0006	433.6	3.6	99.5
VP001-L1-07 - 1	0.5378	0.0067	0.0566	0.0003	0.0689	0.0006	429.7	3.7	90.2

VP001-L1-08 - 1	0.5305	0.0068	0.0570	0.0003	0.0676	0.0007	421.4	4.0	86.2
VP001-L1-09 - 1	0.5345	0.0064	0.0557	0.0003	0.0696	0.0006	433.5	3.5	98.5
VP001-L1-11 - 1	0.5172	0.0091	0.0554	0.0003	0.0677	0.0010	422.1	6.0	98.5
VP001-L1-12 - 1	0.5314	0.0064	0.0555	0.0003	0.0694	0.0006	432.3	3.6	99.9
VP001-L1-13 - 1	0.5652	0.0077	0.0555	0.0003	0.0740	0.0008	460.4	4.6	106.8
VP001-L1-15b	0.5400	0.0082	0.0563	0.0003	0.0697	0.0008	434.5	5.1	93.9

VP001-L1-15 - 1	0.5295	0.0068	0.0561	0.0003	0.0683	0.0006	425.9	3.8	93.4
VP001-L1-17 - 1	0.5421	0.0074	0.0579	0.0004	0.0678	0.0006	423.1	3.8	80.6
VP001-L1-18 - 1	0.5419	0.0079	0.0557	0.0003	0.0707	0.0008	440.3	4.8	100.6
VP001-L1-18b	0.5240	0.0089	0.0555	0.0003	0.0684	0.0011	426.2	6.7	98.6
VP001-L1-19 - 1	0.5314	0.0079	0.0561	0.0003	0.0688	0.0009	428.7	5.2	94.1
VP001-L1-20 - 1	0.5320	0.0064	0.0556	0.0003	0.0693	0.0006	431.9	3.6	98.9

VP001-L1-22 - 1	0.5248	0.0078	0.0560	0.0003	0.0679	0.0009	423.6	5.3	93.8
VP001-L1-23 - 1	0.5393	0.0067	0.0557	0.0003	0.0703	0.0006	437.9	3.8	99.9
VP001-L1-24 - 1	0.5268	0.0066	0.0557	0.0003	0.0685	0.0006	427.2	3.6	97.6
VP001-L1-25 - 1	0.5282	0.0063	0.0554	0.0003	0.0692	0.0006	431.1	3.4	101.2
VP002-L1-01 - 1	0.5201	0.0063	0.0556	0.0003	0.0677	0.0006	422.2	3.6	96.6

VP002-L1-02 - 1	0.5680	0.0075	0.0558	0.0003	0.0736	0.0008	457.6	5.1	103.4
VP002-L1-03 - 1	0.5481	0.0085	0.0558	0.0003	0.0713	0.0007	443.7	4.4	100.5
VP002-L1-05 - 1	0.5202	0.0064	0.0605	0.0005	0.0622	0.0008	389.0	5.1	63.0
VP002-L1-06 - 1	0.5014	0.0060	0.0597	0.0007	0.0611	0.0008	382.0	4.6	64.7
VP002-L1-07 - 1	0.5458	0.0212	0.0655	0.0026	0.0605	0.0006	378.9	3.6	49.2

VP002-L1-08 - 1	0.5224	0.0063	0.0556	0.0003	0.0682	0.0006	425.0	3.5	97.8
VP002-L1-09 - 1	0.5376	0.0066	0.0559	0.0003	0.0698	0.0006	434.9	3.6	97.7
VP002-L2-02 - 1	0.5245	0.0070	0.0623	0.0004	0.0610	0.0008	381.6	4.9	56.0
VP002-L2-04 - 1	0.5028	0.0080	0.0570	0.0003	0.0641	0.0009	400.2	5.4	81.9
VP002-L2-06 - 1	0.5419	0.0068	0.0555	0.0003	0.0708	0.0006	441.2	3.9	102.2

VP002-L2-07 - 1	0.5427	0.0065	0.0552	0.0003	0.0714	0.0006	444.4	3.7	105.6
VP002-L2-08 - 1	0.5314	0.0063	0.0556	0.0003	0.0694	0.0006	432.7	3.6	99.6
VP002-L2-10 - 1	0.5199	0.0065	0.0558	0.0003	0.0677	0.0006	422.3	3.7	95.3
VP002-L2-10b	0.5386	0.0072	0.0564	0.0004	0.0692	0.0006	431.6	3.8	92.7
VP002-L2-11 - 1	0.5346	0.0063	0.0553	0.0003	0.0702	0.0006	437.6	3.5	103.1
VP002-L2-11b	0.5418	0.0067	0.0552	0.0003	0.0712	0.0006	443.3	3.6	105.3

VP002-L2-13 - 1	0.5207	0.0063	0.0561	0.0003	0.0674	0.0006	420.3	3.5	92.0
VP002-L2-14 - 1	0.5172	0.0061	0.0557	0.0003	0.0674	0.0006	420.3	3.4	95.9
VP002-L2-16 - 1	0.5248	0.0065	0.0557	0.0003	0.0685	0.0006	427.0	3.6	96.8
VP002-L2-18 - 1	0.5392	0.0108	0.0564	0.0003	0.0697	0.0013	434.4	7.7	93.3
VP002-L2-19 - 1	0.5710	0.0072	0.0554	0.0004	0.0751	0.0008	466.7	4.7	109.4

VP002-L2-20 - 1	0.5283	0.0066	0.0569	0.0003	0.0676	0.0006	421.4	3.7	86.8

Table E.2: Raw zircon geochronology data from session two.

Sample	$^{207}Pb/^{235}U$	$\pm2\sigma$	$^{207}Pb/^{206}Pb$	$\pm2\sigma$	$^{206}Pb/^{238}U$	$\pm2\sigma$	Date(Ma)	$\pm2\sigma$(Ma)	Conc(%)
PJG0080b - 1.d	- 20,677.2529	3,125.5149	0.6925	0.0835	0.2198	0.0195	1,261.3	101.8	34.7
PJG0080b - 2.d	0.6822	0.0533	0.0587	0.0025	0.0808	0.0020	500.6	11.7	84.0
PJG0080b - 3.d	0.7303	0.0324	0.0585	0.0020	0.0882	0.0017	544.8	10.1	94.0
PJG0080b - 4.d	0.6334	0.0106	0.0587	0.0009	0.0761	0.0014	472.9	8.3	86.0
PJG0080b - 5.d	0.6387	0.0205	0.0588	0.0017	0.0772	0.0017	479.5	10.3	86.0
PJG0080b - 6.d	0.6110	0.0184	0.0578	0.0012	0.0754	0.0014	468.3	8.4	89.0
PJG0080b - 7.d	0.6935	0.0116	0.0578	0.0009	0.0816	0.0015	505.9	8.9	98.7

PJG0080b - 8.d	0.6406	0.0218	0.0577	0.0017	0.0801	0.0018	498.3	9.9	91.1
PJG0080b - 9.d	0.6812	0.0130	0.0575	0.0009	0.0815	0.0016	505.2	9.3	101.1
PJG0080b - 10.d	0.6531	0.0170	0.0581	0.0012	0.0809	0.0016	501.4	9.5	92.9
PJG0080b - 11.d	0.6481	0.0201	0.0574	0.0014	0.0809	0.0016	501.4	9.6	97.7
PJG0080b - 12.d	0.6866	0.0257	0.0583	0.0017	0.0845	0.0016	523.2	9.7	92.7
PJG0080b - 13.d	0.6664	0.0201	0.0572	0.0015	0.0831	0.0016	514.5	9.4	99.7
PJG0080b - 14.d	0.6642	0.0315	0.0593	0.0023	0.0804	0.0016	498.7	9.8	78.0
PJG0080b - 15.d	0.6500	0.0228	0.0576	0.0016	0.0819	0.0016	507.4	9.5	94.4

PJG0080b - 16.d	0.6689	0.0259	0.0577	0.0019	0.0828	0.0016	512.6	9.5	96.3
PJG0080b - 17.d	0.6760	0.0252	0.0585	0.0015	0.0828	0.0016	512.6	9.8	93.0
PJG0080b - 18.d	0.5538	0.0255	0.0574	0.0021	0.0688	0.0014	428.8	8.6	69.1
PJG0080b - 19.d	0.6808	0.0404	0.0586	0.0027	0.0830	0.0019	514.0	11.1	81.2
PJG0080b - 20.d	0.6798	0.0250	0.0581	0.0017	0.0831	0.0016	514.8	9.6	90.5
PJG0080b - 21.d	0.6692	0.0257	0.0581	0.0018	0.0818	0.0017	506.9	9.9	91.9
PJG0080b - 22.d	0.4553	0.0219	0.0532	0.0024	0.0639	0.0013	399.2	7.8	79.2
PJG0080b - 23.d	0.4353	0.0242	0.0526	0.0027	0.0601	0.0013	376.4	7.9	68.8

PJG0080b - 24.d	0.6446	0.0147	0.0583	0.0009	0.0779	0.0014	483.8	8.6	89.5
PJG0082b - 1.d	0.6172	0.0185	0.0578	0.0014	0.0776	0.0015	481.6	8.8	93.4
PJG0082b - 2.d	0.6236	0.0159	0.0578	0.0011	0.0775	0.0015	481.2	9.1	94.4
PJG0082b - 3.d	0.8910	0.0348	0.0739	0.0023	0.0870	0.0017	537.8	10.2	52.8
PJG0082b - 4.d	0.4410	0.0345	0.0550	0.0039	0.0563	0.0014	352.7	8.4	47.5
PJG0082b - 5.d	0.4933	0.0258	0.0553	0.0026	0.0632	0.0014	395.2	8.7	67.1
PJG0082b - 6.d	0.5080	0.0200	0.0593	0.0020	0.0600	0.0013	375.6	8.0	60.6
PJG0082b - 7.d	0.6482	0.0136	0.0577	0.0010	0.0779	0.0014	483.8	8.6	92.0

PJG0059b - 1.d	0.6285	0.0290	0.0787	0.0030	0.0584	0.0011	365.7	7.0	32.7
PJG0059b - 2.d	0.4699	0.0366	0.0522	0.0038	0.0642	0.0015	401.1	9.2	56.9
PJG0059b - 3.d	0.6599	0.0514	0.0715	0.0057	0.0646	0.0017	403.6	10.4	38.4
PJG0059b - 4.d	0.4924	0.0121	0.0551	0.0012	0.0651	0.0012	406.3	7.4	91.2
PJG0059b - 5.d	0.5809	0.0186	0.0631	0.0018	0.0656	0.0013	409.8	7.7	57.4
PJG0059b - 6.d	0.6294	0.0404	0.0817	0.0045	0.0548	0.0017	343.9	10.6	29.5
PJG0059b - 7.d	0.4798	0.0233	0.0538	0.0020	0.0647	0.0014	403.9	8.5	84.3
PJG0059b - 8.d	0.5209	0.0383	0.0600	0.0037	0.0625	0.0015	391.6	9.3	51.0

PJG0059b - 9.d	0.5273	0.0189	0.0654	0.0021	0.0584	0.0011	366.1	6.7	48.1
PJG0059b - 10.d	0.5886	0.0133	0.0649	0.0015	0.0630	0.0012	393.7	7.5	52.0
PJG0059b - 11.d	0.4704	0.0213	0.0566	0.0022	0.0606	0.0013	379.0	8.0	71.1
PJG0059b - 12.d	0.5233	0.0309	0.0596	0.0030	0.0654	0.0015	408.4	9.1	56.0
PJG0059b - 13.d	0.4778	0.0141	0.0556	0.0015	0.0621	0.0012	388.6	7.3	86.2
PJG0059b - 14.d	0.4925	0.0124	0.0562	0.0014	0.0633	0.0012	395.6	7.1	84.4
PJG0059b - 15.d	0.5516	0.0213	0.0807	0.0026	0.0496	0.0013	311.8	7.7	26.4
VP008b - 1.d	0.5297	0.0209	0.0552	0.0019	0.0691	0.0014	430.7	8.3	91.1

VP008b - 2.d	0.5245	0.0340	0.0541	0.0030	0.0699	0.0016	435.6	9.3	69.6
VP008b - 1.d	0.6050	0.0386	0.0564	0.0030	0.0781	0.0018	484.8	11.0	76.1
VP008b - 2.d	0.6499	0.0441	0.0689	0.0037	0.0691	0.0014	430.5	8.7	48.5
VP008b - 3.d	0.5072	0.0302	0.0540	0.0028	0.0690	0.0015	430.0	9.1	70.6
VP008b - 4.d	0.5528	0.0382	0.0574	0.0034	0.0698	0.0017	434.9	10.0	60.6
VP008b - 5.d	1.8211	0.2927	0.1615	0.0202	0.0692	0.0029	430.8	17.6	19.6
VP008b - 6.d	0.6743	0.0572	0.0553	0.0038	0.0889	0.0025	548.9	14.6	72.9
VP008b - 7.d	0.9459	0.1488	0.0714	0.0088	0.0803	0.0032	497.1	18.9	38.3

VP012mb - 1.d	0.7494	0.1627	0.0577	0.0067	0.0831	0.0030	514.4	18.1	45.5
VP012mb - 2.d	0.7052	0.0937	0.0609	0.0069	0.0787	0.0026	488.1	15.4	40.6
VP012mb - 3.d	0.6767	0.0470	0.0614	0.0034	0.0805	0.0019	499.0	11.1	64.0
VP012mb - 4.d	0.7993	0.1392	0.0586	0.0076	0.0832	0.0026	515.1	15.3	47.6
VP012mb - 5.d	0.8137	0.1347	0.0641	0.0087	0.0823	0.0029	509.2	17.0	38.5
VP012mb - 6.d	0.7045	0.1540	0.0544	0.0067	0.0812	0.0027	502.9	16.0	48.9
VP012mb - 7.d	0.6387	0.0312	0.0563	0.0021	0.0816	0.0017	505.9	10.4	93.5
VP012mb - 8.d	0.6320	0.0417	0.0575	0.0032	0.0806	0.0020	499.8	11.8	69.6

VP012mb - 9.d	0.7170	0.0944	0.0590	0.0050	0.0835	0.0021	517.1	12.5	59.5
VP012mb - 10.d	0.6706	0.0650	0.0571	0.0041	0.0822	0.0021	509.2	12.7	67.9
VP012mb - 11.d	0.6492	0.0458	0.0567	0.0033	0.0827	0.0019	512.4	11.3	74.5
VP012mb - 12.d	0.8060	0.1479	0.0601	0.0075	0.0790	0.0026	490.1	15.3	43.6
VP012mb - 13.d	0.7594	0.1319	0.0593	0.0080	0.0800	0.0028	495.9	16.7	40.2
VP012mb - 14.d	0.6600	0.0510	0.0574	0.0035	0.0817	0.0018	506.0	11.0	71.2
VP012mb - 15.d	0.9582	0.1956	0.0657	0.0081	0.0790	0.0028	489.6	16.9	39.8
VP012mb - 16.d	0.6869	0.0938	0.0555	0.0055	0.0822	0.0027	509.0	15.8	54.1

VP012mb - 17.d	0.7022	0.0831	0.0604	0.0057	0.0812	0.0024	502.7	14.5	50.7
VP012mb - 18.d	1.1248	0.2468	0.0683	0.0096	0.0834	0.0036	515.7	21.1	37.4
VP012mb - 19.d	0.7648	0.1024	0.0614	0.0067	0.0792	0.0026	490.8	15.5	44.7
VP012mb - 20.d	0.8096	0.1371	0.0606	0.0080	0.0841	0.0030	520.0	17.7	45.8
VP012mb - 21.d	0.6437	0.0660	0.0580	0.0049	0.0787	0.0021	488.1	12.3	60.2
VP012mb - 22.d	0.7539	0.0312	0.0592	0.0019	0.0947	0.0018	583.1	10.8	98.2
VP012fb - 1.d	0.6389	0.0540	0.0548	0.0037	0.0804	0.0019	498.1	11.4	67.0
VP012fb - 2.d	0.7670	0.0819	0.0679	0.0048	0.0775	0.0022	480.8	12.8	47.7

VP012fb - 3.d	0.6491	0.0427	0.0571	0.0030	0.0804	0.0018	498.5	10.9	74.4
VP012fb - 4.d	0.6472	0.0451	0.0570	0.0031	0.0813	0.0018	503.9	10.6	73.8
VP012fb - 5.d	0.6566	0.0442	0.0582	0.0032	0.0820	0.0020	507.9	11.8	76.2
VP012fb - 6.d	0.6685	0.0339	0.0572	0.0022	0.0830	0.0017	513.6	10.1	81.6
VP012fb - 7.d	0.6352	0.0443	0.0569	0.0041	0.0820	0.0019	507.8	11.6	66.8
VP012fb - 8.d	0.6659	0.0311	0.0575	0.0024	0.0821	0.0018	508.8	10.5	82.7
VP012fb - 9.d	0.6323	0.0196	0.0570	0.0015	0.0816	0.0016	505.8	9.7	99.1
VP012fb - 10.d	0.6677	0.0515	0.0577	0.0037	0.0805	0.0020	498.8	11.8	68.5

VP012fb - 11.d	0.6478	0.0333	0.0569	0.0025	0.0830	0.0017	513.9	10.1	86.5
VP012fb - 12.d	0.6838	0.0506	0.0564	0.0030	0.0833	0.0019	515.4	11.3	73.8
VP012fb - 13.d	0.7208	0.0723	0.0649	0.0053	0.0803	0.0020	497.7	12.1	49.7
VP012fb - 14.d	0.6434	0.0477	0.0572	0.0040	0.0827	0.0020	512.1	12.1	62.1
VP012fb - 15.d	0.6442	0.0424	0.0577	0.0034	0.0801	0.0020	496.6	12.2	71.5
VP012fb - 16.d	0.6220	0.0250	0.0571	0.0021	0.0812	0.0016	503.0	9.7	90.8
VP012fb - 17.d	0.6405	0.0400	0.0569	0.0025	0.0795	0.0018	493.1	10.8	82.7
VP012fb - 18.d	0.6696	0.0510	0.0593	0.0038	0.0797	0.0022	494.4	13.3	69.7

VP012fb - 19.d	0.6480	0.0688	0.0550	0.0046	0.0814	0.0020	504.2	12.2	70.4
VP012fb - 20.d	0.6066	0.0464	0.0536	0.0038	0.0814	0.0020	504.4	11.7	69.5
VP012fb - 21.d	0.6465	0.0406	0.0577	0.0033	0.0804	0.0019	498.4	11.3	75.3
VP012fb - 22.d	0.6808	0.0584	0.0578	0.0042	0.0805	0.0021	498.7	12.4	64.6
VP012fb - 23.d	0.7085	0.0482	0.0588	0.0030	0.0825	0.0018	511.1	10.9	78.8
VP012fb - 24.d	0.5349	0.0148	0.0555	0.0015	0.0688	0.0013	429.0	7.9	87.5
VP012fb - 25.d	0.5556	0.0234	0.0584	0.0024	0.0686	0.0014	427.5	8.3	69.1
VP001b - 1.d	0.5528	0.0174	0.0569	0.0015	0.0690	0.0014	429.8	8.2	82.4

VP001b - 2.d	0.5451	0.0259	0.0570	0.0022	0.0676	0.0014	422.3	8.6	75.3
VP001b - 3.d	0.5076	0.0234	0.0572	0.0024	0.0627	0.0013	391.9	8.1	62.9
VP001b - 4.d	0.4809	0.0225	0.0561	0.0023	0.0620	0.0013	387.9	7.8	71.9
VP013b - 1.d	0.5222	0.0186	0.0629	0.0016	0.0579	0.0011	363.0	6.9	52.4
VP013b - 2.d	0.5219	0.0124	0.0566	0.0011	0.0666	0.0012	415.7	7.5	86.6
VP008b - 8.d	0.5273	0.0278	0.0563	0.0024	0.0672	0.0014	419.1	8.5	74.0
VP008b - 9.d	0.5625	0.0252	0.0602	0.0024	0.0666	0.0013	415.5	8.1	64.2
VP008b - 10.d	0.5534	0.0293	0.0593	0.0026	0.0655	0.0014	409.1	8.3	62.5

VP008b - 11.d	1.0028	0.0668	0.1022	0.0050	0.0698	0.0015	435.1	9.3	26.5
VP008b - 12.d	0.6537	0.0545	0.0684	0.0045	0.0666	0.0017	415.6	10.4	45.8
VP008b - 13.d	0.6204	0.0344	0.0697	0.0033	0.0657	0.0014	410.0	8.6	45.6
VP008b - 14.d	0.7474	0.0419	0.0762	0.0043	0.0686	0.0014	427.5	8.7	37.9
VP008b - 15.d	0.5489	0.0218	0.0578	0.0020	0.0691	0.0014	430.7	8.5	76.5
VP008b - 16.d	0.6930	0.0458	0.0752	0.0043	0.0660	0.0013	412.0	7.7	39.9
VP008b - 17.d	0.5324	0.0258	0.0566	0.0023	0.0672	0.0014	419.0	8.3	71.0
VP008b - 18.d	0.5439	0.0209	0.0573	0.0019	0.0683	0.0013	425.8	7.9	78.3

VP008b - 19.d	0.5540	0.0311	0.0600	0.0025	0.0685	0.0024	426.7	14.6	66.5
VP008b - 20.d	0.5495	0.0293	0.0573	0.0025	0.0689	0.0015	429.7	9.2	67.6
VP008b - 21.d	0.5311	0.0196	0.0579	0.0018	0.0665	0.0014	415.1	8.2	74.8
VP008b - 22.d	0.5366	0.0156	0.0581	0.0014	0.0669	0.0013	417.3	8.0	78.0
VP002b - 1.d	0.5176	0.0217	0.0618	0.0024	0.0621	0.0013	388.1	7.6	57.6
VP002b - 2.d	0.4698	0.0167	0.0953	0.0029	0.0370	0.0010	234.3	6.2	15.6
VP002b - 3.d	0.5450	0.0188	0.0598	0.0019	0.0658	0.0014	410.7	8.7	69.2
VP002b - 4.d	0.5593	0.0109	0.0560	0.0007	0.0693	0.0014	432.0	8.6	96.6

VP002b - 5.d	0.3190	0.0143	0.0666	0.0020	0.0357	0.0015	226.2	9.5	28.2
VP002b - 6.d	0.5344	0.0233	0.0566	0.0020	0.0677	0.0014	422.1	8.4	77.4
VP002b - 7.d	18.6570	25.1080	0.0620	0.0100	0.0672	0.0024	419.0	14.6	33.2
VP002b - 8.d	- 2,516.2072	1,158.1777	0.1965	0.0395	0.0687	0.0051	426.6	30.7	16.7
VP002b - 9.d	0.5528	0.0206	0.0696	0.0022	0.0587	0.0012	367.4	7.2	41.1
VP002b - 10.d	0.4913	0.0130	0.0628	0.0016	0.0583	0.0012	365.5	7.1	53.8
VP002b - 11.d	0.5172	0.0147	0.0558	0.0013	0.0669	0.0013	417.6	7.6	90.0
VP002b - 12.d	0.5443	0.0427	0.0596	0.0033	0.0664	0.0018	414.3	11.1	59.0

VP002b - 13.d	0.5319	0.0331	0.0573	0.0029	0.0655	0.0014	409.1	8.2	60.9
VP002b - 14.d	0.5101	0.0145	0.0561	0.0014	0.0658	0.0013	410.6	7.6	87.2
VP002b - 15.d	0.5210	0.0227	0.0552	0.0020	0.0682	0.0014	425.5	8.3	84.8
VP001b - 5.d	0.5160	0.0130	0.0561	0.0013	0.0671	0.0013	418.4	8.0	89.8
VP001b - 6.d	0.5338	0.0229	0.0557	0.0022	0.0701	0.0014	436.6	8.2	88.9
VP001b - 7.d	0.5328	0.0149	0.0561	0.0014	0.0686	0.0014	427.6	8.3	87.4
VP001b - 8.d	0.5837	0.0158	0.0564	0.0012	0.0746	0.0014	464.0	8.5	96.2
VP001b - 9.d	0.5220	0.0171	0.0557	0.0014	0.0682	0.0013	425.3	7.8	92.7

VP001b - 10.d	0.5189	0.0171	0.0562	0.0014	0.0671	0.0013	418.7	7.7	86.3
VP001b - 11.d	0.5826	0.0193	0.0563	0.0016	0.0755	0.0016	469.0	9.4	98.6
VP001b - 12.d	0.5398	0.0205	0.0570	0.0017	0.0686	0.0013	427.6	8.0	77.1
VP001b - 13.d	0.5247	0.0140	0.0558	0.0013	0.0686	0.0013	427.5	7.7	96.2
VP001b - 14.d	0.5269	0.0188	0.0578	0.0018	0.0666	0.0014	415.4	8.6	71.7

Table E.3: Raw titanite geochronology data.

Sample	U/Th	$^{207}Pb/^{235}U \pm 2\sigma$		$^{206}Pb/^{238}U \pm 2\sigma$		Error	$^{238}Pb/^{206}Pb \pm 2\sigma$		$^{207}Pb/^{206}Pb \pm 2\sigma$		Error	Corrected Age (Ma)	Error (2SE)
VP003-1	0.19	1.6608	0.1016	0.0792	0.0035	0.0241	12.7581	0.5655	0.1541	0.0084	0.4083	427.1	23.6
VP003-2	0.34	0.6166	0.0275	0.0696	0.0027	0.0298	14.3875	0.5364	0.0644	0.0018	0.3732	428.3	16.2
VP003-3	0.17	0.7733	0.0380	0.0721	0.0029	0.0523	13.9137	0.5320	0.0781	0.0028	0.3588	435.3	17.7
VP003-4	0.26	0.7038	0.0303	0.0704	0.0027	0.3206	14.2198	0.5238	0.0729	0.0017	0.0595	428.4	16.4
VP003-5	0.18	0.8249	0.0426	0.0723	0.0028	0.0025	13.8545	0.5201	0.0837	0.0035	0.2627	433.3	17.4
VP003-6	0.46	0.6177	0.0250	0.0701	0.0027	0.2695	14.2794	0.5152	0.0640	0.0012	0.2681	431.7	16.3

VP003-7	0.19	2.3469	0.1791	0.0868	0.0038	0.5564	11.6930	0.5213	0.1947	0.0116	-0.1945	437.7	31.0
VP003-8	0.26	0.6218	0.0260	0.0701	0.0027	0.1305	14.2955	0.5435	0.0647	0.0015	0.2417	431.5	16.3
VP003-9	0.33	1.2722	0.0685	0.0759	0.0032	0.3048	13.2789	0.5456	0.1223	0.0049	0.1996	429.6	20.4
VP003-10	0.27	1.4960	0.0637	0.0800	0.0031	0.0329	12.5179	0.4684	0.1361	0.0035	0.4484	443.3	22.5
VP003-11	0.18	0.6980	0.0348	0.0676	0.0027	0.2522	14.8634	0.5809	0.0754	0.0026	0.0824	410.1	15.9
VP003-12	0.22	1.7800	0.0841	0.0772	0.0031	0.0276	13.0378	0.5274	0.1679	0.0056	0.0319	407.4	19.8
VP003-13	0.20	0.8174	0.0499	0.0672	0.0029	0.0467	15.0493	0.6570	0.0898	0.0049	0.3366	399.8	17.1
VP003-14	0.20	0.8016	0.0411	0.0684	0.0027	-0.2129	14.6379	0.5462	0.0839	0.0032	0.5769	409.9	16.2

VP003-15	0.22	1.5094	0.0921	0.0727	0.0033	-0.1154	13.9757	0.6477	0.1535	0.0090	0.5384	393.3	19.1
VP003-16	0.34	0.5922	0.0241	0.0659	0.0025	0.2802	15.2077	0.5828	0.0652	0.0012	0.1734	405.7	15.5
VP003-17	0.23	0.7264	0.0343	0.0701	0.0027	0.0257	14.2716	0.5283	0.0758	0.0026	0.2521	425.0	16.1
VP003-18	0.71	0.7538	0.0599	0.0698	0.0031	0.1690	14.5600	0.6631	0.0801	0.0061	-0.0302	420.6	19.0
VP003-19	0.48	0.6248	0.0251	0.0690	0.0026	0.2614	14.5156	0.5511	0.0657	0.0011	0.2194	424.2	15.8
VP003-20	0.19	1.3055	0.0851	0.0768	0.0034	0.1256	13.1988	0.5857	0.1232	0.0068	0.2437	434.4	22.1
VP003-21	0.32	0.8430	0.0513	0.0706	0.0031	-0.2594	14.2169	0.5866	0.0878	0.0052	0.6121	421.0	18.5
VP003-22	0.41	1.6303	0.0903	0.0783	0.0034	0.0815	12.9218	0.5506	0.1535	0.0074	0.3911	423.0	22.6

VP003-23	0.19	0.9243	0.0543	0.0749	0.0031	0.0803	13.4671	0.5539	0.0891	0.0040	0.2236	445.2	20.2
VP003-24	0.29	1.1742	0.0557	0.0763	0.0031	0.2338	13.1915	0.5416	0.1124	0.0038	0.2917	438.5	20.3
VP003-25	0.37	0.6890	0.0312	0.0725	0.0028	0.1893	13.8047	0.5200	0.0690	0.0019	0.1750	443.6	17.7
VP003-26	0.31	1.5409	0.0819	0.0782	0.0033	0.0515	12.9068	0.5543	0.1438	0.0063	-0.0085	428.7	21.9
VP003-27	0.16	1.2369	0.0825	0.0769	0.0034	0.1592	13.1428	0.6072	0.1163	0.0066	0.2930	439.2	22.2
VP003-28	1.00	0.6381	0.0262	0.0743	0.0029	0.1031	13.4796	0.5141	0.0624	0.0014	0.1483	458.4	18.9
VP003-29	0.32	0.8116	0.0437	0.0748	0.0029	0.2168	13.4149	0.5246	0.0793	0.0032	0.1132	450.9	19.2
VP003-30	0.32	0.7480	0.0340	0.0706	0.0027	0.0043	14.2198	0.5638	0.0777	0.0026	0.3623	426.6	16.6

VP003-31	0.17	0.7577	0.0340	0.0690	0.0027	0.1604	14.5643	0.5923	0.0800	0.0022	-0.0665	415.8	16.0
VP003-32	0.53	0.9047	0.0425	0.0699	0.0027	0.0075	14.3366	0.5521	0.0935	0.0028	0.3255	413.3	15.8
VP003-33	0.30	0.8159	0.0417	0.0705	0.0028	0.1854	14.2133	0.5539	0.0849	0.0033	0.1313	422.2	16.7
VP003-34	0.18	1.9386	0.1091	0.0788	0.0036	0.3290	12.9283	0.5926	0.1853	0.0098	0.2729	404.3	23.4
VP003-35	0.25	1.0068	0.0537	0.0717	0.0029	-0.0260	14.0177	0.6139	0.1024	0.0046	0.3707	418.2	17.5
VP003-36	0.25	1.1176	0.0625	0.0710	0.0029	0.0589	14.1437	0.5568	0.1146	0.0052	0.3990	407.2	17.1
VP003-37	0.15	1.7001	0.1078	0.0781	0.0037	0.0069	13.0549	0.6049	0.1602	0.0106	0.0360	417.3	24.1
VP003-38	0.19	2.0750	0.1156	0.0805	0.0040	0.0767	12.6619	0.6150	0.1909	0.0099	0.5231	409.3	25.8

VP003-39	0.28	0.7820	0.0484	0.0703	0.0031	0.1854	14.2804	0.5668	0.0806	0.0042	0.3220	423.5	18.4
VP003-40	0.21	1.2700	0.0827	0.0730	0.0032	-0.1152	13.8197	0.5865	0.1291	0.0080	0.4703	409.5	19.4
VP004-1	0.16	1.3604	0.0807	0.0767	0.0034	0.0626	13.1103	0.5337	0.1302	0.0067	0.4100	422.6	21.6
VP004-2	0.36	0.9412	0.0485	0.0737	0.0031	0.0815	13.6655	0.5635	0.0934	0.0038	0.3976	432.0	19.4
VP004-3	0.19	1.0549	0.0677	0.0726	0.0031	0.1350	13.8141	0.5395	0.1073	0.0059	0.3403	416.5	18.9
VP004-4	0.20	1.0052	0.0601	0.0731	0.0031	0.0452	13.7747	0.6030	0.1013	0.0054	0.3630	423.0	18.9
VP004-5	0.37	0.5847	0.0234	0.0699	0.0026	0.1514	14.3272	0.5355	0.0608	0.0011	0.1783	432.0	16.1
VP004-6	0.24	0.7085	0.0336	0.0705	0.0027	0.1563	14.2320	0.5641	0.0731	0.0023	0.1046	427.2	16.5

VP004-7	0.36	0.6958	0.0333	0.0719	0.0028	0.0404	13.9687	0.5400	0.0706	0.0025	0.3238	437.7	17.7
VP004-8	0.23	0.6404	0.0291	0.0698	0.0027	0.2619	14.3721	0.5465	0.0670	0.0020	-0.0400	427.3	16.4
VP004-9	0.55	0.8218	0.0405	0.0691	0.0026	0.3981	14.5104	0.5641	0.0863	0.0026	-0.0959	410.3	15.6
VP004-10	0.30	0.7908	0.0483	0.0731	0.0030	0.1461	13.7473	0.5682	0.0785	0.0037	0.1880	439.2	18.8
VP004-11	0.33	0.6252	0.0270	0.0683	0.0026	0.0499	14.6624	0.5624	0.0669	0.0018	0.2872	418.7	15.7
VP004-12	0.37	0.8798	0.0513	0.0714	0.0030	0.0038	14.1261	0.5909	0.0903	0.0045	0.3438	420.9	17.9
VP004-13	0.51	0.6438	0.0276	0.0725	0.0028	0.0443	13.8187	0.5270	0.0645	0.0015	0.2356	445.3	17.5
VP004-14	0.24	0.6042	0.0265	0.0671	0.0026	0.1851	14.9202	0.5566	0.0655	0.0017	0.2314	412.0	15.7

VP004-15	0.21	0.6874	0.0332	0.0703	0.0027	0.1538	14.2378	0.5748	0.0710	0.0023	0.1261	427.9	16.5
VP004-16	0.30	0.7623	0.0363	0.0689	0.0026	0.2378	14.5110	0.5247	0.0807	0.0025	0.0229	413.1	15.5
VP004-17	0.28	0.6647	0.0326	0.0695	0.0027	0.4391	14.4362	0.5615	0.0694	0.0022	-0.1769	423.8	16.2
VP004-18	0.55	0.6168	0.0268	0.0685	0.0026	0.1791	14.5998	0.5803	0.0653	0.0016	0.1733	420.9	15.8
VP004-19	0.30	0.5940	0.0251	0.0689	0.0026	0.1806	14.5442	0.5551	0.0627	0.0014	0.0648	424.5	15.8
VP004-20	0.43	0.7453	0.0363	0.0698	0.0027	0.1243	14.3892	0.5705	0.0779	0.0027	0.2839	420.0	16.4
VP004-21	0.30	0.8447	0.0418	0.0717	0.0029	0.1373	14.0333	0.5743	0.0858	0.0030	0.2769	426.0	17.6
VP004-22	0.24	0.8138	0.0437	0.0704	0.0029	0.1330	14.2325	0.5859	0.0847	0.0036	0.3045	418.8	17.1

VP004-23	0.34	0.6223	0.0282	0.0699	0.0027	0.0866	14.3495	0.5418	0.0646	0.0018	0.2230	429.3	16.3
VP004-24	0.23	0.9476	0.0610	0.0709	0.0030	0.2720	14.1600	0.6013	0.0974	0.0051	0.0380	413.1	17.6
VP004-25	0.26	0.9721	0.0575	0.0715	0.0029	0.1140	14.0427	0.5588	0.0991	0.0048	0.2446	415.6	17.4
VP004-26	3.79	0.8602	0.1258	0.0699	0.0033	0.3358	14.3991	0.6877	0.0892	0.0119	-0.1577	413.3	20.8
VP004-27	0.75	0.5829	0.0258	0.0670	0.0026	0.2050	14.9822	0.6018	0.0632	0.0016	0.2900	413.1	16.1
VP004-28	0.25	0.8366	0.0476	0.0703	0.0030	0.2872	14.3239	0.5938	0.0872	0.0040	0.1283	416.7	17.7
VP004-29	0.63	0.7568	0.0520	0.0700	0.0033	0.1512	14.4026	0.6277	0.0793	0.0048	0.2762	420.3	19.6
VP004-30	0.23	0.9882	0.0678	0.0714	0.0032	0.1825	14.1765	0.6682	0.1014	0.0062	0.1889	413.5	19.0

VP004-31	0.17	1.0661	0.0637	0.0726	0.0031	0.0978	13.9307	0.5983	0.1073	0.0054	0.2990	416.0	18.5
VP004-32	0.21	0.9313	0.0577	0.0720	0.0030	0.3461	13.9451	0.5774	0.0954	0.0051	0.0190	421.0	18.3
VP004-33	0.37	1.1646	0.0647	0.0732	0.0032	0.2818	13.8248	0.5983	0.1178	0.0055	0.1281	412.2	18.9
VP004-34	0.22	1.2139	0.0648	0.0739	0.0030	0.1487	13.6241	0.5640	0.1197	0.0049	0.2248	414.8	18.3
VP004-35	0.23	1.7629	0.1029	0.0809	0.0035	0.0301	12.4955	0.5825	0.1584	0.0081	0.4399	423.3	24.9
VP004-36	0.20	1.1485	0.0604	0.0763	0.0032	0.0206	13.2262	0.5549	0.1095	0.0045	0.4045	435.5	20.8
VP004-37	0.25	1.5398	0.0798	0.0778	0.0032	-0.0056	12.9438	0.5334	0.1442	0.0056	0.1309	417.8	20.9
VP004-38	0.35	0.7339	0.0332	0.0684	0.0026	0.2449	14.6712	0.5534	0.0780	0.0021	0.0265	411.4	15.6

VP004-39	0.32	0.6241	0.0267	0.0676	0.0026	-0.0282	14.8311	0.5697	0.0672	0.0017	0.1494	414.0	15.7
VP004-40	0.25	0.6254	0.0270	0.0678	0.0026	-0.0300	14.7671	0.5950	0.0669	0.0017	0.3956	415.2	15.7
VP006-1	0.38	4.1395	0.1707	0.0991	0.0039	0.0973	10.1167	0.4186	0.3038	0.0074	0.5829	412.1	17.9
VP006-2	0.81	4.7191	0.1810	0.1021	0.0039	0.2501	9.8186	0.3780	0.3373	0.0052	0.3926	396.1	16.4
VP006-3	0.47	5.2869	0.2029	0.1086	0.0042	0.1234	9.2410	0.3604	0.3545	0.0061	0.6407	405.7	17.7
VP006-4	0.74	7.2949	0.2827	0.1254	0.0049	0.1494	7.9937	0.3159	0.4232	0.0074	0.5815	396.3	19.4
VP006-5	0.60	7.3943	0.2942	0.1254	0.0051	0.2264	7.9819	0.3490	0.4281	0.0093	0.6616	391.2	20.5
VP006-6	0.41	19.3218	0.7558	0.2293	0.0094	0.3413	4.3839	0.1801	0.6141	0.0117	0.6640	358.0	37.4

VP006-7	0.56	4.8502	0.2571	0.1038	0.0044	0.6278	9.6918	0.4199	0.3389	0.0104	-0.1125	401.3	19.7
VP006-8	0.41	12.1703	0.4721	0.1665	0.0067	0.3470	6.0388	0.2406	0.5327	0.0094	0.6394	373.6	25.4
65um-1	1.07	10.9211	0.3609	0.1575	0.0051	0.0323	6.3697	0.2081	0.5042	0.0095	0.6479	390.9	22.8
VP007-1	0.58	3.5951	0.2677	0.0928	0.0041	0.6118	10.8146	0.4803	0.2809	0.0153	-0.2973	403.6	21.5
VP007-2	0.58	3.9303	0.2941	0.0940	0.0045	0.7803	10.7115	0.4907	0.3023	0.0134	-0.4198	392.3	21.4
VP007-3	0.22	0.8903	0.0460	0.0662	0.0027	0.0281	15.1615	0.6196	0.0974	0.0034	0.1029	390.1	15.6
VP007-4	0.83	4.3722	0.1707	0.0978	0.0038	0.0810	10.2303	0.4260	0.3232	0.0060	0.6345	391.2	16.5
VP007-5	0.40	10.9653	0.4585	0.1507	0.0062	0.3005	6.6565	0.2788	0.5319	0.0134	0.4292	339.8	25.4
VP007-6	0.29	11.8207	0.5660	0.1635	0.0071	0.5321	6.1919	0.2739	0.5237	0.0140	0.2700	379.1	29.4

VP007-7	0.63	4.1775	0.2017	0.0975	0.0041	0.3474	10.3113	0.4401	0.3113	0.0099	0.2398	399.6	18.8
VP007-8	0.75	5.5283	0.2128	0.1078	0.0043	-0.0327	9.2970	0.3622	0.3736	0.0073	0.7318	385.6	17.5
VP007-9	0.34	1.1542	0.0945	0.0720	0.0031	-0.1281	13.9877	0.6281	0.1162	0.0082	0.2302	412.7	18.2
VP007-10	0.31	0.9291	0.0534	0.0759	0.0030	0.1399	13.2277	0.5186	0.0891	0.0039	0.1187	451.4	17.7
VP007-11	0.45	6.2571	0.2666	0.1145	0.0048	0.1893	8.7990	0.3763	0.3988	0.0109	0.5833	385.2	20.3
VP007-12	0.17	5.3595	0.2164	0.1105	0.0044	0.0677	9.0869	0.3678	0.3541	0.0078	0.5876	412.9	18.8
VP007-13	0.09	0.7400	0.0337	0.0754	0.0029	0.1586	13.3004	0.5127	0.0715	0.0020	0.2458	459.3	17.6
VP007-14	0.12	12.3957	0.5660	0.1729	0.0071	0.7671	5.8302	0.2418	0.5211	0.0096	-0.1666	404.3	27.3

VP007-15	0.08	0.8140	0.0357	0.0753	0.0029	0.1755	13.2942	0.5220	0.0783	0.0018	0.2226	454.2	17.1
65um-1	0.46	3.0654	0.1143	0.0886	0.0029	0.0034	11.3486	0.3785	0.2522	0.0067	0.5282	406.6	14.4
65um-2	0.86	0.6202	0.0364	0.0676	0.0023	0.1084	14.8552	0.5254	0.0666	0.0033	0.1523	415.3	13.9
65um-3	0.30	2.1714	0.2132	0.0820	0.0050	-0.0300	12.8133	0.8105	0.2061	0.0244	0.6147	407.9	29.3
65um-4	0.43	5.6829	0.1998	0.1101	0.0036	-0.0412	9.0848	0.3186	0.3738	0.0086	0.2968	393.6	16.3
65um-5	0.30	1.1579	0.0700	0.0795	0.0031	0.2481	12.7786	0.5275	0.1055	0.0054	0.2630	461.7	18.1
65um-6	0.30	0.6167	0.0251	0.0699	0.0022	0.1770	14.3162	0.4397	0.0644	0.0017	0.1838	430.6	13.3
65um-7	0.82	3.2530	0.1109	0.0899	0.0029	0.2139	11.1673	0.3554	0.2638	0.0050	0.4406	403.9	13.7
65um-8	0.51	7.4522	0.4378	0.1281	0.0053	0.3587	7.8823	0.3330	0.4219	0.0204	0.2279	405.9	28.8
65um-9	1.07	10.9211	0.3609	0.1575	0.0051	0.0323	6.3697	0.2081	0.5042	0.0095	0.6479	390.9	22.8

Appendix F

Sm-Nd Isotopic Data

Table F.1: Raw Sm-Nd data for LLK and Koonenberry samples analysed as part of this project.

Sample	Geology	Sm (ppm)	Nd (ppm)	$^{147}Sm/^{144}Nd$	$^{143}Nd/^{144}Nd$	eNd (now)	Geol Age T, Ga	TDM1, Ga	eNd
VP004	Gabbro	7.23	32.3	0.13517	0.51257	-1.2	0.43	1.13	2.1
VP006	Dolerite	5.12	19.4	0.15944	0.51270	1.4	0.43	1.26	3.4
VP009	Diorite	7.36	33.5	0.13282	0.51260	-0.6	0.43	1.04	2.9
VP009 re-analyse	Diorite	7.19	32.6	0.13316	0.51262	-0.3	0.43	1.01	3.2
VP012	Gabbro	2.69	7.3	0.22383	0.51313	9.7	0.49	-0.25	8.0
VP012 re-analyse	Gabbro	2.67	7.2	0.22379	0.51310	9.3	0.49	-0.57	7.5
VP013	Basalt	9.15	37.1	0.14922	0.51266	0.5	0.52	1.17	3.6
PJG0059	Porphyritic basalt	3.69	9.9	0.22457	0.51309	8.9	0.4	-0.77	7.5
PJG0080	Dolerite	4.48	16.6	0.16298	0.51244	-3.7	0.509	2.15	-1.6
PJG0082	Gabbro	2.27	6.5	0.21153	0.51303	7.8	0.43	12.44	6.9

PJG0082 replicate	Gabbro	2.32	6.7	0.21049	0.51302	7.7	0.43	7.45	6.9

Appendix G

Trace Element Data

Table G.1: Raw zircon trace element data for concordant analyses

Spot	Ti	Y	Zr	La	Ce	Pr	Nd	Sm	Eu	Gd	Tb	Dy	Ho	Er	Tm	Yb	Lu	Hf	Th	U
VP001-01 - 1	11.7	2035	425765	1.08	74.2	1.84	15.5	15.1	3.15	63.4	17.2	179	62.4	273	54.7	485	97.7	10435	925	819
VP001-02 - 1	17.2	1710	442416	0.80	47.6	1.45	15.0	17.7	3.97	64.1	17.3	173	55.5	236	44.3	388	75.8	8564	482	358
VP001-05 - 1	-	1397	278889	0.99	47.5	1.13	10.7	11.0	2.64	36.5	10.7	116	42.7	196	39.0	364	75.7	6364	658	692
VP001-06 - 1	16.0	2235	463820	0.92	70.8	1.70	17.6	17.6	4.02	69.0	20.0	211	70.6	308	59.1	529	105	10312	955	816
VP001-07 - 1	16.7	974	369042	4.75	57.4	4.48	27.0	14.1	3.21	31.4	8.66	85.1	29.4	132	26.1	248	51.4	9324	528	492
VP001-08 - 1	22.6	1304	443136	0.19	52.7	0.52	7.36	10.3	2.44	42.0	12.1	126	41.8	181	35.5	312	62.8	8687	619	481
VP001-11 - 1	21.0	2249	449724	0.71	61.8	1.61	16.1	17.8	4.50	74.8	21.3	216	72.3	312	59.1	516	103	9303	834	671

VP001-12 - 1	9.83	1367	460829	0.18	52.3	0.48	7.10	11.0	2.47	43.1	12.5	132	43.4	193	38.0	334	66.1	10863	465	435
VP001-14 - 1	19.4	1607	456009	0.96	67.0	1.17	11.8	12.6	2.95	47.3	13.6	145	50.5	229	45.9	416	84.9	10141	743	755
VP001-L1-02 - 1	30.5	2609	431379	0.72	62.6	1.76	17.2	20.8	5.72	96.3	26.1	261	86.0	362	69.5	595	115	7976	964	650
VP001-L1-03 - 1	29.9	3057	444188	0.59	83.3	1.39	18.5	30.5	7.43	128	33.9	322	102	420	77.7	665	126	7983	1063	645
VP001-L1-04 - 1	25.9	2851	432230	0.18	73.0	1.11	16.9	24.8	5.96	110	29.6	293	95.4	391	73.1	624	119	7924	974	612
VP001-L1-07 - 1	25.7	1091	435107	0.15	40.1	0.44	6.47	9.36	2.30	37.7	10.4	106	35.2	154	29.6	271	53.3	8123	332	292
VP001-L1-08 - 1	26.9	2570	437772	0.25	59.9	1.25	15.3	22.5	5.55	94.7	25.6	255	84.4	353	66.9	577	110	7830	917	591
VP001-L1-09 - 1	25.2	2067	430036	0.14	51.2	1.01	13.0	19.3	4.60	79.9	21.7	212	69.0	286	53.8	464	91.0	7880	593	425

VP001-L1-11 - 1	20.0	3170	443184	0.19	89.5	1.27	15.9	23.1	5.34	112	32.1	319	105	439	82.6	709	136	9255	1415	952
VP001-L1-12 - 1	26.8	2168	435659	0.13	53.8	0.94	12.7	19.9	4.89	84.8	22.4	223	72.5	302	56.9	493	95.5	7869	652	455
VP001-L1-15 - 1	20.6	1797	441289	0.24	48.8	1.05	13.1	17.3	4.17	67.3	18.3	185	59.4	251	47.6	417	80.8	8563	535	413
VP001-L1-18 - 1	21.0	2396	436685	0.13	57.6	0.77	10.4	17.4	4.73	85.4	23.5	239	79.5	332	62.1	541	103	8757	842	560
VP001-L1-19 - 1	32.1	1436	449429	0.61	68.7	0.90	9.06	11.0	2.52	44.0	13.1	135	46.5	203	39.3	356	70.0	8822	789	689
VP001-L1-20 - 1	22.1	2251	432282	0.15	57.2	1.01	13.9	20.4	5.05	87.1	23.3	234	75.0	311	59.1	507	98.0	8079	716	492
VP001-L1-22 - 1	17.6	1751	441480	0.70	55.0	1.23	13.0	14.9	3.34	57.1	16.4	164	56.1	243	47.9	423	82.3	10240	699	638
VP001-L1-23 - 1	27.3	2462	431313	0.15	60.2	1.02	13.9	23.7	5.55	96.0	26.3	251	80.5	333	62.0	535	103	7840	801	525

VP001-L1-24 - 1	22.1	2059	426866	0.11	51.3	0.84	11.7	17.5	4.50	77.2	21.3	213	69.6	287	54.2	475	90.6	8278	638	456
VP001-L1-25 - 1	26.3	3153	430610	0.23	78.2	1.24	16.8	29.3	7.41	130	34.3	332	107	442	81.4	703	134	7989	1172	739
VP001-L2-01 - 1	24.2	2046	455718	0.36	64.2	0.98	12.0	18.5	4.33	76.1	21.0	206	67.3	280	53.8	473	90.7	8924	789	580
VP001-L2-02 - 1	25.0	2862	446611	0.27	69.6	1.14	14.4	23.2	5.86	106	29.8	295	95.4	396	74.9	644	124	8241	1099	704
VP001-L2-06 - 1	18.9	1988	441376	0.46	49.9	1.21	13.2	16.2	3.71	65.0	18.6	191	64.1	277	54.4	474	93.5	8671	627	523
VP001-L2-09 - 1	21.6	2469	447586	0.20	63.3	1.04	13.4	20.8	5.02	88.9	24.5	242	80.8	338	63.7	567	108	9206	911	701
VP001-L2-10 - 1	28.3	927	437307	0.31	41.3	0.32	4.26	6.11	1.57	24.9	7.26	81.2	29.3	134	27.4	250	51.8	8141	386	352
VP002-03 - 1	14.5	1947	430860	0.06	82.6	0.25	3.93	6.48	1.80	32.6	11.8	152	60.2	295	62.0	575	117	8882	505	478

VP002-04 - 1	14.1	4868	438233	2.73	172	2.25	25.7	32.8	8.08	136	41.8	458	162	726	143	1264	246	9053	2489	1222
VP002-06 - 1	-	4011	389310	42.6	315	19.5	96.5	36.5	15.7	94.0	29.9	340	123	558	120	1089	231	9753	4188	2881
VP002-09 - 1	25.3	4617	446370	5.88	140	4.82	38.6	27.8	8.26	119	37.3	426	153	688	136	1220	239	9614	2542	1351
VP002-L1-01 - 1	17.2	5203	437538	3.20	140	3.80	31.4	36.9	10.4	153	45.1	489	172	765	151	1345	259	8682	2018	923
VP002-L1-02 - 1	12.8	4131	416816	3.32	124	3.93	32.0	32.1	8.67	125	36.7	393	138	612	119	1061	203	8424	1439	740
VP002-L1-03 - 1	11.6	5358	422750	3.92	187	3.69	33.5	39.0	9.70	161	48.4	514	180	784	154	1351	252	8726	2248	1173
VP002-L1-08 - 1	11.5	4978	434125	2.90	147	1.90	22.7	34.0	8.77	147	43.9	476	165	731	145	1270	242	8633	2004	967
VP002-L1-09 - 1	43.4	3158	439011	4.74	108	5.55	39.6	31.0	10.5	100	28.2	299	104	467	92.9	831	165	8688	1022	588

VP002-L2-06 - 1	14.5	4651	421100	0.96	152	2.46	26.3	34.9	8.87	138	40.9	432	155	682	136	1205	233	9246	2097	1182
VP002-L2-08 - 1	11.3	3378	429341	0.24	89.6	1.23	17.2	24.4	6.31	102	29.5	316	112	499	98.9	891	175	8393	1021	591
VP002-L2-10 - 1	22.1	3075	432438	2.15	102	3.28	24.4	24.0	7.28	91.8	26.7	287	102	461	91.7	826	164	7881	1202	607
VP002-L2-11 - 1	16.9	7219	422576	1.56	199	2.97	39.3	61.8	17.0	251	70.4	722	241	1043	200	1746	329	7741	3014	1053
VP002-L2-13 - 1	27.7	3101	443955	2.11	88.1	3.26	26.7	26.8	7.61	94.2	27.1	290	102	457	90.7	828	164	8632	876	528
VP002-L2-14 - 1	20.8	3876	446307	1.37	106	2.56	25.6	30.9	8.95	118	34.4	361	128	574	115	1015	199	8517	1196	659
VP002-L2-16 - 1	20.0	3551	429171	1.08	96.4	1.89	21.4	27.8	7.78	108	31.0	329	116	521	104	925	182	7967	1170	570
VP002-L2-18 - 1	12.0	3390	443525	3.32	112	4.05	33.2	25.7	7.91	99.2	28.5	309	111	499	101	905	180	9454	1251	759

VP002-L2-20 - 1	28.1	2312	449091	1.50	67.2	2.22	19.0	18.9	5.23	65.3	19.1	210	75.4	344	68.8	612	124	8643	624	422
VP008(#2)-03 - 1	15.9	1011	445851	0.04	15.2	0.10	1.49	2.33	1.50	15.9	5.75	74.7	30.8	157	35.2	361	82.5	7116	180	268
VP008(#2)-11 - 1	-	3747	436165	0.01	2.98	0.04	1.07	4.32	0.31	38.7	19.2	287	125	650	140	1286	253	11534	110	565
VP008(#2)-12 - 1	8.73	825	430413	0.07	22.6	0.49	5.59	6.86	3.14	26.7	7.13	76.4	26.4	121	25.2	250	54.0	6958	314	314
VP008(#2)-15 - 1	26.4	2258	446061	0.44	56.0	1.14	14.7	22.0	5.37	87.6	23.7	231	75.1	311	58.6	503	95.9	7781	636	453
VP008(#2)-22 - 1	7.84	1036	432485	0.04	18.9	0.35	4.94	6.68	3.11	25.9	8.09	90.0	32.8	155	34.4	337	73.5	7939	168	192
VP008(#2)-25 - 1	-	173	448837	0.01	4.73	0.02	0.30	0.43	0.27	2.38	0.94	11.4	5.29	28.4	6.77	76.0	19.1	6459	64	132
VP008-01 - 1	16.6	1757	436282	0.68	40.1	0.99	7.02	7.65	4.01	40.7	12.7	149	55.4	261	53.8	517	111	7351	451	479

VP008-09 - 1	22.3	2343	427971	0.03	6.96	0.31	5.00	10.8	2.23	57.7	18.9	226	81.2	361	69.5	616	116	7182	224	175
VP008-12 - 1	8.61	576	430160	-	11.5	0.07	1.05	1.63	0.88	7.77	2.71	38.8	16.7	91.7	21.8	237	57.0	7731	92	192
VP008-17 - 1	8.40	696	433184	0.01	9.63	0.11	1.63	2.15	1.08	9.72	3.47	46.1	20.3	116	28.4	318	75.4	7936	86	141
VP008-21 - 1	10.9	1195	424826	0.08	23.0	0.19	2.29	3.77	1.42	21.0	7.40	94.4	37.0	186	40.3	390	83.7	7685	183	232
VP008-22 - 1	7.42	309	437819	0.03	7.03	0.10	1.15	1.64	0.78	6.49	1.96	23.9	9.31	48.8	11.3	119	28.4	7998	47	86
VP008-24 - 1	9.72	484	439010	0.01	10.0	0.08	1.13	1.58	0.78	7.35	2.64	34.1	14.4	78.4	18.0	200	49.7	7390	73	149
VP008-28 - 1	11.7	387	439884	0.01	7.92	0.06	0.95	1.39	0.81	6.50	2.23	26.7	11.7	61.8	14.7	159	39.2	7047	52	107
VP008-31 - 1	13.0	480	426476	-	11.1	0.08	1.13	1.87	0.83	8.03	2.56	32.6	14.4	78.5	17.9	193	46.6	6896	66	138

VP008-33 - 1	11.5	1002	424589	0.04	16.7	0.29	4.24	6.58	2.57	29.3	8.45	93.5	32.8	149	30.3	289	60.8	7209	134	143
VP008-35 - 1	17.0	955	429309	0.01	5.42	0.05	0.98	2.25	0.38	15.4	5.82	76.4	30.9	156	32.5	308	62.4	7968	62	99
VP012F-03 - 1	16.4	764	441386	0.01	4.64	0.06	1.22	2.51	0.15	16.5	5.79	70.2	26.1	119	23.4	208	40.2	9991	41	135
VP012F-04 - 1	17.5	2109	445054	0.01	8.25	0.21	4.07	7.63	2.22	46.3	16.0	193	72.4	333	64.5	568	113	8555	127	131
VP012F-05 - 1	14.6	848	458905	-	4.91	0.02	0.96	2.57	0.73	16.0	5.83	73.0	28.3	136	27.5	250	51.3	9792	39	56
VP012F-06 - 1	8.53	1031	440103	-	8.21	0.06	1.08	2.59	0.27	17.1	6.51	84.4	33.3	167	35.0	327	65.2	9231	129	269
VP012F-07 - 1	13.2	1683	428443	-	7.24	0.17	2.94	6.11	1.70	34.8	12.3	152	57.2	266	52.8	461	92.1	8809	103	114
VP012F-09 - 1	15.4	526	435120	-	4.20	0.02	0.40	1.22	0.34	9.34	3.72	45.8	17.5	84.0	17.0	153	32.5	9211	27	71

VP012F-10 - 1	16.8	2265	431480	0.02	9.06	0.24	3.63	8.07	2.16	49.2	16.8	209	77.2	358	67.1	592	117	8658	149	148
VP012F-11 - 1	12.1	643	434618	-	5.25	0.04	0.79	1.74	0.50	10.8	4.32	53.9	21.4	105	22.1	202	42.9	9003	41	67
VP012F-13 - 1	11.7	794	424650	0.01	3.85	0.08	1.30	3.02	0.18	16.5	5.76	70.4	26.3	123	24.5	224	44.8	11048	67	216
VP012F-14 - 1	14.1	622	433374	-	4.99	0.02	0.55	1.75	0.46	10.3	3.87	51.6	20.4	100	20.8	197	42.4	8882	33	58
VP012F-15 - 1	13.7	565	436348	-	4.18	0.02	0.51	1.48	0.45	8.70	3.54	46.0	18.6	93.4	19.6	185	39.7	8838	24	43
VP012F-17 - 1	9.37	476	434262	-	4.80	0.03	0.59	1.12	0.64	6.34	2.43	33.3	14.2	78.8	19.2	207	51.1	9144	58	102
VP012F-18 - 1	14.4	451	438804	-	4.53	-	0.31	1.03	0.26	7.51	2.73	36.6	14.5	72.7	15.3	143	30.3	9346	28	49
VP012F-19 - 1	15.3	2529	438826	0.20	11.4	0.42	4.98	9.38	2.86	56.0	19.3	233	87.3	402	77.5	686	138	8778	176	178

VP012F-20 - 1	13.6	1627	440976	0.00	8.15	0.14	2.42	5.11	1.43	30.9	11.2	137	53.9	264	53.5	493	104	8855	97	135
VP012F-25 - 1	-	750	431924	-	8.40	0.03	0.73	1.40	0.55	8.58	3.38	47.5	21.6	127	31.9	350	86.3	9977	165	355
VP012F-27 - 1	-	66	433236	-	1.11	0.01	0.08	0.15	0.01	1.47	0.58	7.43	2.66	13.0	2.96	30.4	6.90	8249	1	29
VP012F-28 - 1	-	58	441045	-	0.18	-	-	-	0.01	0.94	0.43	5.89	2.35	14.1	3.80	45.9	12.0	8052	1	64
VP012F-30 - 1	12.2	559	428347	-	5.72	0.02	0.42	1.37	0.40	9.35	3.52	46.6	18.6	92.6	19.2	179	38.8	9640	38	67
VP012F-31 - 1	17.0	1290	436116	-	8.06	0.05	1.16	3.09	0.92	19.1	7.18	96.7	41.2	219	47.2	452	99.6	8416	62	129
VP012F-32 - 1	10.9	775	448047	-	5.55	0.02	0.55	1.94	0.52	12.1	4.61	61.4	25.5	127	27.1	254	54.9	9414	38	68
VP012F-34 - 1	15.6	979	432884	-	6.51	0.05	1.01	2.49	0.70	15.2	5.74	76.4	31.5	162	35.0	335	73.9	8599	45	91

VP012F-35 - 1	15.6	1643	421724	0.01	8.13	0.13	2.62	4.80	1.49	30.2	11.2	142	54.7	266	55.2	502	104	8315	90	126
VP012F-36 - 1	16.4	1911	440820	0.01	10.2	0.13	2.24	5.15	1.50	32.1	11.6	154	62.4	312	64.1	597	126	8587	112	172
VP012F-39 - 1	14.7	582	443555	-	4.79	0.03	0.64	1.44	0.41	9.32	3.71	48.5	19.1	95.1	19.7	185	39.5	9020	34	58
VP012F-40 - 1	12.4	758	436041	-	5.46	0.03	0.65	2.21	0.57	12.3	4.71	61.0	24.5	123	25.4	245	52.0	8783	37	65
VP012F-42 - 1	10.5	524	437250	-	5.01	-	0.33	1.31	0.47	9.09	3.30	43.0	17.2	84.7	17.8	166	34.6	9502	34	57
VP012M-05 - 1	12.5	609	445104	-	1.75	0.01	0.34	0.65	0.45	5.11	2.32	35.9	18.0	108	26.4	291	71.1	6458	16	36
VP012M-09 - 1	11.4	662	436364	-	1.98	0.01	0.25	0.74	0.54	6.12	2.54	40.8	19.9	118	27.5	300	72.8	6770	17	37
VP012M-16 - 1	10.7	441	429675	-	1.21	-	0.36	0.94	0.60	6.55	2.59	34.1	14.0	73.7	16.1	167	37.9	7326	13	19

VP012M-17 - 1	9.45	522	446248	-	1.24	-	0.48	0.88	0.55	6.79	2.75	38.7	16.3	86.5	19.6	193	44.5	7524	13	20
VP012M-18 - 1	10.1	901	438482	-	2.65	0.09	1.27	2.26	1.28	14.2	5.18	69.6	28.5	146	32.3	319	71.8	8309	68	79
VP012M-21 - 1	11.5	780	432430	-	4.71	0.03	0.63	1.59	0.48	11.2	4.24	57.3	24.4	128	28.4	279	62.4	8803	40	79
VP012M-24 - 1	11.4	567	434207	-	1.43	-	0.42	1.11	0.61	7.20	2.79	38.9	17.6	96.8	22.4	235	56.7	6857	11	21
VP012M-25 - 1	9.46	563	436067	-	1.49	0.03	0.43	0.91	0.66	7.17	2.77	39.8	17.2	95.6	22.2	236	56.0	6919	14	26
VP012M-26 - 1	17.7	2295	421202	0.02	6.47	0.20	3.16	6.22	2.23	43.3	15.7	200	77.9	364	70.4	628	125	8234	137	137
VP012M-28 - 1	16.3	919	441779	-	2.69	0.02	0.44	1.10	0.61	10.0	3.99	59.9	27.6	155	35.6	360	83.2	7856	12	27
VP012M-30 - 1	10.9	365	439848	-	1.17	0.01	0.16	0.51	0.32	4.19	1.71	24.2	11.2	63.1	14.9	164	40.2	6842	11	25

VP012M-36 - 1	-	256	442982	-	1.05	-	0.08	0.33	0.26	2.75	1.14	17.2	7.68	44.6	10.8	118	29.8	7057	9	19
VP013-03 - 1	7.94	2138	455134	0.05	19.2	0.44	6.60	10.4	4.41	47.1	15.7	183	69.2	334	73.7	723	152	7337	309	367
PJG0059-L1-24 - 1	8.57	1965	445488	0.05	40.6	0.22	3.57	7.80	2.33	40.8	14.1	173	65.5	310	64.0	594	121	9757	260	250
PJG0059-L2-03 - 1	-	3704	431482	0.30	51.4	0.46	6.48	13.7	3.71	68.7	25.3	316	120	580	122	1127	225	9672	549	943
PJG0059-L2-09 - 1	-	3601	449745	1.33	50.5	1.20	10.1	15.1	3.00	72.5	26.9	332	123	568	115	1042	199	10608	364	696
PJG0059-L2-11 - 1	14.1	7444	436919	0.51	186	1.57	21.7	36.8	11.1	187	60.3	693	258	1157	223	1969	377	8027	1653	943
PJG0080-L1-02 - 1	-	5225	425712	8.51	118	7.96	52.3	30.9	4.57	121	40.9	474	175	766	146	1187	214	6442	1199	791
PJG0080-L1-03 - 1	16.8	12817	436591	8.73	221	9.84	81.1	83.0	12.4	360	114	1269	433	1838	333	2629	454	7474	3332	1608

PJG0080-L1-11 - 1	13.1	7755	425869	1.12	91.0	2.10	22.4	35.6	4.70	185	62.0	722	259	1125	208	1696	296	8232	1720	1097
PJG0080-L2-02 - 1	21.2	7851	413628	0.07	23.3	0.45	9.14	25.7	2.70	164	62.1	762	277	1210	221	1765	312	8037	620	352
PJG0080-L2-03 - 1	38.0	5402	423041	0.03	9.27	0.29	7.31	22.2	2.93	136	48.9	562	192	781	137	1051	178	10100	850	349
PJG0080-L2-04 - 1	29.8	4958	426921	0.02	10.8	0.31	6.91	18.9	1.96	120	43.4	504	174	740	129	1016	173	9062	228	187
PJG0080-L2-06 - 1	19.0	11739	412822	0.12	56.2	1.05	18.2	41.4	3.69	248	88.9	1044	360	1546	288	2328	413	11314	2326	445
PJG0080-L2-07 - 1	24.7	5785	432512	0.03	18.2	0.47	9.11	24.1	2.73	145	52.2	598	206	853	149	1153	193	9700	1551	464
PJG0080-L2-10 - 1	23.5	3286	437374	-	9.07	0.23	4.66	13.0	1.54	80.5	28.9	342	119	494	87.8	674	115	9912	482	222
PJG0080-L2-11 - 1	26.4	4430	435094	-	6.44	0.26	4.11	13.0	2.16	92.5	34.2	417	150	644	117	931	165	8419	1085	572

PJG0080-L2-13 - 1	30.6	5184	437322	0.04	17.1	0.44	9.29	23.1	2.18	131	46.6	530	181	737	127	967	160	11010	1116	334
PJG0080-L2-14 - 1	31.7	4616	444757	0.03	10.5	0.32	6.95	19.8	2.13	121	41.8	482	161	651	111	838	139	9838	509	211
PJG0080-L2-15 - 1	59.2	6619	436938	0.03	27.8	0.44	7.73	23.0	3.16	162	57.9	679	234	963	174	1341	229	8061	803	398
PJG0080-L2-16 - 1	43.0	3716	440890	0.02	8.80	0.46	7.99	20.4	2.12	116	38.9	422	135	513	82.3	606	93.5	9587	311	143
PJG0080-L2-21 - 1	35.7	6726	447212	0.04	14.7	0.42	9.75	27.1	3.67	162	59.5	695	242	1009	180	1394	237	7869	282	221
PJG0080-L2-23 - 1	43.5	8758	441081	0.03	75.7	0.46	9.12	25.3	2.51	174	65.7	813	291	1278	238	1896	327	9791	2570	897
PJG0080-L2-24 - 1	43.0	4605	433811	-	27.2	0.32	5.78	16.2	2.00	106	38.8	456	159	670	120	955	163	8321	2087	580
PJG0080-L2-27 - 1	16.3	9730	439955	0.14	75.0	1.07	18.8	43.4	4.17	244	84.0	947	322	1333	236	1838	297	10185	3959	1359

PJG0082-01 - 1	1147	6969	426780	0.26	58.5	1.29	14.7	22.8	5.98	136	49.7	606	222	987	183	1481	255	9175	6160	1930
PJG0082-04 - 1	8.51	1005	450257	0.16	17.2	0.12	1.37	3.03	0.57	18.2	6.77	87.7	34.1	163	32.9	303	62.2	10398	134	204
PJG0082-11 - 1	16.9	1287	451230	-	10.6	0.64	10.9	24.1	3.91	112	27.8	197	40.1	111	16.0	120	21.3	11186	247	424
PJG0082-11b - 1	9.53	1126	504288	0.18	19.2	0.14	1.53	3.39	0.63	20.4	7.59	98.2	38.2	182	36.9	339	69.7	11646	150	228
PJG0082-14 - 1	28.4	2687	438947	0.08	18.0	0.48	5.78	8.65	2.42	52.6	19.6	244	90.9	403	77.3	651	117	8276	1310	633
PJG0082-15 - 1	29.1	8221	436126	0.17	19.4	0.66	10.9	28.5	4.15	185	66.9	805	286	1216	220	1772	307	10006	467	336

Appendix H

Lu-Hf Data

Table H.1: Raw zircon Lu-Hf data

Sample	$^{180}Hf/^{177}Hf$	$\pm 2\sigma$	$^{176}Yb/^{177}Hf$	$\pm 2\sigma$	$^{176}Lu/^{177}Hf$	$\pm 2\sigma$	$^{176}Hf/^{177}Hf$	$\pm 2\sigma$	Age (Ma)	ϵHf	$\pm 2\sigma$
PJG0059-L1-01 - 1	1.88700	0.00014	0.05960	0.00260	0.001852	0.000069	0.282524	0.000033	417	-0.46	0.33
PJG0059-L1-10 - 1	1.88706	0.00014	0.08510	0.00210	0.002769	0.000065	0.282629	0.000036	406	2.78	0.36
PJG0059-L1-18 - 1	2.23000	0.40000	0.14800	0.05600	0.002070	0.000430	0.283000	0.019000	397	15.91	190.00
PJG0059-L2-08 - 1	1.88781	0.00048	0.12520	0.00250	0.004130	0.000120	0.282990	0.000170	398	15.04	1.70

PJG0059-L2-13 - 1	1.88721	0.00015	0.10230	0.00260	0.003580	0.000140	0.282731	0.000060	398	6.01	0.60
PJG0080-L1-05 - 1	1.88758	0.00054	0.19920	0.00710	0.005240	0.000130	0.282950	0.000130	505	15.35	1.30
PJG0080-L2-09 - 1	1.88710	0.00012	0.09080	0.00260	0.002324	0.000052	0.282847	0.000028	524	13.08	0.28
PJG0080-L2-12 - 1	1.88709	0.00015	0.06850	0.00140	0.001819	0.000037	0.282874	0.000040	519	14.11	0.40
PJG0080-L2-18 - 1	1.88870	0.00440	0.14300	0.01100	0.003370	0.000120	0.283220	0.000680	512	25.68	6.80

PJG0080-L2-19 - 1	1.88705	0.00012	0.07720	0.00160	0.002392	0.000058	0.282357	0.000037	508	-4.62	0.37
PJG0080-L2-28 - 2	1.88703	0.00011	0.02292	0.00053	0.000732	0.000012	0.282250	0.000030	508	-7.85	0.30
PJG0082-02 - 1	1.88708	0.00014	0.15530	0.00250	0.004314	0.000032	0.282974	0.000034	504	16.49	0.34
PJG0082-03 - 1	1.88753	0.00051	0.04190	0.00430	0.001270	0.000120	0.282640	0.000200	432	4.14	2.00
PJG0082-09 - 1	1.88715	0.00015	0.03890	0.00160	0.001365	0.000052	0.282740	0.000039	430	7.60	0.39
PJG0082-13 - 1	1.88707	0.00013	0.02609	0.00028	0.000993	0.000034	0.282820	0.000034	430	10.54	0.34
VP001-L1-10 - 1	1.88780	0.00160	0.06850	0.00200	0.002050	0.000044	0.283000	0.000290	422	16.44	2.90

VP001-L1-14 - 1	1.88705	0.00013	0.05168	0.00057	0.001552	0.000021	0.282694	0.000034	425	5.82	0.34
VP001-L2-04 - 1	1.88723	0.00020	0.05750	0.00160	0.001750	0.000059	0.282880	0.000110	432	12.49	1.10
VP002-05 - 1	1.93000	0.16000	0.13800	0.04500	0.002140	0.000510	0.284000	0.027000	422	51.81	270.00
VP002-L1-04 - 1	1.88820	0.00180	0.11500	0.01100	0.003550	0.000310	0.283500	0.001700	423	33.74	17.00
VP002-L2-01 - 1	1.88681	0.00047	0.09750	0.00990	0.003040	0.000300	0.282970	0.000240	423	15.12	2.40
VP002-L2-03 - 1	1.88840	0.00780	0.13790	0.00540	0.004247	0.000068	0.282800	0.001400	423	8.77	14.00

VP002-L2-09 - 1	1.88702	0.00015	0.06940	0.00260	0.002199	0.000077	0.282613	0.000063	432	2.91	0.63
VP002-L2-15 - 1	1.88693	0.00014	0.09780	0.00480	0.002980	0.000140	0.282563	0.000033	423	0.74	0.33
VP008(#2)-07 - 1	1.88670	0.00110	0.02880	0.00490	0.000960	0.000140	0.283210	0.000490	426	24.27	4.90
VP008(#2)-10 - 1	1.88696	0.00013	0.07088	0.00096	0.002218	0.000033	0.282360	0.000029	434	-6.01	0.29
VP008(#2)-23 - 1	1.88693	0.00013	0.06460	0.00550	0.002220	0.000180	0.282763	0.000042	427	8.11	0.42
VP008-02 - 1	1.88700	0.00015	0.06520	0.00250	0.002231	0.000076	0.282750	0.000040	426	7.63	0.40
VP008-04 - 1	1.88712	0.00022	0.02720	0.00190	0.001005	0.000063	0.282823	0.000087	426	10.56	0.87

VP008-08 - 1	1.88704	0.00013	0.02810	0.00300	0.000848	0.000081	0.282541	0.000036	430	0.71	0.36
VP008-13 - 1	1.88693	0.00014	0.02015	0.00053	0.000739	0.000014	0.282698	0.000029	426	6.21	0.29
VP008-16 - 1	1.88704	0.00020	0.03250	0.00170	0.001187	0.000043	0.282733	0.000053	423	7.26	0.53
VP008-25 - 1	1.88712	0.00015	0.02535	0.00043	0.000969	0.000010	0.282688	0.000040	423	5.72	0.40
VP008-32 - 1	1.88706	0.00019	0.02726	0.00057	0.000981	0.000014	0.282698	0.000041	427	6.16	0.41
VP008-34 - 1	1.88697	0.00012	0.01600	0.00270	0.000484	0.000074	0.282683	0.000028	503	7.45	0.28
VP012F-01 - 1	1.88752	0.00018	0.01422	0.00037	0.000461	0.000014	0.282519	0.000039	488	1.32	0.39
VP012F-08 - 1	1.88692	0.00013	0.04770	0.00120	0.001532	0.000022	0.282501	0.000035	499	0.57	0.35

VP012F-12 - 1	1.88715	0.00027	0.01597	0.00027	0.000540	0.000006	0.282562	0.000061	507	3.24	0.61
VP012F-16 - 1	1.88710	0.00016	0.02080	0.00038	0.000686	0.000014	0.282540	0.000034	501	2.28	0.34
VP012F-21 - 1	1.88698	0.00014	0.03840	0.00140	0.001166	0.000036	0.282507	0.000039	490	0.71	0.39
VP012F-24 - 1	1.88703	0.00017	0.05500	0.00140	0.002178	0.000054	0.282698	0.000072	503	7.42	0.72
VP012F-33 - 1	1.88701	0.00015	0.05580	0.00170	0.001711	0.000038	0.282508	0.000036	491	0.59	0.36
VP012F-37 - 1	1.88686	0.00009	0.03910	0.00046	0.001234	0.000005	0.282541	0.000034	496	2.02	0.34
VP012F-38 - 1	1.88704	0.00012	0.02321	0.00032	0.000753	0.000015	0.282490	0.000036	498	0.42	0.36
VP012F-41 - 1	1.88695	0.00012	0.02519	0.00046	0.000822	0.000011	0.282497	0.000033	490	0.47	0.33

VP012M-15 - 1	1.88690	0.00013	0.03211	0.00034	0.001052	0.000021	0.282702	0.000038	506	8.00	0.38
VP012M-19 - 1	1.88703	0.00015	0.04179	0.00042	0.001498	0.000002	0.282759	0.000045	487	9.46	0.45
VP012M-20 - 1	1.88709	0.00012	0.04160	0.00220	0.001304	0.000056	0.282650	0.000033	492	5.77	0.33
VP012M-23 - 1	1.88685	0.00015	0.03600	0.00110	0.001304	0.000022	0.282922	0.000049	488	15.31	0.49
VP012M-27 - 1	1.88709	0.00018	0.04190	0.00170	0.001297	0.000037	0.282749	0.000080	490	9.24	0.80
VP012M-31 - 1	1.88686	0.00017	0.02445	0.00003	0.000914	0.000003	0.282845	0.000035	491	12.78	0.35
VP012M-32 - 1	1.88700	0.00017	0.02740	0.00220	0.001005	0.000092	0.282924	0.000057	511	15.98	0.57
VP012M-36 - 1	1.88702	0.00014	0.02800	0.00140	0.000990	0.000035	0.282924	0.000040	490	15.53	0.40

VP012M-37 - 1	1.88703	0.00018	0.03050	0.00100	0.001172	0.000032	0.282913	0.000046	519	15.71	0.46